DECOMPOSITION OF CARBONATES IN CAPTURE OF CARBON DIOXIDE FROM AMBIENT AIR

by

James Stephen Campbell

B.Sc., The University of Edinburgh, Scotland, 2009

M.Sc., The University of Edinburgh, Scotland, 2012

A THESIS SUBMITTED IN PARTIAL FULFILMENT OF

THE REQUIREMENTS FOR THE DEGREE OF

DOCTOR OF PHILOSOPHY

in

THE FACULTY OF GRADUATE AND POSTDOCTORAL STUDIES

(Chemical and Biological Engineering)

THE UNIVERSITY OF BRITISH COLUMBIA

(Vancouver)

December 2019

The following individuals certify that they have read, and recommend to the Faculty of Graduate and Postdoctoral Studies for acceptance, the dissertation entitled:

Decomposition of Carbonates in Capture of Carbon Dioxide from Ambient Air

submitted by James Stephen Campbell in partial fulfilment of the requirements for

the degree of Doctor of Philosophy

in Chemical and Biological Engineering

Examining Committee:

Professor John Grace, Chemical and Biological Engineering, UBC
Co-supervisor

Professor C. Jim Lim, Chemical and Biological Engineering, UBC
Co-supervisor

Professor Colin Oloman, Chemical and Biological Engineering, UBC
Supervisory Committee Member

Professor Jennifer Love, Chemistry, UBC
Supervisory Committee Member

Professor Paul Watkinson, Chemical and Biological Engineering, UBC
University Examiner

Professor Allan Bertram, Chemistry, UBC
University Examiner

Abstract

Direct Air Capture (DAC) is a technology for absorbing and concentrating CO_2 from air for geological sequestration or utilization. Capture is possible using alkali hydroxide solutions, forming alkali carbonates, with regeneration using lime or hematite. The CO_2-release step in each regeneration process requires high temperature, leading to high cost. A better understanding of the kinetics could reduce temperatures and facilitate integration with sustainable energy.

In lime regeneration of $KOH_{(aq)}$, $CaCO_{3(s)}$ decomposes forming $CaO_{(s)}$ and $CO_{2(g)}$ (+178 $kJ.mol^{-1}$). In this thesis it was found that all CO_2 was released by 780°C during thermogravimetric analysis ($N_{2(g)}$ flow rate of 60 $ml.min^{-1}$, heating rate of 20 $°C.min^{-1}$, particle size <5 μm and sample mass ~3 mg). A novel Accumulation Model was derived to describe the kinetics. Results indicated that the temperature of lime regeneration is tightly constrained by accumulation of reaction-generated $CO_{2(g)}$ in the particle pores and sample interstices.

In hematite regeneration of $NaOH_{(aq)}$, $Fe_2O_{3(s)}$ reacts with $Na_2CO_{3(s)}$, forming $NaFeO_{2(s)}$ and $CO_{2(g)}$ (+164 $kJ.mol^{-1}$). Ball-milling reduced particle size and mixed reactants intimately such that all $CO_{2(g)}$ was released by 760°C (1:1 mole ratio) or 680°C (16:1 mole ratio). 90 % of the sodium was extracted as $NaOH_{(aq)}$ by hydrolysis of $NaFeO_{2(s)}$. A Contact Point Model was used to describe the kinetics in terms of temperature, conversion, mole ratio, particle size and sample compactness. Results indicated that, with correct pre-treatment of the reactants, hematite regeneration could operate at lower temperature than lime regeneration.

Even greater temperature reductions might be achieved using alternative reagents. A multi-criteria decision analysis was used to create a shortlist of seven oxides based on their acidity, solubility, toxicity and price. Each of the seven oxides was ball-milled with $Na_2CO_{3(s)}$ and heated. Bixbyite (Mn_2O_3) showed most promise, reacting with $Na_2CO_{3(s)}$ (1:1 mole ratio) forming $NaMnO_{2(s)}$ and releasing all $CO_{2(g)}$ by 650°C (+132 $kJ.mol^{-1}$). 80 % of the sodium was recovered as $NaOH_{(aq)}$ by hydrolysis of $NaMnO_{2(s)}$. Bixbyite regeneration may therefore allow substantial reduction in the overall cost of Direct Air Capture using $NaOH_{(aq)}$.

Lay Summary

The rising atmospheric CO_2 concentration is causing global temperatures to increase, with possible harmful effects for humans and the environment. Direct Air Capture (DAC) systems are a novel method for removing carbon dioxide from the atmosphere. Alkali hydroxide DAC systems are very expensive due to the high temperature reactions involved. This thesis provides new understanding of these reactions and explores materials which operate at lower temperatures.

Preface

All the work presented in this thesis was completed by the author under the supervision of Professors John R. Grace and C. Jim Lim at the University of British Columbia. MATLAB computer code used to analyze kinetic data was written in collaboration with David Mochulski. Data in Table 4.3 were produced with the help of Xuantian Li.

Manuscripts accepted or destined for publication as a result of the work in this thesis:

Campbell, J.S., Grace, J.R., Lim, C.J. and Mochulski, D.W., 2016. A new diagnostic when determining the activation energy by the Advanced Isoconversional Method. Thermochimica Acta, 636, pp. 85-93.

Li, X., Grace, J.R., Bi, X. and Campbell, J.S., 2016. A new pyrolysis model based on generalized extreme value (GEV) distributions and its application to lignocellulosic biomass. Fuel, 184, pp. 211-221.

Campbell, J.S., Grace, J.R., Lim, C.J. and Li, X., 2019. The Accumulation Model for calcium carbonate decomposition. Submitted.

Campbell, J.S., Grace, J.R., and Lim, C.J., 2019. Kinetics of reaction between sodium carbonate and iron (III) oxide in regeneration of sodium hydroxide solution for Direct Air Capture. Submitted.

Table of Contents

List of Tables

List of Figures

List of Symbols

a	slope for the plot of $\ln A_i$ vs. E_i	$mol.kJ^{-1}$
a_p	slope for the plot of r vs. α_A	m
A	species A	none
A	intrinsic pre-exponential factor	s^{-1}
A_1	intrinsic pre-exponential factor for first reaction	s^{-1}
A_2	intrinsic pre-exponential factor for second reaction	s^{-1}
A_c	Smith's acidity constant	$kJ^{1/2}.mol^{-1/2}$
A_i	pre-exponential factor from peak matching exercise	s^{-1}
A_α	isoconversional pre-exponential factor	s^{-1}
b	intercept for the plot of $\ln A_i$ vs. E_i	none
b_1	correction factor, Accumulation Model	none
b_2	equilibrium constant, Grainy Pellet Model	none
b_p	intercept for the plot of r vs. α_A	m
B	species B	none
c	accumulation parameter	kPa.s
c_b	Campbell number	none
c_B^0	initial molar concentration of $CaCO_3$ in the particle	$kmol.m^{-3}$
c_Q^G	molar concentration of CO_2 in the gas phase	$kmol.m^{-3}$
c_{QS}^G	molar concentration of CO_2 in the gas phase at the particle-gas interface	$kmol.m^{-3}$

c_{QS}^{S}	molar concentration of CO_2 in the particle pores at the particle-gas interface	$kmol.m^{-3}$
C	species C	none
C_{AB}	total number of contact points between all particles of A and B	none
C_{A1_B}	number of contact points between one particle of A and surrounding particles of B	none
$C_{A1\_A,B}$	number of contact points between one particle of A and surrounding particles of A and B	none
C_p	specific heat capacity at constant pressure	$J.K^{-1}.kg^{-1}$
D	species D	none
D_e	effective diffusion coefficient of CO_2 through the pellet	$m^2.s^{-1}$
D_p	particle diameter	m
D_{sl}	sample layer diameter	m
E	intrinsic activation energy	$kJ.mol^{-1}$
E_1	intrinsic activation energy for first reaction	$kJ.mol^{-1}$
E_2	intrinsic activation energy for second reaction	$kJ.mol^{-1}$
E_i	activation energy from peak matching exercise	$kJ.mol^{-1}$
E_α	apparent isoconversional activation energy	$kJ.mol^{-1}$
$\tilde{E}_\alpha$	median apparent isoconversional activation energy	$kJ.mol^{-1}$
$f(\alpha)$	conversion dependency (derivative form)	none
$g(\alpha)$	conversion dependency (integral form)	none
$\Delta G°$	change in standard free energy of reaction	$kJ.mol^{-1}$

$h(P)$	pressure dependency	none
h_c	half the maximum distance of contact between particle A and B	m
h_s	height of sample	m
$\Delta H°$	change in standard enthalpy of reaction	$kJ.mol^{-1}$
$k(T)$	temperature dependency	s^{-1}
k_d	rate constant of the direct reaction in Grainy Pellet Model	$kmol.m^{-2}.s^{-1}$
k_f	rate constant for forward reaction	$l.mol^{-1}.s^{-1}$
k_r	rate constant for reverse reaction	$l.mol^{-1}.s^{-1}$
K_1	correction factor for Contact Point Model	none
K_c	equilibrium rate constant in Grainy Pellet model	$kmol.m^{-3}$
K_{eq}	equilibrium rate constant for CO_2 absorption	none
LD_{50}	lethal dose, 50 %	$mg.kg^{-1}$
m	mass	kg
m_A	mass of transformed species A	kg
m_B	mass of transformed species B	kg
m_A^0	initial mass of species A	kg
m_B^0	initial mass of species B	kg
m_{A1}	mean mass of transformed particle of A at time, t	kg
m_{B1}	mean mass of transformed particle of B at time, t	kg
m_i	initial sample mass	kg
$\bar{m}_i$	mean initial sample mass	kg

m_f	final sample mass	kg
m_t	sample mass at time, t	kg
m_β	number of repeat runs at heating rate β	none
M_A	molar mass of species A	$kg.mol^{-1}$
M_B	molar mass of species B	$kg.mol^{-1}$
n	reaction order	none
n_A	number of particles of species A	none
n_B	number of particles of species B	none
n_A^0	initial number of particles of species A	none
n_B^0	initial number of particles of species B	none
n_s	maximum number of nuclei per one m^2 of contact surface	m^{-2}
n_β	number of different heating rates (β's) used in isoconversional method	none
N	total number of stable nuclei	none
N_M	formal oxidation state of the metal in a compound	none
P	pressure	kPa
P_0	pre-exponential factor of nucleation used in Contact Point Model	s^{-1}
P_1	rate at which potential nucleus will transform into a stable nucleus	s^{-1}
P_{eq}	equilibrium partial pressure	kPa
P_{ext}	external partial pressure	kPa
P_{int}	internal partial pressure	kPa

q	$=\alpha_B/\alpha_A$	none
$\dot{q}_v$	heat sink (or source) term per unit volume of solid due to reaction	$W.m^{-3}$
Q	gas flow rate	$ml.min^{-1}$
r	mean radius of particles as a function of conversion	m
r_0	mean radius of particles at the start of the reaction	m
r_A	mean radius of a spherical particle of species A	m
r_A^0	initial mean radius of a spherical particle of species A	m
r_B^0	initial mean radius of a spherical particle of species B	m
r_f	mean radius of particles at the end of the reaction	m
r_s	initial radius of the sphere with the same surface area as the pellet	m
R	universal gas constant	$kJ.mol^{-1}.K^{-1}$
R'	density ratio used in Contact Point Model	none
s	surface area of contact between one particle of A and one of B	m^2
S	total surface area of contact between all particles of A and B	m^2
S_0	specific surface area	$m^2.kg^{-1}$
S_{sp}	specific surface area of the $CaCO_3$ in Grainy Pellet Model	m^{-1}
$\Delta S°$	change in standard entropy of reaction	$kJ.mol^{-1}.K^{-1}$
t	time	s
t_0	time of reaction initiation	s

t_f	time of reaction completion	s
t_a	time at particular value of α	s
T	temperature	K
T_i	temperature of reaction onset	K
T_f	temperature of reaction completion	K
T_{max}	temperature of maximum reaction rate	K
ΔT_{tl}	radial difference in temperature between sample center and surface due to thermal lag	K
ΔT_{tot}	total radial difference in temperature between sample center and surface	K
ΔT_{sc}	radial difference in temperature between sample center and surface due to self-cooling	K
V_a	apparent volume of sample	m^3
$w_{min,in}$	minimum work input for CO_2 separation	$kJ.mol^{-1}$
W_1	mass weighted contribution of first reaction to total conversion in dual-parallel process	none
W_2	mass weighted contribution of second reaction to total conversion in dual-parallel process	none
x_{CO2}	$CO_{2(g)}$ mole fraction	none
X_B	fraction of total particles which are of species B	none
Z	constant	kPa
α	conversion	none

α_1	conversion for first reaction in simulated dual-parallel process	none
α_2	conversion for second reaction in simulated dual-parallel process	none
α_{af}	ash-free reaction conversion	none
α_A	conversion of reactant A	none
α_B	conversion of reactant B	none
α_{CO_2}	CO_2 lost as a fraction of total potential releasable CO_2	none
α_s	standard reaction conversion	none
β	heating rate	$K.s^{-1}$
γ	compaction factor	none
δ_M	partial charges of the metal ion in a metal oxide	none
κ	thermal conductivity	$W.m^{-1}.K^{-1}$
λ	thermal diffusivity	$m^2.s^{-1}$
ρ_0	initial average density of a two-component powder sample	$kg.m^{-3}$
ρ_A	density of a particle of species A	$kg.m^{-3}$
ρ_B	density of a particle of species B	$kg.m^{-3}$
ρ_{cry}	crystalline density	$kg.m^{-3}$
ρ_f	final average density of a two-component powder sample	$kg.m^{-3}$
ϕ_i	initial voidage	none
χ	electronegativity constant	none
Ω_α	optimization indicator	none

List of Abbreviations

AAH-DAC	aqueous alkali hydroxide direct air capture
AIC	advanced isoconversional method
BECCS	bioenergy with carbon capture and storage
BET	Brunauer–Emmett–Teller
CCS	carbon capture and storage
CCU	carbon capture and utilization
CDR	carbon dioxide removal
CFC	chlorofluorocarbon
CPM	Contact Point Model
CSP	concentrated solar power
DAC	direct air capture
EOR	enhanced oil recovery
GHG	greenhouse gas
HAS	hyperbranched aminosilica

HTGR	high temperature gas-cooled reactor
HUM	hybrid ultramicroporous material
IAM	integrated assessment model
ICM	industrial carbon management
IL	ionic liquid
IPCC	International Panel on Climate Change
KCE	kinetic compensation effect
MCM	mobil composition of matter
MEA	monoethanolamine
MOF	metal organic framework
NFC	nano-fibrillated cellulose
NIMBY	not in my back yard
PEG	poly(ethylene glycol)
PEI	poly(ethyleneimine)
RCP	representative concentration pathway

SBA	ordered mesoporous silica
SEM	scanning electron micrography
TGA	thermogravimetric analysis
UBC	University of British Columbia
USDOE	United States Department of Energy
WEO	World Energy Organization
WGIII	working group 3
XRD	X-ray diffraction

Acknowledgements

I could not have been blessed with two better supervisors - John R. Grace and C. Jim Lim. Dr. Grace is the most humble, intelligent, supportive, patient, hardworking and caring man I know. He helped me become comfortable with the vastness of what I don't know. He never forced my path, only nudged it now and again. Dr. Lim has been an incredible support and has always been there for me when I needed guidance, offering me great encouragement and giving me new ways to approach problems. I am truly lucky and honored to have been the last PhD student under their joint supervision. Special thanks go to my great uncle George Cook and his wife Mary for giving me this amazing opportunity to start a new life in Vancouver. George's stamina is inspiring. What George has built and achieved leaves me in awe (although I'm pretty sure George couldn't have done it without Mary by his side). I hope to emulate him and create wealth and prosperity like he has and continue the tradition of Scottish scientists and engineers who make a difference in the world. If I achieve just 1 % of what he has, I will be very happy. Almost no one has helped me more over these four years than David Mochulski. He really changed the way I think and taught me that there is an answer to everything if you are willing to sit down and define the problem properly. David is truly a friend for life. I have received so much help over the past four years I can't begin to thank everyone. Clive Brereton for his unrelenting genius and humour and especially for his great advice regarding electrochemical processes. Siamak Elyasi and Jeffery Hoi for getting the project rolling before I arrived and passing on what they had learned. Colin Oloman for taking such a precise look at my work and helping me take my research to a new level of accuracy. Also, Jennifer Love and Tony Bi for their excellent

feedback on my work. Thanks go to Prof. Kevin Smith for donation of some transition metal oxides. Xuantian Li for inventing, not one, but two entirely novel kinetic methodologies and involving me in their development. I would like to thank Alex Wong for all his hard work as my summer intern. He set a high standard and impressed everyone in the department with his maturity and hard work. Shawn Mansfield and Scott Renneckar for allowing me to use their TGA instrument and to work in their lab in the Forestry department. Doug, Alex, Serge, Gordon and everyone at the department workshop for building necessary equipment and for their technical advice throughout the years. Branden Beatty - the catalyst for my move to Vancouver and for all his help getting set up when I arrived. Mijung Cho for always being there when I needed help with the most temperamental TGA in existence - she is one of the sweetest girls I have ever met. Sina Tebianian for teaching me how to program in MATLAB and for making me laugh when I needed it most. Andrew Knight for his help with particle size characterization. Anita Lam, Lan Kato and Jenny Lai for help with XRD. Jacob Kabel for his help with SEM. John Petkau and Nancy Heckman for interesting discussions about the statistical implications of my work. Naoko Ellis and Susan Nesbit for their support and encouragement and for giving me new opportunities outside of research which contributed greatly to my personal growth. Jay Schmitt for helping me during a few tough spots. To my best friend, Arthur Fonville, who will always be in my memory. I miss him very much. I would like to thank the smartest person I know, my brother Kenneth, for surprising me every day with a new perspective on something I always assumed I knew to be true. Finally, I am extremely grateful to Carbon Management Canada, Carbon Engineering and the Bill Gates Foundation, and the Natural Science and Engineering Research Council of Canada which provided the funding for the work.

Dedication

Dedicated to my parents:

Colin and Mary-Anne Campbell

Chapter 1: Introduction

1.1 Global warming

Carbon dioxide (CO_2) is Earth's most abundant, long-lived, non-condensing, radiative forcing gas (Parry et al., 2007). Consumption of fossil fuels, as well as widespread deforestation, has caused the atmospheric CO_2 concentration to increase by 100 ppmv in the past 100 years, and is thought to be causally related to a ~1°C rise in average global surface temperature within the same period (Hansen et al., 2010). Further increases in the average global surface temperature could have costly and possibly irreversible consequences for humans and the environment, including more severe weather, mass extinction and ocean acidification (Pachauri et al., 2014). International cooperation will be needed in order to find a cost-effective solution for this global problem.

1.2 Dealing with global warming

Keith (2000) defines four approaches to dealing with global warming and its consequences. These are:

1) Adaptation: Living with the problem by modifying human behavior, e.g. building barriers to sea level rise.
2) Geoengineering: Fixing the problem by intentional large-scale manipulation of the environment, e.g. by aerosol injection into the stratosphere.
3) Mitigation: Avoiding fossil fuel consumption by reducing energy intensity and switching to low-carbon energy production, e.g. solar and nuclear power.

4) Industrial Carbon Management (ICM): Continuing to use fossil fuels while sequestering or using the CO_2, e.g. Carbon Capture and Storage (CCS) and Carbon Capture and Utilization (CCU).

Adaptation is an ongoing process, but can be costly, especially during periods of large or rapid transformation. Geoengineering solutions often involve unknown social and environmental consequences. Thus, although it is likely that all four approaches will be necessary to one degree or another, mitigation and ICM have dominated the political discourse, see for example the Paris Agreement which aims to keep the increase in global average surface temperature below 2°C relative to pre-industrial times (OECD, 2016).

There are two main approaches to mitigation: 1. Reducing energy intensity and 2. Energy switching (i.e. from fossil to renewable energy). Improving energy efficiency and reducing its demand is seen as the fastest, cheapest and safest way to reduce CO_2 emissions. However, Sorrell (2015) argues that reducing energy intensity in order to cut emissions is severely limited owing to the strong relationship between energy consumption and economic growth. Ultimately, humanity's fossil fuel-based infrastructure must be replaced by non-fossil energy sources including wind, solar, hydropower, geothermal and nuclear.

In the meantime, fossil fuel will remain the driving force of our energy, industry and transportation, particularly in the developing world (OECD, 2016). Thus, a global-wide transition to renewable energy could take as long as a century (Sovacool, 2016). Industrial Carbon Management (ICM), i.e. Carbon Capture and Storage (CCS) and Carbon Capture and

Utilization (CCU), permit us to continue using fossil fuels while reducing CO_2 emissions, enabling the transition to a low-carbon economy in a cost-effective manner. ICM is reviewed in the next section.

1.3 Industrial Carbon Management (ICM)

1.3.1 Carbon Capture and Storage (CCS)

Many industries, such as fossil-fuel power plants, release huge quantities of CO_2 to the atmosphere. Carbon Capture and Storage (CCS) technology allows for continued energy production using fossil fuel but with reduced CO_2 emissions. There are three main approaches to CCS:

1) Post-combustion capture where CO_2 is separated from flue gas after a fossil fuel has been burned in air.
2) Pre-combustion capture where the fossil fuel is converted to syngas, which is a mixture of mostly H_2 and CO. The syngas is usually steam treated to form CO_2 and H_2. The CO_2 is captured and the H_2 used for energy.
3) Oxyfuel capture which involves burning the fuel in denitrified air, giving only CO_2 and H_2O as products.

Post-combustion capture will be essential for retrofitting existing plants. However, it has a higher energy demand than the pre-combustion capture and oxyfuel capture methods owing to a lower CO_2 partial pressure in the flue gas due to N_2 dilution. On the other hand, pre-combustion and oxyfuel methods have much higher investment and production costs (Kanniche et al., 2010).

In all three approaches, the captured CO_2 is pressurized to greater than 73 atm, forming a dense liquid that can be transported by pipeline or ship to a storage site and injected into rock pores deep below the Earth's surface. Metz et al. (2005) suggests that there is at least 2000 $GtCO_2$ of geological storage capacity, and maybe even as much as 200,000 $GtCO_2$, greatly exceeding the capacity needed for sequestration (200 $GtCO_2$).

1.3.2 Carbon Capture and Utilization (CCU)

Carbon Capture and Utilization (CCU) involves capturing and recycling CO_2. One advantage of CCU over CCS is its potential profitability. There are two different categories of CCU: physical and chemical (Rafiee et al., 2018). In physical utilization, the CO_2 remains chemically unchanged. Applications include fire extinguishers, refrigerants, aerosol propellants, beverage carbonation, welding medium, dry ice, solvents, Enhanced Geothermal Systems (EGS) and power generation using supercritical CO_2 as a replacement for the steam cycle. In chemical utilization, CO_2 is transformed into a new molecule. For example, methanol (Reller et al., 2014), polyurethane (Langanke et al., 2014), ethanol and biodiesel (Cuellar-Bermudez et al., 2015), urea (Bose et al., 2015), concrete (Monkman and MacDonald, 2017), methane (Veselovskaya et al., 2017), carbon monoxide (Chen et al., 2017), formic and acetic acid (Medrano-García et al., 2018), formate salts (Kar et al., 2018) and oxazolidinones (Hanusch et al., 2019) to name just a few. Such transformations can occur thermally, electrochemically, or biologically and usually require a catalyst, or in the latter case, an enzyme. Although CCU might be more attractive than CCS due to its potential profitability, a full Life cycle analysis (LCA) comparison is essential,

since CCU can have other adverse environmental consequences (Cuéllar-Franca and Azapagic, 2015).

1.4 Limitations of ICM

Figure 1.1 shows a summary of roughly 300 baseline and 900 mitigation scenarios taken from the scientific literature, categorized by CO_2-equivalent concentration by 2100 (Pachauri et al., 2014). Baseline scenarios (i.e. no mitigation) lead to representative concentration pathways (RCPs) between RCP6.0 and RCP8.5 (i.e. <3-5°C, respectively). To stabilize atmospheric CO_2 concentration between 430-480 ppmv (RCP2.6) and limit human induced warming to less than 2°C relative to pre-industrial times, a zero CO_2 emissions level should be achieved by 2080. Such a drastic reduction will require strong mitigation action, including widespread switching from fossil to non-fossil energy sources, as well as a global roll-out of Carbon Capture and Storage (CCS) technology and Carbon Capture and Utilization (CCU) (Gibbins and Chalmers, 2008).

There are approximately 200 CCS projects in operation (or in development) worldwide with about 40 of these at the industrial scale (Global CCS Institute, 2018). In order to meet a 2°C maximum warming target, many thousands of similar projects would need to become operational in the coming decades. However, even if a CCS roll-out of this magnitude were to be achieved, 30-50 % of global anthropogenic CO_2 emissions from small, dispersed stationary and mobile sources would go uncaptured (Lackner et al., 2001). This is because end-of-pipe capture from mobile sources, including airplanes and cars, is impractical given their intermittent operation and constraints on size and weight (Damm and Fedorov, 2008). In addition, transporting CO_2 from

small, distributed sources would be logistically complex and highly resource-consumptive. As such, alternative solutions are needed.

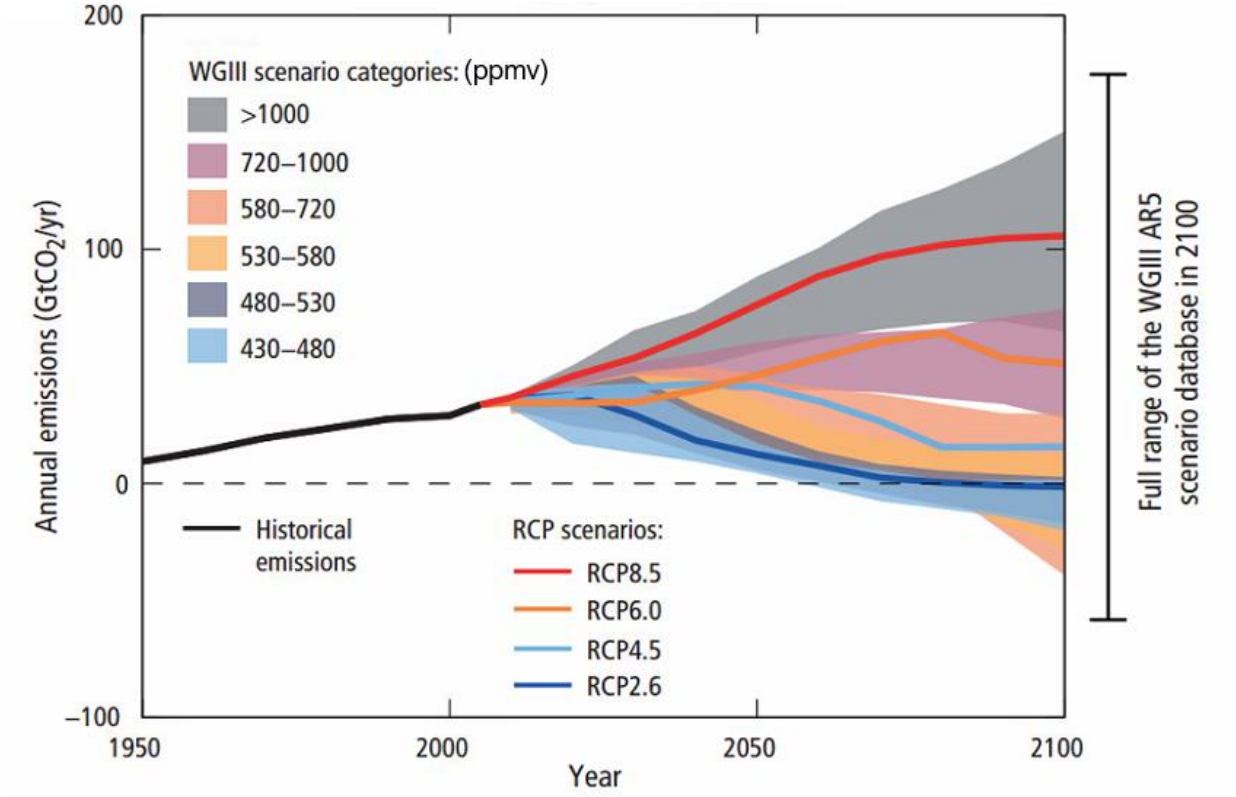

Figure 1.1 – Emissions of CO_2 alone in the Representative Concentration Pathways (RCPs) (lines) and the associated scenario categories used in Working Group 3 (WGIII). Coloured areas show 5 to 95 % range. The WGIII scenario categories summarize the wide range of emission scenarios published in the scientific literature and are defined based on CO_2-equivalent (CO_2-eq) concentration levels (in ppmv) in 2100. Roughly 300 baseline scenarios and 900 mitigation scenarios are categorized by CO_2-eq by 2100. The CO_2-eq includes forcing due to all GHGs (including methane, nitrous oxides, halogenated gases and tropospheric ozone), aerosols and albedo change (Pachauri et al., 2014).

1.5 Cardon Dioxide Removal (CDR)

Carbon dioxide removal (CDR) from the atmosphere could offer a scalable and economical solution to deal with small, distributed and mobile emitters. CDR can be achieved by restoration

or enhancement of the Earth's natural sinks (e.g. afforestation) or by artificial means (e.g. using technology to remove CO_2 from the air such as Direct Air Capture (DAC)). CDR decouples the capture stage from the point of emission by capturing and storing emissions from anywhere in the world using the atmosphere as the delivery mechanism (Keith et al., 2006).

1.6 Two ways to think about CDR

Figure 1.2 shows the cost of abatement of all the world's current global CO_2 emissions by end-of-pipe approaches.

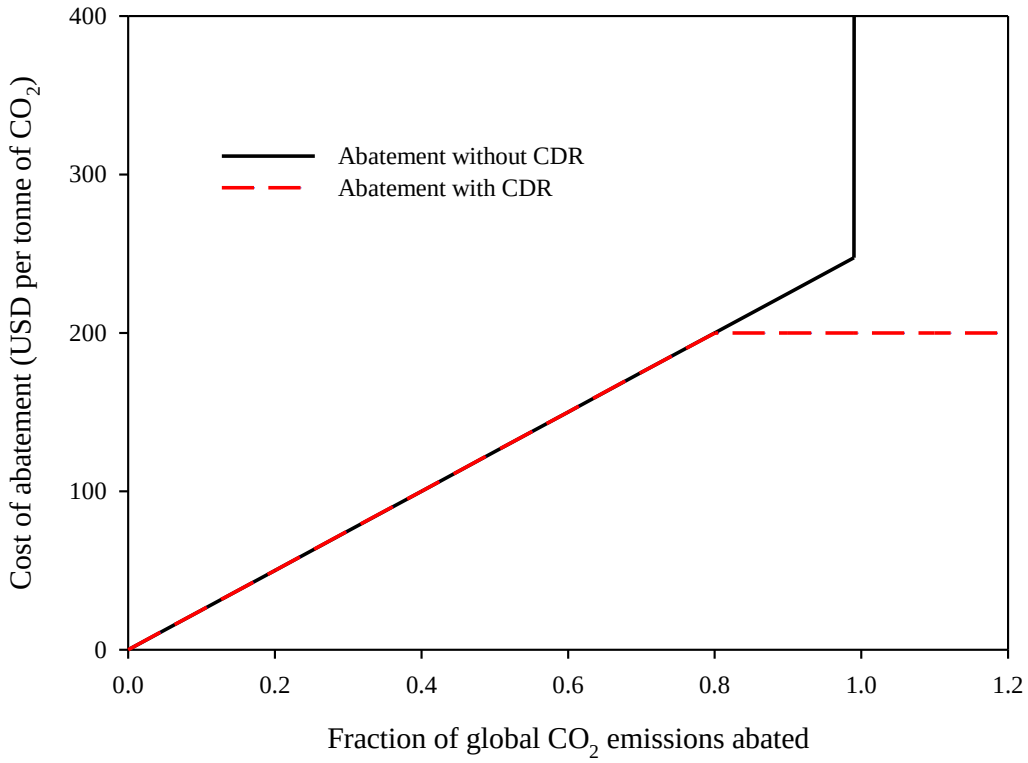

Figure 1.2 – Approximate cost of abatement as a fraction of total global CO_2 emissions abated (Keith et al., 2006).

As the capture fraction of global emissions approaches 1, the cost goes to infinity. For example, it becomes increasingly difficult to separate 100 % of the CO_2 leaving a power plant in a cost-effective manner. Instead, 90 % is proposed to be removed. CDR enables large-scale removal of CO_2 from the air at a lower cost than if end-of-pipe approaches were used for 100 % capture. CDR places a ceiling on the cost of abatement since the separation cost is a function of the CO_2 concentration, and ambient air has the lowest CO_2 concentration. CDR also allows the fraction of CO_2 abated to exceed 1 at a flat cost for the capture stage since there is very little difference in cost when capturing CO_2 in very dilute concentrations. For example, the cost of capturing CO_2 from air at a concentration of 400 ppmv is only slightly more than capturing CO_2 from air with a concentration of 500 ppmv. In summary, Figure 1.2 reveals two distinct ways to think about the function of CDR (Meadowcroft, 2013):

1) Emissions offsetting: CDR activities that take place in the lead-up to capture of 100 % of total global CO_2 emissions in order to meet a target CO_2 concentration.
2) Climate recovery: CDR activities that take place after 100 % of total global emissions have been captured so that the CO_2 overshoots and then approaches a target concentration from above.

These two approaches are now discussed.

1.6.1 CDR for emissions offsetting

CDR could offset CO_2 emissions to avoid overshoot of a tolerable atmospheric CO_2 concentration target. Indeed, CDR may be essential to meet strict stabilization scenarios (see

WGIII scenarios, 430-580 ppmv, in Figure 1.1). End-of-pipe CCS is unable to deal with small, distributed and mobile CO_2 emitters in a cost-effective manner. The aviation industry, for example, is projected to increase its contribution to total CO_2 emissions relative to other sectors due to the difficulty in converting to non-fossil energy (Sgouridis et al., 2011). By participating in CDR, the aviation industry could balance their CO_2 budget in a cost-effective manner.

The CO_2 capture fraction from large point source emitters such as power plants is likely to be constrained at ~90 % for economic and regulatory reasons. CDR could be used to capture whatever CO_2 remains uncaptured by CCS so that the combination of CCS and CDR is more cost-effective than either alone. CDR could also be used to offset emissions from leakage associated with CO_2 sequestration in geological formations (van der Zwaan and Smekens, 2009). In so doing, CDR would put a fixed price on the leaked CO_2 (Lackner et al., 2012).

Due to rapid mixing in the Earth's atmosphere, the CO_2 concentration is approximately the same at any global location. Thus, emissions on one side of the globe can be compensated for by capture on the other, allowing able nations who are dissatisfied with the international mitigation effort to offset emissions of those nations which are unable to act or content to do little or nothing. Parson (2006) argues that so called "free-rider compensation" would be well within the financial capability of the US or some collection of nation states. However, effort to reduce CO_2 concentrations might be met with resistance from certain geographical regions which benefit from increased temperatures, or from societies which have come to terms with the altered climate through adaptation.

In addition, constant global atmospheric CO_2 concentration allows CDR to be located where it can bring about CO_2 removal at lowest cost. For example, a country which has plentiful renewable energy, e.g. Iceland, could use excess geothermal energy to capture CO_2 from the atmosphere and sell carbon credits to countries who wish to continue emitting.

1.6.2 CDR for climate recovery

Note that many of the WGIII scenarios (see Figure 1.1) leading to atmospheric concentrations of 430-480 ppmv CO_2 equivalent require net negative emissions after 2050, as do many scenarios that reach between 480 and 720 ppmv by 2100. These "overshoot" scenarios would allow the CO_2 concentration to exceed a particular level and then approach the target from above after a period of net negative emissions. Integrated Assessment Models (IAMs), such as DIAM (Keith et al., 2006), GCAM (Calvin et al., 2013), REMIND (Kriegler et al., 2013) and WITCH (Chen and Tavoni, 2013), have been used to assess the potential of CDR to contribute to long-term climate stabilization. In these studies, CDR was found to reduce the cost of tackling worst-case climate scenarios by replacing near-term mitigation with a future period of net negative emissions. This has led some (Preston, 2013) to point out that the option to defer action could lead to dangerous complacency. Although IAMs show that CDR is most effective in worst-case scenarios, they take care to emphasize that CDR is not an "emergency response". Tavoni and Socolow (2013) estimate reasonable CDR rates of approximately 1 ppmv.yr^{-1} and conclude that CDR would be suitable for dealing with a "chronic" threat (i.e. new information becomes available which leads to the judgment that current climate is unfavorable relative to climate with

lower CO_2 concentration) and unsuitable for dealing with an "acute" threat (i.e. decade-or-so civilization-threatening emergency).

It is likely that CDR will be used for both emissions offsetting and climate recovery to varying degrees. Some CDR will be installed initially for mitigation of those emissions which cannot be tackled easily by conventional approaches. Then, if the atmospheric CO_2 concentration is deemed to have passed an unacceptable limit, CDR could be deployed at greater scale for the purpose of climate recovery. The extent to which CDR is used for mitigation will depend primarily on its cost, whereas the degree to which CDR will play a role in climate recovery will depend on the threat level and the pace at which CDR can be deployed (Meadowcroft, 2013).

1.7 Methods of CDR

There are several methods for direct removal of CO_2 from the atmosphere. Some of these merely enhance the Earth's pre-existing removal mechanisms, such as increasing ocean alkalinity, while others are entirely technological, like Direct Air Capture (DAC). A brief description and comparison of these is given here.

1.7.1 Ocean alkalization and fertilization

The Earth's oceans have both chemical and biogeochemical mechanisms for removing CO_2 from the atmosphere. The sea's capacity to absorb CO_2 chemically can be enhanced by increasing its alkalinity using Na_2CO_3 or CaO (Kheshgi, 1995), $CaCO_3$ (Harvey, 2008), $Ca(OH)_2$ obtained from electrochemical splitting of $CaCO_3$ (Rau et al., 2007), or by electrochemically removing HCl from seawater (House et al., 2007). However, the secondary effects on the ocean ecosystem

due to contaminants and locally high pH are unknown (Hartmann et al., 2013). Fertilization of biologically unproductive ocean waters has been proposed for sequestering anthropogenic carbon dioxide (CO_2) using iron (Zeebe and Archer, 2005). However, it can be difficult to calculate exactly how much CO_2 has been sequestered (Gnanadesikan and Marinov, 2008), and risks due to anoxia and hypoxia are uncertain (Boyd, 2013).

1.7.2 Afforestation

Forestation of one hectare of land can extract and store an eventual 500 tCO_2 from the atmosphere in 100 years (Pacala and Socolow, 2004). In addition to CO_2 removal, afforestation improves water management and purification, provides habitats for fauna and conserves biodiversity. However, in order to bring about a 50 ppmv reduction in the atmospheric CO_2 concentration, the current forested land area would need to be 1/3 greater globally (Socolow et al., 2011). Given that the worldwide net trend is toward increasing deforestation (Kindermann et al., 2006), mainly to meet the requirement for animal agriculture (Margulis, 2004), it seems unlikely that afforestation will contribute significantly to CDR (Le Quéré et al., 2009).

1.7.3 Biochar

Biomass can be burned in oxygen-poor conditions forming useful gases such as CO, H_2, and CH_4 in variable proportions, in addition to a solid residue called biochar (Sohi et al., 2010). The half-life of biochar is estimated to be anywhere from 10-100,000 years depending on its composition (Spokas, 2010). Hence biochar has the potential for long-term storage of carbon. When added to the soil, biochar enhances its properties and promotes plant growth (Powlson et al., 2011) although the potentially negative effects on soil quality also need to be considered (Quilliam et

al., 2012). Matovic (2011) suggest that pyrolyzing just 10 % of the world's biomass waste and burying it could offset all fossil fuel produced CO_2 for the year. David Keith, from Carbon Engineering, suggests that, in an energy-hungry world, it would be much better to oxidize the biomass, harness its full potential energy and then capture and store the resulting CO_2 (Levitan, 2010). If true, biochar is likely to be a niche technology for application to low-quality soils where its addition gives a high return on investment, rather than as a large-scale global CDR technology.

1.7.4 Terrestrial mineralization

Minerals containing basic metal oxides, e.g. MgO-containing olivine, remove CO_2 from the atmosphere over many thousands of years forming minerals containing stable carbonates such as $MgCO_3$. The amount of CO_2 absorbed per year by this mechanism is very small owing to the minimal exposure of these rocks to the atmosphere and the very low reaction rates at atmospheric conditions. These naturally occurring reactions can be enhanced by mining, crushing and dispersing these minerals or using various reactor technologies (Romanov et al., 2015). The CO_2 absorption potential of mineral deposits containing the necessary Na, Mg, K and Ca ions far exceeds the CO_2 that could be emitted from the remaining fossil fuel reserves, and the cost of CO_2 capture has been estimated to be about 20-40 USD per tonne (Kohler et al., 2010). However, large-scale mining operations come with extreme localized environmental problems (Schuiling and Krijgsman, 2006). CDR by this method is therefore a trade-off between unseen, difficult-to-quantify, global environmental benefit and intense, localized, highly visible environmental destruction (Rau et al., 2007; Hartmann and Kempe, 2008). Electrochemical

methods could facilitate mineralization of CO_2. For example, Yun et al. (2017) investigated simultaneous production of NaOH and HCl via electrolysis of NaCl from seawater and CO_2 capture (30 % CO_2 by mole in N_2) to form of $Na_2CO_{3(aq)}$ and $NaHCO_{3(aq)}$. Mehmood et al. (2016) describe a similar process. Electrochemical processes which enable capture and regeneration to occur concurrently in one unit could lower the capital expenditure considerably.

1.7.5 Biomass Energy with Carbon Capture and Storage (BECCS)

Biomass combustion for energy (BE) can be coupled with CCS to give a process that produces heat and power, while also capturing CO_2. This could double the benefit, capturing CO_2 first by photosynthesis to produce the initial biomass, and secondly by capturing and storing the CO_2 formed during combustion. Typically, fast-growing energy crops, such as sugar cane, remove more CO_2 per area than slow-growing native trees (Möllersten et al., 2003). Thus, a dedicated plantation of sugar cane used as a feedstock for BECCS would reduce the land requirement for an equivalent quantity of CO_2 reduction by afforestation. However, wider implications of BECCS, including risks to food security, biodiversity, harvesting needs, water management and soil losses, must be considered (Wiltshire and Davies-Barnard, 2015).

1.7.6 Direct Air Capture (DAC)

Direct capture of CO_2 from the atmosphere (DAC) is a technological process which uses a sorbent material to remove CO_2 from ambient air. The sorbent material is then regenerated using energy to produce a nearly pure stream of CO_2 which can be stored in a geological storage site or converted into useful products. DAC has a much smaller land requirement than afforestation or BECCS and fewer side effects than other CDR approaches. However, the energy requirement is

high, such that, if this energy were not provided by non-carbon-based forms of energy, more CO_2 could be released than captured (Zeman, 2007; House et al., 2011).

1.8 Discussion of CDR methods

All these CDR technologies are likely to ultimately play some role in global CO_2 management. Although BECCS and DAC are more expensive than other forms of CDR, they have several advantages: large capacity and near permanent storage of CO_2 (Lackner, 2003); minimal side effects; fewer NIMBY effects and a total CO_2 avoided which is easier to calculate (Shepherd, 2009).

BECCS, rather than DAC, is often the choice technology in climate overshoot models (Kriegler et al., 2013; Fuss et al., 2014) due to its lower estimated cost (McLaren, 2012). However, BECCS depends on the availability of biomass and thus comes with a substantial requirement for land. DAC, on the other hand, could be coupled with nuclear or geothermal energy, giving a land footprint hundreds of times smaller than BECCS. There is also large uncertainty about sustainable levels of bioenergy, potentially limiting the use of BECCS as a CDR technology (Creutzig et al., 2012). Thus, if CDR is to be employed at large-scale, BECCS would likely need to be complemented by other technologies such as DAC that are not dependent on biomass. Theoretically, CO_2 capture by DAC can be co-located with CO_2 storage, opening disposal sites otherwise of no interest, such as the mid-ocean Kerguelen Plateau (Goldberg et al., 2013). BECCS siting decisions are more tightly constrained.

Bioenergy and CCS are two industrially mature technologies. The option of combining them has been demonstrated successfully at the world's first BECCS project in Illinois, US (Biorecro, 2011). DAC, on the other hand, is undeveloped, with just seven startup companies at the pilot stage as of 2019: Carbon Engineering, (Canada), Global Thermostat (USA), Climeworks, (Switzerland), Antency (Netherlands), Hydrocell (Finland), Infinitree (USA) and Skytree (Netherlands). Addressing this imbalance, together with the need to consider all options, provides the motivation for this thesis, which, from here onward, is only concerned with DAC as a tool for CDR.

1.9 Historical experience with CO_2 removal from air

Direct Air Capture (DAC) for climate mitigation is a recent concept (Lackner et al., 1999). However, CO_2 removal from air for industrial purposes has been practiced for over half a century. For example, in cryogenic air separation plants, CO_2 must be removed to avoid fouling and clogging of equipment by formation of dry ice (Greenwood and Pearce, 1953; Rege et al., 2000; 2001). In closed-circuit breathing systems e.g. in submarines (Blachly and Ravner, 1965), spacecraft (Schaefer, 1964), rebreather diving (Belmabkhout et al., 2010), mining (Holquist et al., 2014), and medical applications (Murray et al., 1999), the CO_2 concentration must be maintained at less than 1 % to avoid negative impacts of prolonged exposure on human health (Langford, 2005). CO_2 removal is vital for alkaline fuel cells (McLean et al., 2002) and iron-air batteries (Öjefors and Carlsson, 1978) due to stable carbonate formation and its detrimental effect. These applications demonstrate the technical feasibility of CO_2 capture from air. However, they are small-scale and at no point involve concentration and pressurization of CO_2

into a pure stream. In addition, these applications are optimized mainly around reducing CO_2 concentration to some target level. DAC on the other hand will be optimized around cost per mass of CO_2 captured.

By mass transfer standards, CO_2 is at a very low concentration in atmospheric air (0.04 % by volume), and thus a huge volume (1.4e6 m^3) of air must be processed for every ton of CO_2 captured (at 100 % capture; 298 K; 101 kPa). Changing the temperature or pressure is economically prohibitive in cases where the mass of gas to be processed greatly exceeds the mass of CO_2 captured (Lackner et al., 1999). This rules out cryogenic and membrane-based separation processes and effectively limits DAC to sorption-type separations.

1.10 Sorbent-based DAC

A typical DAC unit design based on sorption would include a capture stage, where atmospheric air passes over the surface of a sorbent material which selectively removes CO_2. Since CO_2 is an acid gas, the sorption process usually relies upon a basic solid or liquid sorbent. The CO_2-loaded sorbent then passes to the regeneration stage where CO_2 is desorbed and the sorbent returned to

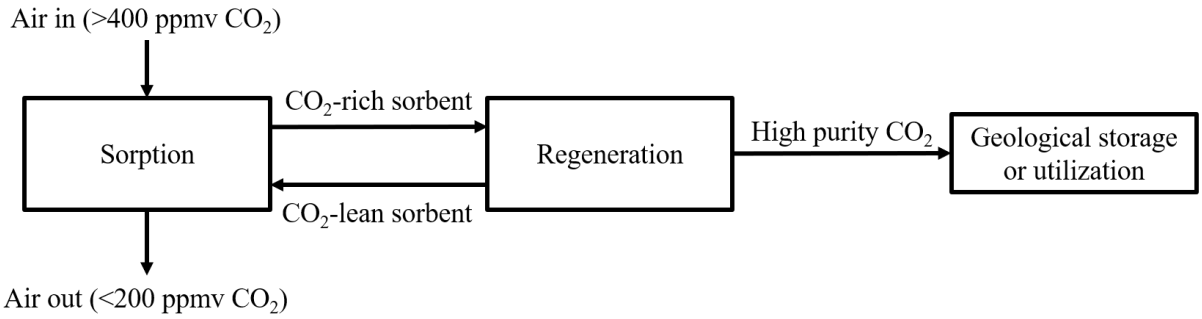

Figure 1.3 – Simplified flow diagram for DAC based on liquid or solid sorption.

capture-readiness. The high-purity CO_2 released during regeneration is sent to a compression stage where it is converted to a supercritical fluid for transportation and storage (see Figure 1.3).

1.11 Minimum work of CO_2 separation from air

Figure 1.4 shows that the minimum separation work, $w_{min,in}$, decreases with increasing natural log of the inverse CO_2 mole fraction. Assuming an initial atmospheric CO_2 concentration of 400 ppmv, then $w_{min,in}$=9-21 kJ.mol^{-1} (at 100 % capture; 298 K; 101 kPa). Therefore, even though the

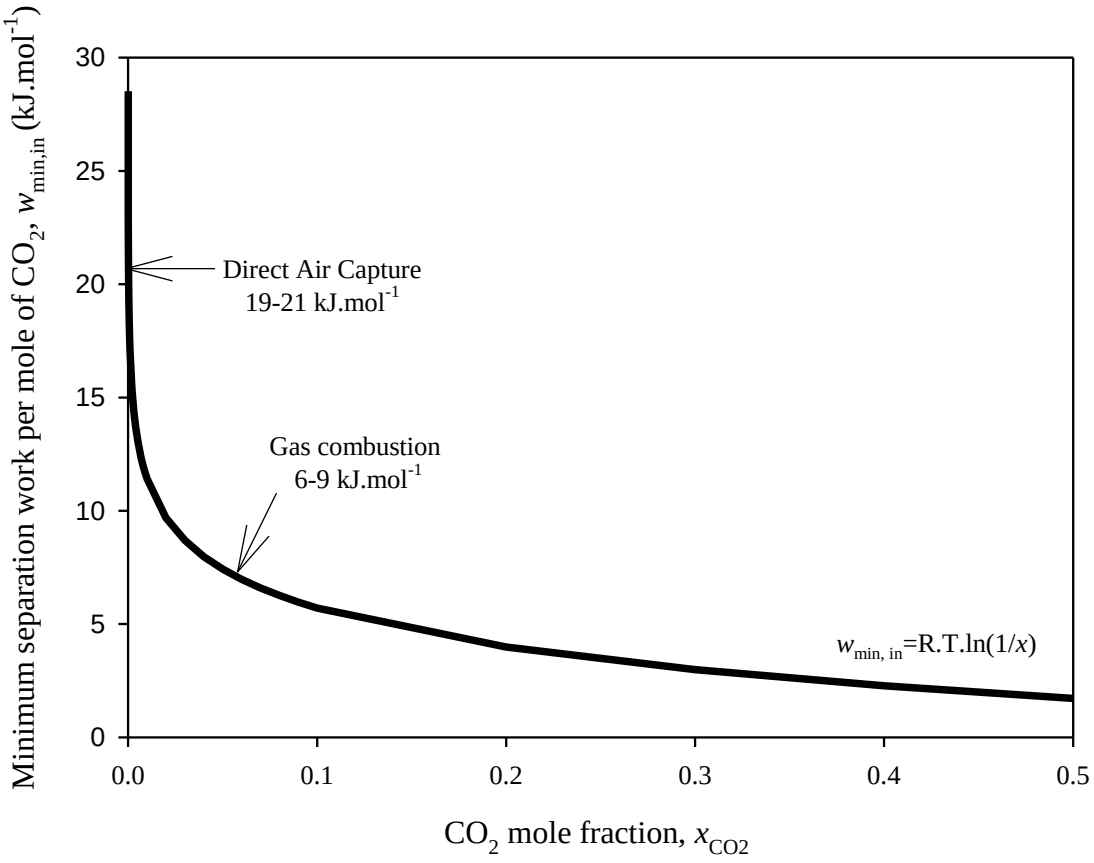

Figure 1.4 – Minimum separation work per mole of CO_2 vs. CO_2 mole fraction, assuming 100 % capture and ideal gas behaviour at a temperature of 298 K.

CO_2 concentration in air is 100 times less than in the flue gas of a natural gas combustion plant, the minimum work is just double. By this simple analysis, DAC seems energetically feasible. However, achieving the minimum work requires infinitesimal mass transport driving forces, which in turn require equipment of infinite size or infinite time for separation. The actual energy needed for any separation is higher than the theoretical minimum. For example, a monoethanolamine-based capture unit for a 320 MW natural gas power plant consumes 20-30 times the theoretical minimum separation energy (Desideri and Paolucci, 1999). For DAC, House et al. (2011) suggest that this factor could be much greater.

1.12 Balance between absorption rate and regeneration energy

As already mentioned, the actual energy of separation will be higher than the theoretical minimum. The main reason for this is that to achieve a reasonable rate of reaction between CO_2 and the sorbent, the standard change in enthalpy of reaction ($\Delta H°$) will be more negative than it would be if the reaction could be performed in infinite time. Thus, regeneration of the sorbent requires considerable energy. Generally, the lower the CO_2 concentration, the more negative must be the enthalpy of reaction to achieve the necessary uptake rate, and consequently the greater the regeneration energy. Most CO_2 capture reactions follow:

$$\mathrm{D} + \mathrm{CO_2} \Leftrightarrow \mathrm{DCO_2} \qquad 1.1$$

where D is the sorbent material (solid or liquid). The equilibrium constant is given by:

$$K_{\mathrm{eq}} = \frac{k_{\mathrm{f}}}{k_{\mathrm{r}}} = e^{\frac{-\Delta G°}{RT}} \qquad 1.2$$

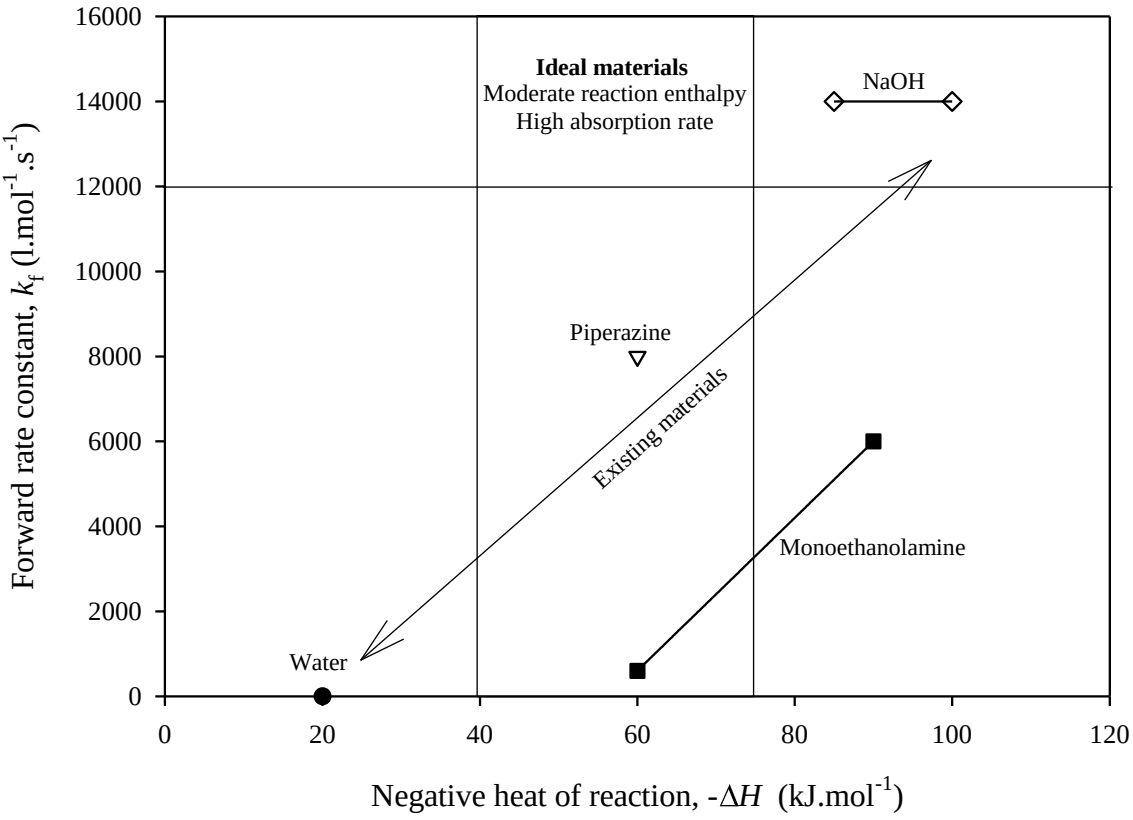

Figure 1.5 – Forward rate constant vs. negative heat of reaction for selected CO_2 capture reactions. Points connected by lines represent a range of values from the literature owing to differences in experimental conditions (Socolow et al., 2011).

where K_{eq} is the equilibrium constant, k_f is the rate constant of the forward reaction, k_r is the rate constant of the reverse reaction, $\Delta G°$ is the change in the standard Gibbs free energy for the reaction, R is the ideal gas constant and T is the absolute temperature. $\Delta G°$ for the reaction is determined by:

$$\Delta G° = \Delta H° - T\Delta S° \qquad 1.3$$

where $\Delta S°$ is the standard change in entropy. Since almost all CO_2 capture reactions follow Eq. 1.1, $\Delta S°$ is approximately constant regardless of the nature of D, and thus $\Delta G°$ depends

predominantly on $\Delta H°$. This gives a positive correlation between k_f and $-\Delta H°$ (see Figure 1.5). The correlation is only approximate because, in reality, reaction rates also depend on the kinetics and mass transfer. As indicated by the box labelled "Ideal Materials" in Figure 1.5, an ideal sorbent would have a moderately negative reaction enthalpy (40-80 kJ.mol^{-1}) and a large forward rate constant for reaction with CO_2 (>12000 l.mol^{-1}.s^{-1}).

1.13 Sorbents for DAC

Sorbents should capture CO_2 at ambient conditions, since pressurizing or heating/cooling large quantities of air would be uneconomical. Sorbents should have low cost and be able to undergo many thousands of capture cycles over their lifetime. Sorbents should be non-toxic to humans and the environment. In addition, the mining, processing and manufacture of the sorbent materials should not have adverse effects on the environment, and any CO_2 produced in these stages must be considered in the overall carbon balance for the capture system. In the rest of Section 1.13, we review several solid and liquid sorbents for DAC and discuss their advantages and disadvantages.

1.13.1 DAC using solids

1.13.1.1 Inorganic chemisorbents

Solid NaOH, $NaHCO_3$ and Na_2CO_3 (Nikulshina et al., 2008) have all been investigated for CO_2 capture from air, but absorption rates were very low and regeneration temperatures high (>1200 K). $Ca(OH)_2$ (Nikulshina et al., 2006; Nikulshina et al., 2007) and CaO (Nikulshina et al., 2009; Nikulshina and Steinfeld, 2009) give higher rates of absorption, but only at higher temperatures (>673 K). CO_2 capture from air should proceed at ambient temperature to be economical.

Similarly, slow CO_2 capture kinetics limit MgO and $Mg(OH)_2$ to non-regenerable forms of sequestration i.e. mineralization (Stolaroff et al., 2005). Colombo (1973) found that $Zn(OH)_2$ could not be regenerated, and ZnO had a low absorption capacity for CO_2. LiOH has been used for CO_2 removal in submarines (Norfleet and Horn, 2003), but the Li_2CO_3 formed cannot be regenerated in any practical way. Silver oxide (AgO) showed good CO_2 absorption and low energy regeneration (Colombo, 1973; Heinrich, 2003), but would likely be prohibitively expensive for large-scale air capture.

1.13.1.2 Inorganic physisorbents

Clinoptilolite, γ-alumina (Rege et al., 2000), zeolite 13X (Kumar et al., 2015), Li-LSX (low silica type X), K-LSX, and NaX (Stuckert and Yang, 2011) have very low selectivity for CO_2 in humid air. Metal-organic frameworks (MOF) (Mg-MOF-74/ Mg-dobdc) and the hybrid ultramicroporous material (HUM) (SIFSIX-3- Ni) perform slightly better (Kumar et al., 2015), but are very expensive. It is not feasible to dry large quantities of air, and so sorbents must function effectively in the presence of water. Thus, inorganic physisorbents are unlikely to offer a solution to DAC without enhancement, usually in the form of amine functionalization.

1.13.1.3 Class I, II and III supported organoamines

The selectivity for CO_2 over H_2O for solid sorbents such as silica, zeolites (e.g. MCM-41), carbon fibers and polymers can be greatly increased by surface attachment of amines (Satyapal et al., 2001; Goeppert et al., 2010; Olah et al., 2010). When monomer organoamines such as pentaethylenehexamine (PEH), tetraethylenepentamine (TEP), monoethanolamine (MEA) and diethanolamine (DEA) or polymer organomamines such as poly(ethyleneimine) (PEI) are

physically bonded onto the support, they are referred to as Class I supported amines. These tend to suffer performance loss over repeated capture cycles due to volatilization or leaching of the amines. In DAC, the contactor is open to the atmosphere, and leakage of potentially harmful amines could have negative consequences for human and environmental health, as well as capture efficiency.

To overcome this problem, aminosilanes can be chemically grafted to solid surfaces with available hydroxyl groups to give Class II organoamines. Typical supporting materials include covalently bonded carbon scaffold (Lu et al., 2013), nanofibrillated cellulose (NFC) (Gebald et al., 2011), and mesoporous silica (SBA-15) (Stuckert and Yang, 2011). Class II supported amines show much higher absorption capacity and selectivity for CO_2 than ungrafted inorganic physisorbents and are more stable than Class I supported amines.

Class III supported organoamines are similar to Class II but are prepared by in-situ polymerization. Hyperbranched aminosilicas (HAS) (Hicks et al., 2008) are fabricated by one-step ring-opening of aziridine monomers to inorganic surfaces, followed by polymerization. By manipulation of the silica-to-aziridine ratio, the amine content of the final product can be fine-tuned. Higher amine content results in greater capacity and selectivity for CO_2, but slower adsorption kinetics, due to mass transfer limitations from pore blockage.

1.13.1.4 Anion exchange resins

Anion exchange resins consist of quaternary ammonium functional groups attached to a polystyrene backbone with hydroxide (OH^-) or carbonate (CO_3^{2-}) counter ions (Wang et al.,

2011; 2013; Lackner and Wright, 2012). Absorption/desorption cycles work by moisture swing. Kinetic experiments suggest that the anionic exchange resins are able to take-up CO_2 at a rate comparable to a 1 mol.l^{-1} NaOH solution. However, the requirement for quick dehydration limits the use of these resins to dry, warm conditions.

1.13.2 DAC using liquids

1.13.2.1 Aqueous amine solution

Monoethanolamine (MEA) is currently the favoured sorbent for end-of-pipe CCS and sets a lower bound on the cost of CO_2 capture from large point sources. However, MEA is not capable of efficiently removing CO_2 at 400 ppmv (Socolow et al., 2011). MEA and other alkanolamines are known (Lepaumier et al., 2009) to degrade in the presence of oxygen, as well as being harmful to the environment (Veltman et al., 2010). For these reasons, ethanolamine solutions are not suitable for CO_2 removal from ambient air.

1.13.2.2 Moderately alkaline solutions with a catalyst

Water and dissolved carbon dioxide react forming carbonic acid (Eq. 1.5). Then protons can be released forming bicarbonate (Eq. 1.6) and carbonate (Eq. 1.7) ions. The zinc-containing metalloenzyme carbonic anhydrase is known to accelerate the formation of carbonic acid (Eq. 1.5) by 8 orders of magnitude (Bao and Trachtenberg, 2006).

$$CO_{2(g)} \rightarrow CO_{2(aq)} \quad (1.4)$$

$$CO_{2(aq)} + H_2O_{(l)} \rightarrow H_2CO_{3(aq)} \quad (1.5)$$

$$H_2CO_{3(aq)} \rightarrow H^+_{(aq)} + HCO^-_{3(aq)} \quad (1.6)$$

$$HCO^-_{3(aq)} \rightarrow H^+_{(aq)} + CO^{2-}_{3(aq)} \quad (1.7)$$

However, this enzyme only functions within narrow pH and temperature windows and may be decomposed by microorganisms (Socolow et al., 2011). Synthetic catalysts that mimic carbonic anhydrase have been investigated for DAC (Aines & Friedman, 2008). Although they have lower rate constants, they operate over a wider range of pH and temperature.

1.13.2.3 Ionic liquids

Ionic liquids (ILs) are low-melting-point salts with tunable properties generated by structural modifications. ILs are under investigation as an alternative to alkanolamines for pre- and post-combustion capture due to their low volatility and potentially lower regeneration energy (Ramdin et al., 2012). Chen et al. (2017) developed a task-specific ionic liquid, [P4444][p-2-O], and a pyrene-based conjugated polymer for direct CO_2 capture from air and its further photoreduction to CO under visible light irradiation. Amine functionalized ILs introduce chemical as well as physical interaction, greatly improving absorption capacity at low CO_2 partial pressures. Even so, they are costly and difficult to scale up.

1.13.2.4 Inorganic chemisorbents in solution

Herzog (2003) envisioned flat CO_2 sinks consisting of large shallow pools of $Ca(OH)_2$ solution. The $CaCO_3$ formed would then precipitate and accumulate at the bottom of the pools. However, the solubility of $Ca(OH)_2$ in water is very low (0.025 $mol.l^{-1}$) at ambient temperature, so CO_2 uptake is severely mass transfer limited (Lackner et al., 1999). Aerosol formation using spray devices has been proposed (Stolaroff et al., 2008) to increase the rate of mass transfer, but absorption rates are much lower than for alkali hydroxide solutions. Most cost studies have centered on wet-scrubbing using NaOH due to its favourable reaction kinetics with low CO_2

concentration gas (Baciocchi et al., 2006; Zeman, 2007; Stolaroff et al., 2008; Socolow et al., 2011). Maintaining good solution-to-air contact has been achieved using new thin-film pulsed alkali hydroxide solution air contactors which greatly improved solution-to-air contact (Holmes et al., 2013) and higher concentrations of sodium hydroxide were found to reduce evaporative water losses (Mahmoudkhani and Keith, 2009). KOH solutions have even higher rates of absorption than NaOH (Bandi et al., 1995; Stucki et al., 1995; Keith et al., 2018). K_2CO_3 solution has been used for industrial CO_2 removal (at high partial pressure) for over 50 years (Benson et al., 1954) and a similar process was patented by Polak and Steinberg (2012) for CO_2 capture from ambient air, later resulting in founding of the company Coaway LCC, which was announced as one of the finalists in the Virgin Earth Challenge in 2011.

1.14 Front-runner technologies for DAC

Two types of sorbent-based DAC technology have emerged as front-runners: 1. DAC using sodium hydroxide (Zeman, 2007) or potassium hydroxide (Keith et al., 2018) which we will refer to collectively as aqueous alkali hydroxide Direct Air Capture (AAH-DAC) and 2. DAC using amine-based solids (Ping et al., 2018) or MOFs (Sinha et al., 2017) which we will refer to collectively as solid-DAC. In AAH-DAC, CO_2 is absorbed, and thus sorbents are regenerated at high temperature (>1173 K), whereas in solid-DAC, CO_2 is adsorbed and sorbents are regenerated at lower temperature (<673 K). Consequently, solid-DAC is highly attractive as it enables integration with low temperature heat, particularly waste heat from industrial processes, leading to lower operating costs. Despite the higher temperature for regeneration, there are several other important advantages of AAH-DAC over solid-DAC: 1. Alkali hydroxide solutions

tend to be less sensitive to changes in environmental conditions, such as temperature, humidity and wind velocity. For example, strong winds carry more particulate material, such as dust and pollen. In the case of liquids, particulate material can be easily removed by filtration, whereas solid sorbents become clogged or damaged. 2. In AAH-DAC the capture solution can be transferred between absorber and regenerator easily by pumping, whereas regenerating solid sorbents requires changing the temperature, pressure or humidity of the entire chamber, or physically moving the sorbents between chambers. 3. In solid-DAC the sorbents are heated directly, and cooling times are often long, limiting throughput. 4. AAH-DAC operates continuously, increasingly the number of full load hours and lowering the cost. 5. In AAH-DAC, the surface of the solution in contact with air is constantly renewed, leading to smaller absorbers and lower capital costs whereas in solid-DAC, larger absorbers are needed. 6. In AAH-DAC, crystallization of solid carbonates from capture solutions enables temporary storage of CO_2 in a stable form. Thus, AAH-DAC enables easy integration with intermittent solar and wind power. 7. In AAH-DAC the CO_2-rich capture solution from several absorbers can be pumped to a central processing facility and combined for regeneration, benefitting from economies of scale. 8. AAH-DAC captures in excess of 1 million tonnes of CO_2 per year, whereas solid-DAC is estimated to capture less than 360 thousand tonnes of CO_2 per year (Fasihi et al., 2019). 9. Organoamines, and MOFs, used in solid-DAC are often toxic to the environment. 10. Sodium hydroxide is one of the cheapest CO_2-sorbents available and accessible almost everywhere on Earth. (Potassium hydroxide is about 10x more expensive than sodium hydroxide). These advantages are just some of the reasons that AAH-DAC remains cost competitive with solids-DAC despite the higher temperature needed for regeneration (Fasihi et al., 2019). However, in

the coming decades, it is quite likely that both approaches could be used for DAC, each filling different market niches. For example, smaller-scale solid-DAC could integrate well with industrial waste heat streams for CO_2 capture and conversion processes, whereas AAH-DAC might be better suited to large-scale capture of CO_2 with geological sequestration, powered by renewable energy such as solar thermal. In each system, there is a major focus area of research which arises from techno-economic assessment (Socolow et al., 2011). In solid-DAC, there is a large incentive to find better, cheaper sorbents, whereas in AAH-DAC there is a large incentive to find ways to lower the regeneration temperatures. In this thesis, only AAH-DAC will be considered, and therefore lowering the temperature of these systems is the impetus for this thesis project. In the next section, methods for regeneration of aqueous alkali hydroxides are reviewed.

1.15 Converting alkali carbonate to alkali hydroxide

As mentioned in the previous section, sodium and potassium hydroxide solutions have emerged as frontrunner sorbents for DAC. In these systems, $NaOH_{(aq)}$ or $KOH_{(aq)}$ absorb CO_2 from the ambient air to form $Na_2CO_{3(aq)}$ and $K_2CO_{3(aq)}$ respectively. To regenerate the sorbent solution, the carbonate must be converted back into hydroxide. There are two main methods for regenerating hydroxide from their carbonates: thermal and electrochemical. Both are reviewed here.

1.15.1 Thermal regeneration

1.15.1.1 Conventional causticization

It would be ideal if Na_2CO_3 or K_2CO_3 could be separated from the solution as a solid, decomposed to form $Na_2O_{(s)}$ or $K_2O_{(s)}$ and then hydrolyzed to form $NaOH_{(aq)}$ or $KOH_{(aq)}$.

Unfortunately, Na_2CO_3 cannot be easily separated from solution due to its high solubility in water (341 $g.l^{-1}$ at 301 K). Even more so in the case of K_2CO_3 (1120 $g.l^{-1}$ at 293 K). Further, these carbonates do not decompose at appreciable rates until very high temperatures (>1273 K), and, even then, formation of Na or K vapor renders these processes unworkable. The pulp and paper sector solved (Dahl, 1884) these various problems over 100 years ago using "conventional causticization", which is one part of the Kraft cycle (see Figure 1.6).

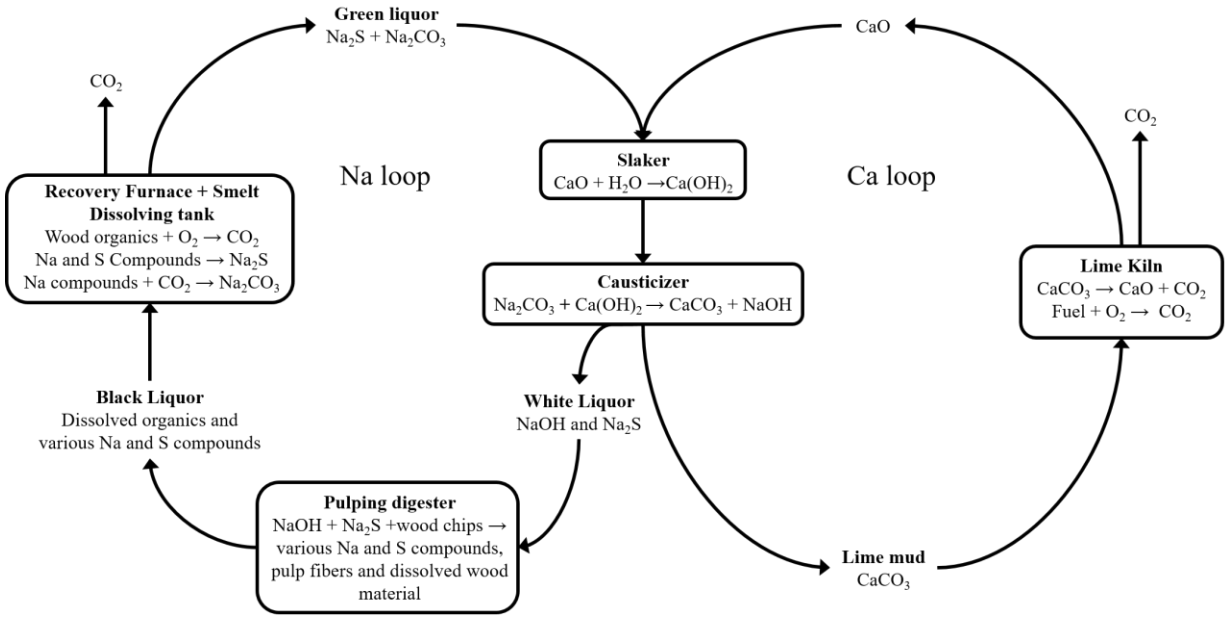

Figure 1.6 – Kraft cycle used in the pulp and paper industry.

In the Kraft cycle, wood is digested in a solution of NaOH and Na_2S, known as "white liquor", which breaks the bonds between lignin and cellulose. The cellulose fibers are separated and used to make pulp. The remaining "black liquor" consists of lignin and hemicellulose, mixed with Na and S compounds. The black liquor is dried to 80 % solids and burned in a recovery boiler to produce the heat energy needed to power the plant and convert the Na and S compounds into

Na_2S and Na_2CO_3 which form a smelt at the bottom of the boiler. The smelt is dissolved in diluted white liquor to form green liquor which is reacted with caustic lime, $Ca(OH)_{2(s)}$, to form $NaOH_{(aq)}$ and $CaCO_{3(s)}$. The $CaCO_{3(s)}$ precipitate is removed, and the remaining white liquor returns to the digester. Finally, the $CaCO_{3(s)}$ is decomposed, and the resulting $CaO_{(s)}$ is hydrated to form $Ca(OH)_{2(s)}$, completing the cycle.

Lackner et al. (1999; 2001) first proposed adapting the Kraft cycle for DAC (see Figure 1.7). Since then, several studies have used this system as a benchmark for techno-economic assessment (Keith et al., 2006; Baciocchi et al., 2006; Zeman, 2007; Stolaroff et al., 2008). More recently, the Canadian company Carbon Engineering built a DAC pilot demonstration facility (365 $t(CO_2).yr^{-1}$) in Squamish, British Columbia based on regeneration of $KOH_{(aq)}$ using CaO (Keith et al., 2018).

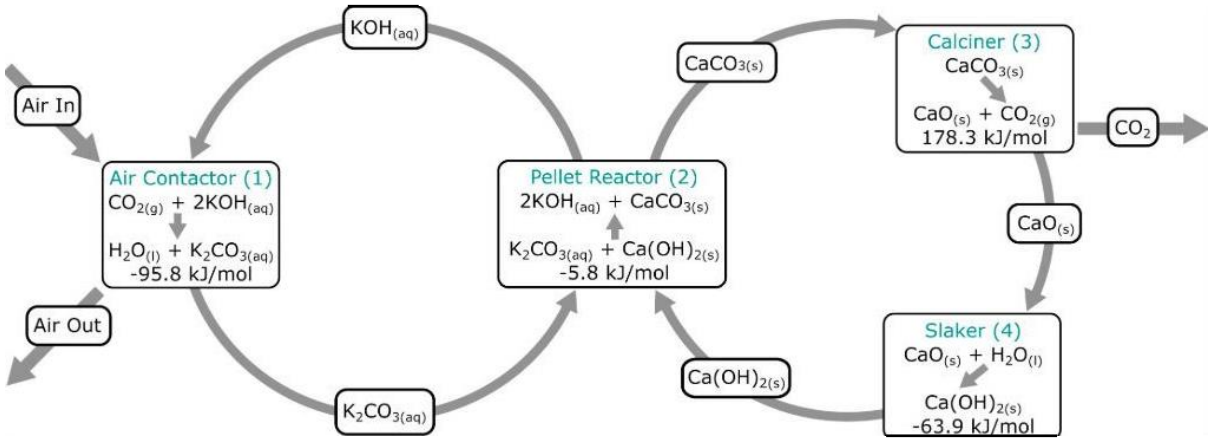

Figure 1.7 – DAC using $KOH_{(aq)}$ with regeneration by conventional lime causticization (Keith et al., 2018).

DAC based on a long-established, large-scale industrial process such as the Kraft cycle minimizes technical and scale-up risks. However, cost estimates for the process are high: 600 USD per tonne of CO_2 captured (Socolow et al., 2011), with some estimates as high as 1000 USD per tonne of CO_2 (House et al., 2011). Keith et al. (2018) calculate a levelized cost for their DAC process based on absorption by KOH solution to be in the range of 94 to 232 USD per tonne. In each study, costs are dominated by the decomposition stage which requires a minimum of 178 kJ.mol^{-1} of heat to be provided at high temperature (~1173 K) (Keith and Ha-Duong, 2003).

For DAC to be economically feasible, there is a strong incentive to lower the temperature of the decomposition step. Lower temperatures not only result in energy savings and cost reductions, but also open DAC systems to integration with new types of carbon-free energy source. For example, a high-temperature gas-cooled nuclear reactor (HTGR) has an outlet temperature of 1123 K. Thus, a chemical transformation which requires temperatures of 1173 K to sustain a reasonable rate of reaction, such as decomposition of $CaCO_3$, cannot be easily integrated with heat from HTGRs.

The theoretical minimum energy requirement for converting Na_2CO_3 to NaOH is 109 kJ per mol of CO_2 at 298 K, and a similar value for converting K_2CO_3 to KOH. Regeneration of NaOH or KOH by conventional causticization, which involves decomposition of $CaCO_3$, has a much greater energy demand (ΔH=178 kJ.mol^{-1} at 298 K) than the thermodynamic minimum. In addition, decomposition of $CaCO_3$ requires a temperature of ~1173 K at 1 atm of CO_2 (Socolow et al., 2011). Thus, there is a strong incentive for alternative regeneration pathways with lower

temperature and energy demand. Substitute cations such as Mg have been investigated. Although, $MgCO_3$ decomposition requires less energy (ΔH=118 kJ.mol^{-1} at 298 K) and lower temperature than $CaCO_3$ decomposition, it fails to provide the causticization rates required for a workable process (Vandendoren, 2017). Other hydroxides of alkali earth metals, such as $Ba(OH)_2$ provide higher causticization rates than $Mg(OH)_2$ and $Ca(OH)_2$, but the resulting carbonate requires greater energy and temperature for decomposition. There does not seem to be an obvious viable alternative reagent for regeneration of aqueous alkali hydroxides using conventional causticization. Therefore, to find alternative low-temperature pathways, unconventional methods of causticization must be explored.

1.15.1.2 Unconventional causticization

Unconventional causticization involves decomposition of Na_2CO_3 in the presence of a sodium-poor amphoteric or acidic oxide with the general formula Na_xMO_y, to form a sodium-rich oxide:

$$Na_2CO_3 + Na_xMO_y \rightarrow Na_{x+2}MO_{y+1} + CO_2 \quad 1.8$$

The sodium-rich oxide, $Na_{x+2}MO_{y+1}$, forms NaOH upon contact with water:

$$Na_{x+2}MO_{y+1} + H_2O \rightarrow Na_xMO_y + 2NaOH \quad 1.9$$

This pathway has more favourable thermodynamics and kinetics than decomposition of pure Na_2CO_3 and thus enables release of CO_2 at a lower temperature. The oxide functions as a sodium carrier, preventing Na vapor losses. Although this section focusses mainly on regeneration of NaOH, similar methods can be used for regenerating KOH from K_2CO_3 (Ho, 2004).

Unconventional causticization can be categorized according to the solubility of Na_xMO_y. If Na_xMO_y is soluble, then the term used to describe the process is autocausticization, whereas, if Na_xMO_y is insoluble, then the process is termed direct causticization. Both are reviewed here.

1.15.1.2.1 Autocausticization

Autocausticization using borates was developed in the late 1970s (Janson, 1977; 1978; Janson and Pekkala, 1977; 1978). Unlike the conventional Kraft process, the causticization reagent is present throughout the entire system (see Figure 1.8).

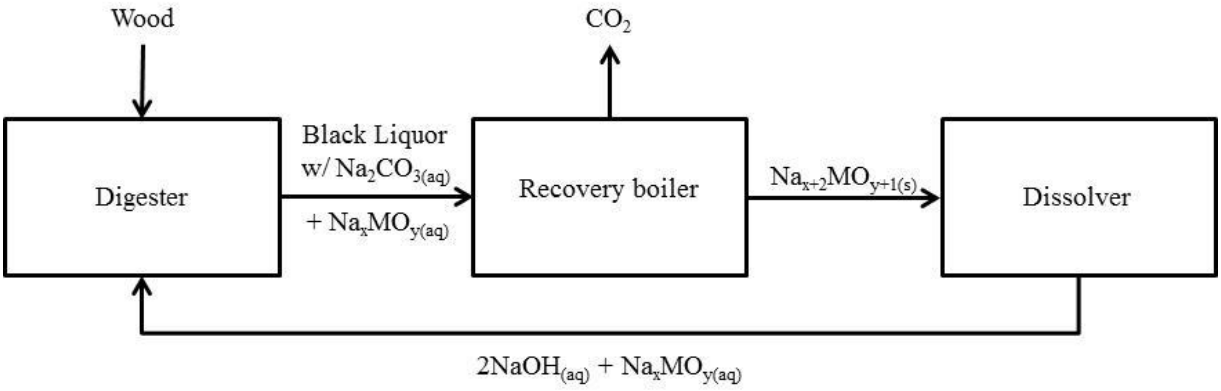

Figure 1.8 – Simplified process diagram for autocausticization.

The main reaction which occurs in the recovery boiler is between sodium carbonate and sodium metaborate:

$$Na_2CO_{3(s,l)} + NaBO_{2(s,l)} \rightarrow Na_3BO_{3(s,l)} + CO_{2(g)} \quad 1.10$$

although up to 12 different sodium borate complexes are thought to form (Milman and Bouaziz, 1968). The sodium orthoborate is then hydrolyzed to form $NaOH_{(aq)}$:

$$Na_3BO_{3(s,l)} + H_2O_{(l)} \rightarrow \ NaBO_{2(aq)} + 2NaOH_{(aq)} \quad 1.11$$

The autocausticization reaction (Eq. 1.10) has a lower enthalpy (127.6 kJ.mol^{-1} at 1073 K) than decomposition of $CaCO_3$ and thus the process has a reduced cost of energy. In addition, the borate process is simpler than conventional causticization and has a lower capital cost.

Despite the benefits of autocausticization, the process has never been commercialized, primarily because the high viscosity of the boronated black liquor causes severe operating difficulties (Janson and Söderhjelm, 1988). Partial autocausticization on the other hand, which uses both borates and lime, has been successfully commercialized in Sweden, Brazil, Indonesia and the United States (Tran and Vakkilainnen, 2008).

Reagents other than borates have been studied. For example, disodium phosphate was found to be a more effective decarbonizing reagent than borate, but the products of hydrolysis were not sufficiently alkaline for pulp digestion (Janson, 1979).

It is not clear how autocausticization could be applied to Direct Air Capture. First, the presence of soluble sodium borates would significantly alter the properties of the capture solution. Second, the borates and Na_2CO_3 would need to be separated from the capture solution which can be difficult due to their solubility. In the pulp process, an evaporator is used to remove most of the water prior to causticization in the recovery boiler. Evaporating large amounts of water is simply not feasible for DAC as it is too energy intensive. In addition, the capture solution leaving the air contactor has a composition of 1-4 mol.l^{-1} NaOH and less than 1 mol.l^{-1} of Na_2CO_3 (Mahmoudkhani and Keith, 2009). NaOH is "sticky" and highly corrosive at elevated

temperatures. For these reasons, regeneration of NaOH using autocausticization is not considered further in this thesis.

1.15.1.2.2 Direct causticization

Chemical pulping using direct causticization, like autocausticization, has fewer steps and lower energy consumption than conventional lime causticization (see Figure 1.9). However, unlike in autocausticization, the Na_xMO_y species is insoluble and can be more easily separated from $NaOH_{(aq)}$. This makes it easier to adapt direct causticization for Direct Air Capture since Na_xMO_y is not present in the capture stage, just the regeneration side. Nevertheless, the problem of high Na_2CO_3 solubility remains. For DAC to be practical, Na_2CO_3 must be separated from the capture solution as a solid. In the pulping process, the water content of the black liquor is reduced by evaporation. As already mentioned, heating large volumes of capture solution is simply too costly for DAC. To solve this issue, Mahmoudkhani et al. (2009) described a two-stage crystallization process for separation of pure and relatively dry anhydrous sodium carbonate from $NaOH/Na_2CO_3$ solution leaving the contactor. In the first stage, sodium carbonate decahydrate ($Na_2CO_3.10H_2O$) is crystallized by lowering the temperature of the $NaOH/Na_2CO_3$ solution by ~10 K. Crystals must be grown to large enough size for removal with minimal solution carry-over. In the second stage, $Na_2CO_3.10H_2O_{(s)}$ is dissolved and sent to another crystallization unit, where anhydrous Na_2CO_3 is produced.

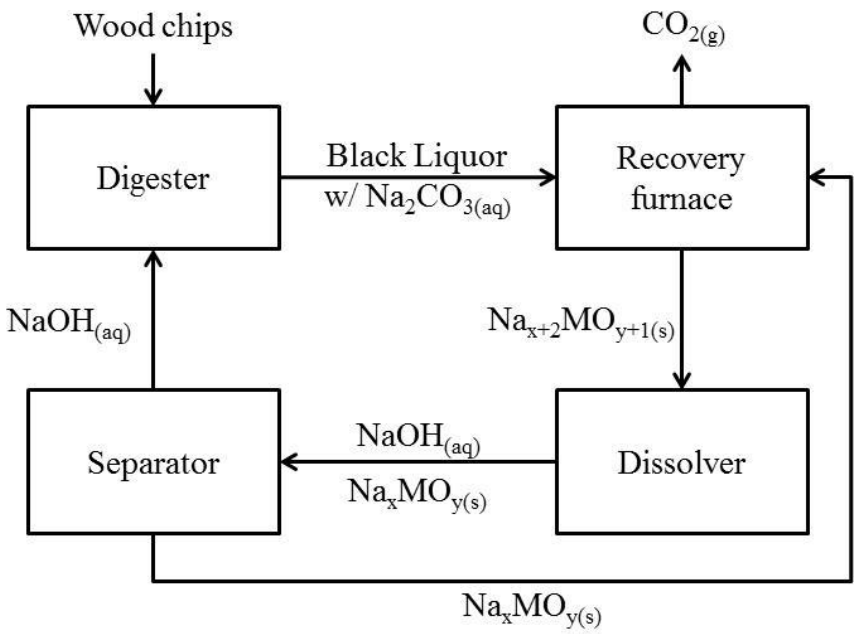

Figure 1.9 – Simplified process diagram for direct causticization.

To our knowledge, the only reagent for direct causticization which has been commercialized and practiced on an industrial scale is hematite, Fe_2O_3. Production of NaOH from Na_2CO_3 and Fe_2O_3 was patented by Lowig (1878) and used commercially in the U.S.S.R for decades. Nearly a century later, the Lowig process was adapted and patented for direct causticization of soda liquors in the pulp and paper industry as an alternative to the Kraft process (Nagano et al., 1974). The Direct Alkali Regeneration System (DARS) was commercialized by Associated Pulp and Paper Mills (APPM) in Burnie, Tasmania (1977) and at a Danish straw pulp-mill run by Fredericia Cellulose in 1988. The Burnie mill recovered 95 tonnes of NaOH per day (Grace, 1981). The DARS process (Covey, 1984) eliminates the need for the lime cycle since addition of Fe_2O_3 allows direct decomposition of Na_2CO_3 in the black liquor recovery stage. However, Kraft pulping liquors contain sodium sulfide, Na_2S, which would react with Fe_2O_3 forming stable iron

sulfides. This meant that the DARS process was only applicable to pulping of low-sulfur-content biomass.

Application of the Lowig/DARS process to DAC is promising for three main reasons: 1. Sulfur concentration in ambient air is negligible and thus stable iron sulfides will not be a problem; 2. Past commercialization of Lowig/DARS demonstrates scalability; 3. Iron ore is inexpensive and widely abundant. Consequently, Carbon Engineering proposed a DAC process based on NaOH with regeneration via Fe_2O_3 (Keith and Mahmoudkhani, 2002). Their process involves the crystallization of $Na_2CO_{3(s)}$ from NaOH capture solution followed by reaction with a fluidized bed of $Fe_2O_{3(s)}$ forming $NaFeO_{2(s)}$ which is then hot-water leached to recover NaOH. Other than a summary of the materials and energy balances (Dai et al., 2010), no other details have been released by the company.

The enthalpy of reaction between Na_2CO_3 and Fe_2O_3 is 164 $kJ.mol^{-1}$ which is 14 $kJ.mol^{-1}$ lower than for $CaCO_3$. However, the proposed operating temperature is the same, i.e. 1173 K (Covey, 1984) or higher e.g. 1273 K (Nagai, 2001). Thus, as with conventional causticization, the main cost of the process is in the regeneration.

1.15.2 Electrochemical regeneration

A huge variety of electrochemical methods for CO_2 capture and storage or utilization are possible. In this section, electrolysis is introduced, and studies related to electrolysis of alkali carbonates are reviewed. The advantages and disadvantages of electrochemical and thermal regeneration are discussed.

1.15.2.1 Introduction to electrolysis

Electrolysis is a technique that uses a direct electric current (DC) to drive a non-spontaneous chemical reaction. Electrodialysis is a method for transporting ions from one solution (diluate) through an ion-exchange membrane to another solution (concentrate) under an applied electric potential difference. An ion-exchange membrane is a semi-permeable membrane that transfers specific dissolved ions, while obstructing other ions or neutral molecules. When the electric field is applied, negatively charged ions migrate towards the positively charged electrode while positively charged ions migrate towards the negatively charged electrode. Overall, ion concentration increases in the concentrate and decreases in the diluate. Either, or both, electrolysis and electrodialysis are used in regeneration of NaOH.

In some electrolysis applications involving aqueous solutions, the following reaction occurs at the anode:

$$H_2O_{(l)} \rightarrow 2H^+_{(aq)} + \frac{1}{2}O_{2(g)} + 2e^- \quad 1.12$$

while the following reaction occurs at the cathode:

$$2H_2O_{(l)} + 2e^- \rightarrow H_{2(g)} + 2OH^-_{(aq)} \quad 1.13$$

The hydrogen or oxygen gas can be dissipated, recycled or collected. Alternatively, bipolar membranes can be used which enables water splitting without generating H_2 and O_2:

$$H_2O_{(l)} \rightarrow H^+_{(aq)} + OH^-_{(aq)} \quad 1.14$$

In electrolysis of alkali carbonate solutions, carbonate ions are provided by the alkali carbonate feed. For example:

$$Na_2CO_{3(aq)} \rightarrow 2Na^+_{(aq)} + CO^-_{3(aq)} \quad 1.15$$

which react with protons formed by the water-splitting reaction (Eq. 1.12 or 1.14) enabling release of CO_2 according to:

$$CO^{2-}_{3(aq)} + H^+_{(aq)} \rightarrow HCO^-_{3(aq)} \quad 1.16$$

$$HCO^-_{3(aq)} + H^+_{(aq)} \rightarrow H_2CO_{3(aq)} \quad 1.17$$

$$H_2CO_{3(aq)} \rightarrow H_2O_{(l)} + CO_{2(g)} \quad 1.18$$

Hydroxide ions formed by water-splitting reactions (Eq. 1.13 or 1.14) are then combined with alkali cations to form the alkali hydroxide. In the case where the feed stream is a solution of sodium carbonate, then:

$$Na^+_{(aq)} + OH^-_{(aq)} \rightarrow NaOH_{(aq)} \quad 1.19$$

By combining Eqs. 1.14-1.19, the overall reaction in the cell is:

$$Na_2CO_{3(aq)} + H_2O_{(l)} \rightarrow 2NaOH_{(aq)} + CO_{2(g)} \qquad \Delta H = +109\ \text{kJ.mol}^{-1}\ \text{at}\ 298\ \text{K} \quad 1.20$$

In the next section we review different approaches for electrolytic regeneration of $NaOH_{(aq)}$, or $KOH_{(aq)}$, and $CO_{2(g)}$ from carbonate solutions.

1.15.2.2 Literature review

Gilligan et al. (1982) patented a method for electrolytic production of $NaOH_{(aq)}$ from Na_2CO_3 (or $NaHCO_3$), with co-production of $CO_{2(g)}$. The cell is composed of two-compartments separated by a cation exchange membrane. Sodium carbonate solution is fed into the anodic compartment where CO_2 is produced. Sodium ions pass through the cation exchange membrane reacting with hydroxide ions in the cathodic compartment producing $NaOH_{(aq)}$. At the anode, $O_{2(g)}$ is produced alongside $CO_{2(g)}$ while $H_{2(g)}$ is produced at the cathode. These gases can be collected and sold or utilized. Alternatively, $H_{2(g)}$ produced at the cathode can be sent to the anode, also known as a hydrogen depolarized anode, where it reacts with $O_{2(g)}$, forming water, reducing the cell voltage and enabling creation of high purity $CO_{2(g)}$.

Pletcher et al. (1993) patented a similar method for production of $NaOH_{(aq)}$ and $CO_{2(g)}$ by electrolysis of $Na_2CO_{3(aq)}$, with $H_{2(g)}$ recycled to the anode. However, in this case the cell has just one compartment and no ion-exchange membrane. Instead, carbonate and/or bicarbonate ions enter the pores of the anode via its wet side, and $CO_{2(g)}$ and $H_2O_{(l)}$ are formed inside the anode. Most of the $CO_{2(g)}$ leaves on the dry side of the anode. This design minimizes the accumulation of CO_2 bubbles at the anode and reduces loss of NaOH by reaction with CO_2, thus lowering the cell voltage.

Corbett and Salina (1981) patented a system to remove CO_2 from the atmosphere using a weak NaOH solution to form $Na_2CO_3/NaHCO_{3(aq)}$. For regeneration of the capture solution, $Cl_{2(g)}$ was bubbled through the CO_2-rich solution to form $NaCl_{(aq)}$, $NaOCl_{(aq)}$ and $CO_{2(g)}$. NaOCl was then heated to release $O_{2(g)}$ and create more $NaCl_{(aq)}$. Finally, the $NaCl_{(aq)}$ was treated by chlor-alkali

electrolysis to form $H_{2(g)}$, $Cl_{2(g)}$ and $NaOH_{(aq)}$. This is a rather complex system with many process steps. In addition, the use of $Cl_{2(g)}$ can lead to formation toxic organo-chlorine compounds in the environment.

Bandi et al. (1995) removed 75 % of the CO_2 from air using a 2 $mol.l^{-1}$ KOH solution in a 2 m long, packed column. The $K_2CO_{3(aq)}$ formed was acidified using $KHSO_{4(aq)}$ to form $K_2SO_{4(aq)}$ and $CO_{2(g)}$. $KHSO_{4(aq)}$ and $KOH_{(aq)}$ were then recovered by electrolysis. Although, $KOH_{(aq)}$ solutions have higher rates of absorption than $NaOH_{(aq)}$ their regeneration requires more energy.

Stucki et al. (1995) proposed removing CO_2 from the atmosphere using microporous hollow fiber membranes through which a $KOH_{(aq)}$ flowed. The $K_2CO_{3(aq)}$ product was recycled to $KOH_{(aq)}$ and $CO_{2(g)}$ by electrolysis. $H_{2(g)}$ was produced from water concomitantly, complemented by additional $H_{2(g)}$ prepared in a separate electrochemical cell, and then combined with $CO_{2(g)}$ to form a gas mixture with a H_2:CO_2 mole ratio of 3:1, which is ideal for making methanol.

Lackner and Wright (2007) patented several different methods for regenerating $NaOH_{(aq)}$ from $Na_2CO_{3(aq)}$ composed of different permutations of electrochemical and non-electrochemical processes. The four electrochemical processes include: 1. Separation of a salt e.g. $Na_2CO_{3(aq)}$ into its acid and base by means of electrolysis with bipolar membranes; 2. Electrochemical separation of the capture solution into distinct streams of $NaOH_{(aq)}$ and $Na_2CO_{3(aq)}$; 3. Electrochemical separation of $Na_2CO_{3(aq)}$ into $NaHCO_{3(aq)}$ and $CO_{2(g)}$ by means of electrolysis with bipolar membranes; 4. Electrochemical separation of $NaHCO_{3(aq)}$ into $NaOH_{(aq)}$ and $CO_{2(g)}$ by means of electrolysis with bipolar membranes or using a hydrogen electrode. The seven processes that do

not involve electrochemistry are: i. A membrane processes that uses a concentration gradient to eliminate hydroxide ions creating a carbonate, or bicarbonate rich solution; ii. A temperature swing process to separate $Na_2CO_{3(s)}$ from $NaOH_{(aq)}$; iii. Thermal or pressure swing processes which convert $NaHCO_{3(aq)}$ into $Na_2CO_{3(aq)}$ and $CO_{2(g)}$ iv. Precipitation of $NaHCO_{3(s)}$ from $NaHCO_{3(aq)}$ by evaporation or thermal swing; v. Thermal decomposition of $NaHCO_{3(s)}$ or $Na_2CO_{3(s)}$; vi. Acid neutralization of $NaOH_{(aq)}$ to carbonate, or further, to bicarbonate; vii. Acid neutralization of streams containing $NaHCO_{3(aq)}$ or $Na_2CO_{3(aq)}$ to produce $CO_{2(g)}$. Different permutations of electrochemical (1-4) and non-electrochemical steps (i-vii) create a variety of different pathways for regeneration of $NaOH_{(aq)}$. For example, one regeneration method involves precipitation of $Na_2CO_{3(s)}$ from the capture solution by temperature swing (process ii), re-dissolving the Na_2CO_3 then separating it into $NaHCO_{3(aq)}$ and $NaOH_{(aq)}$ by means of electrolysis with bipolar membranes (process 1), followed by reaction of $NaHCO_{3(aq)}$ with a weak acid to produce $CO_{2(g)}$ and a salt of the weak acid (process vii) followed by electrolysis of the sodium acetate to produce $NaOH_{(aq)}$ and the weak acid (process 1), thus completing the cycle.

Using a $KCO_3/KOH/KHCO_3$ fuel-cell concentrator, Eisaman et al. (2011) captured and concentrated CO_2 from air using 350 $kJ.mol^{-1}(CO_2)$ at 23 % current efficiency and a current density of 0.5 $mA.cm^{-2}$. At such low current densities, very large membrane areas are needed which could be difficult to scale up economically. To solve this issue, they put forward a preliminary design for a high-pressure, pH-controlled bipolar membrane electrolysis concentrator consuming 62 $kJ.mol(CO_2)^{-1}$ at 85 % current efficiency and 100 $mA.cm^{-2}$, allowing membrane areas 200 times smaller than for the fuel cell concentrator.

Nagasawa et al. (2009) investigated three different cell designs for electrolysis of Na_2CO_3/$NaHCO_3$ solution. The design featuring two compartments bounded by bipolar membranes and divided by a cation exchange membrane had the lowest energy consumption.

1.15.2.3 Advantages and disadvantages of electrochemical regeneration

Electrochemical methods are highly attractive for DAC because they can be easily integrated with seasonal, geographical and intermittent forms of renewable electric energy (tidal, wind, solar etc.). In addition, electrochemical methods can operate at low temperature (<373 K) and atmospheric pressure conditions. This enables rapid startup and shutdown and high process safety. On the other hand, electrochemical cells could operate at high pressure, reducing the energy demand for $CO_{2(g)}$ compression in the case of transport and geological storage. Electrochemical methods also have the potential to be more streamlined than thermal methods since CO_2 capture and regeneration can occur simultaneously in one unit, whereas thermal processes are composed of several units. Electrochemical regeneration can take place entirely in solution form, avoiding the need for complex solids handling equipment.

Despite these advantages, out of the seven companies currently operating DAC facilities, none use electrochemical methods (Fasihi et al., 2019). This is because the power needed for electrochemical methods is estimated to be ~7 $MJ.kg^{-1}$ of CO_2 (Bandi et al., 1995; Stucki et al., 1995) which is equivalent to a primary energy requirement of about 14 $MJ.kg^{-1}$ of CO_2 (assuming 50 % power generation efficiency). This is slightly less than double the primary energy requirement for thermal regeneration using lime. In addition, the price of electricity is estimated to be 56 $USD.MWh_{el}^{-1}$, compared to a cost of 22 $USD.MWh_{th}^{-1}$ and 28 $USD.MWh_{th}^{-1}$

for low (<373 K) and high (>1173 K) temperature heat respectively (Fasihi et al., 2019). Additionally, as a general rule, electrochemical capital costs for large-scale plants are higher than the thermochemical equivalents, (although not so much for small scale and remote applications). As a result of lower power demand, lower cost of heat, and lower capital cost, DAC systems based on thermal regeneration of NaOH are more competitive than technologies which use electrochemical methods.

Nevertheless, electrochemical methods will become increasingly attractive as the cost of renewable electricity continues to fall in the coming decades. For the same reason, microwave regeneration methods could grow in appeal since they enable targeted heating of CO_2-capture sites in solid sorbents reducing their heating and cooling times (Campbell, 2012). In this thesis however, only standard thermal regeneration of aqueous alkali hydroxide is considered since this method has been successfully demonstrated at the pilot scale by Carbon Engineering, and it was they who first commissioned our group to investigate methods for lowering the temperature of this process.

1.16 DAC energy supply

In this section we review some of the types of heat and power supplies that are expected to be integrated with DAC.

1.16.1 Natural gas

Thermal regeneration of alkali hydroxide for DAC includes decomposition of carbonate, such as $CaCO_3$. Natural gas-fired kilns have been proposed (Baciocchi et al., 2006; Socolow et al., 2011;

Keith el at., 2018) to provide the high temperature energy for decomposition of $CaCO_3$. Burning natural gas in air would require secondary CO_2 capture, most likely based on amine scrubbing technology, causing greater complexity and added cost. Alternatively, natural gas could be burned in an oxyfuel kiln producing (after condensing water) a stream of pure CO_2 for compression. This approach would require expensive pressure swing air separation technology to denitrify the air. In such a case, switching from $CaCO_3$ to a low temperature unconventional causticization method could save energy. For example, Mahmoudkhani and Keith (2009) suggest that decomposition using titanates reduces the energy demand by ~50 % compared to decomposition using $CaCO_3$, reducing demand for natural gas and oxygen. However, any process based on natural gas perpetuates the continued depletion of a finite natural resource and are thus not sustainable in the long-term. Synthetic natural gas could be used, but this has a very high cost. Instead, non-fossil fuel sources of energy need to be considered.

1.16.2 Wind power

Goldberg et al. (2013) investigated the remote Kerguelen plateau in the Indian Ocean for its large wind energy resources (47 $TWh.yr^{-1}$), vast geological storage capacities (over 1500 Gt CO_2), and almost no NIMBY opposition. They estimate that approximately 75 Mt $CO_2.yr^{-1}$ could be captured and stored at an operating cost of 3.5 billion USD per year and upfront capital expenditure of 10 billion USD per tonne. However, this study did not address the difficulty of integrating an inherently unstable and intermittent power supply with an air capture system. In order to address this, Li et al. (2015) investigated a DAC system comprised of 4000 units (208 kW for each unit, total of 832 MW) powered by an off-grid wind-power farm (rated output of

931 MW) supported by 75,000 lead-acid batteries (2 V, 1000 A.h, for a total of 15 MWh). They found that optimal operation was achieved when each device in the CO_2 capture system (e.g. absorber, calciner, slaker, etc.) was considered a separate load rather than as a whole system, since each device has a different limit on power fluctuation. When the wind power was insufficient to power the whole DAC system, some of the devices could instead be powered and products accumulated for future processing when the wind was stronger. In summary, DAC integrated with wind power is technically feasible, but capital intensive, and off-grid integration is certainly complex.

1.16.3 Solar thermal

Almost every young person tries to burn paper with a magnifying glass. Concentrated solar works by the same principle using optical mirrors instead of lenses. The solar energy enters a tube filled with liquid water, generating steam which powers a turbine, in the same way as conventional fossil fuel-based power generation (Sangster, 2014). Instead of generating electrical power, solar energy can be used directly to achieve chemical conversion in a reactor. For example, Meier et al. (2005) designed and built a solar multitube rotary kiln for decomposition of $CaCO_3$ at 1300 K for CaO production. Meier et al. (2006) estimated the cost of solar-produced CaO to be double the selling price of conventional lime, but with as much as 95 % of the CO_2 avoided. Nikulshina et al. (2006, 2007, 2008, 2009) investigated (both experimentally and by thermodynamic analysis) solar-powered DAC based on absorption using different solid inorganic chemisorbents capable of withstanding the very high temperatures needed for the decomposition reactions. For example, CO_2 was removed from air using $Ca(OH)_{2(s)}$, forming $CaCO_3$ which was

decomposed at 1473 K. The total energy consumption was 2485 kJ.mol^{-1} CO_2 captured (Nikulshina et al., 2006; 2007). They also studied carbonation-decomposition cycles of $NaOH_{(s)}$. Complete thermal decomposition of Na_2CO_3 into Na_2O and CO_2 was achieved after 15 min at 1273-1673 K (Nikulshina et al., 2009). These studies prove that concentrated solar power (CSP) reactors can drive decomposition reactions. It seems likely that lower temperature regeneration can also be achieved using CSP, yielding significant savings in energy and enabling the use of less exotic high-temperature materials. CSP could be attractive in uninhabited desert regions with high and reliable solar irradiation.

1.16.4 Nuclear

Steinberg and Dang (1975; 1977) investigated methanol/methane production using H_2 from water splitting, with CO_2 obtained from the air using a cooling tower as part of the capture system. Alkali hydroxides and carbonate absorbents were regenerated by electrolysis using electricity provided by the plant. Lewis and Martin (1979) patented a similar process, but with thermally driven regeneration. Kubic and Martin (2010) proposed using K_2CO_3 solutions to cool the nuclear reactors and pre-heat the solution before air capture. Corbett (1986) patented a process for producing methanol using air-derived CO_2 and seawater-derived H_2 powered by an on-board nuclear reactor. Light water reactors produce heat at relatively low temperatures, which is why Steinberg and Dang (1975) and others have focused on electrolytic regeneration or thermal regeneration of the bicarbonate form (which can be regenerated to the K_2CO_3 sorbent at lower temperatures). This led Mahmoudkhani and Keith (2009) to speculate about integration of the decomposition step with a high-temperature gas-cooled nuclear reactor (HTGR). A typical

design involves a Brayton closed-cycle gas turbine using helium. The reactor outlet temperature is 1123 K. They suggest that this temperature is insufficient to power the decomposition of $CaCO_3$ which is often the base case for regeneration of NaOH for DAC (Socolow et al., 2011). However, regeneration using titanates occurs at lower temperature (1072 K) which would facilitate integration of DAC with HTGR. They argue that HTGRs would be the lowest cost source of carbon neutral high-grade heat (Deutch et al., 2003). HTGR has a number of advantages over natural-gas-fired kilns, the most obvious being no additional CO_2 formation requiring additional separation equipment. According to Price and Blaise (2002) there is sufficient accessible uranium on the planet to run all human civilization at a power of ten times the current level for thousands of years. However, short and long-term risks must be considered (Christodouleas et al., 2011).

1.16.5 Heat from industry

Another possibility for supplying energy to DAC is via heat integration with industrial processes. Johnson et al. (2008) estimate that as much as 20 to 50 % of world industrial energy consumption dissipates as waste heat, and that between 18 and 30 % could be utilized. Heat is available at a variety of temperatures below 873 K from many industrial processes such as pulp and paper mills, cement plants, steel and glass making, metal casting and aluminium production. The lower the temperature of the regeneration stage in DAC, the more options there are for integration. Fasihi et al. (2019) estimate that access to “free” industrial waste heat could reduce the cost of some DAC technologies by 40 to 57 %. In CCU processes, such as synthetic fuel

production, waste heat could be sent to a nearby DAC facility which in turn provides the necessary CO_2 for the utilization process.

1.17 Lowering the temperature of aqueous alkali hydroxide DAC

The high rate of CO_2 absorption by sodium and potassium hydroxide make them excellent sorbents for capture of CO_2 from ambient air. If DAC using sodium or potassium hydroxide solution were to be rolled out today on a massive scale, the most reliable methods for regeneration are conventional causticization using lime (for $KOH_{(aq)}$ or $NaOH_{(aq)}$) or direct causticization using hematite (for $NaOH_{(aq)}$). This assumption is based on the proven track record of the Kraft and DARS processes for regenerating hundreds of tons of sodium hydroxide solution per day in the pulp and paper industry. However, both regeneration processes involve decomposition of a metal carbonate at high temperature (>1173 K) leading to high operating cost, which is a serious obstacle to the viability of Direct Air Capture. A lower regeneration temperature would facilitate integration with heat from industrial processes, nuclear or renewables, rather than natural gas, making DAC more sustainable and reducing its operating cost. If successful, large-scale, low cost DAC could play a key role in the global strategy to mitigate climate change.

Such high temperatures are primarily a result of the thermodynamics of these reactive systems, in particular the high enthalpy of carbonate decomposition. The thermodynamics give some indication of the temperature at which these reactions proceed spontaneously. For example, at a given CO_2 partial pressure, the carbonate decomposition becomes feasible at a temperature where $\Delta G=0$. From equilibrium thermodynamics we know that higher CO_2 partial pressure

requires higher decomposition temperature. However, in reality, thermodynamic models have limited predictive ability and do not give information about how fast these decomposition reactions proceed. For example, Archer et al. (2013) used an analytical model based on equilibrium thermodynamics for prediction of $CaCO_3$ decomposition onset temperatures at different pressures. It was found that the difference between the predicted and measured temperatures was of the order of 100 K. This discrepancy is proposed to be due to kinetic and mass transfer factors. Archer et al. (2013) conclude that purely thermodynamic models are insufficient, and that kinetic approaches are needed. Therefore, the main aim of this thesis is to better understand the kinetic factors which affect the temperature of carbonate decompositions in existing regeneration systems.

Temperature reductions in DAC might also be made possible using different reaction pathways. There does not seem to be an obvious viable alternative reagent to lime in regeneration of aqueous alkali hydroxides by conventional causticization. However, some studies show that replacing hematite with titanium oxide in direct causticization is possible (Mahmoudkhani and Keith, 2009). Therefore, the second objective of this thesis is to investigate alternatives to hematite which enable CO_2 to be released at a lower temperature.

Chapter 2: Thesis objectives

2.1 First objective

In the introduction, two proven methods for large-scale regeneration of alkali hydroxide solutions ($NaOH_{(aq)}$ and $KOH_{(aq)}$) were described: conventional causticization using lime (CaO) and direct causticization using hematite (Fe_2O_3). Both methods involve reactions of alkali carbonates ($CaCO_3$ and Na_2CO_3 respectively) which require high temperatures to release CO_2 at sufficient rates. A better understanding of the factors which influence the reaction rates, i.e. the kinetics, could lead to improved reactor design and/or a lower operating temperature.

Although the kinetics of $CaCO_3$ decomposition have been a subject of intense study for over a century, controversies regarding the precise pressure dependency of the decomposition rate still exist. Moreover, recent advances in the computational methods of kinetic analysis can provide a more accurate analysis. For the reaction between $Fe_2O_{3(s)}$ and $Na_2CO_{3(s)}$, very little reliable kinetic information is available and is thus deeply needed.

Ideally, in order to design better reactors and potentially lower the cost of DAC, it is desirable to have simple expressions for the reaction rates as functions of time, temperature and the properties of the solid and gas phases. Based on this reasoning, the first and main objectives of this thesis can be stated as follows:

To develop and parameterize a simple kinetic model for 1. The rate of $CaCO_3$ decomposition and 2. The rate reaction of Fe_2O_3 and Na_2CO_3, in terms of temperature, conversion and any other relevant variables, which accounts for all the experimental data.

2.2 Second objective

Socolow et al. (2011) assessed the economic viability of CO_2 capture using $NaOH_{(aq)}$ with regeneration by conventional lime causticization. Their analysis revealed that regeneration dominates the overall cost of the process due to the heat required at high temperature to overcome the thermodynamic and kinetic barriers for $CaCO_3$ decomposition. To reduce this cost, they propose some key questions to be addressed in future work:

"In air capture systems where a second material (e.g. $CaCO_3$) is required to concentrate the CO_2-carrying entity prior to CO_2 release, can materials be developed that lower the temperature of CO_2 release? Can catalysts be developed to reduce the activation energy needed for CO_2-release processes?" (Socolow et al., 2011).

In the introduction it was mentioned that replacements for CaO in conventional causticization are unlikely to be viable. On the other hand, there is considerable potential for alternatives to Fe_2O_3 in direct causticization, e.g. TiO_2 (Mahmoudkhani et al., 2009), which have more favourable thermodynamics and kinetics. Therefore, the second objective of this thesis can be stated as follows:

To test a range of oxides with the potential to replace Fe_2O_3 in direct causticization, with a focus on finding pathways which enable CO_2 to be released at lower temperatures.

If achieved, these two main thesis objectives could provide concrete ways to reduce the temperature and cost of aqueous alkali hydroxide Direct Air Capture.

Chapter 3: Theory

During study of carbonate decompositions, a new methodology called "The Method of Maximum Permutations" was developed to improve the accuracy of the determined parameters needed for kinetic models. This chapter is mainly intended to provide the context for this method. For those readers concerned only with reactions related to Direct Air Capture, this chapter can be skipped.

3.1 Introduction

Chemical kinetics is a branch of physical chemistry which aims to quantify the rates of chemical processes. For solid-gas reactions the rate of conversion, dα/dt, is given by:

$$\frac{\mathrm{d}\alpha}{\mathrm{d}t} = k(T).f(\alpha).h(P) \qquad 3.1$$

where α is the conversion, t is the time, T is the temperature, P is the pressure and $k(T)$, $f(\alpha)$ and $h(P)$ are the functions describing the temperature, conversion and pressure dependencies respectively. In the rest of this chapter, $h(P)$ is assumed to be a constant for the sake of simplicity but is addressed in Chapter 4.

3.2 Conversion dependency

There are 22 mathematical models commonly used to describe $f(\alpha)$ for reactions involving solids (see Table 8.1 in Appendix A). These models are derived by assuming a rate-limiting step, or steps, due to chemical reaction (R_2, R_3, F_1-F_3), diffusion (D_1-D_6), nucleation (P_2-P_5) or nucleation and growth (A_2-A_4). The assumed geometry of the particle determines the final form

of the derived expression. For example, the contracting geometry models (R_x) assume that the rate is controlled by a chemical reaction occurring at the reactant-product interface. This interface advances steadily towards the axis in the case of a cylindrical particle (R_2) or towards the center in the case of a spherical particle (R_3). Full derivations for most of these models can be found in Khawam and Flanagan (2006). The simple models included in Table 8.1 are often too simplistic to capture the essential features of real reactions involving solids. More complex models, for example, the Valensi-Carter model (Carter, 1961) have fared better. Indeed, in this thesis, these simple models were not found to provide adequate descriptions for the conversion dependency of the rate of carbonate decompositions. As we will see, in Chapters 4 and 5, more sophisticated models had to be derived.

3.3 Defining conversion

Experimental conversion data obtained at different temperatures or heating rates allow the rate of a chemical process to be parameterized. In homogenous systems, such as gases and liquids, the concentration of reactants or products is often used to determine the conversion. In reactive solid systems, it can be difficult to measure the concentration of reactants or products. Instead, some other property of the sample, such as heat flow or sample mass, is recorded and used to determine the conversion. Thermogravimetric analysis (TGA) is a method for continuously measuring the mass of a sample as a function of time and/or temperature. For this reason, TGA has been used in the study of chemical processes such as desorption, adsorption, sublimation, vaporization, oxidation, reduction and decomposition.

A decomposing solid may undergo multiple periods of mass change during heating. Thus, the first step in obtaining conversions from TGA data is to inspect the mass vs. time data, or mass vs. temperature data and extract the mass values from the time period, or temperature range, that is of interest to the investigator. Then the reaction progress can be calculated using the ash-free conversion, α_{af}:

$$\alpha_{\mathrm{af}} = \frac{m_{\mathrm{i}} - m_t}{m_{\mathrm{i}} - m_{\mathrm{f}}} \qquad 3.2$$

where m_{i} is the initial mass, m_{f} is the final mass and m_t is the mass at time, t. In the case that m_{f} is chosen to be 0:

$$\alpha_{\mathrm{s}} = \frac{m_{\mathrm{i}} - m_t}{m_{\mathrm{i}}} \qquad 3.3$$

where α_{s} is the standard conversion. In the ash-free definition the conversion is the fraction of the total that can be converted (leaving the "ash" behind) and in the standard definition the conversion is the fraction of the total mass that has been converted. The choice of the ash-free or standard conversion depends on the intended use. Typically, the ash-free conversion is used in determination of the kinetic parameters because it accounts for the quantity of unreactive material, which can vary between subsamples, thus facilitating stable convergence of the computer algorithms used in kinetic analysis. The standard conversion is often used for presentation of data, since it better conveys the absolute mass lost (or gained). Both definitions are used in this thesis depending on the situation.

3.4 Temperature dependency

The temperature dependence of the rate is usually described by a semi-empirical equation called the Arrhenius equation:

$$k(T) = A\exp\left(\frac{-E}{RT}\right) \tag{3.4}$$

where *A* is the pre-exponential factor which is related to the frequency of collisions of sufficient energy and their orientation upon collision, and *E* is the intrinsic activation energy barrier for conversion from reactants to products (see Figure 3.1). *R* is the universal gas constant. By combining Eqs. 3.1 & 3.4 and assuming $h(P)$=constant:

$$\frac{\mathrm{d}\alpha}{\mathrm{d}t} = A\exp\left(\frac{-E}{RT}\right) f(\alpha) \tag{3.5}$$

Knowledge of the "kinetic triplet" – *A*, *E* and $f(\alpha)$ – allows the reaction rate to be determined at any given temperature and conversion. Determination of the kinetic triplet (parameterization) requires conversion data at multiple different constant temperatures (isothermal) or constant heating rates (non-isothermal).

3.5 Isothermal vs. non-isothermal data collection

Thermogravimetric data can be gathered isothermally, i.e. holding the temperature constant, measuring the mass loss over time and then analyzing the data using an isothermal calculation method. However, this approach has fallen out of favour in the field of solid-state and solid-gas-state kinetics for several reasons. First, there must always be a period of temperature ramping to

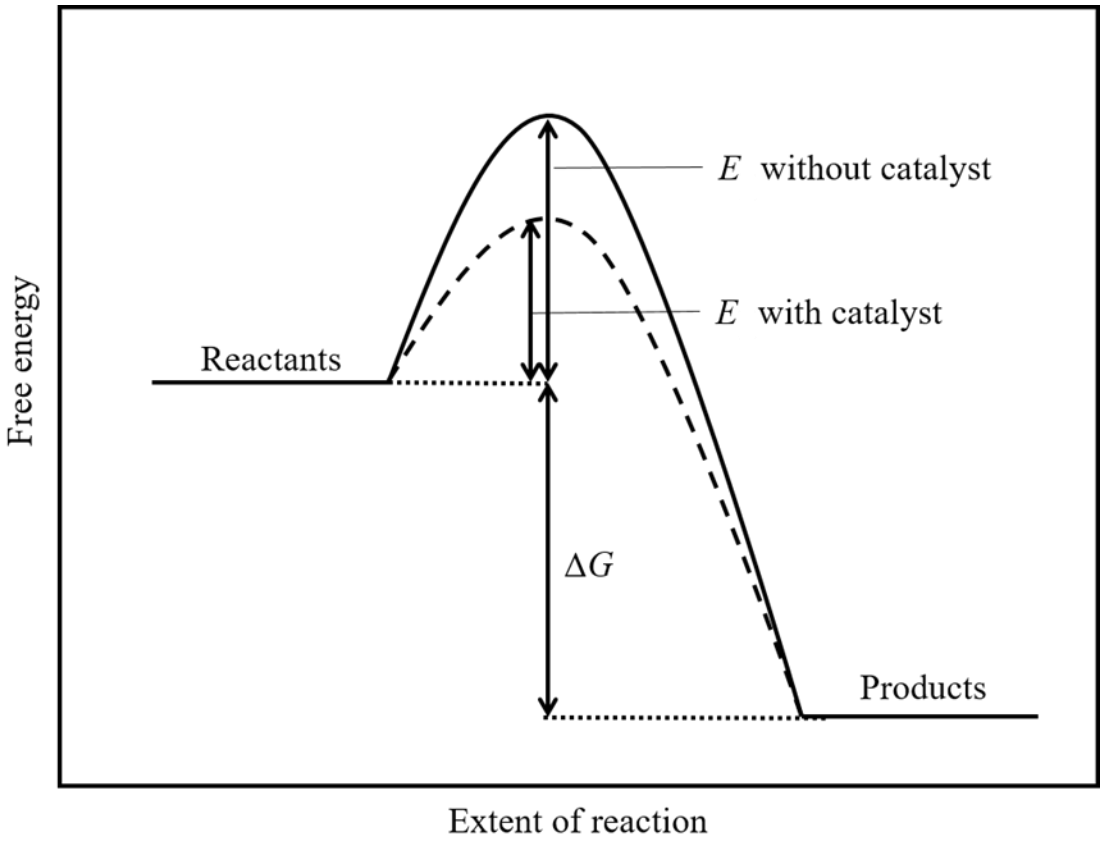

Figure 3.1 – Intrinsic activation energy for catalyzed vs. uncatalyzed reactions.

reach the intended temperature during which some reaction is bound to occur. Second, it may be difficult to obtain data reaching full conversion within a reasonable time at low temperatures. Conversely, at higher temperatures the reaction can reach completion before the isothermal period even begins. For these reasons, non-isothermal data collection is preferable, with TGA data normally gathered at a constant heating rate (β):

$$\beta = \frac{\mathrm{d}T}{\mathrm{d}t} = constant \qquad 3.6$$

Combining 3.4, 3.5 and 3.6 gives:

$$\frac{\mathrm{d}\alpha}{\mathrm{d}T} = \frac{A}{\beta}\exp\left(\frac{-E}{RT}\right)f(\alpha) \qquad 3.7$$

where dα/dT is referred to as the non-isothermal reaction rate. Non-isothermal TGA provides conversion data as a function of temperature which, in turn, is a function of time.

There are two different approaches for obtaining the kinetic parameters from non-isothermal data – model-fitting and model-free.

3.6 Model-fitting vs. model-free methods

Model-fitting methods make assumptions about the conversion dependency of the reaction. Often these methods involve minimizing the difference between the data points of experimental conversion (or rate) data and simulated conversion (or rate) data by adjusting both A and E for a particular $f(\alpha)$. Minimization can be achieved by linear or non-linear regression. On its own, model-fitting to a single curve is now recognized as unreliable for determination of kinetic parameters (Vyazovkin and Wight, 2000). This can be illustrated with a simple example. Figure 3.2 shows that a simulated "experimental" rate curve with a particular kinetic triplet can be well-fitted by a model curve with a different kinetic triplet. Thus, despite the excellent fit, the solution is wildly inaccurate.

The source of the curve-fitting problem lies in the parameters A and E which are mathematically decoupled from the conversion and time (Mochulski, 2014). This results in a linear relationship between ln$A$ and E known as the kinetic compensation effect:

$$\ln A = aE + b \qquad 3.8$$

where *a* and *b* are the linear fitting parameters. Therefore, in order to decouple *A* and *E* and reach a solution, a good first approximation of one or the other is needed. These can be obtained using model-free methods.

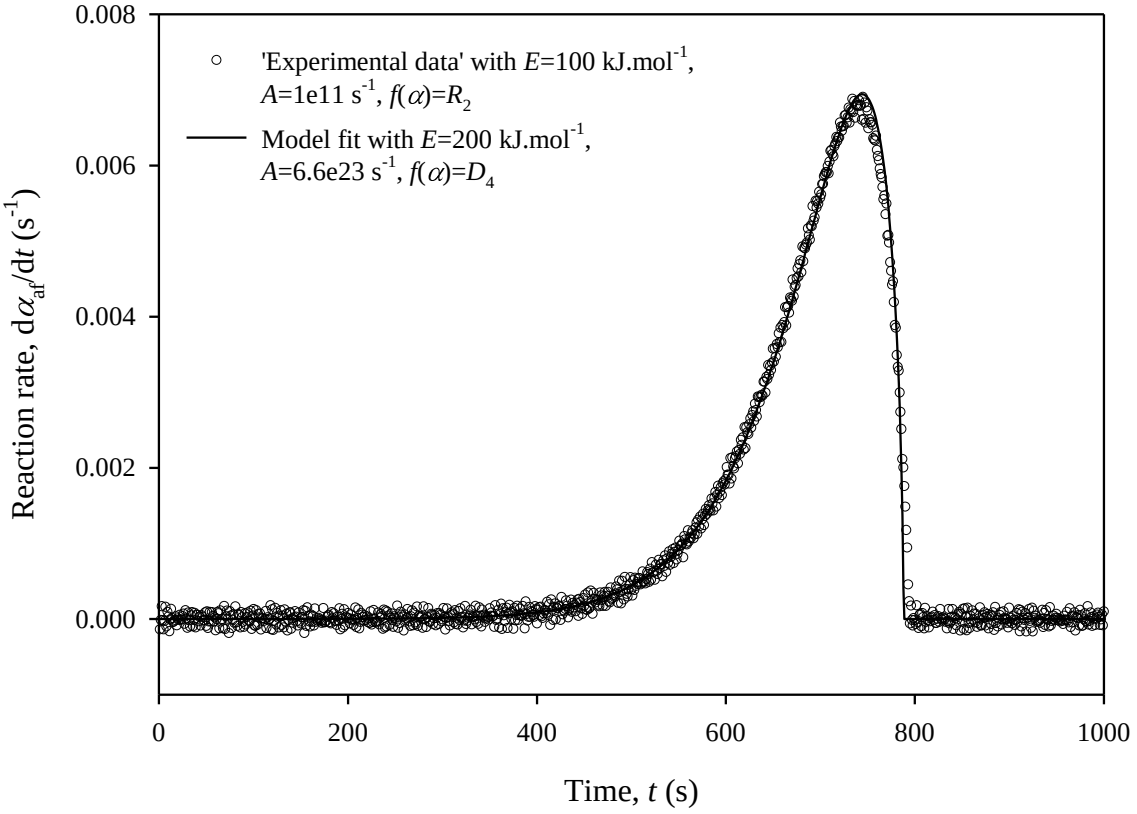

Figure 3.2 – Reaction rate vs. time for simulated experimental data with a 1 % random error in the conversion values, with good yet incorrect model fit, at β=20 K.min^{-1}.

Model-fitting methods are most useful when combined with model-free estimates of one or more of the kinetic parameters. Model-free methods can provide estimates of the activation energy without specific assumptions about the form of $f(\alpha)$. The terms "model-free" and "isoconversional" are often used interchangeably. However, not all model-free methods, such as the Kissinger (1957) method, are isoconversional. Isoconversional methods produce values of

the activation energy at different values of α. The Kissinger method produces only one value of the activation energy and is therefore not isoconversional.

Isoconversional methods assume that the reaction rate at any fixed value of conversion is a function of temperature only. Assuming $h(P)$ is a constant and then taking the logarithmic derivative of Eq. 3.1 with respect to the reciprocal temperature gives:

$$\left[\frac{\partial \ln(\mathrm{d}\alpha/\mathrm{d}t)}{\partial T^{-1}}\right]_{\alpha} = \left[\frac{\partial \ln k(T)}{\partial T^{-1}}\right]_{\alpha} + \left[\frac{\partial \ln f(\alpha)}{\partial T^{-1}}\right]_{\alpha} \qquad 3.9$$

where the subscript α indicates isoconversional values, i.e., the values related to a specific value of conversion. Since α is constant, $f(\alpha)$ is also constant and Eq. 3.9 becomes:

$$E_{\alpha} = -R\left[\frac{\partial \ln(\mathrm{d}\alpha/\mathrm{d}t)}{\partial T^{-1}}\right]_{\alpha} \qquad 3.10$$

where E_α is the isoconversional activation energy. E_α is often referred to as the "apparent" isoconversional activation energy to distinguish it from the "intrinsic" activation energy, E. It is very difficult to obtain the intrinsic E due to the non-species-specific nature of the measurement techniques (e.g. TGA) and the underlying complexity of solid and solid-gas reactions. Isoconversional methods help reveal this complexity via the dependence of E_α on α. This will be made clearer in Section 3.9 using an example.

3.7 Differential vs. integral isoconversional methods

Isoconversional methods are either differential or integral. Differential methods such as the Friedman method (Friedman, 1964) magnify noise present in conversion data. Thus, integral methods are preferred to differential ones. Integral methods such as the Ozawa-Flynn-Wall (Ozawa, 1965) and Kissinger-Akahira-Sunose (Akahira and Sunose, 1971) methods are based on approximations and have limited accuracy. On the other hand, the Advanced Isoconversional (AIC) method (Vyazovkin, 1997; 2001) uses numerical integration. As a result, it is the most accurate isoconversional method for estimation of E_α (Brown et al., 2000; Vyazovkin et al., 2011). The AIC method is described in the next section.

3.8 The Advanced Isoconversional (AIC) method

In this thesis, E_α is determined using the Advanced Isoconversional (AIC) method. Therefore, it is important to show its derivation. For some linear or non-linear heating program, Eq. 3.5 can be written:

$$\frac{\mathrm{d}\alpha}{\mathrm{d}t} = A\exp\left(\frac{-E}{RT(t)}\right)f(\alpha) \qquad 3.11$$

where $T(t)$ is the heating program describing temperature as a function of time. Separation of variables followed by integration over small time and conversion intervals gives:

$$\big(g(\alpha)\big)_\alpha = \int_{\alpha-\Delta\alpha}^{\alpha} \mathrm{d}\alpha/f(\alpha) = A_\alpha \int_{t_{\alpha-\Delta\alpha}}^{t_\alpha} e^{-\frac{E_\alpha}{RT(t)}}\ \mathrm{d}t \qquad 3.12$$

where $(g(\alpha))_\alpha$ is the integral of $1/f(\alpha)$ over a small conversion interval, A_α is the isoconversional pre-exponential factor and E_α is the isoconversional activation energy. Eq. 3.12 is often written in the literature in the J' integral form:

$$\big(g(\alpha)\big)_\alpha = A_\alpha \int_{t_{\alpha-\Delta\alpha}}^{t_\alpha} e^{-\frac{E_\alpha}{RT(t)}}\,\mathrm{d}t = A_\alpha\, J'\big(E_\alpha, T(t_\alpha)\big) \qquad 3.13$$

There is no analytical solution for Eq. 3.13 and thus numerical integration must be used.

Eq. 3.13 contains two unknowns, E_α and A_α. Assuming that $(g(\alpha))_\alpha$ is constant for different heating programs then:

$$\big(g(\alpha)\big)_\alpha = A_\alpha J'\big(E_\alpha, T_1(t_\alpha)\big) = A_\alpha J'\big(E_\alpha, T_2(t_\alpha)\big) = \text{constant} \qquad 3.14$$

where $T_1(t_\alpha)$ is the temperature function for a particular α using the first heating program and $T_2(t_\alpha)$ is the temperature function for the same α using the second heating program. The assumption that $(g(\alpha))_\alpha$ is a constant independent of the temperature program allows A_α to be eliminated by dividing each J' function by the other:

$$\frac{J'\big(E_\alpha, T_1(t_\alpha)\big)}{J'\big(E_\alpha, T_2(t_\alpha)\big)} = \text{constant} \qquad 3.15$$

$$\frac{J'\big(E_\alpha, T_2(t_\alpha)\big)}{J'\big(E_\alpha, T_1(t_\alpha)\big)} = \text{constant} \qquad 3.16$$

Then, summing 3.15 and 3.16 and minimizing:

$$min\left|\frac{J'\left(E_\alpha, T_1(t_\alpha)\right)}{J'\left(E_\alpha, T_2(t_\alpha)\right)} + \frac{J'\left(E_\alpha, T_2(t_\alpha)\right)}{J'\left(E_\alpha, T_1(t_\alpha)\right)}\right| = \Omega_\alpha = 2 \qquad 3.17$$

E_α is iterated upon until the optimization indicator, Ω_α, is minimized (Campbell et al., 2016). The minimum of the sum of any positive number and its reciprocal is always 2 (see Appendix B). For three heating rates the minimum sum is:

$$\min\left|\begin{array}{c}\frac{J'\left(E_\alpha, T_1(t_\alpha)\right)}{J'\left(E_\alpha, T_2(t_\alpha)\right)} + \frac{J'\left(E_\alpha, T_1(t_\alpha)\right)}{J'\left(E_\alpha, T_3(t_\alpha)\right)} + \frac{J'\left(E_\alpha, T_2(t_\alpha)\right)}{J'\left(E_\alpha, T_1(t_\alpha)\right)} + \frac{J'\left(E_\alpha, T_2(t_\alpha)\right)}{J'\left(E_\alpha, T_3(t_\alpha)\right)} \\ + \frac{J'\left(E_\alpha, T_3(t_\alpha)\right)}{J'\left(E_\alpha, T_1(t_\alpha)\right)} + \frac{J'\left(E_\alpha, T_3(t_\alpha)\right)}{J'\left(E_\alpha, T_2(t_\alpha)\right)}\end{array}\right| = \Omega_\alpha = 6 \qquad 3.18$$

If n_β heating rates are applied, the expression can be generalized to:

$$min\left|\sum_{i=1}^{n}\sum_{j\neq i}^{n}\frac{J'(E_\alpha, T_i(t_\alpha))}{J'\left(E_\alpha, T_j(t_\alpha)\right)}\right| = \Omega_\alpha = n_\beta(n_\beta - 1) \qquad 3.19$$

Minimizing the left-hand side of Eq. 3.19 produces a best estimate for E_α at each value of α. The MATLAB code for the full algorithm can be found in Appendix C.

3.9 Simulated example of Advanced Isoconversional method

The most straightforward reactions are composed of one rate-limiting step, usually described by Eq. 3.5. However, solid and solid-gas reactions tend to be more complex. For example, during heating of a solid powder mixture of MnO_2 and Na_2CO_3 in an inert atmosphere, both $CO_{2(g)}$ and $O_{2(g)}$ can be lost simultaneously. The overall rate of a dual-parallel process such as this might be described by:

$$\frac{\mathrm{d}\alpha}{\mathrm{d}t} = W_1 A_1 exp\left(\frac{-E_1}{RT}\right) f_1(\alpha_1) + W_2 A_2 exp\left(\frac{-E_2}{RT}\right) f_2(\alpha_2) \qquad 3.20$$

where the numerical subscripts denote the two reactions and W is the mass-weighted contribution to the total conversion such that $W_1 + W_2 = 1$. In thermogravimetric analysis the mass change gives the overall extent of conversion (α), which is the sum of the conversions of the individual reactions ($\alpha_1+\alpha_2$). It may be possible, depending on the values of E_1, E_2, A_1 and A_2, to isolate each reaction using a lower heating rate and study these separately.

Isoconversional methods, like the AIC method, are particularly useful for studying complex reactions involving solids, e.g. overlapping parallel reactions, because they produce plots of apparent E_α at successive values of α. Estimates for the intrinsic E's of the contributing reactions can sometimes be drawn from the apparent E_α vs. α plot. In rest of this section, E_α is determined using the Advanced Isoconversional method for a simulated process with a single rate-determining step, as well as a simulated dual-parallel process.

Figure 3.3A shows simulated conversion and rate vs. temperature data for a first-order reaction ($f(\alpha)=1-\alpha$) at heating rates of 2, 4 and 8 K.min^{-1}. Conversion data were constructed by fourth-order Runge-Kutta integration of Eq. 3.5 setting E=120 kJ.mol^{-1} and A=1e8 s^{-1}. Taking the first forward derivative of the conversion data with respect to time gave the corresponding reaction rate. The conversion data at three heating rates, with their corresponding time and temperature values, were then used to determine E_α by the Advanced Isoconversional method by minimization of Eq. 3.19, achieved using the Nelder-Mead method (fminsearch in MATLAB). The J' integral was numerically determined using recursive adaptive Simpson quadrature (quad

in MATLAB). Figure 3.3B shows that the Advanced Isoconversional method accurately estimates the intrinsic activation energy of 120 kJ.mol^{-1} which is independent of the conversion, as expected for a single-step reaction. For a truly single-step reaction, the apparent isoconversional activation energy gives the intrinsic activation energy.

Figure 3.4A shows simulated rate vs. temperature data for a reaction composed of two parallel first-order processes at heating rates of 5, 10 and 20 K.min^{-1}. Conversion data were constructed by fourth-order Runge-Kutta integration of Eq. 3.20 setting E_1=120 kJ.mol^{-1}, E_2=130 kJ.mol^{-1}, A_1 and A_2=1e11 s^{-1}, W_1 and W_2=0.5. Taking the first forward derivative of the conversion data with respect to time gave the reaction rate. The two processes which compose the overall transformation at β=20 K.min^{-1} are shown by dashed lines labeled R1 and R2. Conversion data are not shown in order to avoid overcrowding the figure.

The isoconversional activation energy determined by the Advanced Isoconversional method is shown in Figure 3.4B. As expected, E_α is approximately 120 kJ.mol^{-1} at low conversion and 130 kJ.mol^{-1} at high conversions. However, there is an unanticipated bump in the plot at α=0.6-0.8, corresponding to the point of inflection in the rate data, near where the parallel reactions overlap to the greatest extent. Indeed, the more the reactions overlap, the more difficult it is to discern the intrinsic *E*'s of the contributing reactions from the isoconversional plot (Campbell et al., 2016).

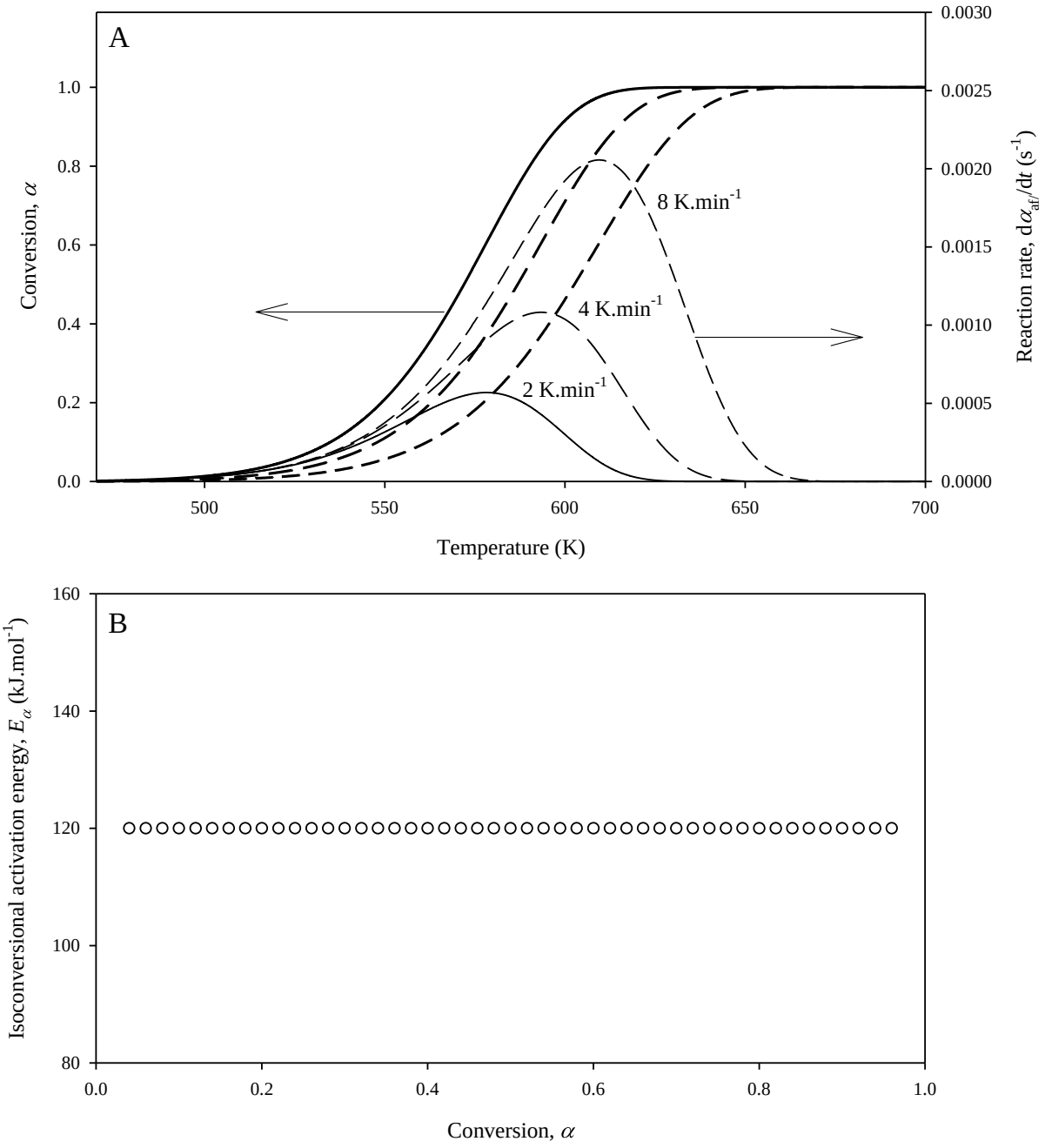

Figure 3.3 – A. Simulated conversion and reaction rate vs. temperature for a first-order reaction at three heating rates. B. Isoconversional activation energy vs. conversion.

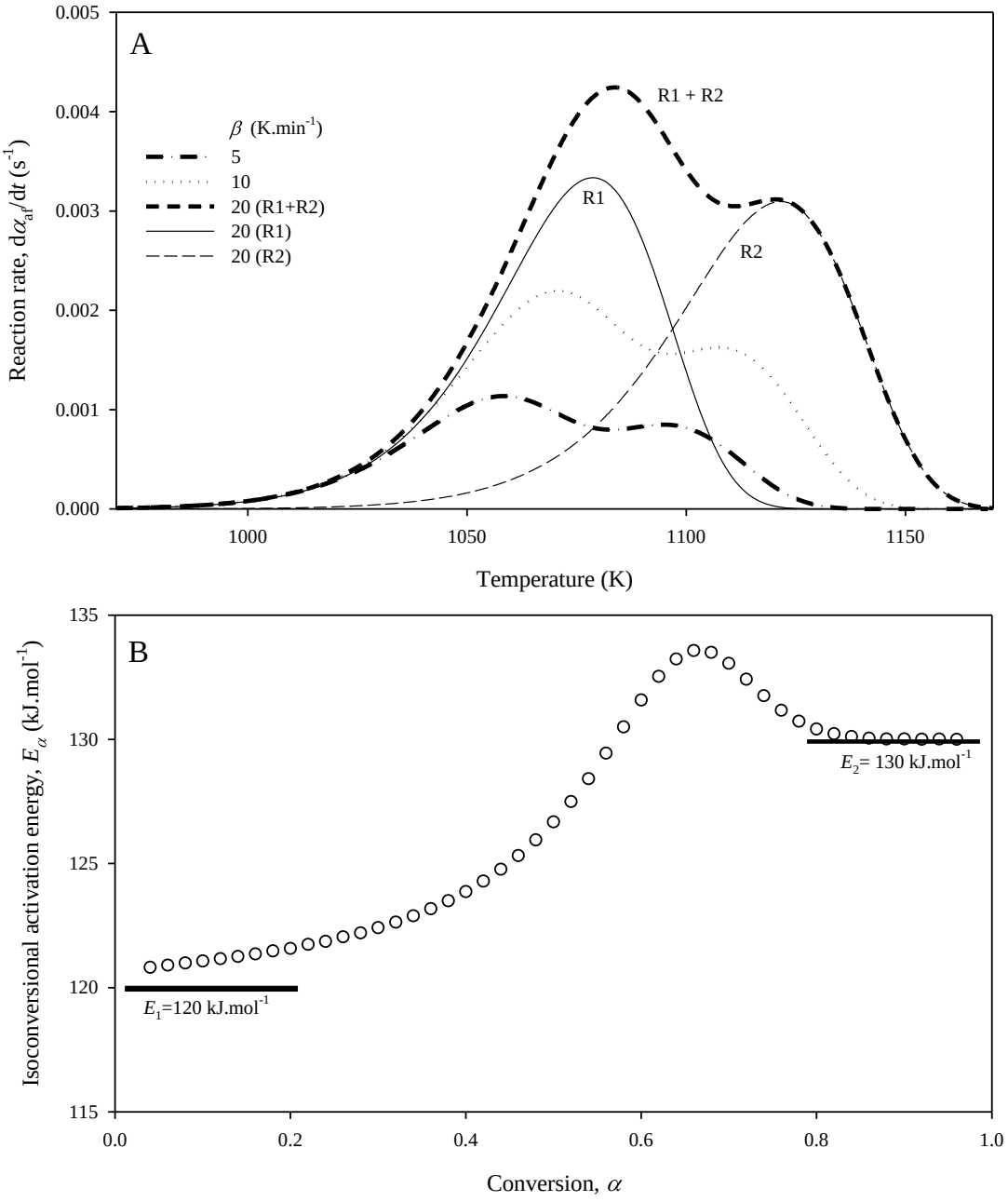

Figure 3.4 – A. Simulated reaction rate vs. temperature for a process composed of two parallel first-order reactions at three heating rates. B. Isoconversional activation energy vs. conversion.

3.10 Method of maximum permutations

Traditionally, data are obtained at three or more heating rates and only one result is determined for E_α vs. α (as was done in Figure 3.3-3.4). It would be preferable to perform repeats and obtain several estimates for E_α, take an average and determine confidence limits. For example, Vyazovkin and Wight (2000) gathered conversion data for the decomposition of ammonium nitrate at five heating rates (2.5, 5, 7.5, 10 and 12.5 K.min^{-1}) with nine repeats (A-I) at each rate (see Table 3.1). From these they obtained nine E_α vs. α results, then determined the mean and "realistic" confidence intervals. Thus, 45 sets of data produced 9 E_α results.

Table 3.1 – Data combinations used by Vyazovkin and Wight (2000) for determination of realistic confidence intervals for the Advanced Isoconversional method at five heating rates with nine repeats at each rate, for gasification of ammonium nitrate. Data could have been alternatively combined to give new results. Highlighted values show one possible permutation of a 59,049 total permutations using data at all 5 heating rates.

Repeat	Heating Rate (K.min^{-1})					E_α
	2.5	5	7.5	10	12.5	
A	2.5A	5A	7.5A	10A	12.5A	E_{α_A}
B	2.5B	5B	7.5B	10B	12.5B	E_{α_B}
C	2.5C	5C	7.5C	10C	12.5C	E_{α_C}
D	2.5D	5D	7.5D	10D	12.5D	E_{α_D}
E	2.5E	5E	7.5E	10E	12.5E	E_{α_E}
F	2.5F	5F	7.5F	10F	12.5F	E_{α_F}
G	2.5G	5G	7.5G	10G	12.5G	E_{α_G}
H	2.5H	5H	7.5H	10H	12.5H	E_{α_H}
I	2.5I	5I	7.5I	10I	12.5I	E_{α_I}

However, Vyazovkin and Wight (2000) could have used different permutations of the data to obtain additional values of E_α. An example of a new permutation is indicated by the shaded boxes in Table 3.1. By crossing the data in this way, Vyazovkin and Wight (2000) could have obtained 9^5=59,049 results instead of just 9. More generally, for any system of data with n_β heating rates and m_β repeats at each heating rate, there will be $m_\beta \wedge n_\beta$ results.

Note also that if one chose to use all the permutations of the data in sets of 3 or 4 heating rates in addition to the sets of 5 heating rates in Table 3.1, there will be $\sum_{g=3}^{n_\beta} \binom{n_\beta}{g} . m_\beta^g$ (where m_β=9, n_β=5) permutations of the data, and thus 66,339 results for E_α at each value of α. Note, 2-heating rate combinations (g=2) are not permitted (Vyazovkin et al., 2014).

From the discussion so far, three main approaches can be identified for estimation of E_α: 1. The "traditional" approach which gives just one estimate for E_α, 2. The "Vyazovkin and Wight (2000)" approach which gives m_β estimates and 3. The "permutations approach" which gives $m_\beta \wedge n_\beta$ estimates. The former two approaches use all the data only once whereas the latter approach uses each data set more than once. As a consequence, the "measurements" are not independent potentially making it hard to interpret the error.

It is also possible to have a system of data collection where the number of repeats at each rate varies. For example, it is known (Vyazovkin et al., 2014) that the accuracy of an estimate of E_α is dominated by the data at the extreme temperatures. Thus, repetition, particularly at the lowest and highest heating rates, is more useful than repetition at the inner heating rates. This means the

"permutations approach" enables data to be collected in an asymmetric manner, with potential for time savings.

Table 3.2 compares the accuracy of the median isoconversional activation energy, $\tilde{E}_\alpha$, estimated by three different methods of data collection. For this, conversion data were simulated at three heating rates (2, 4 and 8 K.min^{-1}) using fourth-order Runge-Kutta integration, with E=239 kJ.mol^{-1}, A=1e12 s^{-1}, $f(\alpha)$=1-α. For the "permutations" method, 7 repeats at each rate were simulated. Conversion data were converted to mass data assuming m_i=10 and m_f=5 and then random error <1 % added. These mass data were then transformed back into conversion data. Using this data, E_α was estimated by the Advanced Isoconversional method at every value of α from 0.04 to 0.96 in steps of 0.02. The J' integral was numerically determined using recursive adaptive Simpson quadrature (quad in MATLAB). Minimization of Eq. 3.19 was achieved using the algorithm "fminsearch" in MATLAB which uses the Nelder-Mead simplex method (Lagarias et al., 1998). This process was repeated for every permutation of the data, as described in Table 3.2, and the median taken to give $\tilde{E}_\alpha$. For the "traditional" approach E_α=$\tilde{E}_\alpha$. The median was found to produce a more accurate estimate than the mean which was more sensitive to outliers.

The "traditional" method returned the least accurate value and the "permutations" method (2(7), 4(7), 8(7)), the best. The "Vyazovkin and Wight" method and "permutations" method (2(7), 4(7), 8(7)) had the same number of data points, but the latter method returned a more accurate value for E_α. Since the accuracy of an estimate for E_α is dominated by the accuracy of the outer (highest and lowest) heating rates, it is advisable to perform more repeats at the outer rates than

at the inner rates (Vyazovkin et al., 2014). Indeed, the estimate of E_α using repeats of the lowest rate, i.e. 2(7), 4(1), 8(1), was more accurate than the estimate using repeats at higher heating rate, i.e., 2(1), 4(1), 8(7), and central heating rate i.e., 2(1), 4(7), 8(1), in that order. Thus, more repeats ought to be performed at the lowest heating rate, then highest heating rate, then any central heating rates. Such an approach could save data collection time.

Table 3.2 – Comparison of different approaches to estimate the median isoconversional activation energy ($\tilde{E}_\alpha$) in the presence of random error for a simulated first-order reaction at three heating rates with intrinsic activation energy (E) of 239 kJ.mol^{-1}.

Approach used	Heating rate (no. of repeats) K.min^{-1}	No. of permutations -	$\tilde{E}_\alpha$ J.mol^{-1}	Error %
Traditional	2(1), 4(1), 8(1)	1	234025	2.08
Vyazovkin and Wight (2000)	2(7), 4(7), 8(7)	7	239880	0.37
Permutations	2(7), 4(1), 8(1)	7	241201	0.92
	2(1), 4(7), 8(1)	7	236187	1.18
	2(1), 4(1), 8(7)	7	236682	0.97
	2(7), 4(1), 8(7)	49	240303	0.54
	2(7), 4(7), 8(7)	147	238517	0.08

3.11 Determining the pre-exponential factor

The natural logarithm of the pre-exponential factor (ln$A$) can be determined using the kinetic compensation effect and the method of invariant kinetic parameters (Lesnikovich and Levchik, 1983; Vyazovkin et al., 2014). Values for A can be obtained which place the peak (maximum rate) of simulated data at the same time as the peak of the experimental data for multiple user-

chosen activation energies (Mochulski, 2014). This can be accomplished by setting an arbitrary activation energy, E_i, and iterating on the pre-exponential factor A_i, guided by a root finding technique, until the derivative of the reaction rate (second derivative of conversion with respect to time) is 0 at the determined value of the peak. Thus, for every input E_i, a value for A_i is obtained. Figure 3.5 illustrates this process for the first reaction from Figure 3.4A with the first-order (F_1) model as the template, although any of the models could have been used.

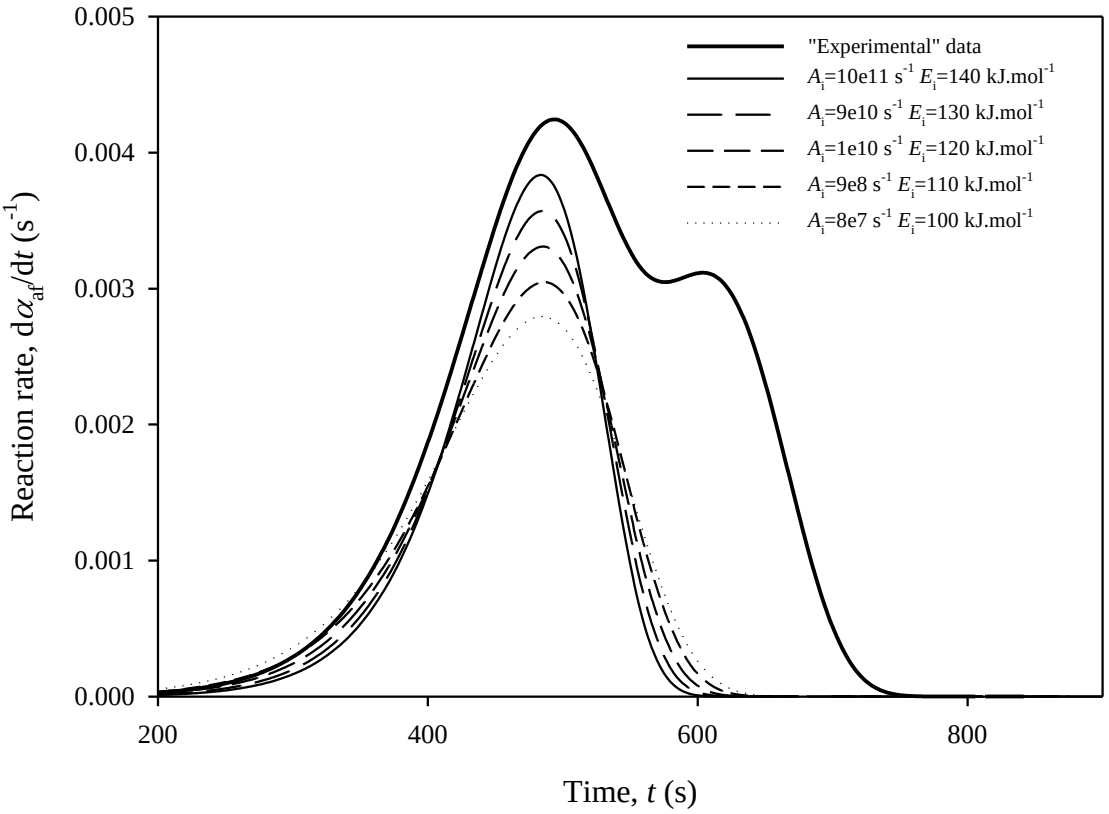

Figure 3.5 – Simulated reaction rate vs. time for two parallel overlapping reactions as described by Eq. 3.20. Also shown are rate data for a first-order reaction with multiple values of E_i and A_i.

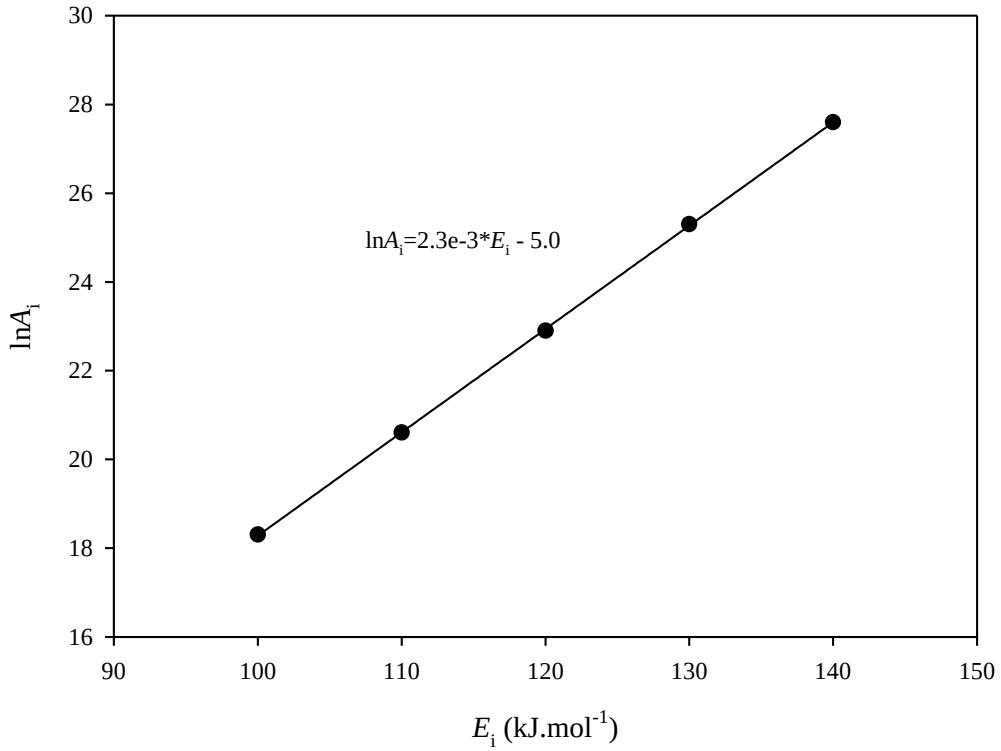

Figure 3.6 – Natural logarithm of the pre-exponential factors vs. the activation energies from the peak matching exercise shown in Figure 3.5.

These E_i and A_i pairs are plotted in Figure 3.6 according to the log-linear relationship known as the kinetic compensation effect:

$$\ln A_i = aE_i + b \tag{3.21}$$

where *a* and *b* are linear fitting parameters obtained from the slope and intercept. Substitution of the isoconversional estimates for activation energy from Figure 3.4 together with *a* and *b* into

$$\ln A_\alpha = aE_\alpha + b \tag{3.22}$$

leads to an estimate for $\ln A_\alpha$ for the first reaction, where A_α is the apparent isoconversional pre-exponential factor. This process is then repeated for the second reaction which will likely show a different kinetic compensation behavior. The intrinsic values of A for the component steps of the overall reaction can be estimated from the plots of $\ln A_\alpha$ vs. α for each of the reactions.

3.12 Determining the conversion dependency

Now that we have unbiased, model-free estimates, for E_α and A_α, all that remains is to determine the conversion dependency, $f(\alpha)$. This can be achieved by testing different forms of $f(\alpha)$ using the isoconversional estimates for E and A as initial guesses then assessing the goodness of fit. For a dual parallel reaction, the fitting process is the same but also includes initial guesses for multiple values of E and A, as well as the reaction contributions, W's. Non-linear regression methods which minimize the residual sum of squares (RSS) between the experimental and predicted conversion data are commonly applied. Curve fitting is performed using the conversion or rate data, or both. A statistical test, such as the F-test, can also be used to determine whether the differences in RSS between the experimental and predicted data are significant. For example, for the multi-step example given in Section 3.9, we would use guesses for the intrinsic activation energies of 120 and 130 kJ.mol^{-1} with corresponding values for A=1e10 and 9e10 s^{-1} which were determined by the kinetic compensation effect, together with some reasonable guess for W_1 and W_2 for the first and second reactions respectively, and then cycle through all 20 x 20 combinations of $f(\alpha)$ (see Table 8.1) in order to find a solution which gives the best overall fit. However, as we will see in the next chapter, the pressure dependence, $h(P)$, must also be considered.

Chapter 4: Kinetics of calcium carbonate decomposition

4.1 Introduction

The thermal decomposition of calcium carbonate is described by the reversible production of solid calcium oxide and release of gaseous carbon dioxide:

$$\mathrm{CaCO_{3(s)}} \Leftrightarrow \mathrm{CaO_{(s)}} + \mathrm{CO_{2(g)}} \qquad \Delta H = +178\ \mathrm{kJ.mol^{-1}}\ \text{at}\ 298\ \mathrm{K} \qquad 4.1$$

For over a century, calcium carbonate decomposition has been a focus of considerable study due to its importance in geological, biogeochemical and industrial processes. In the last decade, there has been renewed interest in this reaction, owing to the urgent need for Carbon Capture and Storage (CCS), and more recently, Direct Air Capture (DAC). One such DAC technology involves removal of CO_2 from the air using $KOH_{(aq)}$, which forms $K_2CO_{3(aq)}$ (Keith et al., 2018). The $KOH_{(aq)}$ is regenerated by reaction of $Ca(OH)_{2(s/l)}$ with $K_2CO_{3(aq)}$ to form $CaCO_{3(s)}$ which is then decomposed according to Eq. 4.1. The $CaO_{(s)}$ formed is hydrolyzed to complete the cycle. Calcium carbonate is especially attractive for regeneration due to its wide availability, low cost, and harmlessness to the environment. However, the temperature (~1173 K) and energy required for its decomposition are high, leading to a large overall cost for the process (Socolow et al., 2011). Lower temperatures might be achieved with better understanding of the decomposition. Attempts have been made to predict $CaCO_3$ decomposition temperature using equilibrium thermodynamic models, but have fallen short (Archer et al., 2013). Instead, the kinetic approach has been more successful (Escardino et al., 2008). Previous breakthroughs in kinetic understanding have resulted in improved lime kiln energy and production efficiency (Moffat and Walmsley, 2005).

Typically, kinetic analysis involved determination of the kinetic triplet – E, A and $f(\alpha)$ – allowing prediction of the rate at any temperature and conversion via Eq. 3.5. There have been many thousands of attempts to determine the kinetic triplet of $CaCO_3$ decomposition over the last century. In a summary of 200 published values (Maciejewski and Reller, 1987), E was found to range from 47 kJ.mol^{-1} to as much as 3828 kJ.mol^{-1}, and the pre-exponential factor, A, was found to vary by several orders of magnitude. A variety of conversion dependencies, $f(\alpha)$, have been proposed to describe the reaction, most commonly first-order (F_1), contracting sphere (R_3) and contracting cylinder (R_2), with reaction orders, n, of 1, 2/3 and 1/2 respectively. Most of the results summarized by Maciejewski and Reller (1987) were obtained using model-fitting methods. Typically, this involved fitting Eq. 3.5 to experimental data by assuming one of the conversion dependencies in Table 8.1, then finding values of A and E which give the best fit. As explained in Section 3.6, this approach leads to non-unique solutions owing to the kinetic compensation effect. Moreover, these studies often assume CO_2 concentration is negligible and that the reaction can be described by a single-step with a single value of the activation energy. However, as Garn (1990) have pointed out, single-step kinetics are rarely observed in reactions involving solids. More often, solid-state transformations consist of multiple different single-step processes, in parallel and/or series, each with its own unique activation energy barrier. It is for this reason that model-free methods, particularly isoconversional methods, have risen in popularity. Isoconversional methods determine the apparent activation energy, E_α, at multiple values of reaction conversion, α (Section 3.8). Table 4.1 summarizes some recent estimates of E_α for decomposition of $CaCO_3$ obtained by isoconversional methods. In this case, E_α is found to range from as low as 163 kJ.mol^{-1} to as much as 675 kJ.mol^{-1}. Although this range is smaller

Table 4.1 – Estimates of isoconversional activation energy (E_α) for calcium carbonate decomposition and main experimental conditions in the literature at a furnace pressure of 101 kPa(abs) unless otherwise stated. N.S.=Not Specified.

E_α		Mass	Heating Rates	Particle Size	Gas	Isoconversional method	Reference
kJ.mol^{-1}		mg	K.min^{-1}	-	-	-	-
α~0	α~1	-	-	-	-	-	-
216	184	5	1, 2, 4, 8, 16, 32	N.S.	Argon	Ozawa-Flynn-Wall	Sanders and Gallagher (2002)
200	180	10	2, 5, 10, 15	3x2x1mm	Air	Ozawa-Flynn-Wall	Rodriguez-Navarro et al. (2009)
213	190	10	5, 10, 15, 20	<74 μm	Nitrogen	Ozawa-Flynn-Wall	Chen and Liu (2010)
220	175	N.S.	0.5, 1, 5, 10, 20, 40, 80	N.S.	Nitrogen	Advanced Isoconversional	Farjas et al. (2010)
190	170	50	Quasi-isothermal	N.S.	Nitrogen	Budrugeac	Budrugeac (2011)
300 675	190 300	10	5, 10, 20, 30, 40	545 μm	Air CO_2 15 %	Vyazovkin	Ávila et al. (2012)
182	163	20	5, 10, 20, 30, 50	10 μm	Nitrogen	Advanced Isoconversional	Tan et al. (2014)
205 275	190 225	2	7.5, 10, 15	40 μm	Nitrogen Vacuum (0.01 Pa)	Advanced Isoconversional	Wang et al. (2017)

than the one summarized by Maciejewski and Reller (1987), it is still significant. Furthermore, all isoconversional estimates of E_α decrease with increasing α.

Clearly, thermal decomposition of $CaCO_3$ is kinetically complex and cannot be adequately described by Eq. 3.5. Other models which tackle the complexity have made some progress, for example, the "Modified Random Pore Model" (Khinast et al., 1996), the chemisorption-desorption model (Beruto et al., 1984), the "Grainy Pellet Model" (Escardino et al., 2008), and the "Thermochemical Model" (L'vov, 2014; 2015b). The relative success of these models is due to the inclusion of a pressure dependence term, $h(P)$, which accounts for the effect of CO_2 on the reaction rate. Since the reaction is reversible, the presence of CO_2 in the system will retard the overall decomposition. Failure to consider the pressure dependency, and, in turn, its dependency on the sample and experimental conditions, explains the discrepancies in the kinetic parameters summarized by Maciejewski and Reller (1987) as well as the decrease in E_α with increasing α which has been revealed by isoconversional methods (see Table 4.1). However, Maya et al. (2018) state: "although it is known that increasing CO_2 partial pressure diminishes the rate, there is still no agreement about its precise dependence". In this chapter, a new pressure dependence for $CaCO_3$ decomposition is derived, and experimental data are collected to test the model. Both model-free and model-dependent methods are used for determination of the kinetic parameters.

4.2 Accumulation Model theory

In this section, a new pressure dependence for $CaCO_3$ decomposition is derived. The form of the pressure dependence, $h(P)$, (which was first introduced in Eq. 3.1) can be derived in a number of

ways. One of the most cited derivations is perhaps the one from Reading et al. (1991) who assume the reversible decomposition proceeds via an activated complex:

$$\mathrm{CaCO_{3(s)}} \Leftrightarrow [\mathrm{CaCO_3}]^{\ddagger} \rightarrow \mathrm{CaO_{(s)}} + \mathrm{CO_{2(g)}} \quad 4.2$$

$$\mathrm{CaO_{(s)}} + \mathrm{CO_{2(g)}} \Leftrightarrow [\mathrm{CaCO_3}]^{\ddagger} \rightarrow \mathrm{CaCO_{3(s)}} \quad 4.3$$

where $[\mathrm{CaCO_3}]^{\ddagger}$ is the activated complex. Then, using transition-state theory and equilibrium thermodynamic arguments Reading et al. (1991) derived the following pressure dependence:

$$h(P) = 1 - \frac{P_{\mathrm{ext}}}{P_{\mathrm{eq}}} \quad 4.4$$

where P_{ext} is the partial pressure of the CO_2 in the furnace and P_{eq} is the equilibrium partial pressure. Similar expressions for the pressure dependence of reversible decompositions have been derived (Pavlyuchenko and Prodan, 1961; Barret, 1968; Searcy and Beruto, 1978; Reading et al., 1991; Vyazovkin and Linert, 1995; Tan et al., 2011), as well as various semi-empirical relationships specific to $CaCO_3$ decomposition (Dennis and Hayhurst, 1984, Silcox et al., 1989, Milne et al., 1990, Khinast et al., 1996, Hu and Scaroni, 1996, Garcia-Labiano et al., 2002; Liavitskaya and Vyazovkin, 2017). The effect of P_{ext} on the rate of $CaCO_3$ decomposition has been studied extensively (Darroudi and Searcy, 1981; Khinast et al., 1996; Galan et al., 2013; Valverde and Medina, 2015). Stanmore and Gilot (2005) provide a good review of the many theoretical and empirical pressure dependencies in the literature. P_{eq} is given by:

$$P_{\mathrm{eq}} = \mathrm{constant} * \exp\left(\frac{-\Delta G}{RT}\right) = Z\exp\left(\frac{-\Delta H}{RT}\right) \quad 4.5$$

where ΔG is the change in free energy of reaction, ΔH is the change in enthalpy of reaction and Z is a constant, which can be expressed in terms of reaction entropy change. Different empirical relationships for P_{eq} can be found in Silcox et al. (1989), Hu and Scaroni (1996) and Garcia-Labiano et al. (2002). Combining Eqs. 3.1, 3.4, 4.4 and 4.5 gives:

$$\frac{\mathrm{d}\alpha}{\mathrm{d}t} = A\exp\left(\frac{-E}{RT}\right) f(\alpha)\left[1 - \frac{P_{\mathrm{ext}}}{Z\exp\left(\frac{-\Delta H}{RT}\right)}\right] \qquad 4.6$$

According to Eq. 4.6, when P_{ext} increases, the reaction shifts to higher temperature. Taking the isoconversional derivative of the rate (see Section 3.6) of Eq. 4.6 gives:

$$E_\alpha = -R\left[\frac{\partial \ln(\mathrm{d}\alpha/\mathrm{d}t)}{\partial T^{-1}}\right]_\alpha = E + \Delta H\left(\frac{P_{\mathrm{ext}}}{P_{\mathrm{eq}} - P_{\mathrm{ext}}}\right) \qquad 4.7$$

where E_α is the apparent isoconversional activation energy and is not to be confused with the intrinsic activation energy, E. Inspection of Eq. 4.7 shows that as P_{ext} approaches P_{eq}, E_α takes on very large values. It also shows that when temperature increases, E_α approaches E. Thus, in thermal analysis experiments, different CO_2 partial pressures and different temperature programs will produce different values of E_α. Indeed, the very large values of E_α obtained by Ávila et al. (2012) correspond to a high CO_2 concentration in the furnace atmosphere (see Table 4.1). Moreover, Eq. 4.7 shows that when P_{ext} is greater than zero, E_α decreases with increasing α, since P_{eq} increases with increasing temperature (see Eq. 4.5) and higher conversions correspond to higher temperatures. Thus, the conversion dependency of the isoconversional activation energy revealed in Table 4.1 is a result of the temperature dependency of the equilibrium partial

pressure. However, Eq. 4.6 does not account for CO_2 which is generated by the reaction. For example, it has been shown (Criado et al., 1990; Ortega, 2001) that $CaCO_3$ decomposition rate curves shifted to higher temperature, and changed shape, when the argon purge gas flow rate was decreased. These changes are attributed to the accumulation of product CO_2 and the consequent retarding of the decomposition rate. Criado et al. (1990) attempted to describe this phenomenon using a rate equation which takes into consideration the internal partial pressure, P_{int}:

$$\frac{\mathrm{d}\alpha}{\mathrm{d}t} = A\exp\left(\frac{-E}{RT}\right) f(\alpha)\left[1 - \frac{P_{\mathrm{int}}}{Z\exp\left(\frac{-\Delta H}{RT}\right)}\right] \qquad 4.8$$

P_{int} is simply defined as the CO_2 partial pressure, generated by reaction. Temperature-programmed desorption (TPD) techniques (Criado et al., 1987) indicate that the partial pressure of the gas in the "close vicinity of the sample" is proportional to the reaction rate:

$$P_{\mathrm{int}} = c\frac{\mathrm{d}\alpha}{\mathrm{d}t} \qquad 4.9$$

where c is the accumulation parameter with units of kPa.s. Inserting Eq. 4.9 into Eq. 4.8 and rearranging gives:

$$\frac{\mathrm{d}\alpha}{\mathrm{d}t} = \frac{A\exp\left(\frac{-E}{RT}\right) f(\alpha)}{1 + \frac{cA}{Z}\exp\left(\frac{\Delta H - E}{RT}\right) f(\alpha)} \qquad 4.10$$

An increase in c simulates the effect of increased product gas accumulation. Taking the isoconversional derivative of Eq. 4.10 gives:

$$E_\alpha = E\left(\frac{P_{\text{eq}}}{P_{\text{eq}} + c.k(T).f(\alpha)}\right) + \Delta H\left(\frac{c.k(T).f(\alpha)}{P_{\text{eq}} + c.k(T).f(\alpha)}\right) \quad 4.11$$

Eq. 4.11 shows that, when $c>0$, E_α varies with temperature and conversion. When c is large, E_α approaches ΔH. The effect of accumulation on E_α has been demonstrated using simulated data (Ortega, 2008) but not, to our knowledge, experimentally. According to this model, the discrepancies in Table 4.1 could be interpreted as due to differences in the degree of CO_2 accumulation. Thus, different flow regimes and temperature programs will produce different values of E_α.

The model described by Criado et al. (1990) cannot account for the reaction rate at different CO_2 partial pressure in the furnace atmosphere (i.e. when $P_{\text{ext}}>0$). Conversely, the models derived by Reading et al. (1991) and others, do not account for the accumulation of self-generated CO_2. Therefore, an obvious and novel modification ought to include the sum of P_{ext} and P_{int}:

$$\frac{\mathrm{d}\alpha}{\mathrm{d}t} = A\exp\left(\frac{-E}{RT}\right)f(\alpha)\left[1 - \frac{P_{\text{ext}} + P_{\text{int}}}{Z\exp\left(\frac{-\Delta H}{RT}\right)}\right] \quad 4.12$$

Substituting Eq. 4.9 into Eq. 4.12 and re-arranging gives:

$$\frac{\mathrm{d}\alpha}{\mathrm{d}t} = \frac{Z\exp\left(\frac{-\Delta H}{RT}\right) - P_{\text{ext}}}{\frac{Z}{Af(\alpha)}\exp\left(\frac{E - \Delta H}{RT}\right) + c} \quad 4.13$$

From here on, this new model is referred to as the "Accumulation Model". Eq. 4.13 shows that when P_{ext} is small compared to c, self-generated CO_2 influences the decomposition rate. When

both P_{ext} and c are negligible, the rate of decomposition will be controlled by the intrinsic kinetics (which in this derivation is first-order chemical reaction for the forward decomposition). Taking the logarithm of the isoconversional derivative of Eq. 4.13:

$$E_\alpha = E\left(\frac{P_{\mathrm{eq}}}{P_{\mathrm{eq}} + c.k(T).f(\alpha)}\right) + \Delta H\left(\frac{P_{\mathrm{eq}}}{P_{\mathrm{eq}} - P_{\mathrm{ext}}}\right) - \Delta H\left(\frac{P_{\mathrm{eq}}}{P_{\mathrm{eq}} + c.k(T).f(\alpha)}\right) \qquad 4.14$$

From Eq. 4.14 a new dimensionless number can be defined, the Campbell number, c_b:

$$c_{\mathrm{b}} = \frac{c.k(T).f(\alpha)}{P_{\mathrm{ext}}} \qquad 4.15$$

According to Eq. 4.14 and 4.15, when $c_b >> 1$, E_α approaches ΔH whereas, when $c_b << 1$, E_α approaches E. The Campbell number enables concise description of the behavior of E_α for this model in terms of one dimensionless number. Beyond this, its practical applications are unknown.

Some (L'vov et al., 2002; L'vov and Ugolkov, 2004; L'vov, 2015a; L'vov, 2015b) described $CaCO_3$ decomposition functioning under two different regimes, or modes: the equimolar mode ($P_{ext} \sim P_{eq}$; $E_\alpha >> E$) and the isobaric mode ($P_{ext} << P_{eq}$; $E_\alpha \sim E$). However, L'vov overlooked the unique contribution that reaction-generated CO_2 plays in controlling the decomposition rate. The work presented in this thesis allows definition of a third regime, the accumulation mode ($P_{int} \sim P_{eq}$; $E_\alpha \sim \Delta H$).

The effect of T (via β), P_{ext} and c on rate curves and E_α can be demonstrated using simulated data. Conversion data were constructed by fourth-order Runge-Kutta integration of Eq. 4.13 with

A=2e8 s^{-1}, Z=2e10 kPa, ΔH=180 $kJ.mol^{-1}$ and $f(\alpha)=(1-\alpha)$. Different combinations of β, P_{ext}, c and E gave six sets of data, labelled A to F in Table 4.2.

Table 4.2 – Different combinations of parameters used in simulating the Accumulation Model. See Figure 4.2 for E_α results.

Data set	β ($K.min^{-1}$)	P_{ext} (kPa)	c (kPa.s)	E ($kJ.mol^{-1}$)
A	0.5, 2, 8	0	0	170
B	0.5, 2, 8	5e−3	0	170
C	8, 32, 128	5e−3	0	170
D	0.5, 2, 8	0	50	170
E	0.5, 2, 8	0	50	190
F	8, 32, 128	0	50	170

The reaction rates were obtained by taking the first forward derivative of the conversion with respect to time. Only some of these rate data are presented in Figure 4.1 for the purpose of demonstration. The six data sets were then run through the Advanced Isoconversional algorithm in MATLAB producing one value of E_α for each value of α (see Figure 4.2).

Figure 4.1 shows that increasing P_{ext} shifted the reaction onset to higher temperature. The reaction endpoint also shifted to higher temperature, but less significantly. On the other hand, increasing c increased the endpoint temperature, but did not affect the onset temperature. On moving to a higher heating rate, P_{ext} can be seen to have little effect on the shape and position of the rate curve, whereas the effect of c remained considerable.

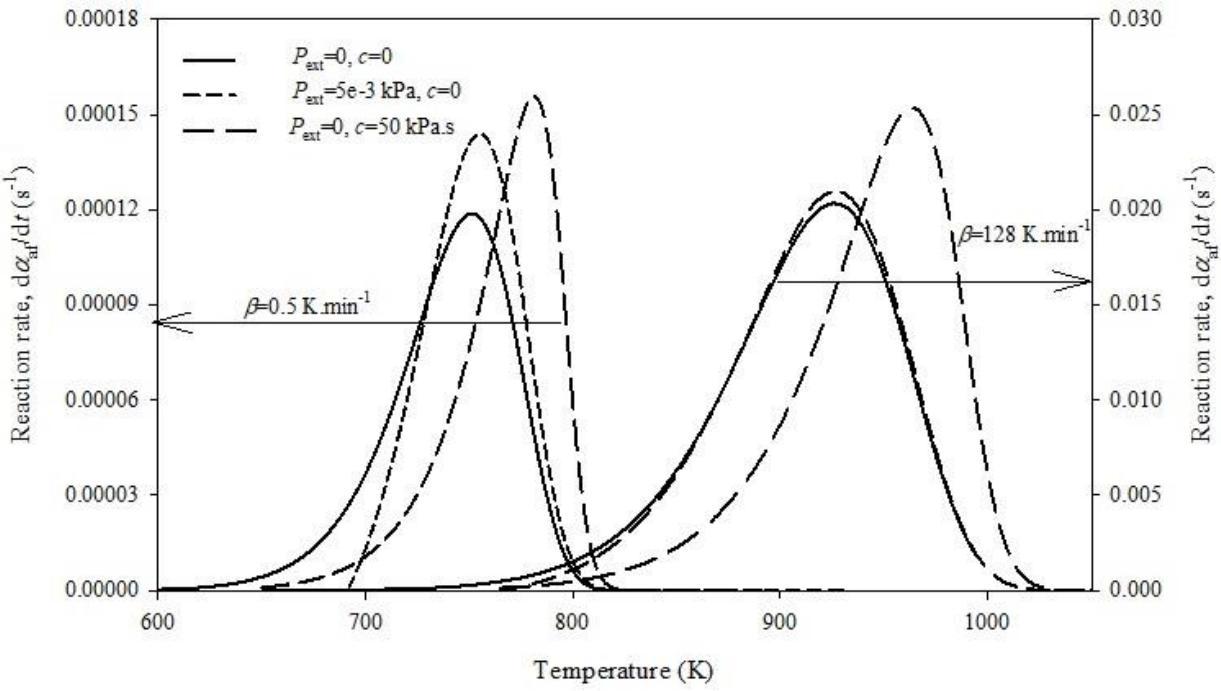

Figure 4.1 – Simulated reaction rate vs. temperature for the Accumulation Model (see Eq. 4.13) with different values of β, P_{ext} and c (E=170 kJ.mol^{-1}).

Figure 4.2 shows the effect of changing P_{ext}, c and T (via β) on E_α. When both P_{ext} and c are zero, E_α approximates E (see data set A). As P_{ext} increased, E_α increased (compare data sets A and B). For P_{ext}=5e−3 kPa, as β increased, E_α approached E (compare B and C). When P_{ext}>0, E_α decreased with increasing α (see both B and C). Similar patterns were simulated by Tan et al. (2011). As c increased, E_α approached ΔH (compared data sets A and D). Ortega (2008) showed that E_α decreased with increasing c, but failed to emphasize that this is because E_α is approaching ΔH. The effect of c on E_α was less significant when E>ΔH (compare D and E). For c>0, it was found that as β increased, E_α shifted towards E (compare D and F). For very large β, E_α approached a value intermediate between E and ΔH which depended on the value of c.

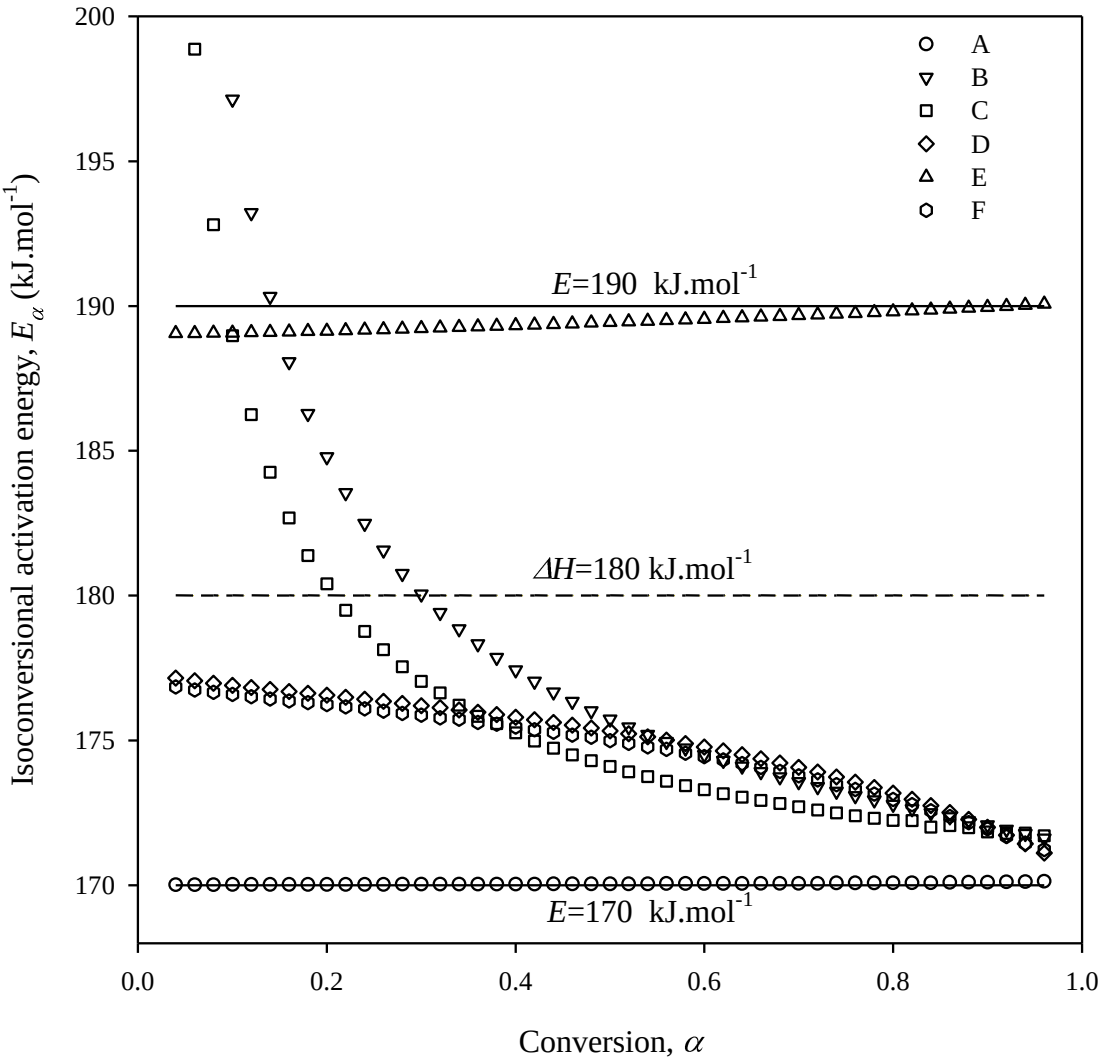

Figure 4.2 – Isoconversional activation energy vs. conversion for the Accumulation Model simulated with different values of β, P_{ext}, c and E (see Table 4.2).

The simulations show that the values of the isoconversional activation energy depend on the internal (pores and interstices) and external (furnace atmosphere) CO_2 partial pressures as well as the heating rate. In the rest of this chapter, the thermal decomposition of $CaCO_3$ is studied over a range of experimental conditions in order to evaluate the descriptive accuracy of the

Accumulation Model. Where applicable, E_α will be determined by the Advanced Isoconversional method.

4.3 Experimental methodology

4.3.1 Sample characterization

Calcium carbonate (calcite polymorph) was purchased from Sigma Aldrich (CAS No. 471-34-1, Product No. 310034, Japanese Limestone, Lot. MKBV0812V, purity >98 %). Approximately 5 g were ball-milled in an air-sealed hardened steel canister using a SPEX 8000 mixer/miller, with 18 steel balls of 3 mm diameter and 1 steel ball of 5 mm diameter in a 2:1 powder-to-ball mass ratio, at 1080 cycles per minute for 1 h.

Scanning electron micrograph (SEM) images of the $CaCO_3$ particles were obtained using a Hitachi S-3000N microscope with Tungsten filament optic (secondary electron resolution 3.5 nm under vacuum, magnification 1000x, working distance 10-20 mm, accelerating voltage 20 kV). The sample was dispersed onto a carbon adhesive disc affixed to a 12.5 mm diameter aluminium stub.

The multi-point Brunauer–Emmett–Teller (BET) surface area was determined by a Quantachrome Autosorb-1 Instrument with nitrogen as the adsorbent gas before and after milling.

The particle size distribution (PSD) was obtained by a Malvern Instruments, Mastersizer 2000 laser diffractometer with a Scirocco dry feeding accessory. The result was taken as the mean of three repeats.

4.3.2 Thermogravimetric analysis

4.3.2.1 Basic set-up

Thermogravimetric data for decomposition of $CaCO_3$ were gathered by a TA Instruments Q-500 Series TGA (weighing precision +/−0.01 %). Open top platinum pans with a depth of 1 mm and radius 5 mm were used to hold the sample. The thermocouple was positioned ~1 mm above the sample such that the sample temperature was represented as accurately as possible without touching the material and potentially interfering with mass measurement. Dry, high-purity N_2 (99.8-99.999 %) was used as a purge gas with a cross-flow of 60 $ml.min^{-1}$ and a down-flow of 40 $ml.min^{-1}$ at a pressure of 105 kPa(abs). The TGA is equipped with two mass flow controllers to control the flow rates of these gases to the balance and furnace. A diagram for the Q500 TGA set-up is given in Figure 4.3.

The CO_2 concentration of the feed stream was 2-5 ppmv, according to the specifications of the Parker, Domnick-Hunter Nitrogen generator. The pressure in the furnace chamber was approximately 105 kPa(abs). An empty pan was heated under the same conditions as the sample. The resulting apparent mass data were subtracted from the corresponding values in the sample runs, correcting for buoyancy effects. The TGA was shared with other lab users, most of whom were studying biomass decomposition. Consequently, organic matter coated the furnace interior over time. These organic residues must be periodically burned-off by heating the furnace to 1000 K in air and holding for 30 min. If this cleaning process was not performed on a regular basis (weekly), $CaCO_3$ decomposition data became affected.

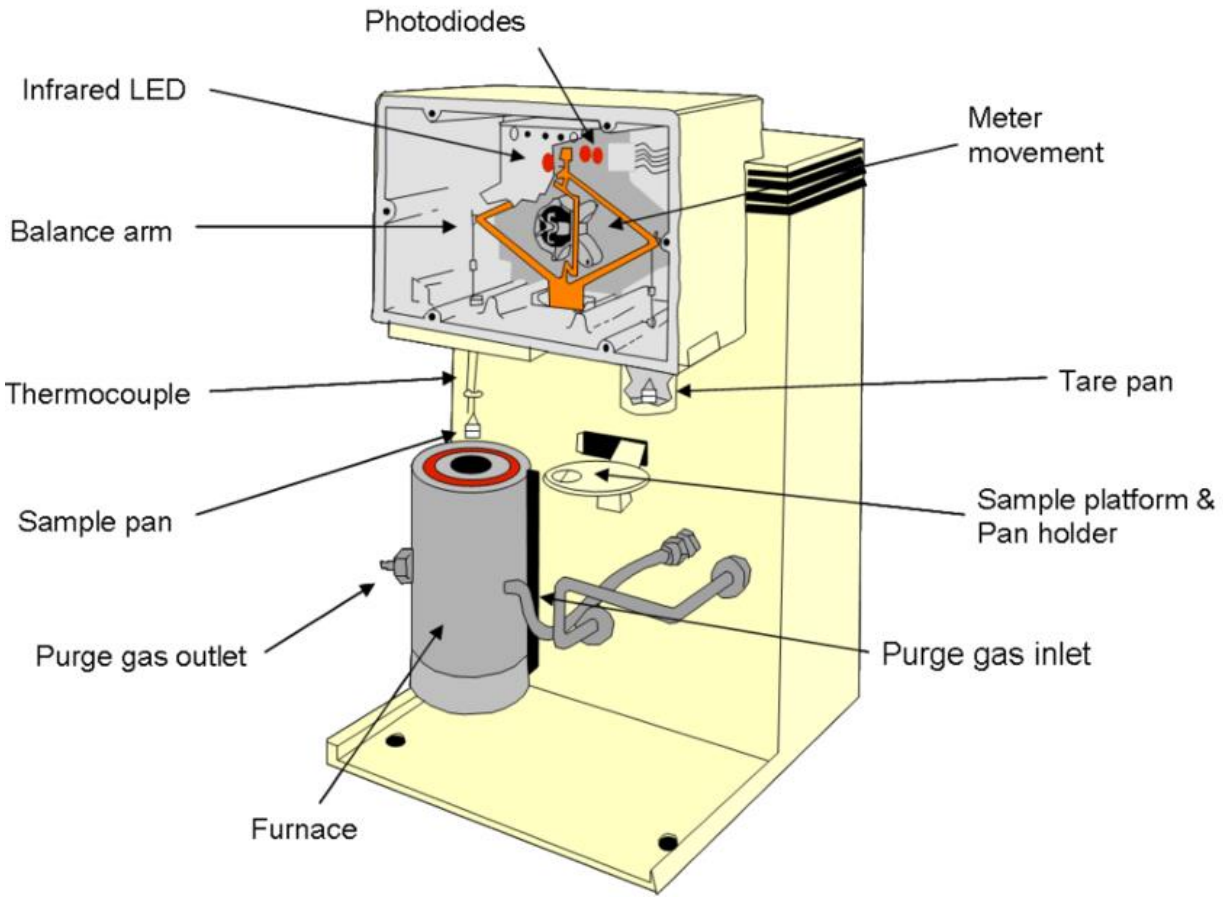

Figure 4.3 – Simple diagram of Q500 TGA

4.3.2.2 Minimizing sample thermal gradients

Since the sample has a lower thermal diffusivity than the rest of the experimental assembly, its temperature will be slightly lower. This effect, known as "thermal lag", has been shown to create variation of the isoconversional activation energy with conversion (Khawam and Flanagan, 2005). Additionally, for an endothermic solid-gas reaction such as $CaCO_3$ decomposition, it is possible for the rate of heat consumption due to reaction to exceed the rate of heat transfer through the sample, resulting in a sample temperature lower than the surroundings. This

phenomenon, known as "self-cooling", has also been shown to affect kinetic parameter determination (Brown and Galwey, 1989) and create variation of E_α with α (L'vov, 2007). Thermal gradients due to both thermal lag and self-cooling must be minimized for accurate determination of the kinetic parameters.

Lyon et al. (2012) provide a simple equation for estimating the total difference between the center and surface temperatures, ΔT_{tot}, of a cylindrical sample of thickness, h_{s}, as a result of both thermal lag and self-cooling:

$$\Delta T_{\text{tot}} = \left(\frac{\beta}{2\lambda} + \frac{\dot{q}_v}{\kappa}\right) {h_{\text{s}}}^2 \qquad 4.16$$

where β is the heating rate (K.s^{-1}), $\dot{q}_v$ is the heat sink (or source) term per unit volume of solid due to reaction, κ is the thermal conductivity of the solid sample and λ is the thermal diffusivity. Eq. 4.16 is an approximation for the temperature differential between the center and surface at T_{max}. It does not take into account the change in the sample composition with increasing conversion. More accurate methods for determination of sample thermal gradients in TGA analysis can be found in Lyon et al. (2012) and in Sánchez-Rodríguez et al. (2014).

According to Eq. 4.16, in order to minimize thermal gradient in the sample, $\dot{q}_v$, h_{s} and β must be minimized. The heat sink, $\dot{q}_v$, can be minimized by increasing the sample volume (increasing voidage) and by reducing the reaction rate. The sample thickness, h_{s}, can be minimized by reducing the sample mass and spreading the sample thinly on the bottom of the pan. Minimizing the heating rate, β, is less straightforward. Isoconversional methods require a minimum of three

heating rates to reveal "possible non-Arrhenius temperature dependencies" (Vyazovkin and Dranca, 2004; Chen and Vyazovkin, 2009), with four or more rates offering "extra benefit" (Vyazovkin et al., 2014). The exact choice of these heating rates partly depends on how much time a researcher is willing to spend on data collection. Low heating rates, such as 0.1 $K.min^{-1}$ can be found in the literature (e.g. Cooney et al., 1983), but are time consuming. Rates >1 $K.min^{-1}$ are more typical. Once a minimum heating rate has been chosen, the maximum heating rate should be 10-20 times greater to ensure that the reaction is studied over a sufficiently wide range (Vyazovkin et al., 2014) since the quality of kinetic parameter estimation increases with increasing range of reciprocal temperatures of isoconversional points. According to the Kissinger (1957) equation, a plot of the reciprocal of the temperature at the maximum rate ($1/T_{max}$) vs. the natural logarithm of the heating rate ($\ln\beta$) gives a straight line. In order that the points on this line be equidistant, the heating rate, β, must follow a geometric progression, i.e. each heating rate should be greater than the previous one by a common factor (Farjas and Roura, 2011). Vyazovkin et al. (2014) recommend that this factor be 2, in order that the rate maxima at different heating rates be sufficiently separated in the temperature dimension. In this work, 0.5 $K.min^{-1}$ was chosen as the lowest heating rate, since data collection could be achieved overnight (12 h run time). Thus, a series of heating rates, such as 0.5, 1, 2, 4… $K.min^{-1}$ would be appropriate. In this thesis work, it was found that the lowest possible $CaCO_3$ sample mass was 0.1 mg at a heating rate of 0.5 $K.min^{-1}$. This is because at less than 0.1 mg, the noise-to-signal ratio became unacceptable.

Table 4.3 shows the results of the simulated temperature difference between the center and surface of a powdered spherical sample of $CaCO_3$ decomposing at the maximum reaction rate. The sample surface temperature differential (ΔT_{tot}) was calculated using Eq. 4.16 assuming a crystalline density (ρ_{cry}) of 2710 kg.m^{-3}, heat capacity (C_p) of 0.8 kJ.kg^{-1}.K^{-1}, thermal conductivity (κ) of 2 W.m^{-1}.K^{-1}, initial voidage (ϕ_i) of 0.8, sample layer diameter (D_{sl}) of 0.005 m, reaction enthalpy (ΔH) of 178 kJ.mol^{-1}, maximum reaction rate ($d\alpha/dt_{max}$) of 2 min^{-1}, heating rate (β) of 128 K.min^{-1} and particle diameter (D_p) 50 μm.

Due to the large enthalpy of reaction, the temperature difference due to self-cooling (ΔT_{sc}) is found to have one to three orders of magnitude greater effect than the temperature difference due to thermal lag (ΔT_{tl}). The results suggest that for a sample mass less than 2 mg and heating rates less than 128 K.min^{-1} conversion data shift by no more than a few degrees, and the error in E_α due to thermal gradients is less than 5 %. By comparison, with the conditions of sample mass and heating rate used in previous literature (see Table 4.1) errors in E_α due to thermal gradients likely exceed 5 %.

Table 4.3 – Contribution of thermal lag (ΔT_{tl}) and self-cooling (ΔT_{sc}) to total radial temperature difference between center and surface (ΔT_{tot}) calculated using Eq. 4.16 for decomposing $CaCO_3$ powder at different initial sample masses (m_i), at β=128 K.min^{-1}.

m_i (mg)	0.5	1	2	4	8	16	32
ΔT_{tl} (K)	0.00	0.00	0.01	0.05	0.20	0.80	3.30
ΔT_{sc} (K)	0.02	0.09	0.36	1.45	5.79	23.2	92.7
ΔT_{tot} (K)	0.02	0.09	0.38	1.50	6.00	24.0	96.0

4.3.2.3 Thermogravimetric data collection

For determination of $\tilde{E}_\alpha$ four sets of thermogravimetric data were obtained for decomposition of $CaCO_3$ for the following milling pre-treatment, mean initial sample mass ($\overline{m_i}$) and heating rates (see Table 4.4).

Table 4.4 – Four combinations of sample pre-treatment, mean initial sample mass ($\overline{m}_i$) and heating rate (β) used in determination of the median isoconversional activation energy ($\tilde{E}_\alpha$). See Figure 4.17 for results (labelled with codes i-iv).

Code	Pre-treatment	$\overline{m_i}$	β (number of repeats)				
-	-	mg	K.min^{-1}				
i	Ball-milled	0.2	0.5 (x4)	1 (x1)	2 (x1)	4 (x1)	8 (x4)
ii	Ball-milled	0.2	8 (x4)	16 (x1)	32 (x1)	64 (x1)	128 (x4)
iii	Ball-milled	0.9	0.5 (x4)	1 (x1)	2 (x1)	4 (x1)	8 (x4)
iv	Un-milled	0.9	0.5 (x4)	1 (x1)	2 (x1)	4 (x1)	8 (x4)

Data at the lowest and highest heating rates of each set (i.e. 0.5, 8 and 128 K.min^{-1}) were repeated. Intermediate rates were not repeated for the reasons discussed in Section 3.10. A narrow distribution of initial sample masses from run to run was difficult to achieve due to the extremely low masses tested. Therefore, six or seven runs were performed at the highest and lowest heating rates of each set and four chosen such that $\overline{m_i}$ at the lowest and highest heating rates were almost equivalent.

4.3.3 Data processing and analysis

After blank subtraction for buoyancy effects, data within the temperature range of mass loss were selected and transformed to conversions between 0 and 1 with the aid of Eq. 3.2. Conversion values were smoothed in Excel using a moving average with interval of 50. The

corresponding rate curves were obtained by taking the first forward derivative with respect to time.

The smoothed conversion data, with their corresponding time and temperature values, were then used to determine E_α by the Advanced Isoconversional method by minimization of Eq. 3.19, achieved using the Nelder-Mead method (fminsearch in MATLAB). The J' integral was numerically determined using recursive adaptive Simpson quadrature (quad in MATLAB). Every possible 4-rate permutation of the data was used to give 16 estimates for E_α at each value of α in the 0.04 to 0.96 range in steps of 0.02 and the median was then taken. E_α at α<0.04 and α>0.96 were omitted, because those estimates have been found to be sensitive to minor errors in baseline determination (Vyazovkin et al., 2011). The accuracy of the median isoconversional activation energy, $\tilde{E}_\alpha$, depends on the number of heating rates used, their relative rates, the number of repeats, the scatter in the repeat data and how the data are processed. It has been shown (Vyazovkin and Wight, 2000) that a realistic relative error in the activation energy can be as much as ~20 %, even with nine repeats at each of five heating rates. None of the studies in Table 4.1 used repeats in order to increase the confidence in their estimate, which is perhaps a result of the time-consuming nature of both data collection and processing. Therefore, to our knowledge, this is the first study to use repeat data to determine E_α for $CaCO_3$ decomposition.

For the model-fitting procedure, conversion curves were simulated based on fourth-order Runge-Kutta integration of Eq. 4.18. Corresponding rate curves were obtained by taking the first forward derivative with respect to time. The temperature dependence of the equilibrium decomposition pressure P_{eq} (in kPa) was given by Silcox et al. (1989) as:

$$P_{\mathrm{eq}} = 1.98\mathrm{e}10 * \exp\left(\frac{-183.1}{RT}\right) \qquad 4.17$$

It was found that the CO_2 partial pressure of the N_2 purge gas, P_{ext}, could not provide the appropriate fit to all the data and a correction factor, b_1, was introduced, such that Eq. 4.13 became:

$$\frac{\mathrm{d}\alpha}{\mathrm{d}t} = \frac{Z\exp\left(\frac{-\Delta H}{RT}\right) - b_1.P_{\mathrm{ext}}}{\frac{Z}{Af(\alpha)}\exp\left(\frac{E-\Delta H}{RT}\right) + c} \qquad 4.18$$

The value of E was estimated from the results for $\tilde{E}_\alpha$ by assuming the estimates at high heating rate (8-128 K.min^{-1}) gave a good approximation for the forward decomposition reaction. A_α was determined using the method of invariant kinetic parameters. Then values of c, b_1, and A were modified until the simulated conversion and rate data matched the experimental conversion and rate data. The pressure correction factor, b_1, approximately corresponded to $T_2/298*P_{\mathrm{ext}}$, where T_{i} is the temperature of the furnace when $CaCO_3$ decomposition initiated. The conversion and rate data were fit simultaneously, rather than independently, for more consistent fitting results.

4.4 Results

4.4.1 Particle characterization

SEM images for un-milled $CaCO_3$ (see Figure 4.4) indicate crystallites of major dimension 5-10 μm with parallelepiped geometry. Most of these are fused together in clusters, some as large as 50 μm. By comparison, the ball-milled particles are greatly reduced in size (<1 μm) and have irregular geometry.

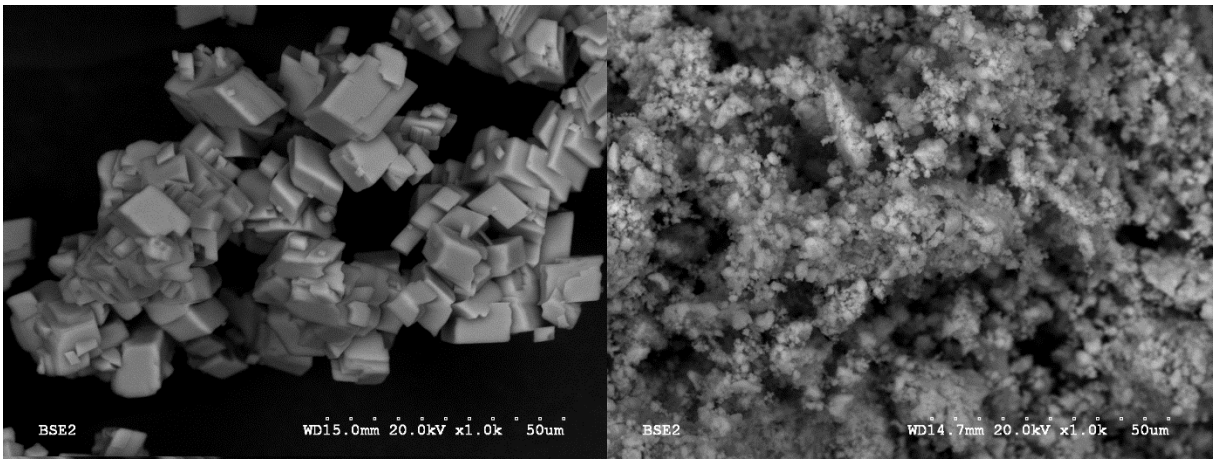

Figure 4.4 – SEM images for $CaCO_3$, un-milled (left) and ball-milled (right).

Multipoint BET surface areas were determined to be 0.112 $m^2.g^{-1}$ and 4.483 $m^2.g^{-1}$ for the un-milled and ball-milled sample respectively, corresponding to a 40-fold increase in the surface area upon milling. The approximate particle radius of a sphere, r_0, can be determined by the relation $r_0=3/(\rho.S_0)$ where ρ is the density ($kg.m^{-3}$) and S_0 is the specific surface area ($m^2.kg^{-1}$). Assuming $CaCO_3$ density of 2710 $kg.m^{-3}$, r_0=10 μm and r_0=250 nm for the un-milled and ball-milled samples respectively. These values agree well with the SEM images. Figure 4.5 shows the results of laser diffraction. For the un-milled sample, >90 % by volume of the crystallites were between 5 and 50 μm in diameter. For the ball-milled sample, the distribution was much wider. However, SEM images suggest that the particles registering as >5 μm in the laser diffractometer are agglomerates. Thus, the ball-milled sample behaves cohesively, which is typical of Geldart C particles.

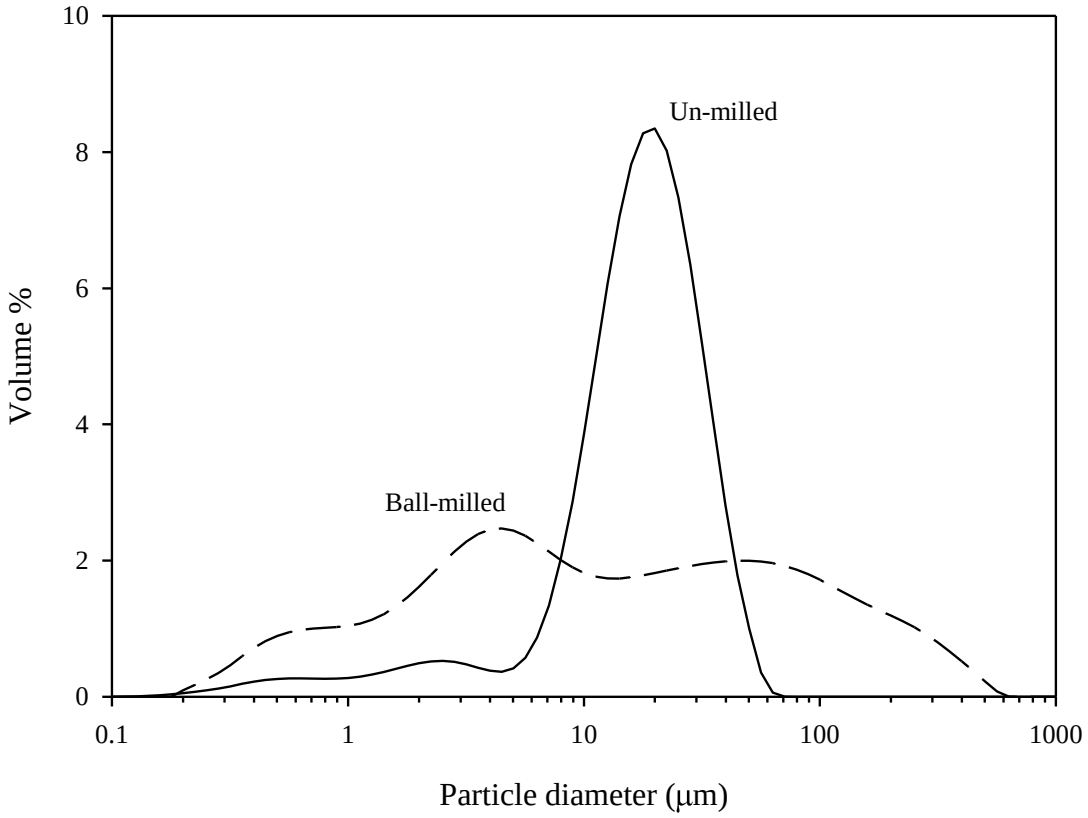

Figure 4.5 – Particle size distribution for un-milled and ball-milled $CaCO_3$ determined by laser diffraction.

4.4.2 Conversion data and Accumulation Model fits

Conversion data for decomposition of ball-milled and un-milled $CaCO_3$ at different sample mass, heating rate and N_2 flow rate are shown in Figure 4.8-4.16. There is a negative linear relationship between the natural logarithm of the initial sample mass, $\ln(m_i)$, and the reciprocal of the temperature of maximum reaction rate, $1/T_{max}$ (see Figure 4.6).

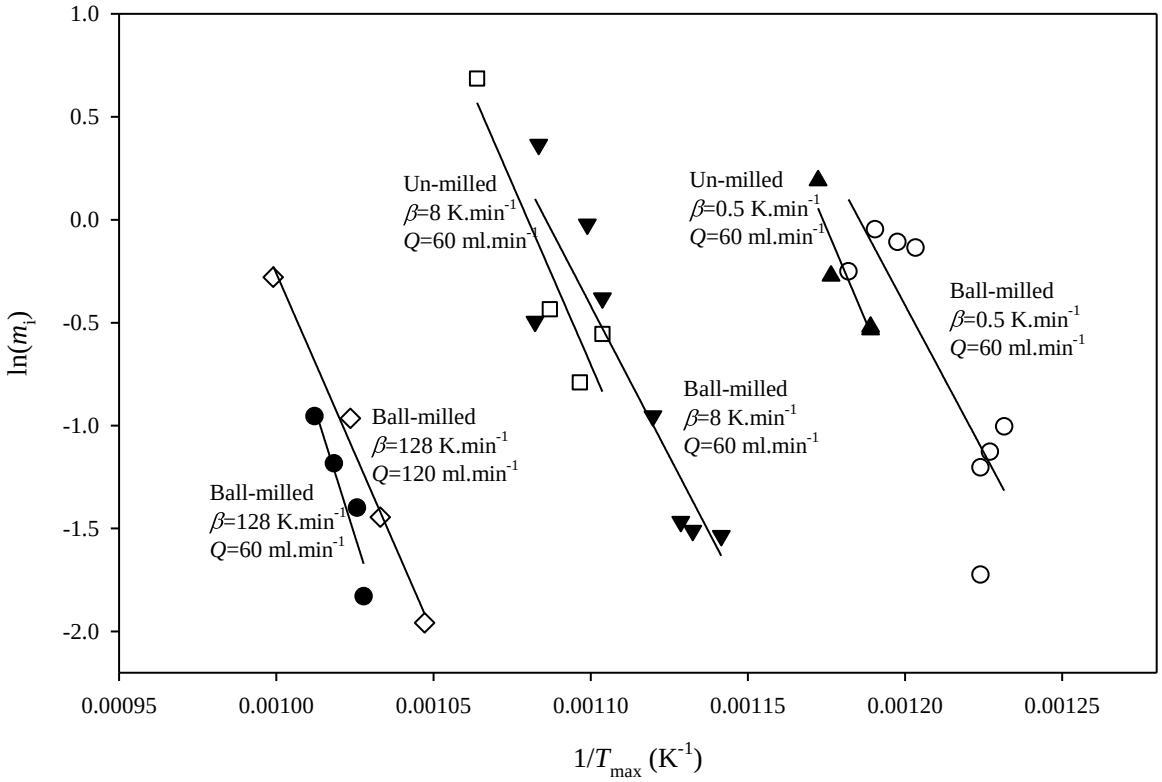

Figure 4.6 – Natural logarithm of initial sample mass vs. reciprocal of temperature corresponding to maximum decomposition rate of un-milled and ball-milled $CaCO_3$, at different heating rates and N_2 gas flow rates.

As the heating rate increased, conversion data shifted to higher temperatures owing to the shorter residence time. As mass increased, conversion data shifted to higher temperatures. This shift was greatest at higher conversions, causing the slope of the experimental conversion data to decrease with increasing initial sample mass. Figure 4.6 shows that ball-milling prior to thermal decomposition shifted conversion data to lower temperatures. This shift was most noticeable at smaller mass. An increase in the $N_{2(g)}$ flow rate shifted conversion data to lower temperatures. This shift was most noticeable at smaller mass.

Table 4.5 – Fitting parameters for decomposition of ball-milled $CaCO_3$. See Figure 4.8-4.13 for fitted data (solid lines), labelled by codes A-H.

β K.min^{-1}	Q ml.min^{-1}	Code -	m_i mg	T_{max} K	T_i K	A s^{-1}	b_1 -	c kPa.s
0.5	60	A	0.366	812	760	6.5e8	6	65
0.5	60	B	0.324	815	760	8.5e8	5	85
0.5	60	C	0.178	817	760	9.0e8	5	57
0.5	60	D	0.300	817	760	9.0e8	4	80
0.5	60	E	0.873	831	775	4.0e8	14	200
0.5	60	F	0.898	835	760	5.5e8	5	155
0.5	60	G	0.955	840	775	5.0e8	8	220
0.5	60	H	0.778	846	775	5.0e8	8	165
1	60	A	0.202	828	787	8.5e8	14	70
1	60	B	0.945	862	776	2.8e8	7	220
2	60	A	0.179	848	775	7.5e8	9	55
2	60	B	0.658	875	795	4.0e8	20	150
4	60	A	0.173	877	780	9.0e8	11	35
4	60	B	0.713	891	776	8.0e8	20	155
8	60	A	0.215	876	790	1.3e9	15	70
8	60	B	0.221	883	790	1.1e9	15	80
8	60	C	0.231	886	790	1.4e9	15	50
8	60	D	0.385	893	790	1.2e9	15	50
8	60	E	0.684	906	805	7.0e8	25	140
8	60	F	0.978	910	800	5.5e8	30	240
8	60	G	1.441	923	800	7.0e8	25	115
8	60	H	0.610	924	810	4.0e8	30	210
16	60	-	0.408	912	800	1.3e9	40	80
32	60	-	0.567	957	850	8.0e8	130	105
64	60	-	0.326	975	852	1.7e9	130	100
128	60	A	0.160	973	840	8.5e8	80	20
128	60	B	0.247	975	840	8.5e8	80	30
128	60	C	0.306	982	840	9.5e8	85	43
128	60	D	0.385	988	840	9.2e8	85	65
128	120	A	0.141	955	840	9.0e8	90	4
128	120	B	0.236	968	840	6.0e8	100	15
128	120	C	0.381	977	840	1.1e9	80	50
128	120	D	0.757	1001	850	5.5e8	75	130

Table 4.6 – Fitting parameters for decomposition of un-milled $CaCO_3$. See Figure 4.14-4.16 for fitted data (solid lines), labelled by codes A-D.

β K.min^{-1}	Q ml.min^{-1}	Code -	m_i mg	T_{max} K	T_i K	A s^{-1}	b_1 -	c kPa.s
0.5	60	A	0.587	841	774	8.5e8	11	220
0.5	60	B	0.594	841	800	8.5e8	22	230
0.5	60	C	0.762	850	790	8.4e8	15	200
0.5	60	D	1.210	853	770	5.5e8	9	360
1	60	-	0.895	863	798	6.0e8	15	260
2	60	-	1.072	875	790	7.0e8	15	140
4	60	-	1.137	886	805	1.4e9	30	120
8	60	A	0.574	906	840	9.0e8	75	155
8	60	B	0.454	912	829	1.2e9	42	105
8	60	C	0.648	920	829	1.3e9	40	150
8	60	D	1.987	940	835	8.0e8	60	345

The experimental conversion data were fitted to Eq. 4.18. The best fits are shown in Figure 4.8-4.16. The values of Z and ΔH were 1.98e10 kPa and 183 kJ.mol^{-1} respectively (Silcox et al., 1989). The conversion dependency, $f(\alpha)$, was assumed to be first-order (Reading et al., 1999). The value of the intrinsic activation energy, E, was estimated to be 185 kJ.mol^{-1} under the assumption that E_α approaches E at high temperature. This was estimated by taking the mean of the last 10 values of the isoconversional activation energy, E_α, which was calculated using decomposition data at β=8-128 K.min^{-1} (labelled "ii" in Table 4.4 and Figure 4.17). The CO_2 partial pressure in the N_2 purge gas, P_{ext}, was estimated to be 1 Pa at a CO_2 concentration of 3.5 ppmv, furnace temperature of 800 K and pressure of 105 kPa(abs). The values of A, c, and b_1

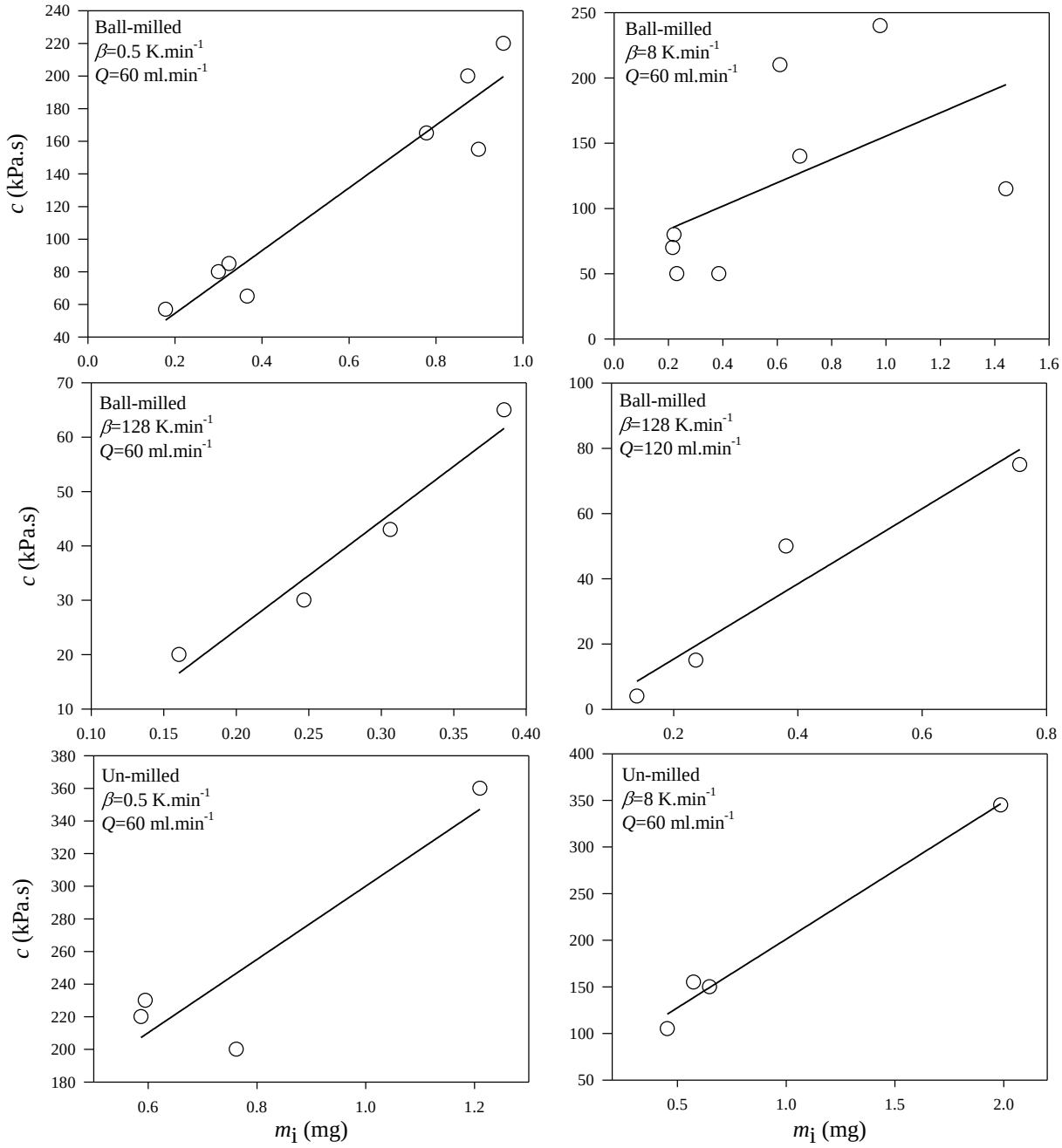

Figure 4.7 – Accumulation parameter (defined in Eq. 4.9) vs. initial sample mass for different $CaCO_3$ particle sizes, heating rates and N_2 flow rates.

were varied until a good fit was achieved (see Table 4.6). The pre-exponential factor, A was found to range from 3e8 to 14e8 s^{-1} and seemed to have no clear dependency on heating rate, mass or particle size. The fitted values of A agreed with the range of isoconversional pre-exponential factor (A_α) values which were estimated using the kinetic compensation effect and the method of invariant kinetic parameters. There was a positive linear correlation between the accumulation parameter, c and the initial sample mass (see Figure 4.7). The pressure correction factor, b_1, gave no correlation with initial sample mass but increased with increasing heating rate.

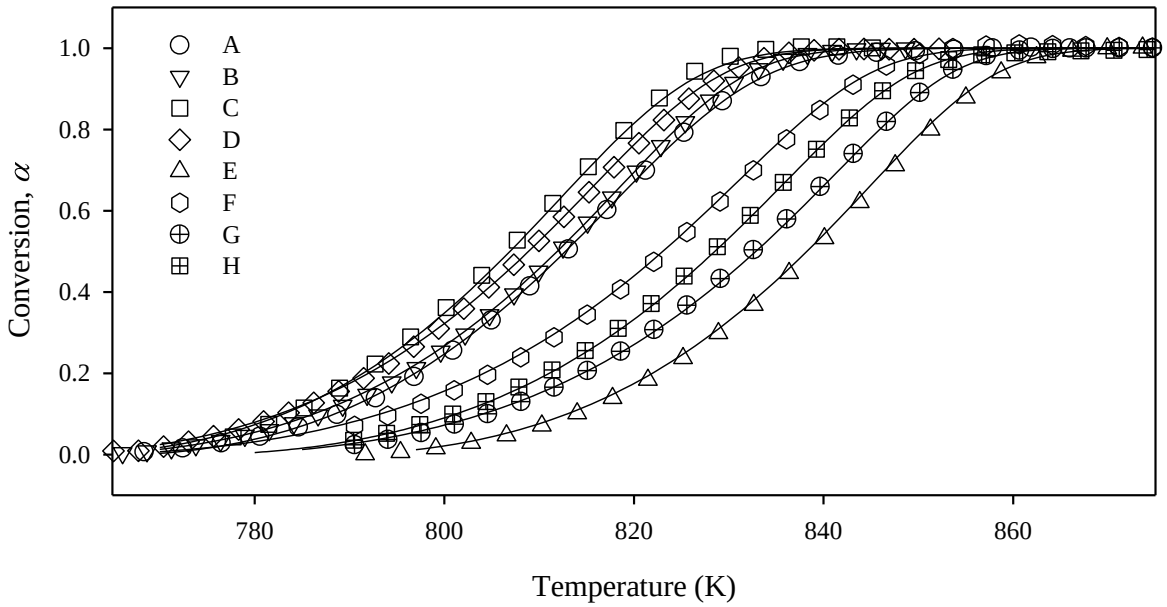

Figure 4.8 – Conversion vs. temperature data for decomposition of ball-milled $CaCO_3$ at β=0.5 $K.min^{-1}$ and Q=60 $ml.min^{-1}$ with fits to Eq. 4.18. See Table 4.5 for fitting parameters.

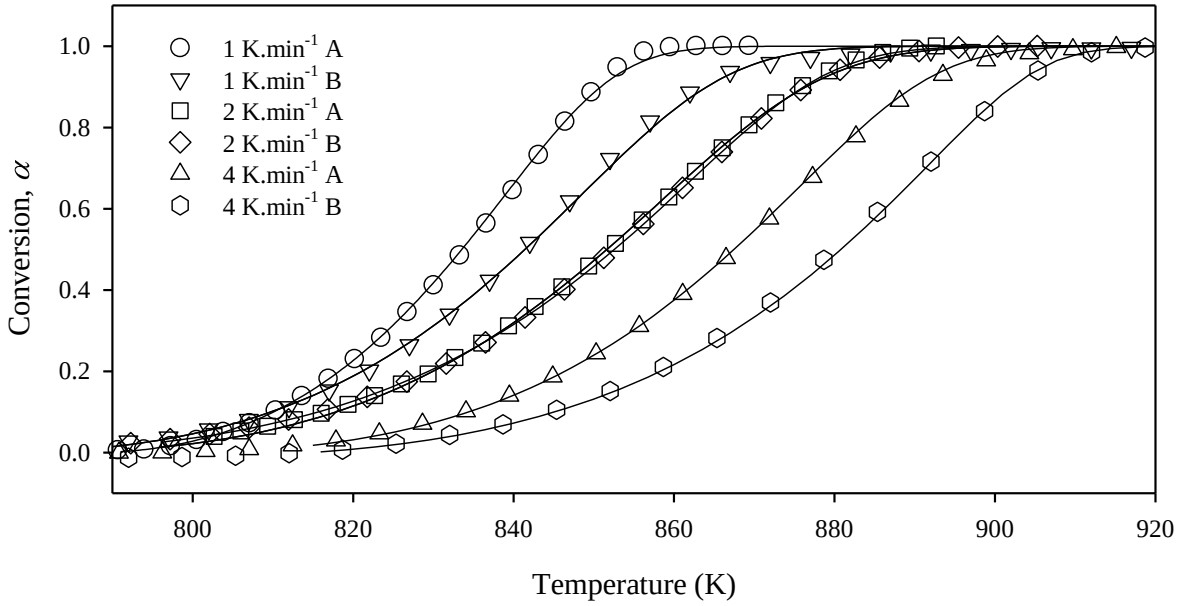

Figure 4.9 – Conversion vs. temperature data for decomposition of ball-milled $CaCO_3$ at β=1, 2 and 4 K.min^{-1} and Q=60 ml.min^{-1} with fits to Eq. 4.18. See Table 4.5 for fitting parameters.

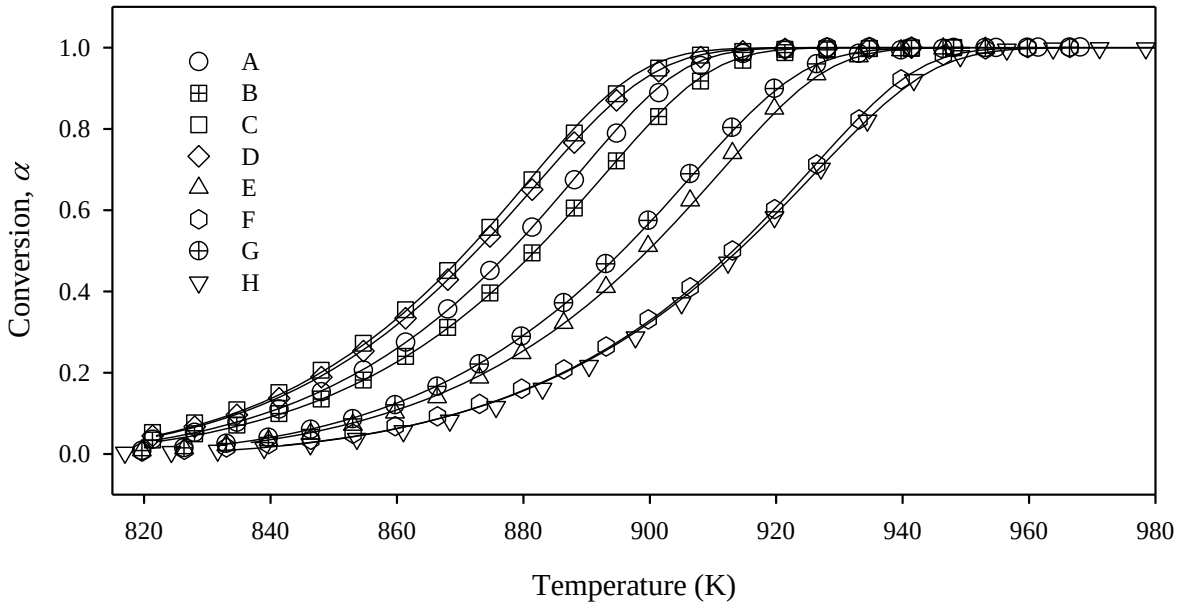

Figure 4.10 – Conversion vs. temperature data for decomposition of ball-milled $CaCO_3$ at β=8 K.min^{-1} and Q=60 ml.min^{-1} with fits to Eq. 4.18. See Table 4.5 for fitting parameters.

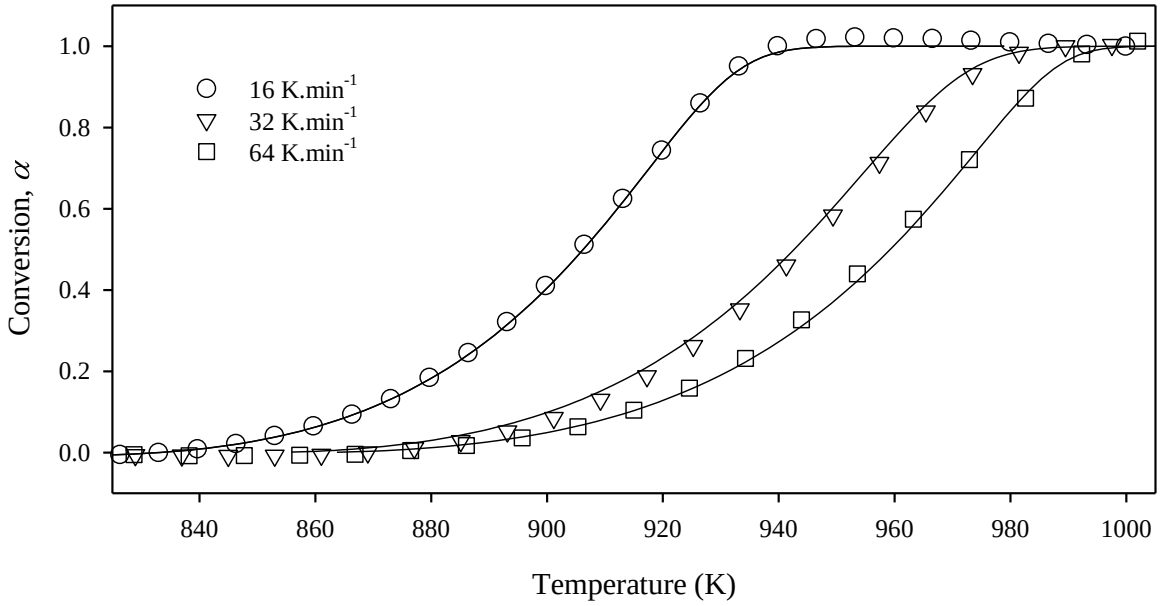

Figure 4.11 – Conversion vs. temperature data for decomposition of ball-milled $CaCO_3$ at β=16, 32 and 64 K.min^{-1} and Q=60 ml.min^{-1} with fits to Eq. 4.18. See Table 4.5 for fitting parameters.

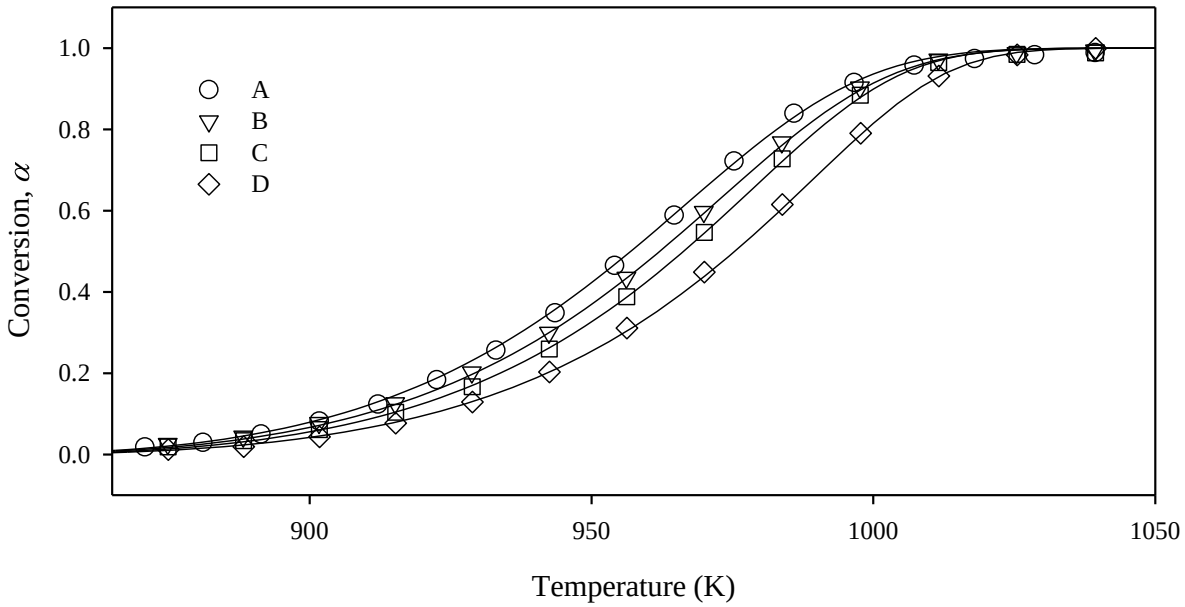

Figure 4.12 – Conversion vs. temperature data for decomposition of ball-milled $CaCO_3$ at β=128 K.min^{-1} and Q=60 ml.min^{-1} with fits to Eq. 4.18. See Table 4.5 for fitting parameters.

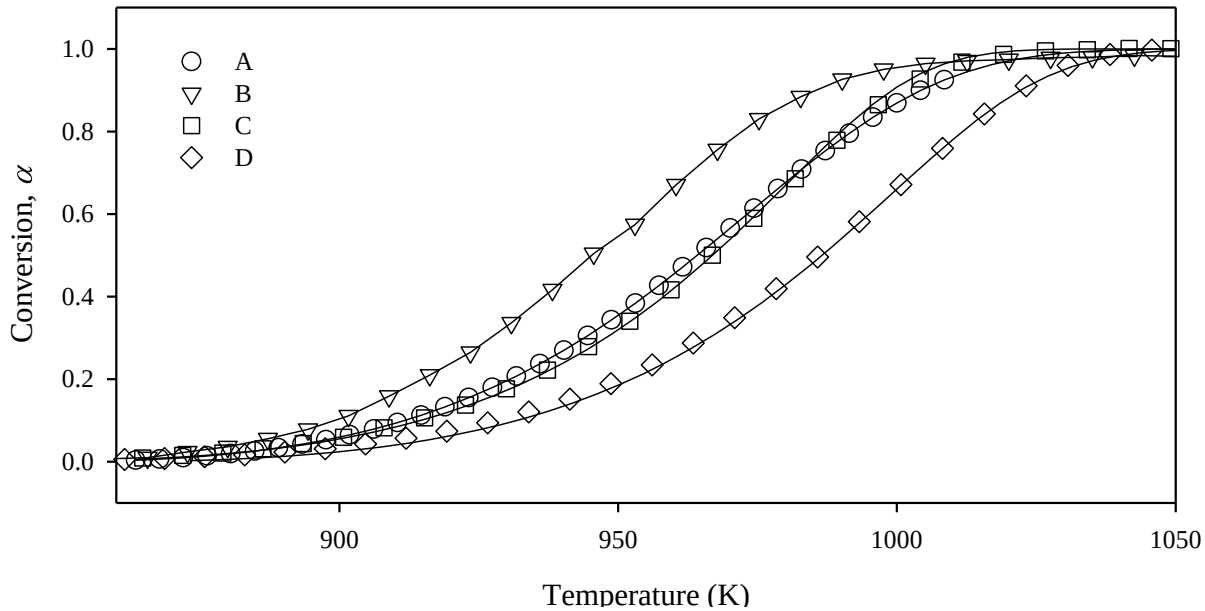

Figure 4.13 – Conversion vs. temperature data for decomposition of ball-milled $CaCO_3$ at β=128 K.min^{-1} and Q=120 ml.min^{-1} with fits to Eq. 4.18. See Table 4.5 for fitting parameters.

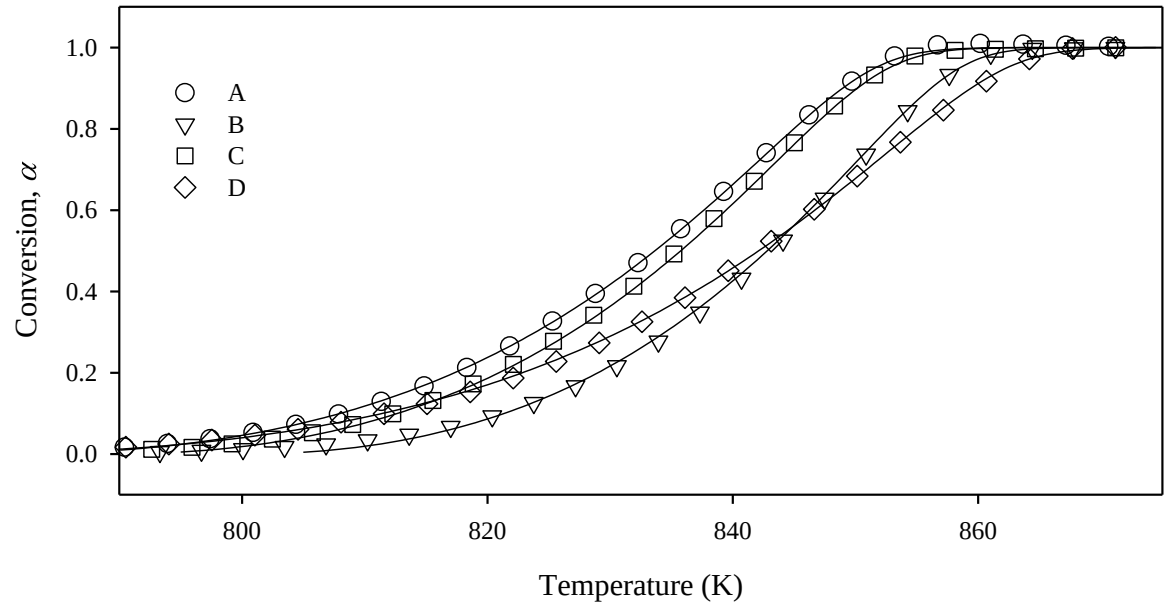

Figure 4.14 – Conversion vs. temperature data for decomposition of un-milled $CaCO_3$ at β=0.5 K.min^{-1} and Q=60 ml.min^{-1} with fits to Eq. 4.18. See Table 4.6 for fitting parameters.

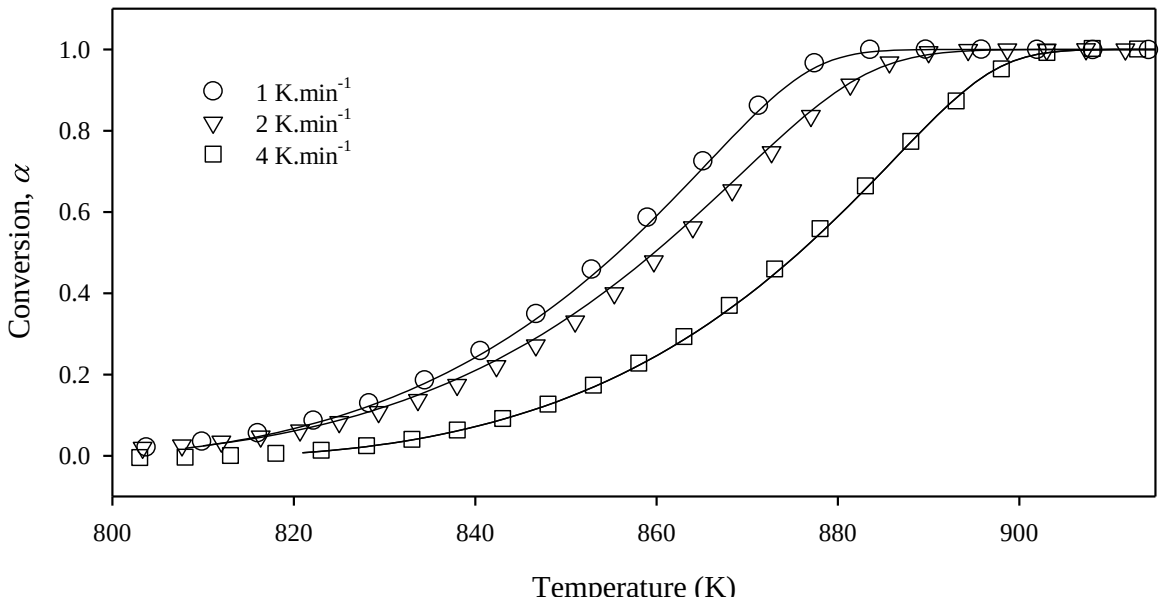

Figure 4.15 – Conversion vs. temperature data for decomposition of un-milled $CaCO_3$ at β=1, 2 and 4 K.min^{-1} and Q=60 ml.min^{-1} with fits to Eq. 4.18. See Table 4.6 for fitting parameters.

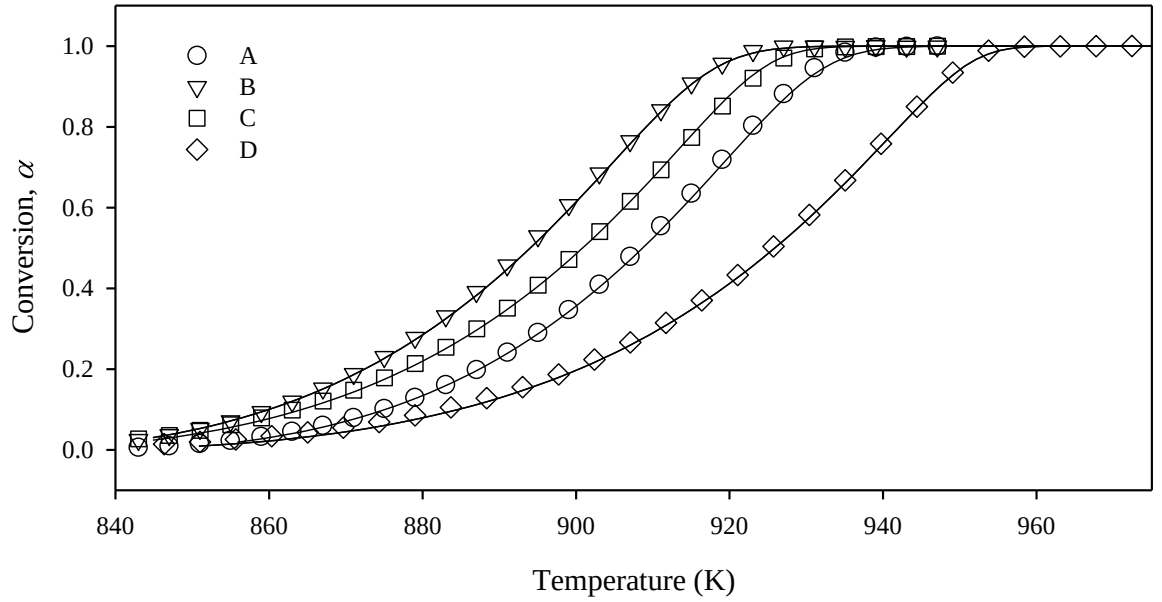

Figure 4.16 – Conversion vs. temperature data for decomposition of un-milled $CaCO_3$ at β=8 K.min^{-1} and Q=60 ml.min^{-1} with fits to Eq. 4.18. See Table 4.6 for fitting parameters.

4.4.3 Isoconversional activation energy

The median isoconversional activation energies for codes i to iv (see Table 4.4 for code descriptions) are shown in Figure 4.17 as a function of conversion, α.

i. β=0.5-8 K.min^{-1} vs. ii. β=8-128 K.min^{-1}

$\tilde{E}_\alpha$ estimated using the lower heating rate range (i) decreased from ~250 kJ.mol^{-1} at low conversion to ~210 kJ.mol^{-1} at high conversion, whereas $\tilde{E}_\alpha$ estimated using the higher heating rate range (ii) decreased from ~220 kJ.mol^{-1} to ~174 kJ.mol^{-1}. Therefore, increasing the heating rates by a factor of 16 decreased $\tilde{E}_\alpha$ by ~30 to 36 kJ.mol^{-1}.

i. $\overline{m_i}$=0.2 vs. iii. C. $\overline{m_i}$=0.9 mg

$\tilde{E}_\alpha$ estimated using $\overline{m_i}$=0.2 mg (i) decreased from ~250 kJ.mol^{-1} at low conversion to ~210 kJ.mol^{-1} at high conversion, whereas $\tilde{E}_\alpha$ estimated with $\overline{m_i}$=0.9 mg (iii) decreased from ~225 kJ.mol^{-1} to ~200 kJ.mol^{-1}. Therefore, increasing the initial sample mass by a factor of 4.5 decreased $\tilde{E}_\alpha$ by 10 to 25 kJ.mol^{-1}.

iii. un-milled vs. iv. ball-milled

$\tilde{E}_\alpha$ for un-milled $CaCO_3$ (iii) decreased from ~260 kJ.mol^{-1} at low conversion to ~215 kJ.mol^{-1} at high conversion, whereas for ball-milled $CaCO_3$ (iv) $\tilde{E}_\alpha$ decreased from ~225 kJ.mol^{-1} to ~200 kJ.mol^{-1}. Therefore, ball-milling decreased $\tilde{E}_\alpha$ by 15 to 35 kJ.mol^{-1}.

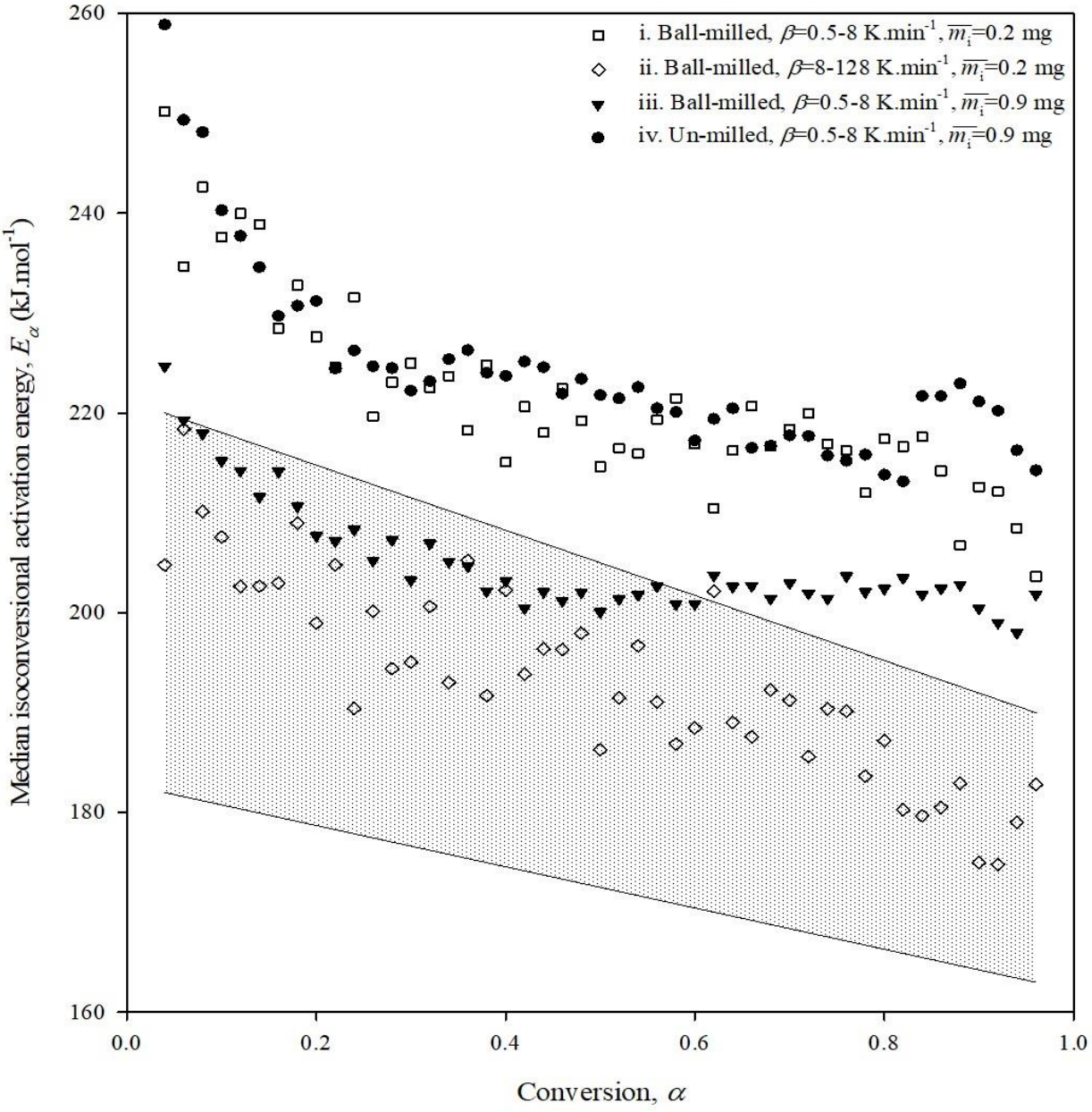

Figure 4.17 – Median isoconversional activation energy vs. conversion for un-milled and ball-milled $CaCO_3$ under different conditions of mass and heating rate. The shaded area represents the range of isoconversional estimates in flowing air and nitrogen from Table 4.1.

4.5 Discussion

4.5.1 Heating rate

As the heating rate, β, increases, the sample residence time decreases and conversion data shift to higher temperatures. A 16-fold increase in the heating rate resulted in a ~40 kJ.mol^{-1} drop in $\tilde{E}_\alpha$ (compare estimates i and ii in Figure 4.17). Higher heating rates correspond to higher temperatures (due to shorter residence times) which increases P_{eq} and decreases E_α. This effect was simulated in Figure 4.2 (compare B and C). Essentially, at low temperatures, the reaction occurs near equilibrium while at high temperatures the reaction occurs far from equilibrium.

4.5.2 Sample mass

As the sample mass increases it becomes increasingly difficult to disperse the powder as a thin layer. Instead, particles form a pile. Figure 4.18 shows a simple schematic of two decomposing $CaCO_3$ samples of different mass, which occupy identical open top sample pans. When the mass is increased, the CO_2 flux doubles but the sample-to-gas contact area (dashed line) remains the same. This causes CO_2 to accumulate in the interstices of the sample. The interstitial CO_2 partial pressure rises to a maximum since it is proportional to the instantaneous reaction rate (see Eq. 4.4). This accounts for the observed shift of experimental conversion data to higher temperature with increasing mass (see Figure 4.8-4.16) as well as the positive linear relationship between the sample mass and the accumulation parameter, c (see Figure 4.7). The accumulation parameter, defined in Eq. 4.9, is likely some function of the sample size and geometry. According to simulations (see Figure 4.2), increasing the value of c decreased E_α. Indeed, experimentally

determined values of E_α were found to decrease when the sample mass increased (compare i and iii in Figure 4.17).

Gallagher and Johnson (1973) also observed a mass dependence of $CaCO_3$ decomposition. In this case, the kinetic parameters were determined using the Freeman-Carroll method which assumes that the reaction rate is described by Eq. 3.5. Extrapolating E and $\ln A$ to zero sample mass gave values of infinity. Gallagher and Johnson (1973) concluded that the mass dependence of the thermal decomposition is a composite of several factors including bulk bed (or pile) geometry, particle size, self-cooling and CO_2 accumulation, among other things. While their conclusions seem reasonable, their method of kinetic analysis ignores the pressure dependency of the rate. In the Accumulation Model, extrapolation to hypothetical zero mass can be simulated by setting c=0 which corresponds to a decomposing sample with no accumulation of product CO_2.

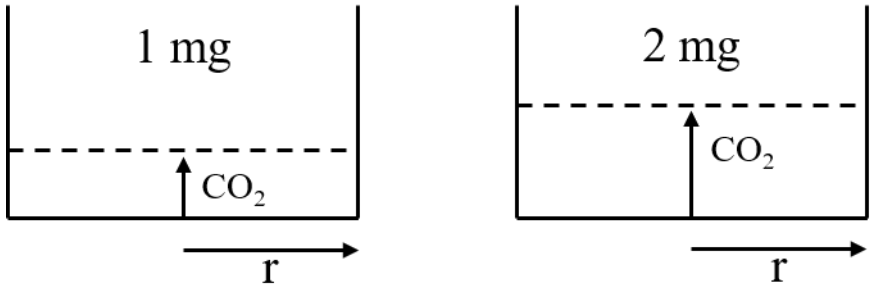

Figure 4.18 – Simple model diagram of thermally decomposing $CaCO_3$ samples of different mass in open top pans. When mass increases but surface-to-gas contact area remains the same, product CO_2 accumulates in the sample.

4.5.3 Gas flow rate

According to simulations (see Figure 4.1-4.2), increasing the accumulation parameter, *c*, which represents greater difficulty in removing reaction-generated CO_2, caused an increase in T_{max}, and E_α. Indeed, it was observed (see Figure 4.6), that T_{max}, increased with a decrease in the N_2 purge gas flow rate. In addition, the fitted values of the accumulation parameter, *c*, were found to increase with decreasing flow (see Table 4.6). Thus, it seems that, when the N_2 flow rate is reduced, CO_2 is permitted to accumulate above the sample at a greater rate, reducing the overall forward rate of decomposition. Unfortunately, due to time restrictions, the trend in E_α could not be tested.

Similar results are found in the literature. For example, Criado et al. (1990) found that T_{max} increased by ~40 K when the He flow rate was increased from 25 to 150 ml.min^{-1} (at β=10 K.min^{-1}) and proposed this to be due to increased efficiency with which CO_2 was removed from the system. This is a very large temperature shift compared to that seen in this work. There are several conceivable reasons for this. For example, it is possible that the discrepancy was due to the difference in geometry and/or flow regime which is known to influence the residence time of CO_2 in the furnace (Archer et al., 2013). The Q-500 TGA used in this study combines cross-flow and vertical-flow which is better for removing product gases than designs which have only vertical-flow. Unfortunately, Criado et al. (1990) did not provide any details about the furnace dimensions or flow regimes used. It is also possible that the discrepancy is due to the higher diffusivity of CO_2 in He compared to that in N_2. For example, Archer et al. (2013) found that the

residence time of CO_2 produced during the decomposition of $CaCO_3$ in the furnace was greater in He than in N_2 over a wide range of flow rate.

Criado et al. (1990) used the Freeman-Carroll method to determine the kinetic parameters. It was shown that the *E*, *A* and the reaction order, *n*, all decreased with decreasing purge gas flow rate. However, little kinetic understanding can be obtained from a model-dependent analysis which ignores the pressure dependence of the rate. Curiously, Criado et al. (1990) did not attempt to fit Eq. 3.4 to their data, despite proposing it.

4.5.4 Particle size

Figure 4.19 shows a simple model of two decomposing $CaCO_3$ particles of different radius. For a thirty-six-fold increase in radius, r_p, the mass of the particle, m_p, increases fifty-thousand-fold, whereas the outer surface area, s_p, only increases one-thousand-fold, assuming that the particle shape is independent of particle size. Therefore, in larger particles, the quantity of CO_2 produced by the reaction is much greater per unit of outer surface area. This causes CO_2 to accumulate in the pores of the larger particle increasing the rate of the reverse reaction. The effect of CO_2 accumulation on E_α was simulated in Figure 4.2 by increasing the accumulation parameter, *c*. Larger particles ought to have greater values of *c*, and thus E_α should decrease. However, as can be seen in Figure 4.17 (comparing iii and iv), E_α is greater for the un-milled sample. Therefore, intraparticle CO_2 accumulation cannot account for, or only partially accounts for, the effect of particle size on the decomposition.

Khinast et al. (1996) derived a complex model based on chemical reaction, product layer diffusion, pore diffusion, external thin-film diffusion and heat transfer. The reaction rate is assumed to be directly proportional to the local reaction surface area per unit volume. Similarly, Escardino et al. (2008) derive a Grainy Pellet Model based on chemical reaction followed by intra- and inter-particle CO_2 diffusion where the reaction rate is assumed to be proportional to the total inner and outer interface area which is a function of the initial specific surface area and the conversion. Sometimes however, terms related to the surface area or particle size are not explicit in the rate equation but are lumped in with the pre-exponential factor. For example, Koga and Criado (1997) propose that "the influence of the particle size distribution is understood

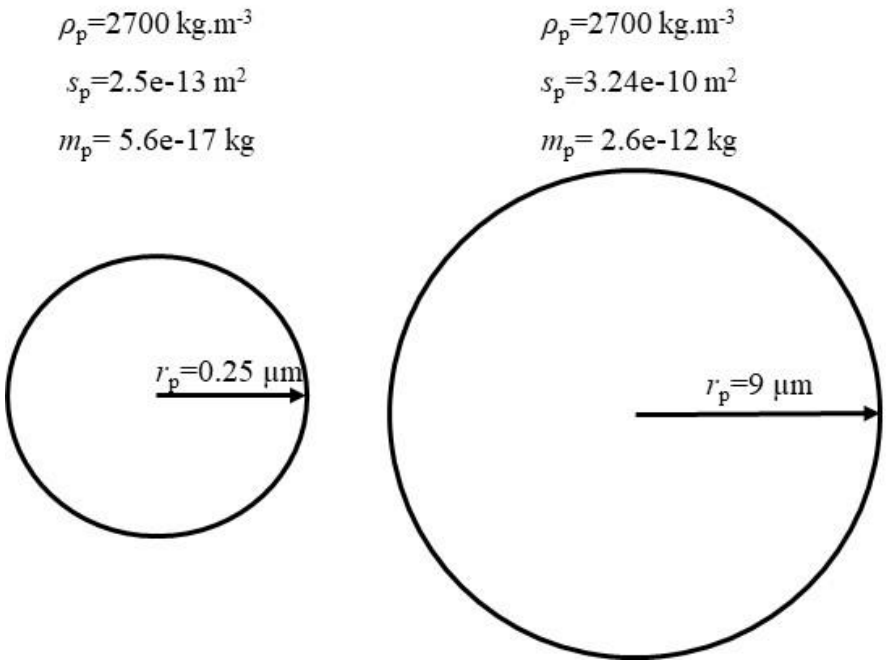

Figure 4.19 – Simple model diagram for thermally decomposing $CaCO_3$ particles of different size. When the radius increases by a factor of 36, the mass (and thus quantity of CO_2 produced by reaction) increases by a factor of 50,000. However, the outer surface area only increases by a factor of 1300. This causes greater accumulation of CO_2 in the pores of the larger particle.

as the summation of the parallel reactions with the same activation energy and different apparent pre-exponential factors". Sánchez-Rodríguez et al. (2017) suggest that particle size influences the rate of decomposition via the pre-exponential factor, *A*, which is proportional to the reciprocal of the square of the diameter. Li et al. (2003) reported that a reduction in particle size by grinding gave corresponding decreases in the apparent *E* and *A*. By curve fitting using Eq. 3.5 and assuming a contracting sphere model (R_3), they obtained E=144 kJ.mol^{-1} and ln$A$=22.0 for particles of diameter 5 μm, but E=97 kJ.mol^{-1} and ln$A$=16.7 for particles of 50 nm diameter. They suggested that this difference was due to defects and stresses in the crystal lattice, as well as increases in surface area and aggregation effects. Although the results are not presented here, it was found that, when simulating the Accumulation Model, increasing *A* shifted conversion curves to lower temperature and increased their amplitude. The shift is also seen in experimental data when increasing the surface area of the system. Similarly, it was found that increasing *A* increased E_α for P_{ext}>0. As seen in Figure 4.17, ball-milling decreased E_α (see comparing iii and iv). Therefore, the effect of increased surface area on the rate of chemical reaction cannot fully account for the observations in this thesis or indeed others (Koga and Criado, 1997; Li et al., 2003; Escardino et al., 2008). Alternatively, it has been hypothesized that a decrease in particle size causes a decrease in the intrinsic activation energy, *E*. Some (Boldyrev, 2006; Küçük and Yildiz, 2006) have suggested that mechanochemical activation by ball-milling can lower the activation energy and increase the rate of some solids, attributing this to an increased concentration of microstrains and shear stresses. Studies using constant rate thermal analysis to minimize the effect of CO_2 accumulation (Criado et al., 1987; Criado et al., 1992) found that *E* decreases with increasing particle size. They suggest that this is due to an increase in the fraction

of weakly bound surface $CaCO_3$ molecules. A decrease in E can account for both the shift of conversion data to lower temperature as well as the decrease in E_α. Particle size has also been theorized to affect the kinetics of adsorption/desorption (Beruto et al., 1984) as well as nuclei formation during an induction period (Khinast et al., 1994). In summary, it is more than likely that particle size (as well as particle shape, surface area and surface texture) have a complex effect on the rate.

4.5.5 Conversion dependency of E_α

All estimates of E_α in this work, and in the literature, decrease with increasing conversion (see Figure 4.17). This is because at lower conversions, corresponding to lower temperatures, P_{eq} has a magnitude approaching P_{ext} resulting in large values of E_α (see the second term on the right-hand side of Eq. 4.14). On the other hand, at higher conversions, corresponding to higher temperatures, P_{eq} is much greater than P_{ext}, and E_α approaches E. These effects were simulated in Figure 4.2. The decrease has also been found to be consistent with the kinetic model proposed by Pavlyuchenko and Prodan (1961), who showed that E_α in the initial stages of a reversible decomposition occurs not far from equilibrium and is characterized by a high value of E_α, decreasing as the system departs from equilibrium.

Alternative explanations for the decreasing dependence of E_α on α are found in the literature. For example, some studies (Sanders and Gallagher, 2002; Rodriguez-Navarro et al., 2009) suggest that $CaCO_3$ decomposes according to a dual-parallel process (see Eq. 3.20) and that the decrease in E_α with reaction progress is due to an increasing contribution from a secondary reaction with a lower intrinsic value of E. However, such models cannot account for the observed decrease in E_α

with increased heating rate (see Figure 4.17). The temperature dependency of P_{eq}, can account for both decreasing E_α with increasing α, and decreasing E_α with increasing β.

Having said this, the equilibrium thermodynamics are not the only source of conversion dependency. Results so far suggest that mass, N_2 flow rate and particle size have a significant influence on the decomposition kinetics. This effect was simulated by increasing the accumulation parameter, c, which decreased E_α particularly at lower conversion, giving it a flatter dependence (see Figure 4.2).

4.5.6 Comment on kinetic compensation effect

The kinetic compensation effect (KCE) featured in several studies (Gallagher and Johnson, 1973; Criado et al., 1990; Li et al., 2003) was not observed in our analysis. It seems unlikely that the KCE is a phenomenon with physical significance, but more likely a mathematical artifact of fitting models which ignore the pressure dependence of the rate.

4.5.7 Comment on conversion dependency, $f(\alpha)$

Contracting geometry models (Gallagher and Johnson, 1973; Halikia et al., 2001; Li et al., 2003; Chen and Liu, 2010), diffusion models (Elder and Ready, 1986) and reaction order models (Koga and Criado, 1998) have all been used to describe the conversion dependency of $CaCO_3$ decomposition. In some cases, multi-model explanations are offered. For example, Rodriguez-Navarro et al. (2009) suggest that $CaCO_3$ decomposes by a mixture of the F_1 and D_1 models, whereas Sanders and Gallagher (2002) suggest that decomposition occurs by two parallel reactions with conversion dependencies $(1-\alpha)^{0.392}$ and $(1-\alpha)^{0.515}$, with mass-weighted

contributions of 26 % and 74 %, respectively. In this thesis it is assumed the reaction is first-order (F_1) in order (Reading et al., 1991). Most studies assume 1/2 or 2/3 order based on contracting geometry models. However, a decomposition process which is first-order (F_1) can have the appearance of lower order, such as 2/3 (R_3) or 1/2 (R_2), due to CO_2 accumulation, when fitting models of the form in Eq. 3.5.

4.5.8 Comment on accumulation parameter, *c*

The reader may have noticed that the accumulation parameter, *c*, has units of kPa.s which are the same as the units of viscosity. This may suggest that the path from the interior reaction sites to the furnace outlet can be compared to the random-walk paths followed by molecules through a viscous fluid. CO_2 must diffuse from its point of formation to the purge gas. If the path is highly "viscous", corresponding to large values of *c*, then transport of the product CO_2 will be inhibited, and it will accumulate. Thus, the accumulation parameter *c* is itself a complex function of the factors affecting diffusion of CO_2 from its formation at the reaction interface to the furnace exit. Specifically, CO_2 must diffuse through the pores of the particle, then through the interstices of the sample and through the gas "film" of accumulated CO_2 surrounding the sample (see Figure 4.20). When the sample is small but the particle size large, intraparticle accumulation will influence the rate. When the sample is large, but the particles are small, interparticle accumulation will control the rate. When the particles and sample are small, but the flow rate is insufficient then accumulation of CO_2 in the furnace will limit the rate. For small particles, small sample size and high purge gas flow rate, chemical reaction controls the rate. Similar

explanations are given by Escardino et al. (2013) who studied the rate of thermal decomposition of large grainy pellets of $CaCO_3$ and proposed the following model:

$$\frac{\mathrm{d}\alpha}{\mathrm{d}t} = \frac{1}{c_{\mathrm{B}}^{0}} \frac{K_{\mathrm{c}} - b_2 . c_{\mathrm{Q}}^{\mathrm{G}}}{K_{\mathrm{c}}/(k_{\mathrm{d}} . S_{\mathrm{sp}}(1-a)^{n}) + r_{\mathrm{s}}^{2}/3D_{\mathrm{e}}} \tag{4.19}$$

where c_{B}^{0} is the initial mole concentration of $CaCO_3$ in the pellet, K_c equilibrium constant of reaction, k_d is the rate constant of the direct reaction, $b_2 = c_{\mathrm{Qs}}^{\mathrm{S}}/c_{\mathrm{Qs}}^{\mathrm{G}}$ (where $c_{\mathrm{Qs}}^{\mathrm{G}}$ is the mole concentration of CO_2 in the gas phase at the pellet-gas interface and $c_{\mathrm{Qs}}^{\mathrm{S}}$ is the mole concentration of CO_2 in the pellet pores at the pellet-gas interface), $c_{\mathrm{Q}}^{\mathrm{G}}$ is the mole concentration of CO_2 in the gas phase, S_{sp} is the specific surface area of the $CaCO_3$ pellet, r_{s} is initial radius of the sphere with the same surface area as the pellet, n is the reaction order, and D_e is the effective diffusion coefficient of CO_2 through the pellet. By comparison with Eq. 4.13 it can be seen that the accumulation parameter, c, is proportional to the square of the pellet size (r_{s}^{2}) divided by 3 times the effective diffusivity ($3D_e$) (assuming that diffusion through the pellet is rate-limiting). Despite their different derivations, it is reassuring that the rate equations for the Grainy Pellet Model (Eq. 4.19) and the Accumulation Model (Eq. 4.18), are so similar.

4.5.9 Comment on correction factor, b_1

The CO_2 concentration in the purge gas during our experiments was 3.5 ppmv. Therefore, at a temperature of 800-1000 K and furnace pressure of 105 kPa, the value of P_{ext} was approximately 1e−3 kPa. However, this value of P_{ext} does not give the correct onset temperature to fit the simulated data to the experimental data, even when correcting for the increase in pressure with

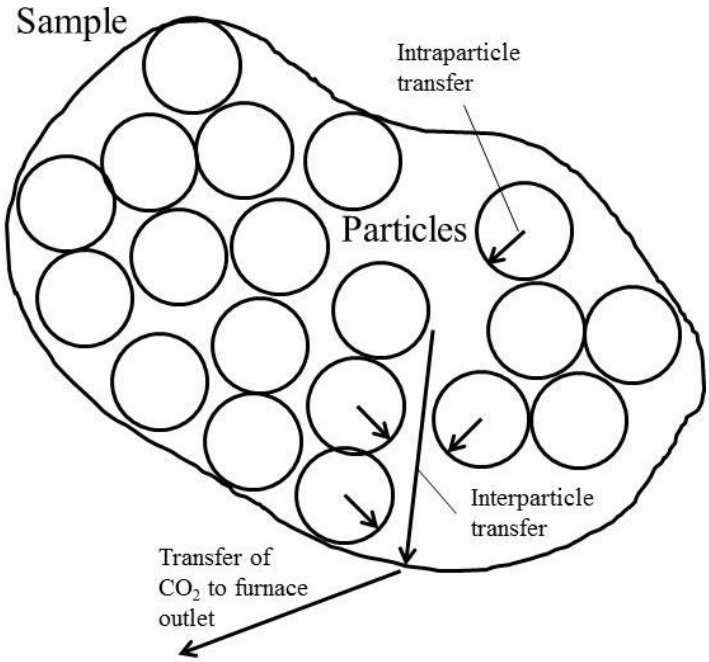

Figure 4.20 – Simple model diagram for transport of CO_2 out of thermally decomposing $CaCO_3$ sample.

temperature (Gay-Lussac's law). To improve the fit, a constant was introduced, b_1. This constant, b_1, was found to increase with the heating rate. The need for this additional parameter tells us that the Accumulation Model provides an insufficient description of the reaction kinetics. Indeed, it is known (Jensen et al., 2005) that CO_2 formed by the reaction becomes chemically or physically adsorbed on CaO surfaces, delaying the reaction onset. Differences in adsorption properties could explain the requirement for the b_1 parameter. A similar hypothesis was put forward by Escardino et al. (2013) in their Grainy Pellet Model (see Eq. 4.19). Monitoring the exact pressure in the TGA furnace should occur in future experiments so that P_{ext} can be determined accurately as a function of time.

4.6 Conclusion

A new model, here named the "Accumulation Model", is proposed to describe the rate of $CaCO_3$ decomposition (see Eq. 4.18). The model is derived by combining transition-state theory and equilibrium thermodynamics (Reading et al., 1991) with a simple accumulation parameter to account for the effect of reaction-generated CO_2 (Criado et al., 1990). The lower the value of the accumulation parameter, the greater the efficiency of the experimental set-up in removing reaction-generated CO_2.

Thermogravimetric data were gathered for decomposition of $CaCO_3$ at constant heating rates. The effects of ball-milling, N_2 flow rate, sample mass and heating rate were investigated. The apparent isoconversional activation energy, E_α, was determined using the Advanced Isoconversional method. A novel data processing method is used which crosses repeat runs at the highest and lowest heating rates, in all their permutations, allowing a more accurate median isoconversional activation energy, $\tilde{E}_\alpha$. The isoconversional pre-exponential factor, A_α, was determined by the method of invariant kinetic parameters. These isoconversional values were used to estimate the intrinsic parameters, E and A, for $CaCO_3$ decomposition. The intrinsic parameters were then used to anchor the fitting of the Accumulation Model. The accumulation parameter, c, was found to increase proportionally with sample mass and the correction factor, b_1, was found to increase roughly in accordance with the heating rate. The Accumulation Model correctly predicted the decrease in the isoconversional activation energy with an increase in initial sample mass. The thesis' objective "To develop and parameterize a simple kinetic model for the rate of $CaCO_3$ decomposition in terms of temperature, conversion and any other relevant

variables, which account for all the experimental data" has been reasonably achieved using the novel Accumulation Model.

The results indicate that the only way to reduce the temperature of $CaCO_3$ decomposition in Direct Air Capture systems is to reduce c and/or P_{ext}. To reduce the accumulation parameter, c, $CaCO_3$ crystals or pellets should be small and porous for efficient CO_2 removal to prevent back-reaction with CaO. To reduce P_{ext}, the pressure of the reactor could be reduced. However, this would require expensive equipment to create vacuum conditions. Alternatively, P_{ext} could be reduced using a sufficient quantity of purge gas with low CO_2 partial pressure, such as steam. The steam could then be separated by condensation. However, large quantities of steam may be needed to keep CO_2 partial pressure low, requiring a great deal of energy for evaporation. A more radical approach could be to pelletize $CaCO_3$ in combination with a highly dielectric material, then heat using microwave irradiation. This would allow for targeted heating and could reduce the purge gas requirement.

Ultimately, Direct Air Capture using sodium and potassium hydroxide solutions with lime regeneration is tightly constrained by the intrinsic thermodynamics and kinetics of $CaCO_3$ decomposition as well as CO_2 accumulation in the pores and interstices. Therefore, new regeneration pathways are needed to reduce the temperature and cost of DAC. One potential pathway, investigated in the next chapter, is regeneration using hematite.

Chapter 5: Reaction of sodium carbonate with iron (III) oxide

5.1 Introduction

A prototype Direct Air Capture (DAC) system has been constructed by Carbon Engineering in Squamish, Canada, which is capable of removing approximately 300 tonnes of CO_2 from the air every year. The CO_2 is captured using potassium hydroxide solution. The lime cycle is then used to regenerate the capture solution thus making the process cyclical (see Figure 1.7). Keith et al. (2018) calculate a levelized cost for this process of 94 to 232 USD per tonne of CO_2 captured, dependent on energy costs. Although less than previous cost estimates (Socolow et al., 2011; House et al., 2011), Keith's estimate still greatly exceeds the typical CO_2 market price.

Most of the cost for this type of DAC is due to the high temperature heat required to decompose $CaCO_3$. As discussed in the previous chapter, the temperature of $CaCO_{3(s)}$ decomposition is limited by its intrinsic thermodynamics and kinetics. Therefore, in order to achieve lower temperatures and reduce costs, alternatives approaches are needed. One possible alternative, already mentioned in Section 1.15.1.2.2, is to capture CO_2 from the air using sodium hydroxide solution with regeneration using hematite, Fe_2O_3.

Production of $NaOH_{(aq)}$ from $Na_2CO_{3(s)}$ using $Fe_2O_{3(s)}$ was patented by Lowig (1878) and used commercially in the U.S.S.R for several decades. The reaction proceeds via:

$$Fe_2O_{3(s)} + Na_2CO_{3(s)} \Leftrightarrow 2NaFeO_{2(s)} + CO_{2(g)} \qquad \Delta H = +164\ \text{kJ.mol}^{-1} \text{ at } 298\ \text{K} \qquad 5.1$$

then hydrolysis according to:

$$2NaFeO_{2(s)} + H_2O_{(l)} \Leftrightarrow 2NaOH_{(aq)} + Fe_2O_{3(s)} \quad \Delta H = -80.9\ \text{kJ.mol}^{-1} \text{ at } 298\ \text{K} \qquad 5.2$$

Nearly a century later, these same reactions were used as the basis of the Direct Alkali Regeneration System (DARS) for direct causticization of soda liquors in the pulp and paper industry. The process was patented by Nagano et al. (1974) and then commercialized by Associated Pulp and Paper Mills in Burnie, Tasmania (1977) and at a Danish straw pulp-mill run by Fredericia Cellulose in 1988. The Burnie mill regenerated 95 tonnes of NaOH per day (Grace, 1981). The Direct Alkali Regeneration System has fewer process units than the Kraft method, since addition of Fe_2O_3 allows direct decomposition of Na_2CO_3 in the black liquor recovery stage (Covey, 1984). However, the system is only viable for low-sulfur-content biomass, since sulfur reduces Fe_2O_3 and forms stable FeS (Maddern, 1986).

Carbon Engineering first suggested adapting the Lowig/DARS process for DAC (Keith and Mahmoudkhani, 2012). A simplified process diagram is shown in Figure 5.1. Regeneration of NaOH capture solution requires two-step crystallization of $Na_2CO_{3(s)}$ by temperature swing, followed by reaction with $Fe_2O_{3(s)}$ in a fluidized bed. To complete the cycle, the $NaFeO_{2(s)}$ product is hot-water leached to recover $NaOH_{(aq)}$ and $Fe_2O_{3(s)}$.

This process is promising for a number of reasons: 1. The reaction of Na_2CO_3 with Fe_2O_3 requires less energy than $CaCO_3$ decomposition. 2. FeS formation, observed in the DARS process, is not an issue in DAC since sulfur concentration is negligible in ambient air. 3.The concentration of $NaOH_{(aq)}$ leaving the leacher can exceed that of the CaO process. 4. Past commercialization of Lowig/DARS is proof of its scalability. 5. Fe_2O_3 is inexpensive.

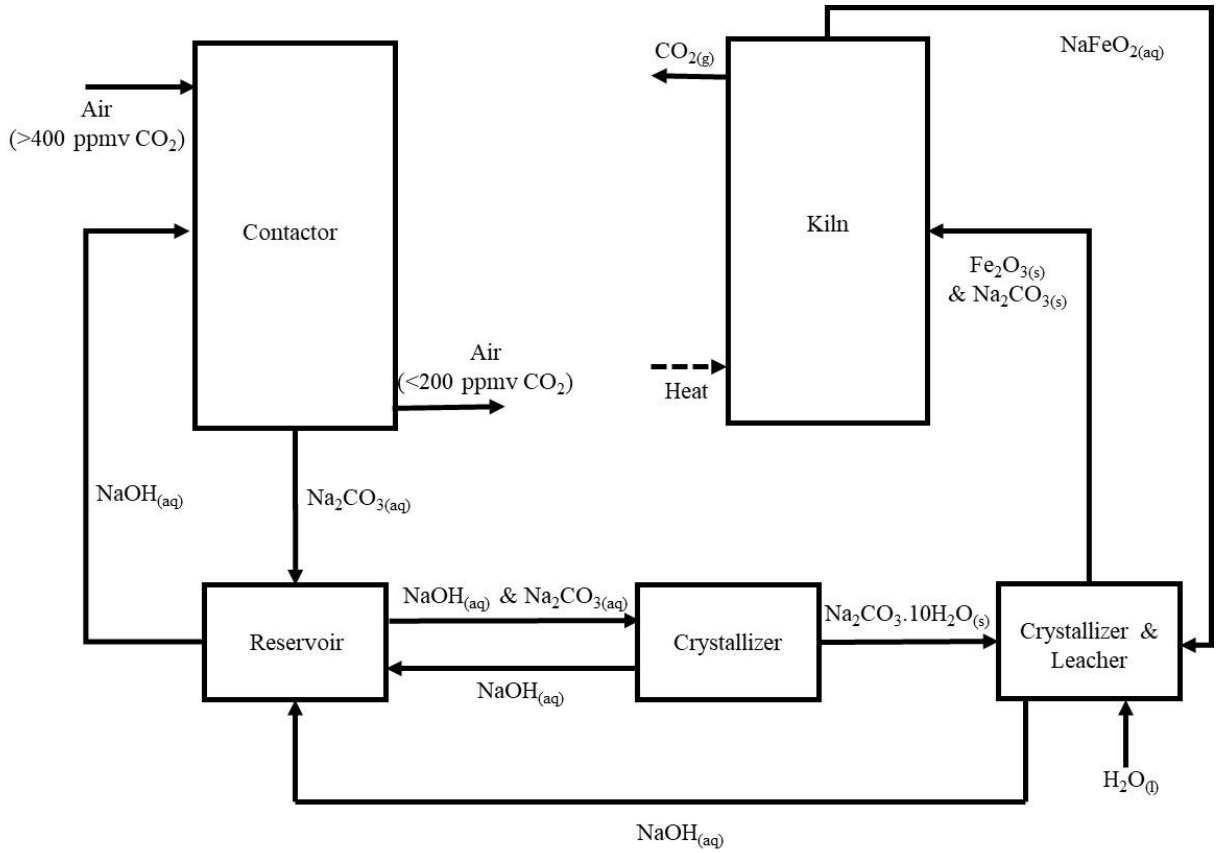

Figure 5.1 – Simplified process diagram for CO_2 capture from air using $NaOH_{(aq)}$ with regeneration using Fe_2O_3.

There may also be potential for the Fe_2O_3 process to operate at lower temperature than the CaO process. A range of temperatures for reaction of Fe_2O_3 and Na_2CO_3 have been reported in the literature (see Table 5.1).

The enthalpy of reaction between Fe_2O_3 and Na_2CO_3 is 164 kJ.mol^{-1}, which is 14 kJ.mol^{-1} lower than for $CaCO_3$. However, the proposed DARS operating temperature is the same, i.e. 1173 K (Covey, 1984) or higher, e.g. 1173-1273 K (Nagai, 2001). This hints at a strong kinetic limitation

present in the reaction. Unfortunately, there is very little kinetic information in the literature regarding this reaction. Experimentally determined values of E include 79.5 kJ.mol^{-1} (Frei and Čáslavská, 1965), 85.6 kJ.mol^{-1} (Kiiskilä and Valkonen, 1979) and 278 kJ.mol^{-1} (Colović et al., 1994), all assuming the reaction to be first-order with respect to the conversion (an assumption which is made without much justification). Povarov and Sokolova (2009) calculate E=52-100 kJ.mol^{-1} and A=27-3641 s^{-1} dependent on the Fe_2O_3:Na_2CO_3 mole ratio. Several of these investigators collected data isothermally and/or used only model-dependent methods for kinetic parameter determination. Such methods are now considered inaccurate, and therefore a fresh look at the reaction kinetics is desperately needed.

Table 5.1 – Approximate temperature ranges from the literature for the reaction of Fe_2O_3 and Na_2CO_3 in air atmosphere unless otherwise indicated. N.S.=Not Specified.

T (K)	Mole ratio	Product	Reference
1023-1273	1-10	β-$NaFeO_2$	Otsubo and Yamaguchi (1961)
1523	0.625	$Na_3Fe_5O_9$	Romers et al. (1967)
973-1173	>1	$NaFeO_2$	Nagano et al. (1974)
873-1073	1	α- and β-$NaFeO_2$	Takeda et al. (1980)
1073 (Ar)	1	$NaFeO_2$	Kaneko et al. (2001)
1173-1273	N.S.	$NaFeO_2$	Nagai (2001)
1123-1173 (CO_2)	1	α-$NaFeO_2$	Takasu et al. (2019)

The objective of this chapter is to study the kinetics of Eq. 5.1 using the thermogravimetric method and then find and parameterize a simple expression for the reaction rate in terms of the time, temperature, conversion and any other relevant variables. The reaction of Fe_2O_3 and K_2CO_3

is also investigated. As in the previous chapter, the isoconversional activation energy, E_α, is determined by the Advanced Isoconversional method. Better understanding of the kinetics will help assess hematite's potential for lower temperature regeneration of alkali hydroxide solutions in Direct Air Capture systems.

5.2 Contact Point Model (CPM) theory

Although the results are not shown in this thesis, it was found that several of the most commonly used models for solid and solid-gas reactions (described in Table 8.1) provided good fits for some of the Fe_2O_3 and Na_2CO_3 reaction data. However, each model was only applicable within narrow limits of particle size, mole ratio and heating rate. For example, the F_1 model was found to fit well for a ball-milled mixture of Fe_2O_3 and Na_2CO_3 in a 16:1 mole ratio whereas the F_2 model was found to fit better at a 1:3 mole ratio. Thus, a more comprehensive model was required. The relatively unknown Contact Point Model (CPM), originally proposed by Fătu (1988), was found to fit reaction data over a much wider range of conditions. The CPM describes the rate of reaction between two solid powders, forming two different products. In this section, the CPM is described, with a small adaptation for formation of just one reaction product, instead of two.

$$\mathrm{A_{(s)} + B_{(s)} \rightarrow C_{(s)}} \qquad 5.3$$

The mechanism involves nucleation of a new product phase C in the surface area of contact, *s*, between particles of A and B, followed by growth of these nuclei due to counter-diffusion of molecules or ions through the product layer until full conversion of the limiting reactant, A (see

Figure 5.2). For derivation of the model, nucleation is assumed to be the rate-limiting step. The total number of particles and total mass of the system is assumed to be conserved.

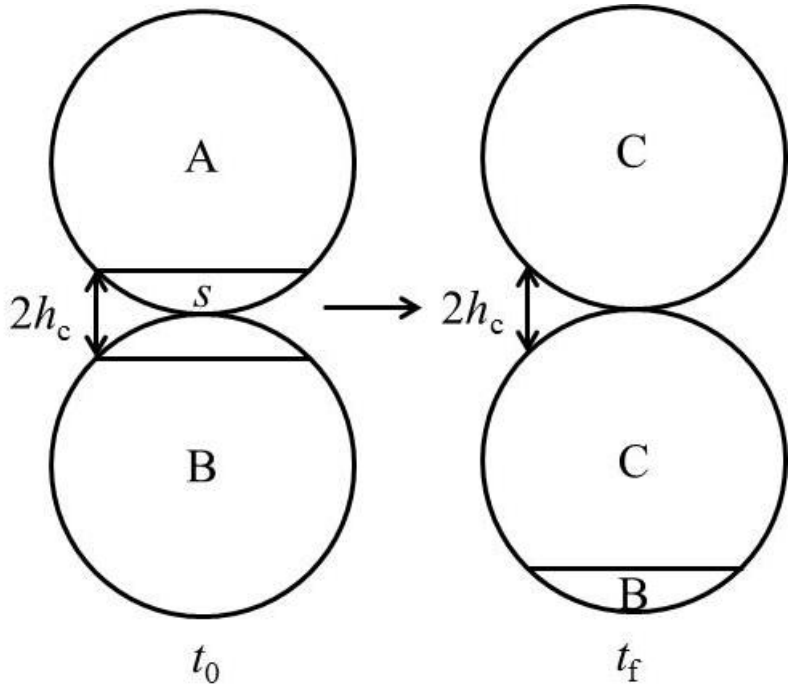

Figure 5.2 – Simple model diagram of particles A and B reacting to give product C at the surface area of contact, *s*, where $2h_c$ is the maximum distance of interaction, with counter-diffusion until A is consumed.

The rate of stable nuclei formation is given by:

$$\frac{\mathrm{d}N}{\mathrm{d}t} = P_1 . n_s . \exp\left(\frac{-E}{RT}\right) . S \qquad 5.4$$

where N is the total number of stable nuclei, n_s is the maximum number of possible nuclei in a unit surface (m^{-2}), S is the total interaction surface area between all particles of A and B (m^2) and P_1 is the rate, or probability (Fătu, 1988), that a potential nucleus will transform into a stable nucleus (s^{-1}), given by the Arrhenius equation:

$$P_1 = P_o . \exp\left(\frac{-E}{RT}\right) \quad 5.5$$

where P_o is the pre-exponential factor for nucleation and E is the activation energy barrier for nucleation. Conversion of A is defined by:

$$\alpha_A = \frac{m_A}{m_A^o} \quad 5.6$$

where m_A is the mass of transformed A at time, t, and m_A^o is the initial mass of A. Since every stable nucleus becomes product, Eq. 5.6 can be written:

$$\alpha_A = \frac{N . m_{A1}}{m_A^o} \quad 5.7$$

where m_{A1} is the mean mass of a transformed particle of A at time, t. The derivative with respect to time, t, gives:

$$\frac{d\alpha_A}{dt} = \frac{m_{A1}}{m_A^o}\frac{dN}{dt} \quad 5.8$$

Combining Eqs. 5.4, 5.5 and 5.8 gives:

$$\frac{d\alpha_A}{dt} = \frac{P_o . n_s . m_{A1}}{m_A^o} \exp\left(\frac{-E}{RT}\right) . S \quad 5.9$$

Now, an expression for the total interaction surface area, S, is needed. First, the surface area of interaction between two particles, s, is derived from the geometry of a spherical cap each of height, h_c which is approximately equal to 5 Å (Fătu, 1988) (see Figure 5.2). Thus:

$$s = 2\pi . r_{\mathrm{A}} . h_{\mathrm{c}} \qquad 5.10$$

where r_A is the mean radius of a particle of A. The total surface area of interaction between all reactant particles, *S*, is given by:

$$S = 2\pi . r_{\mathrm{A}} . h_{\mathrm{c}} . C_{\mathrm{AB}} \qquad 5.11$$

Now, an expression for the total number of contact points between reactants (C_{AB}) is required:

$$C_{\mathrm{AB}} = C_{\mathrm{A1\_B}} * n_{\mathrm{A}} \qquad 5.12$$

where the number of particles of reactant A, n_A, is given by the total mass of transformed A, $m_A^0(1 - \alpha_A)$, divided by the mean mass of one transformed particle of A, m_{A1}:

$$n_{\mathrm{A}} = \frac{m_{\mathrm{A}}^0(1 - \alpha_{\mathrm{A}})}{m_{\mathrm{A1}}} \qquad 5.13$$

In Eq. 5.12, C_{A1_B} is the number of contact points between one particle of A and surrounding particles of B:

$$C_{\mathrm{A1\_B}} = C_{\mathrm{A1\_A,B}} * X_{\mathrm{B}} \qquad 5.14$$

where $C_{A1\_A,B}$ is the number of contact points between one particle of A and surrounding particles of A and B (see Eq. 5.20), and X_B is the fraction of the total particles in the sample which are of reactant B:

$$X_{\mathrm{B}} = \frac{n_{\mathrm{B}}}{n_{\mathrm{A}}^0 + n_{\mathrm{B}}^0} = \frac{\frac{m_{\mathrm{B}}^0}{m_{\mathrm{B1}}}(1-\alpha_{\mathrm{B}})}{\frac{m_{\mathrm{A}}^0}{m_{\mathrm{A1}}} + \frac{m_{\mathrm{B}}^0}{m_{\mathrm{B1}}}} \quad 5.15$$

where α_{B} is the conversion of species B, where m_{B}^0 is the initial mass of B and where m_{B1} is the mean mass of a transformed particle of B at time, *t*. Since the mass of one particle of A (and similarly for B) is given by:

$$m_{\mathrm{A1}} = 4/3\pi.(r_{\mathrm{A}})^3.\rho_{\mathrm{A}} \quad 5.16$$

where ρ_{A} is the density of a particle of A, then

$$X_{\mathrm{B}} = \frac{1 - q\alpha_{\mathrm{A}}}{1 + R'} \quad 5.17$$

where

$$R' = \frac{m_{\mathrm{B}}^0}{m_{\mathrm{A}}^0}\left(\frac{r_{\mathrm{A}}^0}{r_{\mathrm{B}}^0}\right)^3 \frac{\rho_{\mathrm{A}}}{\rho_{\mathrm{B}}} \quad 5.18$$

where ρ_{B} is the density of particle B, and

$$q = \frac{\alpha_{\mathrm{B}}}{\alpha_{\mathrm{A}}} = \frac{M_{\mathrm{B}}}{M_{\mathrm{A}}}\frac{m_{\mathrm{A}}^0}{m_{\mathrm{B}}^0} \quad 5.19$$

where M_{A} and M_{B} are the mole masses of A and B respectively. $C_{\mathrm{A1\_A,B}}$ is determined using the Kissing number problem (see Figure 5.3).

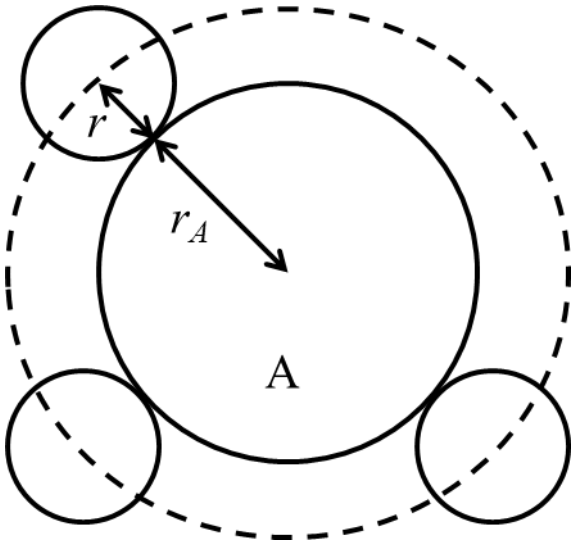

Figure 5.3 – Simple model diagram depicting contacts between a particle of A and surrounding particles of A and B used in determination of $C_{A1\_A,B}$, where *r* is the mean radius of the grains (A and B) which changes with conversion.

The number of contacts is proportional to the square of the ratio of the surface of the sphere with radius (r_A+r) (dashed line) to the circular area with radius *r*:

$$C_{\mathrm{A1\_A,B}} = 4K_1.\gamma\left(1+\frac{r_{\mathrm{A}}}{r}\right)^2 \qquad 5.20$$

where K_1 is a constant approximately equal to 1 when particles of A and B have similar radii.

The compaction factor, γ, is given by:

$$\gamma = \frac{\frac{m_{\mathrm{A}}^{\mathrm{o}}}{\rho_{\mathrm{A}}}+\frac{m_{\mathrm{B}}^{\mathrm{o}}}{\rho_{\mathrm{B}}}}{V_{\mathrm{a}}} \qquad 5.21$$

where ρ_A and ρ_B are the densities of A and B, such that $m_A^o/\rho_A + m_B^o/\rho_B$ is the true volume of the reactants, and V_a is the volume of the crucible occupied by the sample. It is assumed that the

compaction factor does not change during the reaction. The mean radius, r, of the particle changes with conversion according to:

$$r = a_{\mathrm{p}} + b_{\mathrm{p}}.\,\alpha_{\mathrm{A}} \qquad 5.22$$

where a_{p} and b_{p} are the linear fitting parameters. When $\alpha_{\mathrm{A}}=0$, $r=r_0$, where r_0 is the mean radius of the grains at the start of the reaction and when $\alpha_{\mathrm{A}}=1$, $r=r_{\mathrm{f}}$, where r_{f} is the mean radius of the grains at the end of the reaction. Solving for these conditions gives:

$$r = r_0\left[1 + \left(\frac{r_{\mathrm{f}}}{r_0} - 1\right)\alpha_{\mathrm{A}}\right] \qquad 5.23$$

where r_{f}/r_0 can be determined using:

$$\frac{r_{\mathrm{f}}}{r_0} = \left(\frac{\rho_0}{\rho_{\mathrm{f}}}\right)^{1/3} \qquad 5.24$$

where ρ_0 and ρ_{f} are the initial and final mean densities of the sample respectively. Combining Eqs. 5.9, 5.11, 5.12, 5.13, 5.14, 5.17, 5.20 and 5.23 gives:

$$\frac{\mathrm{d}\alpha}{\mathrm{d}t} = \frac{8\pi\gamma r_{\mathrm{A}} h_{\mathrm{c}} P_0 n_{\mathrm{s}}}{1+R'}\exp\left(\frac{-E}{RT}\right)\left(1 + \frac{r_{\mathrm{A}}}{r_0\left[1+\left(\frac{r_{\mathrm{f}}}{r_0}-1\right)\alpha_{\mathrm{A}}\right]}\right)^2 (1-q\alpha_{\mathrm{A}})(1-\alpha_{\mathrm{A}}) \qquad 5.25$$

Eq. 5.25 is the full equation for the rate of reaction between two solids where nucleation in the contact surface is rate limiting (assuming no gas evolution). Decreasing the particle size, increasing sample compaction or increasing the amount of the limiting reactant will increase the number of A-B contact points and therefore increase the reaction rate. When $r_0=r_{\mathrm{f}}=r$, $r_{\mathrm{A}}=r_{\mathrm{B}}=r_0=r$

and for stoichiometric ratio of reactants the reaction rate becomes second-order with respect to α_A.

5.3 Experimental methodology

5.3.1 Jar-mixing

100 g of anhydrous Na_2CO_3 (S263500-Fischer Scientific, Certified ACS Grade ≥ 99.5 %) was added to the top of a stacked column of sieves (Tyler Canadian Standard Sieve Series) with mesh openings of 355, 212, 125, 105, 63, 38 and 32 μm (plus an impervious bottom tray) in descending order and then shaken in a Fritsch Analysette 3 Pro shaker for 20 min at a maximum amplitude of 2.7 mm. Two major particle size fractions were obtained - 212-355 μm (~80 %) and 38-63 μm (~10 %). The other minor fractions were discarded. The two retained Na_2CO_3 fractions were combined with commercial grade α-Fe_2O_3 powder (310050-Sigma-Aldrich, <5 μm, ≥99 % purity) in a 1:1 mole ratio totaling 5 g and jar-mixed by rotational motion in a 100 cm^3 glass sample vial at 60 rpm for 1 h. In addition, 1 mole of 38-63 μm Na_2CO_3 was combined with 3 moles of Fe_2O_3 and jar-mixed in an identical manner to the 1:1 mixture.

5.3.2 Ball-milling and pelletization

Na_2CO_3 (212-355 μm) was combined with Fe_2O_3 (<5 μm) in a 1:1 mole ratio totaling 5 g and ball-milled in an air-sealed, hardened steel canister (250 cm^3) using a SPEX 8000 mixer/miller, with 18 steel balls of 3 mm diameter and 1 steel ball of 5 mm diameter at a 1:5 powder-to-ball mass ratio, at 1080 cycles per minute for 6 min. This process was repeated for periods of 60 and 600 min. For the 600 min treatment, milling was carried out in ten separate 60 min periods separated by 2 h intervals. At the end of the 60 min milling period, the temperature of the powder

mixture was ~433 K (135°C) (measured using Infrared Thermometer). A 1:1 mole mixture of K_2CO_3 (Sigma Aldrich, CAS No. 584-08-07, Product No. 367877, MDL no. MFCD00011382, purity >99.995 %) and Fe_2O_3 was ball-milled for 60 min using the same method.

Where necessary, an MTI 50K press machine (Measurement Technology Inc.) was used to compress ball-milled mixtures into pellets. The die was filled with approximately 10 mg of the 60 min dry ball-milled mixture and pressed to a maximum set compression force of 1000 N to make a single cylindrical pellet of 6.5 mm diameter and <1 mm height.

5.3.3 Sample characterization

Scanning electron micrograph (SEM) images were obtained using a Hitachi S-3000N microscope with Tungsten filament optic (secondary electron resolution 3.5 nm under vacuum, magnification 15 to 100,000x, working distance of 10-20 mm, accelerating voltage 0.3 to 30 kV). The sample was dispersed onto a carbon adhesive disc affixed to a 12.5 mm diameter aluminium stub.

The particle size distribution (PSD) was studied in a Malvern Instruments, Mastersizer 2000 laser diffractometer with a Scirocco dry feeding accessory. The result was taken as the mean of three repeats. For jar-mixed samples, the theoretical particle size distribution was calculated assuming that neither attrition nor agglomeration occurred during mixing by summation of the PSDs for each component of the mixture prior to mixing, then normalization. Indeed, it was found that the measured the distribution differed from the theoretical one (see Figure 5.6).

N_2 absorption isotherms were obtained at 77 K using a Quantachrome Autosorb-1 Instrument. Prior to analysis, 0.5 g of sample was degassed under vacuum at 298 K until a minimum degassing rate of 10 μl.min^{-1} was reached. The specific surface area was estimated by the multi-point Brunauer–Emmett–Teller method (BET).

Molecular structures were investigated using a Philips PW-1730 X-ray diffractometer (XRD). The sample was ground and mounted on a quartz plate coated with petroleum jelly. Data were obtained in a 2θ range of 10–80° using Cu Kα radiation of 50 kV and 30 mA at a scanning rate of 20° per min.

5.3.4 Thermogravimetric analysis

Thermogravimetric data for reaction of Fe_2O_3 and Na_2CO_3 mixtures were gathered by a TA Instruments Q-500 Series TGA (weighing precision +/−0.01 %) from 298 to 1223 K at constant heating rates of 20 K.min^{-1}. Open top platinum pans with a depth of 1 mm and radius 5 mm were used to hold the sample. The thermocouple was positioned ~1 mm above the sample such that the sample temperature was represented as accurately as possible without touching the material and potentially interfering with mass measurement. Dry, high-purity N_2 (99.8-99.999 %) was used as a purge gas with a cross-flow of 60 ml.min^{-1} and a down-flow of 40 ml.min^{-1}. The CO_2 concentration of the stream was 2-5 ppmv, according to the specifications of the Parker, Domnick-Hunter Nitrogen generator. The pressure in the furnace chamber was 105 kPa(abs). An empty pan was heated under the same conditions as the sample. The resulting apparent mass data were subtracted from the corresponding values in the sample runs, correcting for buoyancy

effects. The initial sample mass was approximately 10 mg or less where necessary. The sample was evenly spread onto the bottom of a platinum pan.

5.3.5 Data processing and analysis

Conversion is calculated by the ash-free or standard definitions as described in Section 3.3. Where necessary, conversion is also calculated in terms of CO_2 loss from Na_2CO_3:

$$\alpha_{CO_2}\,(\%) = \frac{\text{moles of } CO_2 \text{ lost}}{\text{initial no. of moles } Na_2CO_3} \text{x} 100 \qquad 5.26$$

The reaction rate was determined taking the first-forward derivative of conversion (ash-free or standard) with respect to time. The isoconversional activation energy (E_α) was determined using the Advanced Isoconversional method. For this, TGA runs were repeated at lower heating rates (β=2, 5 and 10 K.min^{-1}) and masses of 1-2 mg to reduce any heat transfer limitation. The Contact Point Model (Eq. 5.25) was fit simultaneously to both the conversion and rate data where applicable.

Unfortunately, the kinetics of the jar-mixed samples could not be studied easily. This is because part of the reaction occurred in the liquid phase (i.e. >1103 K) causing failure of the algorithm used in determination of the Advanced Isoconversional method.

5.3.6 Determination of NaOH recovery

For determination of the NaOH recovery a hydrolysis and titration procedure was employed. Products of thermal analysis were heated in 50 ml of deionized water at 368 K for 1 h under reflux while being mixed using a magnetic stirrer (PTFE King Scientific 35x6 mm) rotating at 60

rpm. The liquid portion was decanted into a 250 cm^3 volumetric flask with three 20 ml rinses and filled to the mark with deionized water. The solid products were dried in a desiccator for 72 h. A 50 ml portion of the solution was titrated using 0.01 $mol.l^{-1}$ HCl dosed by a Hanna instruments autotitrator while measuring the pH of the solution. Each 0.2 ml dose was administered upon pH stabilization which usually takes a few seconds. The peaks on a first-derivative pH vs. volume curve were used as indicators for the acid titration end-point(s) from which to calculate the number of moles of NaOH and the % NaOH recovery according to:

$$\%\ \text{NaOH recovered} = \frac{\text{moles NaOH}}{2 * \text{moles } CO_2 \text{ produced}} * 100 \qquad 5.27$$

5.4 Results and discussion

5.4.1 Na_2CO_3 (212-355 μm and 38-63 μm)

SEM images (Figure 5.4) reveal that Na_2CO_3 obtained from the 212-355 μm sieve fraction consisted of particles of irregular geometry. The majority of these were cuboids, conjoined at various angles to one another. At greater magnification, the surfaces of these crystals showed rough texture with <5 μm crystallite protrusions. Laser diffraction analysis revealed that more than 73 % by mass of the particles were between 200 and 500 μm in size (see Figure 5.6). The PSD has one major peak which occurred at 300 μm. The D[4,3] was 265 μm.

SEM images (Figure 5.5) for Na_2CO_3 obtained from the 38-63 μm sieve fraction show particles of 40-60 μm in diameter. Greater magnification revealed that these were agglomerates of conjoined cuboid crystals of 1-5 μm in length. The main peak in the PSD (see Figure 5.6)

occurred at 60 μm, but there were also less intense peaks at 10 μm and 600 nm. The D[4,3] was 34 μm, approximately 8 times lower than for the 212-355 μm fraction. BET surface areas were determined to be 0.6 $m^2.g^{-1}$ and 8.8 $m^2.g^{-1}$ for the 212-355 and 36-63 μm fractions respectively.

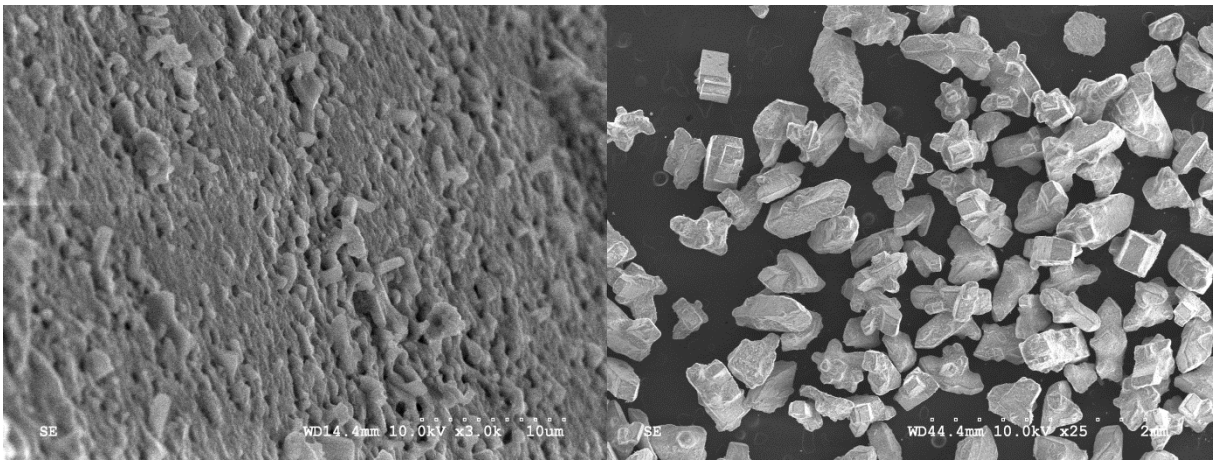

Figure 5.4 – SEM images for Na_2CO_3 from the 212-355 μm sieve fraction at two magnifications.

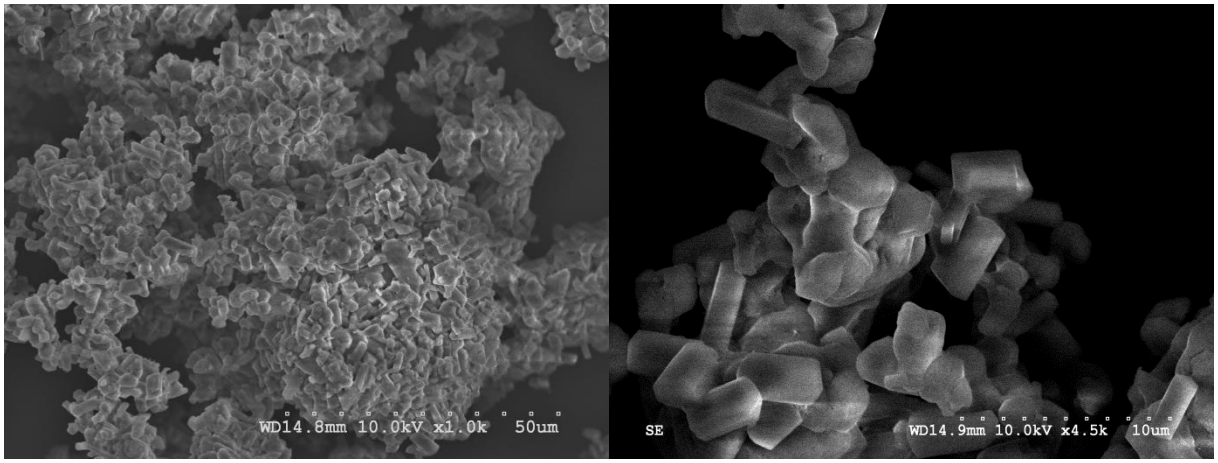

Figure 5.5 – SEM images for Na_2CO_3 from the 38-63 μm sieve fraction at two magnifications.

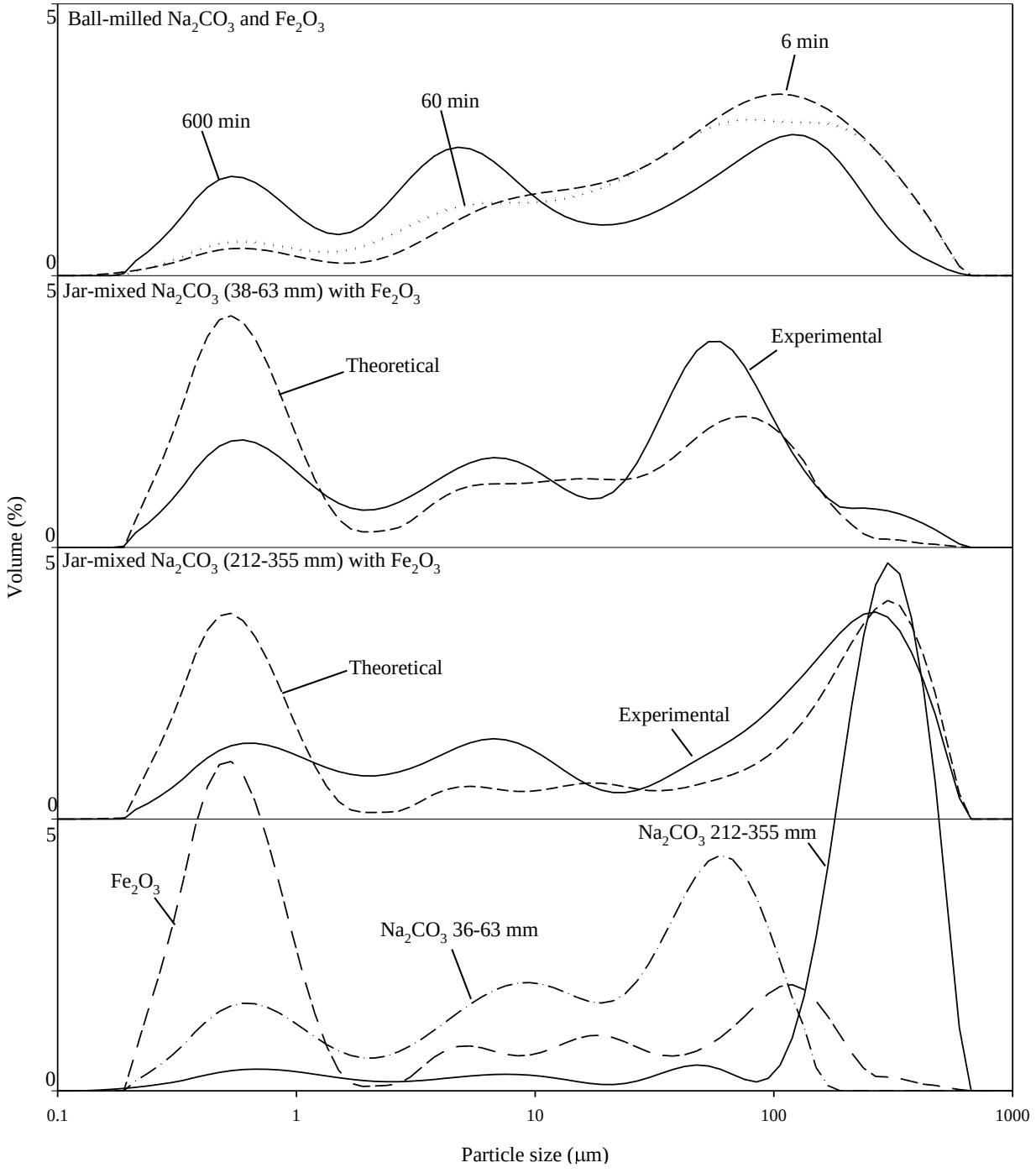

Figure 5.6 – Particle size distributions for Fe_2O_3 (<5 μm), Na_2CO_3 (212-355 and 38-63 μm) and their jar-mixed and ball-milled mixtures (1:1 mole ratio).

Thermogravimetric analysis was performed for each Na_2CO_3 sample at a heating rate of 20 $K.min^{-1}$. For the 212-355 μm fraction, mass loss began at 1088 K with a loss of 2.4 ±0.4 wt % by 1223 K, whereas for the 38-63 μm fraction, mass loss began at 1089 K with a loss of 2.1 ±0.5 wt % by 1223 K. There was only a small difference between the starting decomposition temperatures and weight losses for the two particle size fractions.

Few data are available on the thermal decomposition of Na_2CO_3. Some (Motzfeldt, 1955; Nakamura et al., 1980; Kim and Lee, 2001) have proposed that Na_2CO_3 decomposes in two consecutive steps – CO_2 loss followed by rapid vapourization of $Na_{(g)}$ and loss of $O_{2(g)}$:

$$Na_2CO_{3(s)} \rightarrow Na_2O_{(s)} + CO_{2(g)} \quad 5.28$$

$$Na_2O_{(s)} \rightarrow 2Na_{(g)} + 1/2O_{2(g)} \quad 5.29$$

Steinberg and Schofield (1991) suggest the following series of reactions

$$Na_2CO_{3(s)} \rightarrow Na_2O_{(s)} + CO_{2(g)} \quad 5.30$$

$$2Na_2O_{(s)} \rightarrow 3Na_{(g)} + NaO_{2(s)} \quad 5.31$$

L'vov (2001) proposes the following mechanism:

$$Na_2CO_{3(s)} \rightarrow Na_2CO_{3(l)} \rightarrow 2Na_{(g)} + 0.5O_{2(g)} + CO_{2(g)} \quad 5.32$$

In our tests, no product species were detected by XRD analysis, only Na_2CO_3. However, without a method for transferring and analyzing air sensitive compounds such as Na_2O and NaO_2 this is not surprising. Thermogravimetric analysis was repeated for the 38-63 μm fraction, but with a 200 min hold time at 1223 K (see Figure 5.7). The sample mass fell from 13.01 mg and

stabilized around 1.15 mg, corresponding to a total mass loss of 91.2 %. The stable mass after 160 min indicates that not all the solid sample decomposed into gaseous products. After removal of the sample from the furnace, a partially translucent material coated the bottom of the platinum pan. Between 25 and 160 min, the mass loss curve shows sharp changes, suggesting that sample was being ejected from the holder followed by recoil. Na_2CO_3 is liquid at these temperatures, and therefore pan motion could result in sample spilling from the pan. As a result, an accurate mass balance could not be performed for any of the reactions (Eq. 5.28-5.32). These observations have implications for determining conversion in reactions with Fe_2O_3 at high temperatures since some of the mass loss, albeit very little for the heating rates used here, could be due to gases

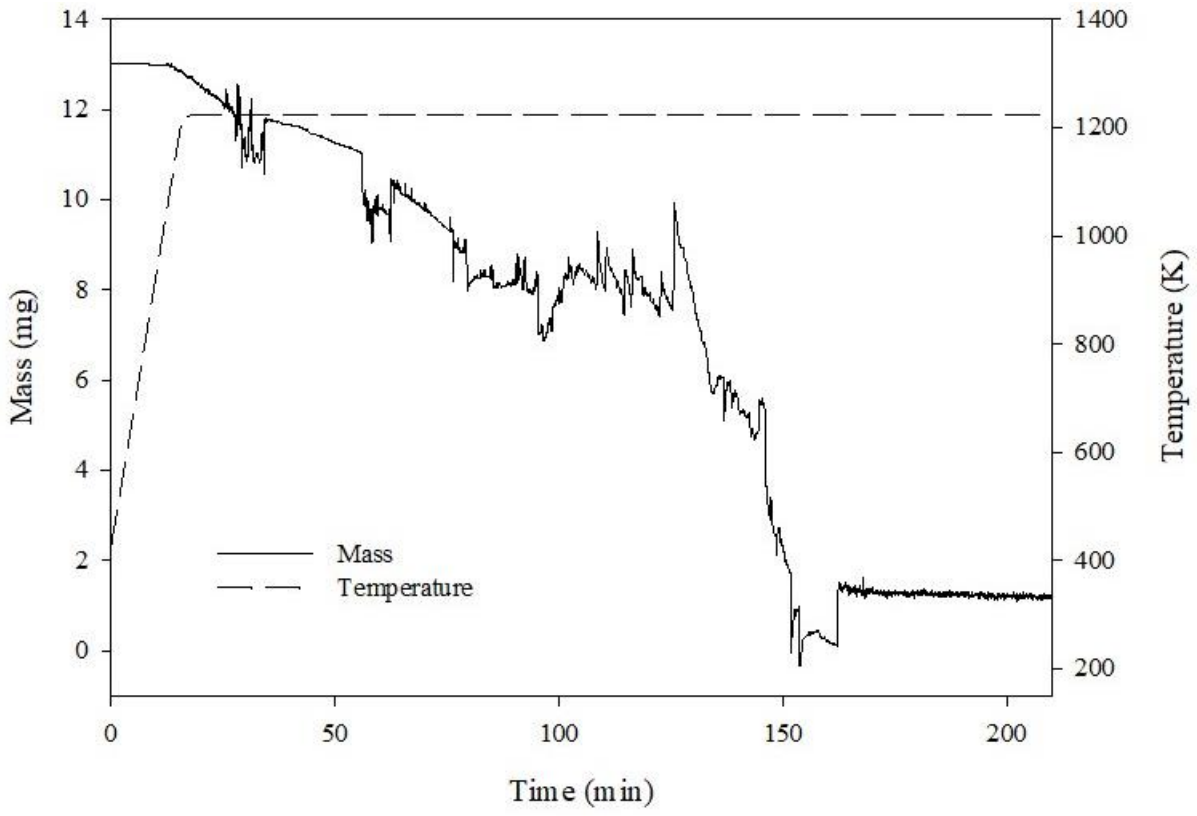

Figure 5.7 – Mass and temperature vs. time for thermal decomposition of Na_2CO_3 (38-63 μm).

other than CO_2. These findings also have implications for a DAC process with regeneration by direct causticization. Na vapour losses and subsequent equipment fouling would be detrimental to a Direct Air Capture process. Indeed, the pulp and paper industry have experienced problems with Na vapourization from Na_2CO_3 melts (Cameron, 1988). In the DARS process specifically, one way of dealing with this was to use higher mole ratios of Fe_2O_3 (Covey, 1984).

5.4.2 Fe_2O_3 (<5 µm)

A powder X-ray diffraction (XRD) pattern for the starting material gave peak matches with rhombohedral α-Fe_2O_3 (see Figure 5.10) The sample had a blood-red color typical of α-Fe_2O_3. When heating to 1223 K at a rate of 20 $K.min^{-1}$, no mass or colour change was observed, indicating that thermal reduction to Fe_3O_4 or FeO did not occur. After heating, all peaks could be matched with α-Fe_2O_3 suggesting that no crystalline phase change had occurred, or if it did, that it reverted to its original form upon cooling.

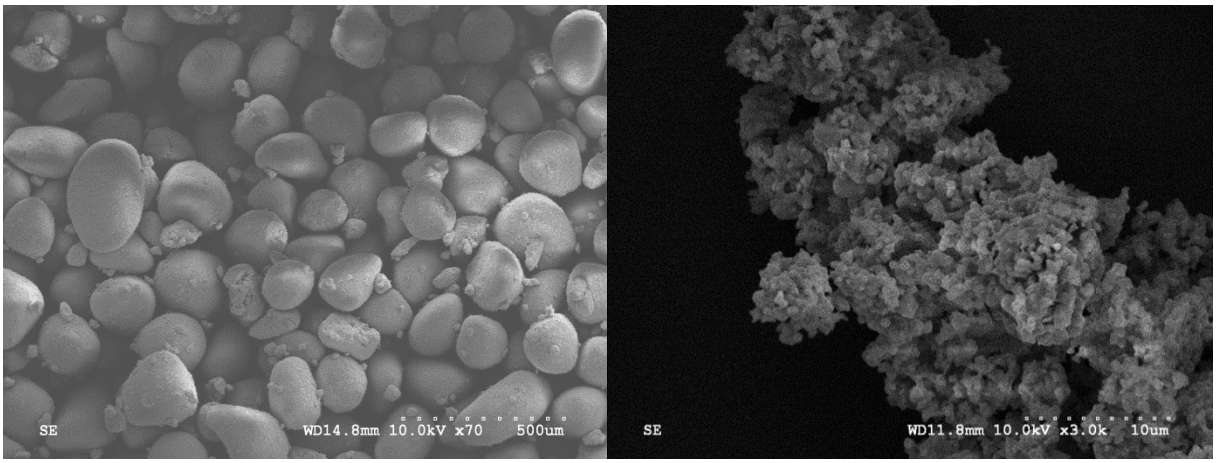

Figure 5.8 – SEM images for Fe_2O_3 (<5 µm) at two magnifications.

Figure 5.8 shows SEM images of Fe_2O_3 particles at two magnifications. The nanoparticles in the highest magnification image have a near-spherical geometry with diameters <1 μm. These particles formed rounded agglomerates with diameters between 50 and 200 μm. The BET surface area of these agglomerates was determined to be 5.31 $m^2.g^{-1}$.

According to the results of laser diffraction in Figure 5.6, >70 % by volume of the particles were distributed between 200 nm and 2 μm with a peak at 600 nm. There were also less intense peaks at 5, 17 and 115 μm. The De Brouckere Mean Diameter (D[4,3]) was 29.6 μm. Most of the particles lay between 200 nm and 2 μm, suggesting that the larger agglomerates seen in the SEM images broke apart when entrained in the gas stream entering the laser diffraction chamber. Indeed, it was observed that these agglomerates broke easily under slight pressure from the end of a spatula. These observations suggest that the agglomerates of Fe_2O_3 will break up during jar-mixing with Na_2CO_3.

5.4.3 Fe_2O_3 and Na_2CO_3 (jar-mixed)

5.4.3.1 Fe_2O_3 (<5 μm) and Na_2CO_3 (212-355 μm)

SEM images (Figure 5.9) for the jar-mixed sample containing the 212-355 μm Na_2CO_3 fraction show two types of particles: irregularly-shaped particles whose geometries resembled the original Na_2CO_3 and spherical agglomerates resembling the original Fe_2O_3 particles. The spherical particles had similar diameters. Pressing spherical particles with the end of a spatula broke them easily, revealing a dark-red interior, while pressing the irregular particles revealed white crystals of Na_2CO_3 which fractured under increased pressure. Analysis of N_2 adsorption isotherms give a BET surface area of 3.8 $m^2.g^{-1}$.

The experimental and theoretical particle size distribution (PSD) for the jar-mixed sample is shown in Figure 5.6. The theoretical PSD was calculated as a sum of the two component PSDs. Comparison of the experimental and theoretical PSDs showed that a large portion of the expected distribution, in the range 0.1-2 μm, which is largely due to the Fe_2O_3 component, has now shifted to the 2-16 μm and 30-240 μm ranges, corroborated by the results of SEM imaging in Figure 5.9. This is caused by agglomeration during mixing. Comparison of the theoretical and experimental PSD's reveal that there was a greater extent of coating on particles <300 μm than on particles >300 μm, an observation not obvious in SEM images.

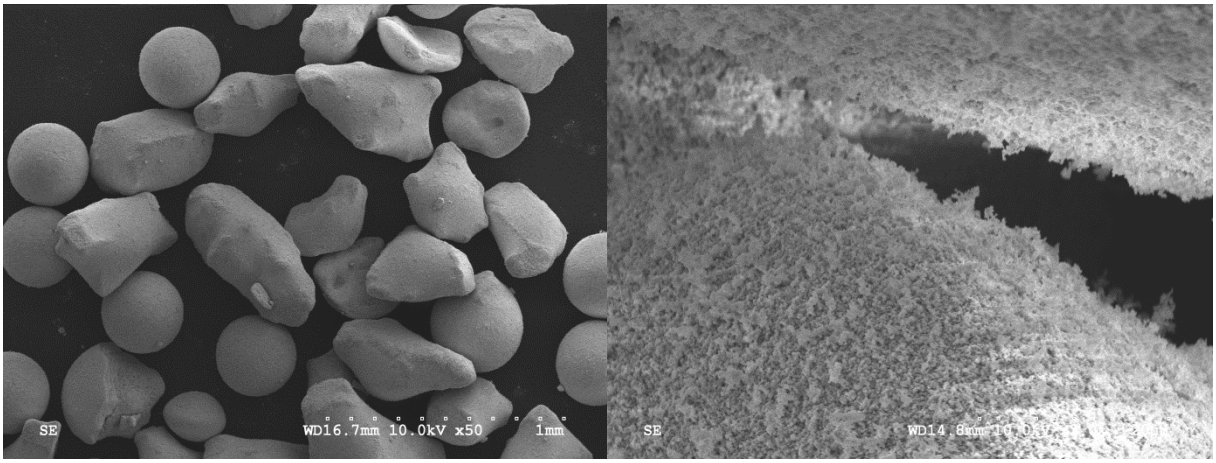

Figure 5.9 – SEM image for a 1:1 mole mixture of Fe_2O_3 (<5 μm) and Na_2CO_3 (212-355 μm) at two magnifications.

Three main parallel processes occur during jar-mixing including: i) Attrition of the initial Fe_2O_3 agglomerates caused by impacts with Na_2CO_3 particles and with the wall of the vessel; ii) Attachment of Fe_2O_3 nanoparticles to Na_2CO_3 surfaces, with the thickest coating occurring at the joints and recesses of the Na_2CO_3 crystals; and iii) Agglomeration into spheres of those Fe_2O_3 particles which failed to coat Na_2CO_3.

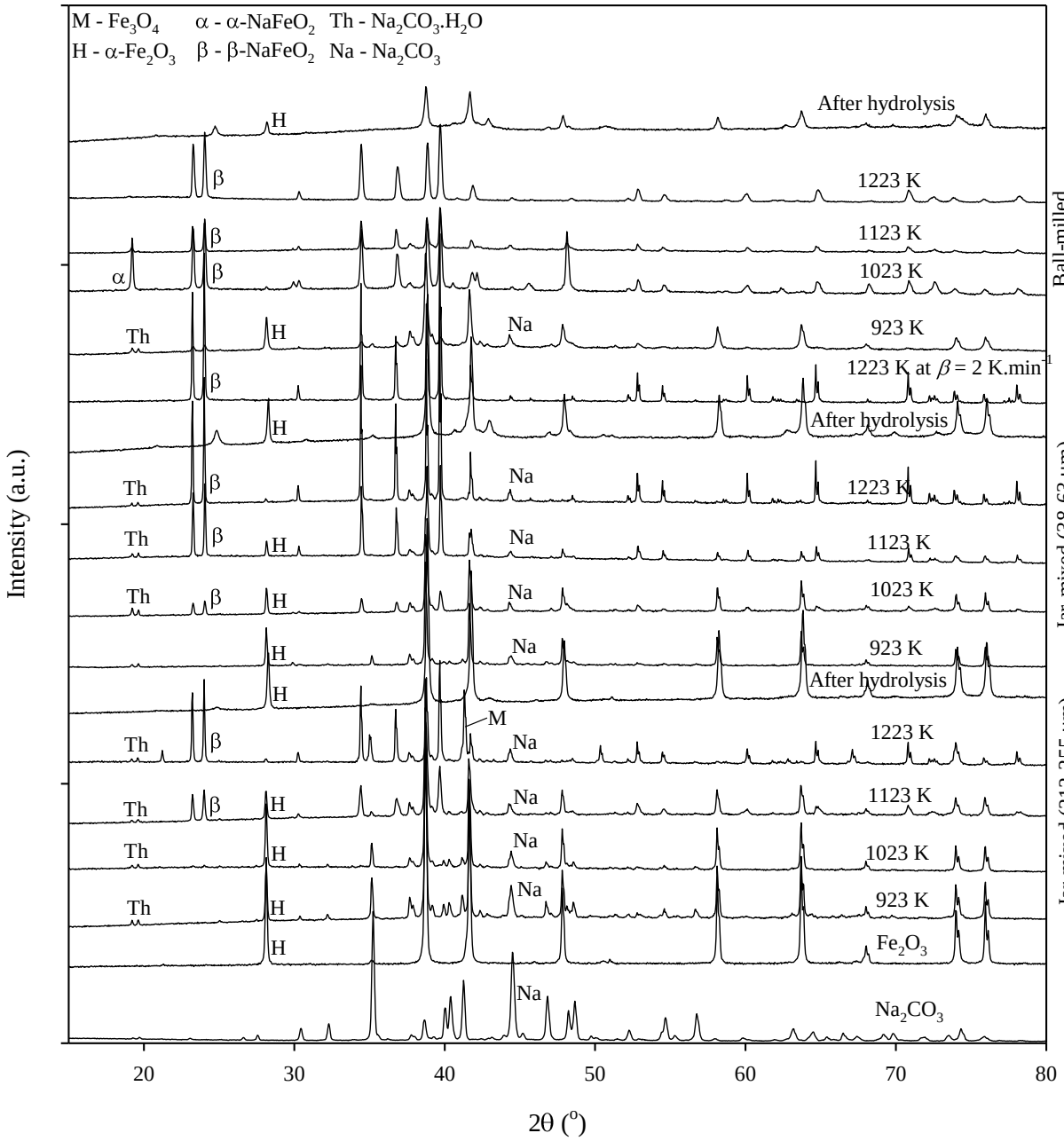

Figure 5.10 – X-ray diffraction patterns for untreated Fe_2O_3, Na_2CO_3, and their jar-mixed and ball-milled samples (1:1 mole ratio) after heating to different temperatures at a rate of 20 $K.min^{-1}$ (unless otherwise specified).

The mixture was heated at β=20 K.min^{-1} to 1250 K. X-ray diffraction data for the products of thermal analysis indicated that the only product was β-$NaFeO_2$, the orthorhombic form of sodium ferrite. Unreacted Fe_2O_3, Na_2CO_3 and $Na_2CO_3.H_2O$ were also present. Thus, the reaction appears to follow Eq. 5.1, in agreement with the literature (Covey, 1984).

Mass loss during thermal treatment of the mixture became noticeable around 810 K, continuing to the maximum temperature of the test (1223 K) (see Figure 5.11). At a heating rate of 20 K.min^{-1}, the reaction period was approximately 20 min in total. From the trend in the data, it is apparent that further mass loss would have continued beyond 1223 K. There was a peak in the rate data at 1111 K. Conversion according to Eq. 5.26 was 1.0 ± 0.8 % by 923 K, 3.4 ± 1.4 % by 1023 K, 43.6 ± 2.4 % by 1123 K and 55.7 ± 6.4 % by 1223 K. The sharp increase in the reaction rate at 1111 K was attributed by Covey (1984) to the rapid movement of Na_2CO_3 over the Fe_2O_3 surfaces near the melting point of Na_2CO_3. Prior to melting the reaction only occurs where Na_2CO_3 and Fe_2O_3 surfaces come into contact. SEM images (see Figure 5.9) show that when Na_2CO_3 particle size is large (212-355 μm) contact with Fe_2O_3 is limited.

Hydrolysis of the reaction products for 1 h gave a NaOH recovery of 93 %, suggesting that ~7 % of the Na was not extracted from the $NaFeO_2$ under the conditions used here. XRD patterns for the remaining solids showed peaks for hematite α-Fe_2O_3 (see Figure 5.10). Kiiskilä and Valkonen (1979) also found that hydrolysis goes to 90 % completion for mole ratios between $0.33 < Na_2CO_3/Fe_2O_3 < 1.5$. Nagano et al. (1974) reported similar values. This agrees well with the results for NaOH recovery in this work.

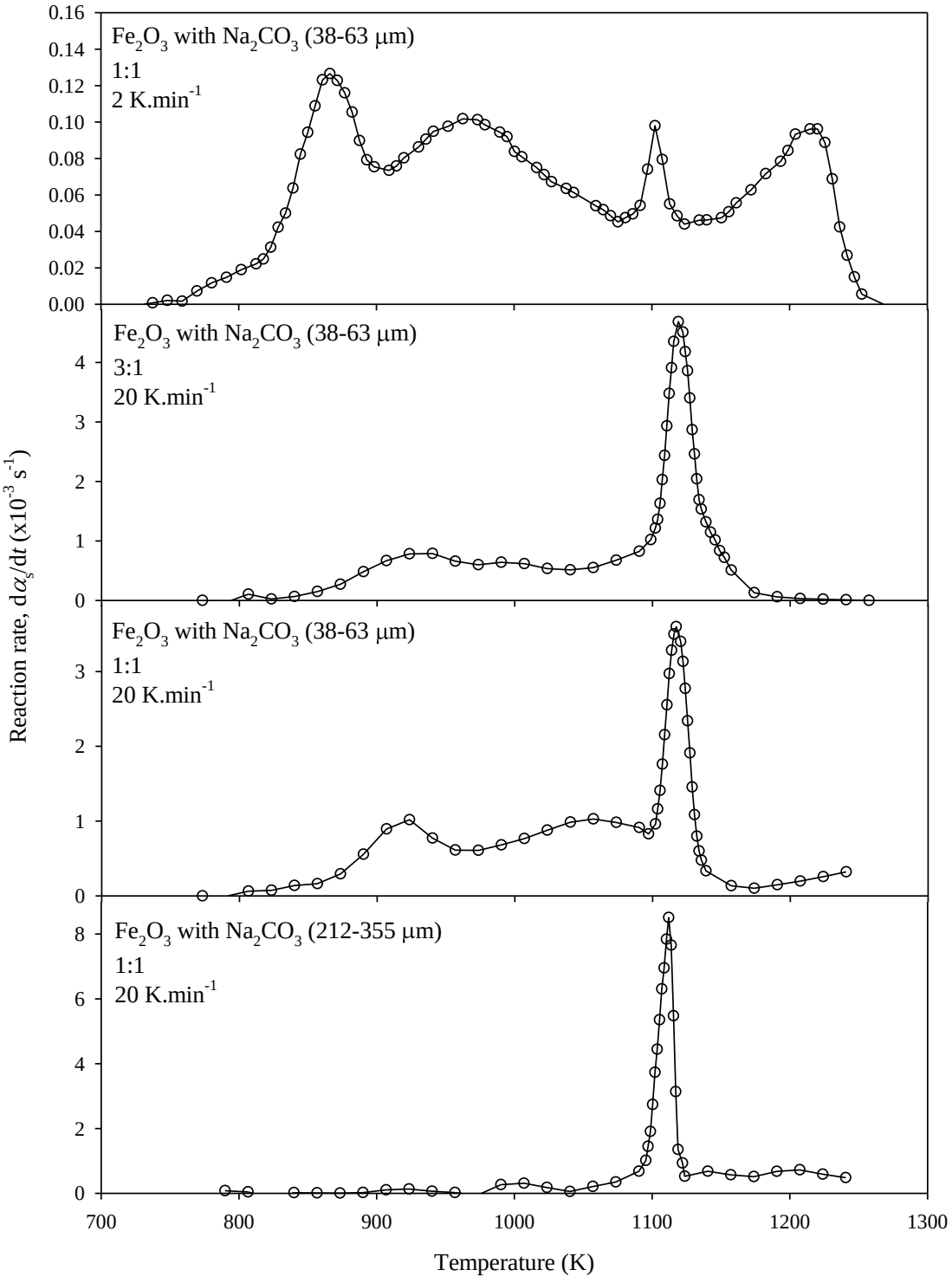

Figure 5.11 – Reaction rate vs. temperature for reaction of jar-mixed Fe_2O_3 (<5 μm) and Na_2CO_3 under different treatments.

5.4.3.2 Fe_2O_3 (<5 μm) and Na_2CO_3 (38-63 μm)

SEM images for the jar-mixed sample containing the 38-63 μm Na_2CO_3 fraction are shown in Figure 5.12. Fe_2O_3 nanoparticles only thinly coat the Na_2CO_3 on some surfaces, in contrast to the high percentage of surface coverage achieved for the mixture containing the 212-355 μm fraction.

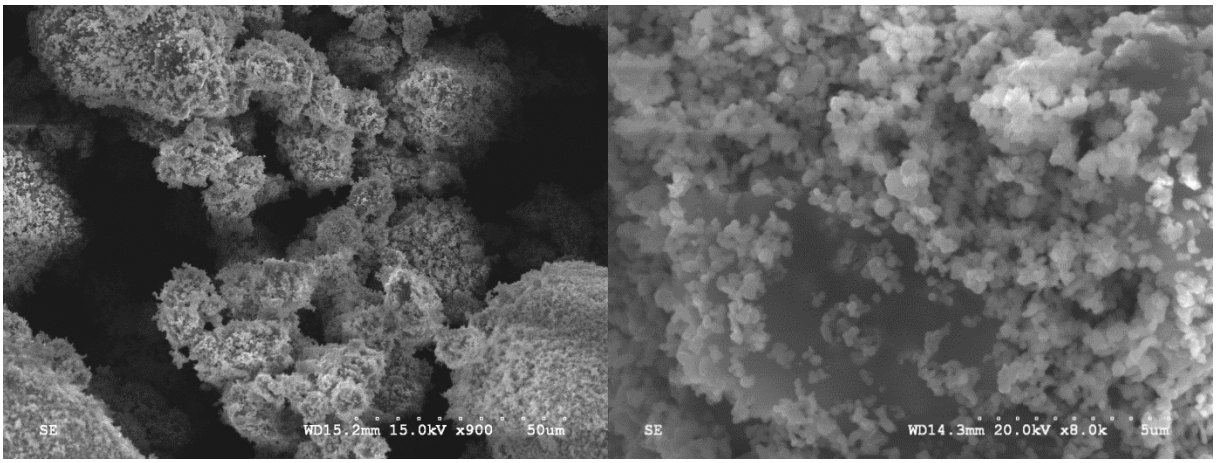

Figure 5.12 – SEM image for a 1:1 jar-mixed sample of Fe_2O_3 (<5 μm) and Na_2CO_3 (38-63 μm) at two magnifications.

Laser diffraction results are shown in Figure 5.6. The peak at 600 nm for the theoretical mixture, which is mostly due to a contribution from Fe_2O_3, is significantly reduced in intensity, while the portions between 2-10 μm and 25-100 μm, which are mostly due to Na_2CO_3, increased in intensity, suggesting that Na_2CO_3 clusters are becoming coated by Fe_2O_3 nanoparticles during mixing. The laser diffraction results correspond well with our analysis of the SEM images in Figure 5.12. Analysis of N_2 adsorption isotherms give a BET surface area of 6.4 $m^2.g^{-1}$ almost double that of the mixture studied in the previous section.

The reaction rate of the mixture varied considerably with temperature (Figure 5.11). Mass loss due to reaction occurred over a wide temperature range, beginning at approximately 773 K, and continued to the maximum temperature of the test (1223 K). At a heating rate of 20 $K.min^{-1}$ this means that the reaction period under study was 20 min in total. There were three peaks in the rate data at temperatures of 917 K, 1043 K and 1106 K, suggesting at least three overlapping reactions. Conversion according to Eq. 5.26 was 16.9 ± 1.4 % by 923 K, 39.5 ± 3.2 % by 1023 K, 80.3 ± 3.7 % by 1123 K and 88.8 ± 3.7 % by 1223 K.

As expected, the mixture containing the 38-63 μm fraction was more reactive than the mixture containing the 212-355 μm fraction. For example, conversion of the mixture containing Na_2CO_3 (38-63 μm) was approximately 17 times greater (at 923 K) and 1.6 times greater (at 1223 K) than the mixture containing the Na_2CO_3 (212-355 μm). Thus, smaller Na_2CO_3 particles resulted in large increases in the reaction rate. This strongly suggests that the reaction rate is a function of the number of contact points, which itself is a function of particle size and the degree of mixing (Povarov and Sokolova, 2009). Indeed, Kiiskilä and Valkonen (1979) have previously pointed out that the reaction is very sensitive to the degree to which Fe_2O_3 and Na_2CO_3 are inter-mixed.

Colour changes were observed as the reaction progressed (Figure 5.13). The initial mixtures were blood-red at room temperature due to Fe_2O_3 and remained so until ~920 K. By 1023 K the products were predominantly mustard-yellow; by 1123 K, the smaller particles were muddy-green, and by 1223 K, black and light-to-dark brown. The products also appear to have sintered. Knick and Kohlmeyer (1940) described the colour of products of mixtures rich in Fe_2O_3 as a mixture of dark grey-blue and yellow-green, whereas products of mixtures poor in Fe_2O_3 were

described as brown. Products of the DARS research plant were usually grey-green (Covey, 1984).

Figure 5.13 – Photographic images of jar-mixed Fe_2O_3 (<5 μm) and Na_2CO_3 (38-63 μm) at 298 K (red), and after heating to 1023 K (yellow), 1123 K (green) and 1223 K (dark-brown).

Peaks in the XRD patterns due to Fe_2O_3 were detectable at all temperatures. Peaks due to Na_2CO_3 were visible until 1123 K, but negligible at 1223 K. By 923 K, there was insufficient conversion for products to become detectable by XRD. At 1023 K, 1123 K and 1223 K, β-$NaFeO_2$ was detectable, with the intensity of the peaks increasing with temperature.

Below 1073 K, there were at least two reactions occurring - one with a peak at 917 K and the other with a peak at 1042 K (see Figure 5.11). This is most likely explained by an initial reaction at Fe_2O_3 to Na_2CO_3 contact points, followed by diffusion processes. The sharp peak in the rate at 1100 K is due to increased mobility of Na_2CO_3 nearing its melting point of 1124 K. At this temperature, near-molten Na_2CO_3 can rapidly diffuse over Fe_2O_3 surfaces which were not yet reached by solids diffusion. At temperatures greater than the melting point, the reaction rate increases again. The likely mechanism here is decomposition of Na_2CO_3 according to

mechanisms discussed in Section 5.4.1. Some $Na_{(g)}$ could be swept away by the purge gas while some could react further with Fe_2O_3 surfaces.

Hydrolysis of the reaction products at 393 K gave a NaOH recovery of 93 %, which was the same as the mixture containing 212-355 μm Na_2CO_3. Thus, the reduction in Na_2CO_3 particle size, although resulting in much higher conversion, did not significantly change the recovery of NaOH.

Covey (1984) suggested that the reaction is sensitive to the initial mole ratio below the melting point. To test this suggestion, 1 mole of Na_2CO_3 (38-63 μm) was combined with 3 moles of Fe_2O_3, jar-mixed and then given the same thermal treatment as the 1:1 mixture. SEM images confirm that Na_2CO_3 surfaces were not visible, as they were completely coated by Fe_2O_3 (Figure 5.14). This is unlike the 1:1 mixture where Na_2CO_3 surfaces were clearly visible in the SEM images.

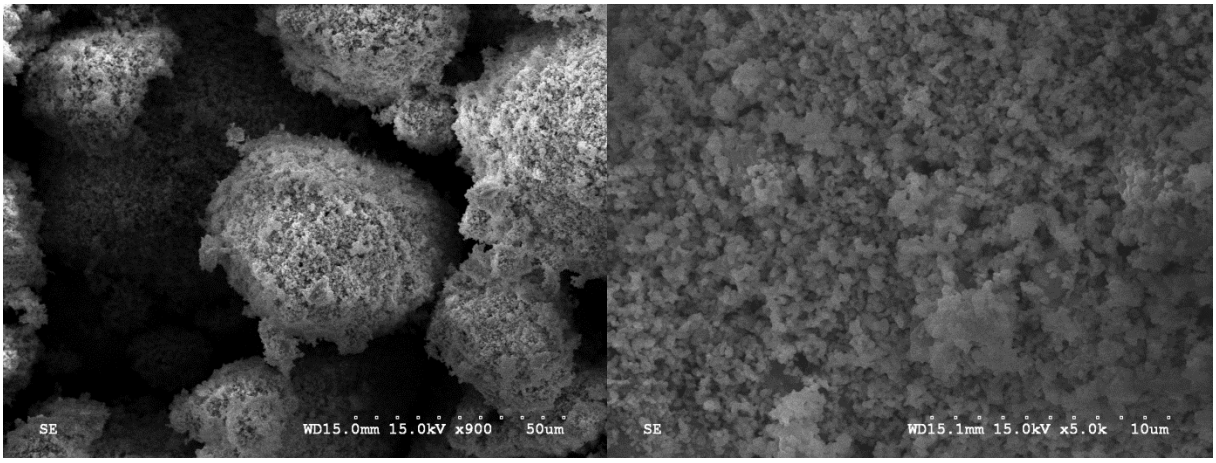

Figure 5.14 – SEM image jar-mixed Fe_2O_3 (<5 μm) and Na_2CO_3 (38-63 μm) (3:1 mole ratio), at two magnifications.

Mass loss for the 3:1 mixture commenced at approximately 800 K, with peaks in the rate at 916 K and 1106 K (see Figure 5.11). Mass loss discontinued at 1176 K suggesting that the reaction was complete. XRD data (Figure 5.10) shows the only reaction product at 1223 K was β-$NaFeO_2$. Conversion according to Eq. 5.26 was 100.9 ± 1.0 % by 1176 K. This is in contrast to the 1:1 mixture where total conversion was just 88 % by 1223 K.

Increasing the Fe_2O_3:Na_2CO_3 mole ratio from 1:1 to 3:1 had little effect on the reactivity of the mixture at temperatures below 1023 K. For example, conversion according to Eq. 5.26 was 16.9 ± 1.4 % by 923 K and 39.5 ± 3.2 % by 1023 K for the 1:1 mixture and 16.0 ± 3.2 % by 923 K and 38.2 ± 3.0 % by 1023 K for the 3:1 mixture. Thus, the reactivity slightly decreased at lower temperatures, despite the increased availability of Fe_2O_3. This is because the reaction rate is limited by the available Na_2CO_3 surface area. At these particle sizes, excess Fe_2O_3 increases the number of Fe_2O_3-Fe_2O_3 contacts but does not significantly increase the number of Fe_2O_3-Na_2CO_3 contacts. In addition, a thicker coating of Fe_2O_3 might suppress the forward decomposition by increasing the barrier to diffusion of CO_2 away from the sample. This finding contradicts Covey's suggestion that increasing the Fe_2CO_3:Na_2CO_3 mole ratio would always increase the reaction rate below the melting point. As the Na_2CO_3 begins to melt, the presence of a large excess of Fe_2O_3 enables the reaction to reach completion whereas the stoichiometric mixture could not.

Thermal analysis of the 1:1 mixture was also performed at a heating rate of 2 $K.min^{-1}$. The reaction began at about 723 K and reached completion by 1253 K (see Figure 5.11) giving a total reaction time of 265 min, which is comparable to the time for which pure Na_2CO_3 was held

isothermally at 1223 K (see Figure 5.7). All peaks in the XRD pattern were well matched by β-$NaFeO_2$ and no peaks due to Na_2CO_3 or Fe_2O_3 were detected (see Figure 5.10). The total conversion, according to the reaction described by Eq. 5.1 was 100.1 %. If $Na_{(g)}$ losses had been significant, then conversion determined according to Eq. 5.1 would be substantially greater than 100.1 %. This means that our assumption of negligible $Na_{(g)}$, $O_{(g)}$ and $O_{2(g)}$ loss in the presence of an equimolar quantity of Fe_2O_3 is reasonable.

The reaction rate of jar-mixed samples of Fe_2O_3 and Na_2CO_3 has been shown to depend on time, temperature, conversion, particle size and the initial mole ratio. Na_2CO_3 reacts with Fe_2O_3 as a solid and liquid forms, and at higher temperatures it may also react in the gaseous state. Reducing Na_2CO_3 particle size from 212-355 μm to 38-63 μm via simple hand-grinding, prior to mixing by jar-mixing, gave large increases in the reactivity of Fe_2O_3-Na_2CO_3 mixtures owing to increased contact between reactants. Further particle size reduction, achieved by mechanical grinding for example, could bring about even greater increases in reactivity. In the next section ball-milling is employed as a means to achieve simultaneous particle size reduction and thorough mixing.

5.4.4 Fe_2O_3 and Na_2CO_3 (ball-milled)

There have been no investigations into the thermal treatment of ball-milled mixtures of Fe_2O_3 and Na_2CO_3, although others (Kosmac and Courtney, 1992; Zdujić et al., 1999; Šubrt et al., 2000; Randrianantoandro et al., 2001) have shown chemical transformations of pure Fe_2O_3 during ball-milling in specific gaseous environments or after long milling times. Randrianantoandro et al. (2001) found that ball-milling transformed α-Fe_2O_3 into nanostructured

powders of maghemite (λ-Fe_2O_3). Zdujić et al. (1999) found that prolonged ball milling (>24 h) reduced α-Fe_2O_3 to Fe_3O_4 in an air-sealed container, but that at a certain oxygen partial pressure within the canister, milling facilitated the reverse process. It is thought (Kosmac and Courtney, 1992) that continued milling transformed α-Fe_2O_3 to FeO. Nakatani and Matsuoka (1983) showed that λ-Fe_2O_3 transforms into Fe_3O_4 more rapidly than α-Fe_2O_3. Šubrt et al. (2000) found that, after 70 h of milling, goethite samples were completely transformed into spherical hematite particles, with a narrow particle size distribution around a mean of ∼17 nm.

5.4.4.1 Ball-milling duration

A mixture of Fe_2O_3 (<1 μm) and Na_2CO_3 (212-355 μm) (1:1 mole ratio) was milled for durations of 6, 60 and 600 min. XRD studies indicated that peaks due to Fe_2O_3, Na_2CO_3 and $Na_2CO_3.H_2O$ broadened with increased milling time which is a consequence of the Scherer effect. No other species were detected, indicating that the reagents were chemically unchanged, even after 600 min of ball-milling. BET surface areas were 4.0, 4.0 and 8.6 $m^2.g^{-1}$ for the 6-, 60- and 600-min ball-milled samples, respectively. Thus, increasing the milling time from 6 to 60 min had little effect on the surface area, but increasing to 600 min more than doubled the surface area.

SEM images for the mixtures are seen in Figure 5.15. Na_2CO_3 particles are visible in images of the 6- and 60-min mixtures, but Fe_2O_3 and Na_2CO_3 species became indistinguishable from one another in the image for the 600 min sample. This indicates that the Na_2CO_3 particle size was significantly reduced after 600 min of ball-milling. There was no obvious difference in the size

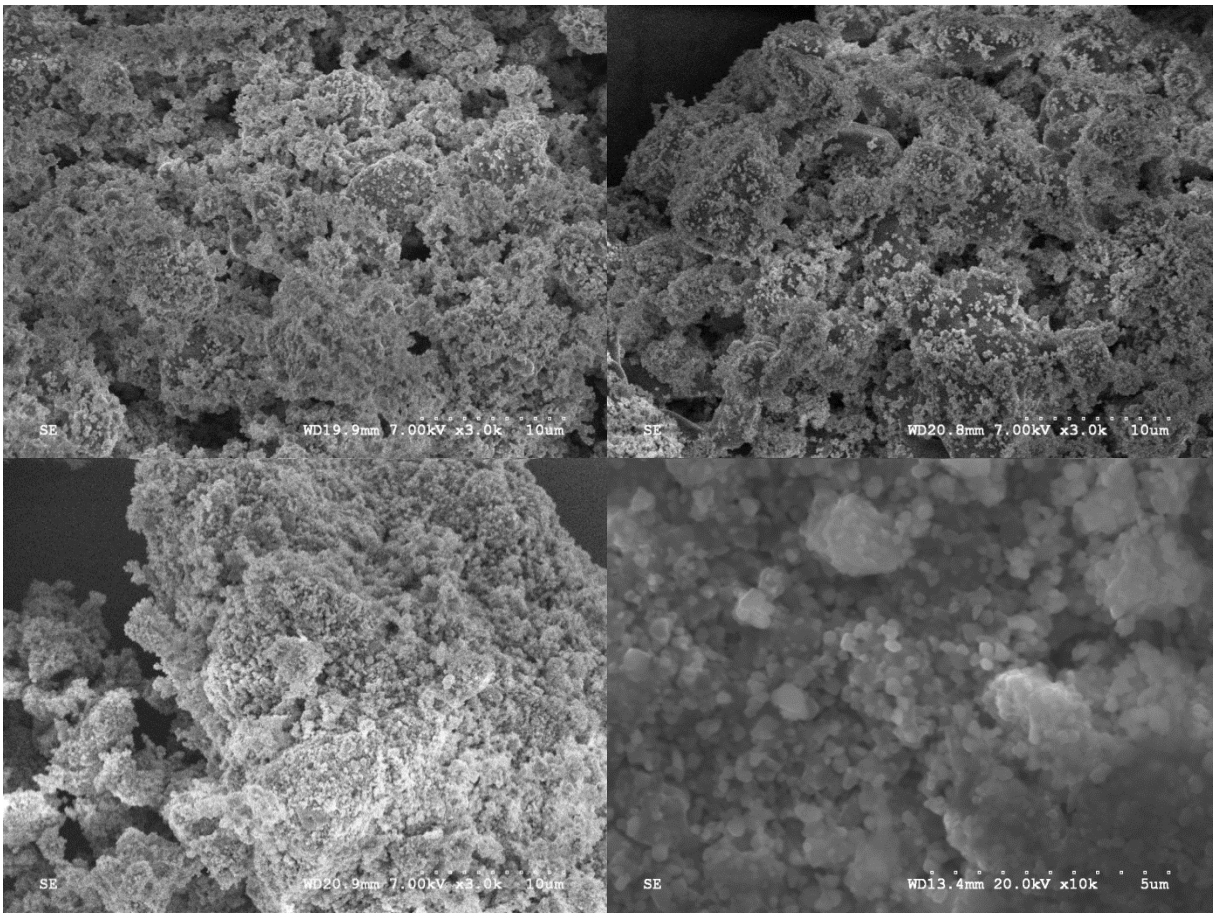

Figure 5.15 – SEM images for mixtures of Fe_2O_3 and Na_2CO_3, in a 1:1 mole ratio, ball-milled for 6 min (top-left), 60 min (top-right), 600 min (bottom-left), and 60 min followed by pelletization (bottom-right).

of Fe_2O_3 particles after 6 and 60 min of ball-milling compared to the starting reagent. Most of the size reduction occurred for the Na_2CO_3 because this reagent had much greater initial particle size and the more-than-double-surface-area of the 600 min sample is therefore primarily a result of Na_2CO_3 size reduction. The 600 min sample exhibited less macro- and meso-porosity than the 6- and 60-min samples, suggesting that some packing had occurred during particle size

reduction. The 6 and 60 min samples show similar PSDs, while the 600 min sample shows greater intensity for peaks at 0.5 and 5 μm (see Figure 5.6).

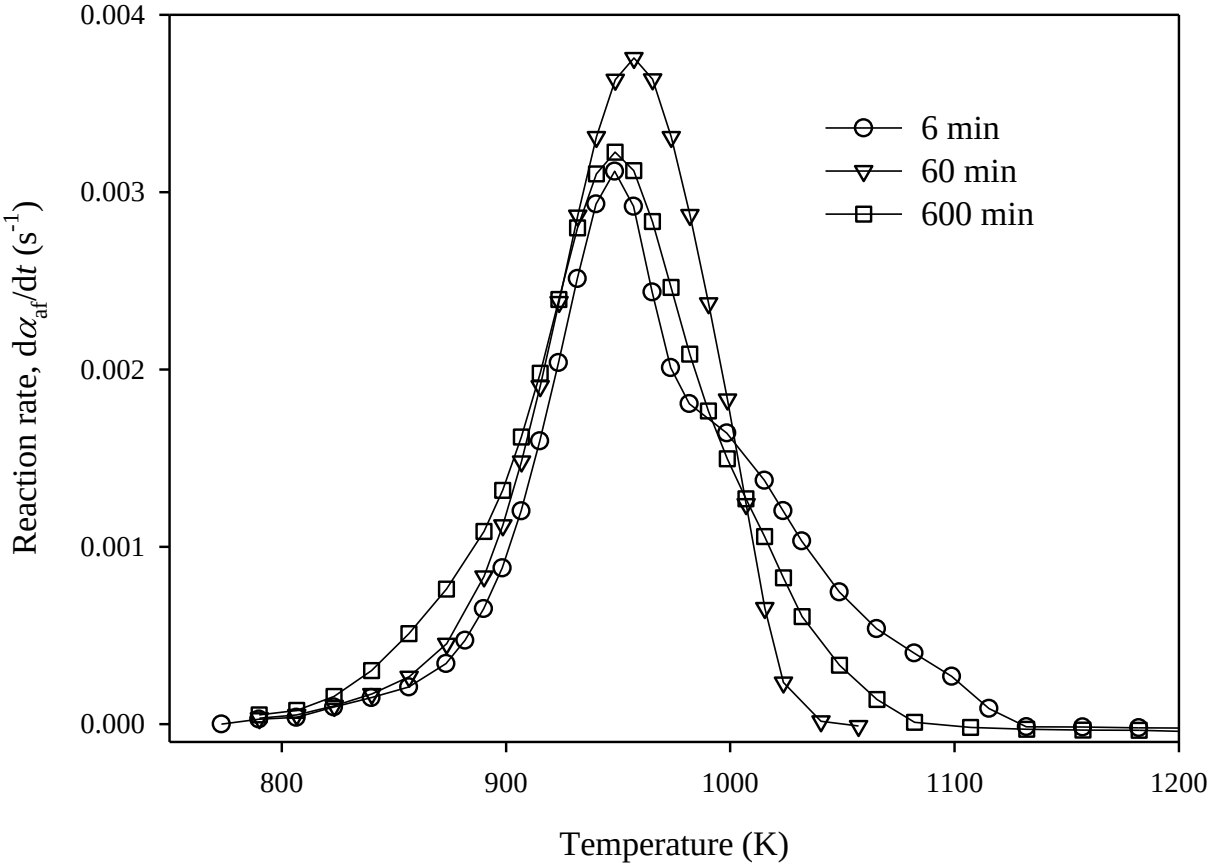

Figure 5.16 – Reaction rate vs. temperature for thermal treatment (β=20 K.min^{-1}) of mixtures of Fe_2O_3 and Na_2CO_3 ball-milled for 6, 60 and 600 min.

The rate data for the three samples are shown in Figure 5.16. The mixture which was milled for 600 min has a higher initial rate of reaction between 800-900 K, than mixtures milled for 6 and 60 min. This is mainly because the particles in the sample, particularly those of Na_2CO_3, are smaller (as seen in SEM images Figure 5.15), leading to increased degree of contact with Fe_2O_3 surfaces, which enables a higher reaction rate. SEM images also show that the mixture which

was milled for 600 min is more compact than the others. Increased compactness is another factor leading to increased contact and higher initial reaction rate. Unexpectedly, the mixture which was milled for 60 min reaches completion before the 600 min mixture, despite reduced particle size and higher compaction. This is primarily because CO_2 diffusion also controls the rate. A greater degree of compaction creates a larger barrier for CO_2 diffusion, leading to accumulation of CO_2 and increase in the rate of the reverse reaction. As shown in the previous chapter (Figure 4.1), CO_2 accumulation is proportional to the forward rate and therefore retards the reactions more at the moderate to high conversions.

5.4.4.2 Initial mole ratio and CPM fits

Figure 5.17 shows reaction rate vs. temperature data for ball-milled mixtures of Fe_2O_3 and Na_2CO_3 at different mole ratios. Rate data for the jar-mixed sample of Fe_2O_3 (<5 um) and Na_2CO_3 (212-355 μm) (1:1 mole ratio) is also shown for comparison. The ball-milled mixture is fully reacted below 1000 K, whereas the jar-mixed sample only reaches a conversion of 56 % by the end of the test. This is because the rate is limited by the number of Fe_2O_3 to Na_2CO_3 contact points. Ball-milling reduced the particle size and increased the number of contact points thus increasing the reaction rate. Hydrolysis of the reaction products of the 1:1 mole ratio mixture gave a NaOH recovery of 95 %, suggesting that ~5 % of the Na was not extracted from the $NaFeO_2$ under the conditions used here. XRD patterns for the remaining solids showed peaks for hematite α-Fe_2O_3 (see Figure 5.10). The recovery of NaOH was therefore slightly higher for ball-milled samples than jar-mixed ones, likely due to a higher surface area leading to increased rate of mass transfer during hydrolysis.

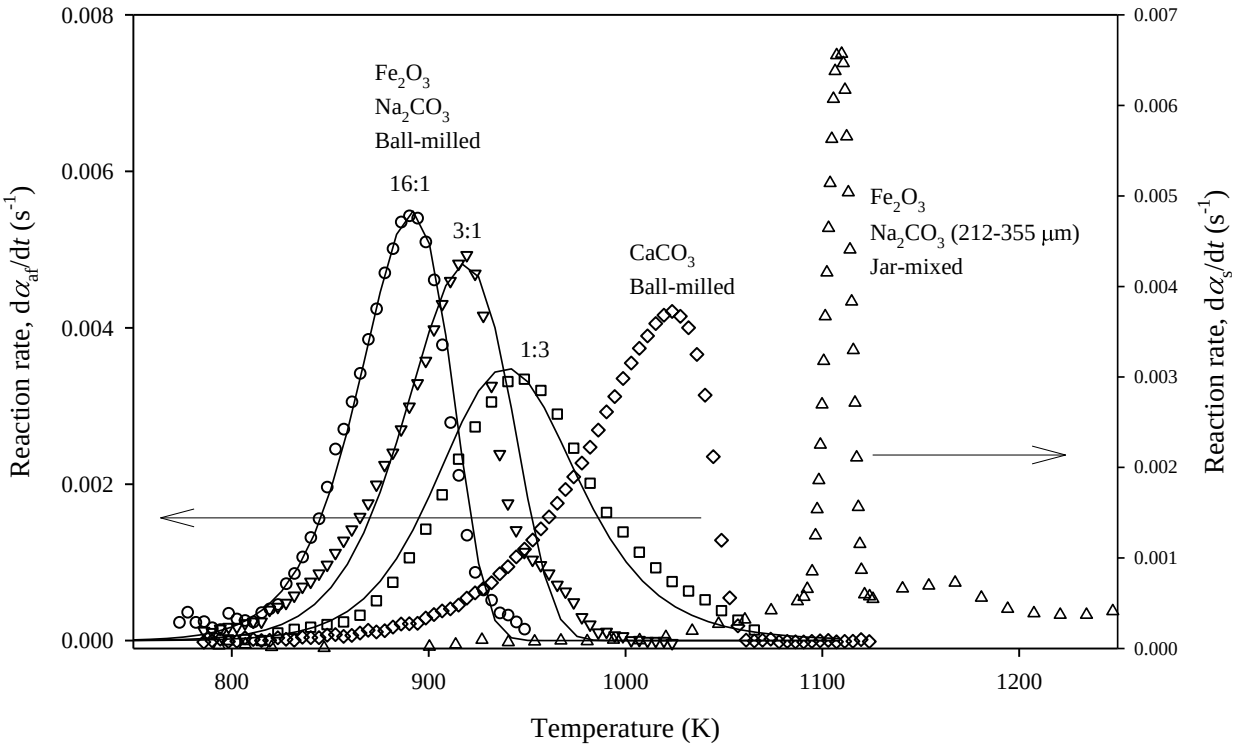

Figure 5.17 – Reaction rate vs. temperature for thermal treatment (β=20 K.min^{-1}) of ball-milled Fe_2O_3 and Na_2CO_3 at different mole ratios. Solid lines show the Contact Point Model fits. Also shown is $CaCO_3$ decomposition rate data (the sample mass is varied such that the total no. of moles of CO_2 lost is approximately the same for each reaction).

Rate data for decomposition of $CaCO_3$ is also shown in Figure 5.17. For the 1:1 ball-milled mixture of Fe_2O_3 and Na_2CO_3, all CO_2 has been released below 1000 K whereas $CaCO_3$ is not fully decomposed until 1060 K. This is a good indication that, with the appropriate pre-treatment, the hematite process can regenerate NaOH for Direct Air Capture at a lower temperature than that of the lime process. The rate data at different mole ratio were well fit by Fătu's (1988) Contact Point Model (CPM) (solid lines in Figure 5.17). The parameters used in the fitting are provided in Table 5.2.

Table 5.2 – Constants used in fitting of Contact Point Model.

Parameter	Symbol	Unit	Value
Radius of Na_2CO_3	r_A	m	1e−5
Radius of Fe_2O_3	r_B	m	1e−7
Density of Na_2CO_3	ρ_A	$kg.m^{-3}$	5.24e3
Density of Fe_2O_3	ρ_B	$kg.m^{-3}$	2.27e3
Density of $NaFeO_2$	ρ_C	$kg.m^{-3}$	4.33e3
Activation energy	E	$kJ.mol^{-1}$	278
Compaction factor	γ	-	1
Contact width	h_c	m	1e−9
Pre-exponential factor of nucleation	P_0	s^{-1}	6e12
Number of nuclei in unit surface	n_s	m^{-2}	4e12
Mole mass of Na_2CO_3	M_A	$kg.mol^{-1}$	0.10599
Mole mass of Fe_2O_3	M_B	$kg.mol^{-1}$	0.15969
Mole mass of $NaFeO_2$	M_C	$kg.mol^{-1}$	0.11083
Heating rate	β	$K.s^{-1}$	0.333
Initial temperature	T_o	K	673

The approximate densities, particle sizes and mole ratios of the actual samples were used in the model. An estimate for the activation energy of 278 $kJ.mol^{-1}$ was obtained from Colović et al. (1994). The pre-exponential factor of nucleation, P_0, was adjusted until the simulated data matched the experimental data. The rate curves at different mole ratio were fit simultaneously. The good agreement across all the data is evidence of the validity of the CPM. The CPM is derived assuming the rate-limiting step is nucleation of $NaFeO_2$ in the surface area of contact between the two reagents. The CPM accounts for the change in the mean particle radius as the reaction progresses, as well as the decreasing number of contact points with increasing conversion. At mole ratios of 1:1 the CPM estimates that 70 Fe_2O_3 particles surround each Na_2CO_3 particle which is an estimate in reasonable agreement with the SEM images (see Figure 5.15).

Increasing the Fe_2O_3 fraction of the mixture lowered the temperature of the process and increased the amplitude of the rate curve. For example, at a mole ratio of 16:1, T_i ~ 800 K, T_{max} ~ 890 K and T_f ~ 950 K whereas at a mole ratio of 1:3, T_i ~ 810 K, T_{max} ~ 940 K and T_f ~ 1060 K. The reason for this is that Fe_2O_3 is the rate limiting reactant and the loss of CO_2 from the sample cannot proceed without a sufficient contact with Fe_2O_3 to enable its decomposition. Points of contact between Fe_2O_3 to Fe_2O_3, and Na_2CO_3 to Na_2CO_3 are unreactive. Only the number of contact points between Fe_2O_3 and Na_2CO_3 are reactive. If a Na_2CO_3 particle was of a size such that it was surrounded by 12 particles of Fe_2O_3, then a 16:1 mole ratio would mean that all 12 of these particles were Fe_2O_3 and not Na_2CO_3, assuming perfect mixing. Thus, high Fe_2O_3 fraction leads to large numbers of Fe_2O_3 to Na_2CO_3 points of contacts and highly reactive mixtures. This can be simulated by decreasing the parameter q in Eq. 5.19. As q approaches 0, Na_2CO_3 approaches infinite dilution, and the reactivity of the system increases.

If the CPM is indeed a complete description of these reactions, then the isoconversional activation energy, E_α, should be constant for different mole ratios and give a good estimate of the intrinsic energy barrier for nucleation which is approximately constant with increasing conversion, α. In order to determine E_α, conversion data are needed at three or more different

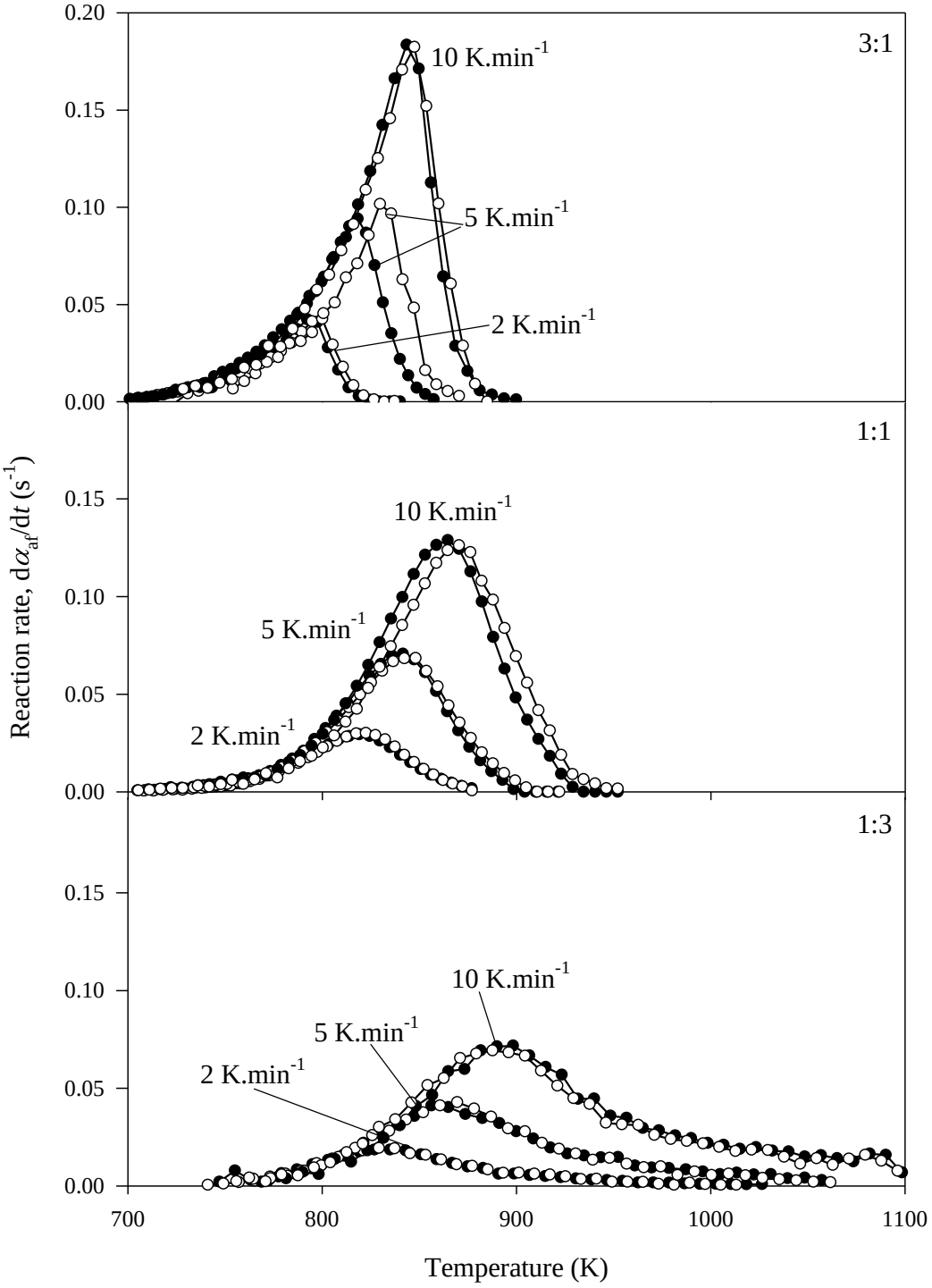

Figure 5.18 – Reaction rate vs. temperature for ball-milled mixtures of Fe_2O_3 and Na_2CO_3 in different mole ratios, at β=2, 5 and 10 K.min^{-1}, with two repeats at each heating rate.

heating rates. Figure 5.18 shows the reaction rate vs. temperature data for mixtures of Fe_2O_3 and Na_2CO_3 in mole ratios of 3:1, 1:1 and 1:3 at β=2, 5 and 10 K.min^{-1}. Figure 5.19 shows the isoconversional activation energy vs. conversion for these same mixtures.

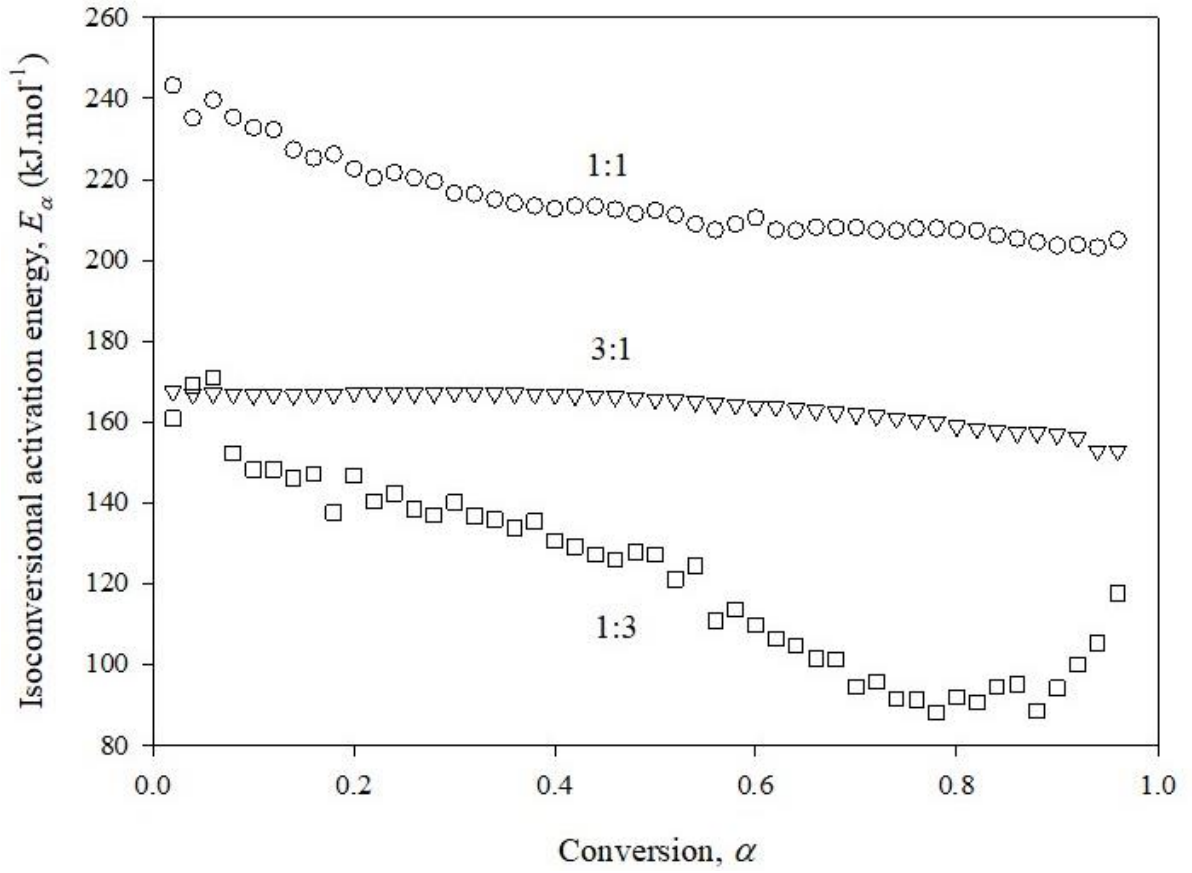

Figure 5.19 – Isoconversional activation energy vs. conversion for reaction of ball-milled Fe_2O_3 and Na_2CO_3 with different mole ratio.

In Figure 5.19, it is observed that E_α is not independent of the mole ratio, and neither is it constant with conversion, α. For a 1:1 mole ratio, E_α is ~240 kJ.mol^{-1} at α=0.96, falling to 210 kJ.mol^{-1} at α=0.96. For a 3:1 mole ratio, E_α is ~170 kJ.mol^{-1} at α=0.96, falling to 160 kJ.mol^{-1} at

α=0.96. For a 1:3 mole ratio, E_α is ~170 kJ.mol^{-1} at α=0.96, falling to 90 kJ.mol^{-1} at α=0.80, before rising again to ~120 kJ.mol^{-1} at α=0.96.

Clearly, these reactions are more complex than suggested by the Contact Point Model. Povarov and Sokolova (2009) who studied this reaction at low conversion (α <0.5) also found that the highest estimate for E_α was obtained at the stoichiometric ratio of the starting reagents but offer no explanation for this finding. The Contact Point Model assumes that only nucleation is rate limiting. However, it is likely that CO_2 diffusion is also controlling the rate. Indeed, the decrease in E_α with increasing α in all three cases is reminiscent of the decrease seen in the E_α with increasing α for decomposition of $CaCO_3$ which was proposed to be due to the temperature effect on the reversible kinetics in the presence of CO_2. It was also shown in the previous chapter that, different $CaCO_3$ sample mass and particle size were found to change the values of E_α. Thus, the most probable explanation for the difference in E_α at different mole ratios is the different rates of CO_2 accumulation which are a result of the physical and chemical properties such as sample porosity, density, surface area and mole ratio.

5.4.4.3 Initial sample mass and pelletization

Reaction rate vs. temperature data for ball-milled mixtures of Fe_2O_3 and Na_2CO_3 is shown in Figure 5.20 for two different sample masses. Increasing the mass from 10 to 30 mg increased T_{max} by ~70 K and T_f by ~40 K. Larger mass increases the rate of inter- and intra-particle CO_2 accumulation, which in turn increases the rate of the reverse reaction. More discussion of this accumulation effect can be found in Sections 4.2 and 4.5.2 in relation to $CaCO_3$ decomposition.

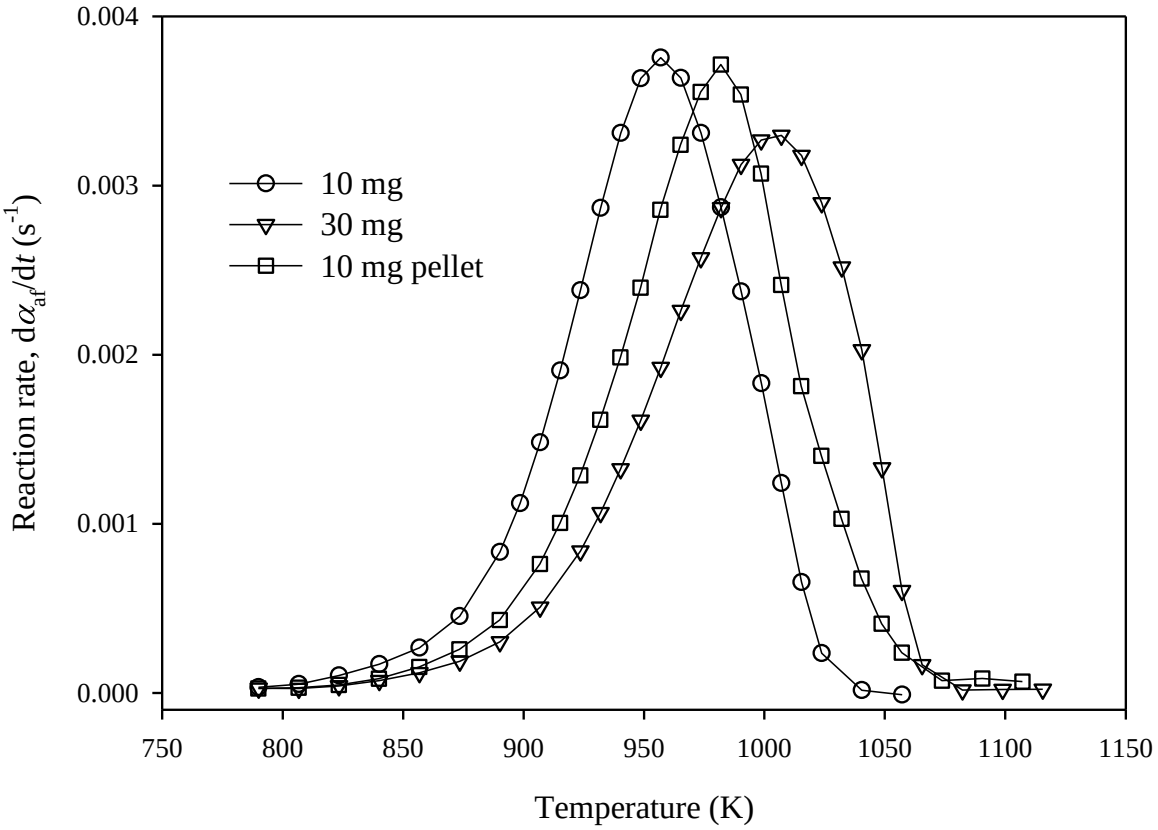

Figure 5.20 – Reaction rate vs. temperature for thermal treatment of Fe_2O_3 and Na_2CO_3 in a 1:1 mole ratio, ball-milled for 60 min at two different initial sample masses, and as a pellet.

Also shown in Figure 5.20, is the reaction rate data vs. temperature for a 10 mg pellet made by compacting the ball-milled mixture of Fe_2O_3 and Na_2CO_3 using a press machine. Compaction shifted T_{max} and T_f to higher temperature by ~20 K and ~30 K, respectively. Compaction reduced the pore volume, which increases interparticle CO_2 accumulation and increases the rate of the reverse reaction. This reduction in interstitial pore volume is evident from SEM images of the uncompacted mixture and the pelletized mixture (see Figure 5.15). It is also evident from measurement of the BET surface area of the pellet was 3.3 $m^2.g^{-1}$ which is a reduction of surface

area compared to the ball-milled powder 4.0 $m^2.g^{-1}$. Reduced pore volume was also seen in the sample after 600 minutes of ball-milling (see Figure 5.15), resulting in a shift of the rate data to higher temperatures (see Figure 5.16).

The reduction in reactivity brought about by pelletization is undesirable from the perspective of Direct Air Capture but may be necessary anyway. Particles of size <5 μm (Geldart group C powders), can be difficult to fluidize since the interparticle forces are much stronger than those resulting from the action of the gas. For example, Nagai (2001) developed a bubbling fluidized bed reactor consisting of a bed material of iron oxide pellets (0.2-1 mm diameter) for direct causticization of black liquor. It was found that gradual attrition of the Fe_2O_3 pellet made fluid operation difficult. The effect of fines on the operation of DARS has been investigated by Covey and Loi Nguyen (1995). The energy requirement of the pelletization would need to be taken into consideration for the real DAC process.

5.4.5 Fe_2O_3 and K_2CO_3 (ball-milled)

Zhang and Zhao (2008) found decomposition of K_2CO_3 began at the melting point of 1164 K whereas Na_2CO_3 began decomposition at the melting point of 1124 K. K_2CO_3 decomposes at higher temperatures than Na_2CO_3. Therefore, K_2CO_3 is also expected to react with Fe_2O_3 at higher temperature than Na_2CO_3.

Milić et al. (2000) found that K_2CO_3 reacts with Fe_2O_3 forming $KFeO_2$ in one stage between 743 and 1223 K at a heating rate of 10 $K.min^{-1}$ in air. The reaction is assumed to proceed via:

$$Fe_2O_{3(s)} + K_2CO_{3(s)} \Leftrightarrow 2KFeO_{2(s)} + CO_{2(g)} \qquad \Delta H = +200.1\ \text{kJ.mol}^{-1} \text{ at } 298\ \text{K} \qquad 5.33$$

An activation energy of 182-186 kJ.mol^{-1} and pre-exponential factor of 1.2-1.7e7 were determined using the Ozawa method (Milić et al., 2000). Joseph and Gnanasekaran (1999) found that the reaction occurred between 900 to 1100 K at 5 K.min^{-1} in pure oxygen. They determined an activation energy of 192-221 kJ.mol^{-1}, pre-exponential factor of 1.3e19-3.8e22 using the Coates-Redfern method. They suggest the conversion dependency is described by the 1D Avrami-Erofeev model (A_2) model. Ndlela and Shanks (2003) synthesized $KFeO_2$ by reaction of Fe_2O_3 and K_2CO_3 at 1073 K in flowing air. The study found that $KFeO_2$ was stable to thermal reduction in H_2 atmospheres. $KFeO_2$ was found to decompose completely after 4 h of exposure to ambient air and that this decomposition is due to reaction with H_2O and CO_2 to form $K_2CO_3.3H_2O$ and $KHCO_3$ (Stobbe et al., 1992). Fan et al. (1990) prepared $KFeO_2$ by reacting α-Fe_2O_3 with K_2CO_3 in a 1:1 ratio for 2 h in flowing air. $K_{1+x}Fe_{11}O_{17}$, where x=0-1, was synthesized by reaction of α-Fe_2O_3 and K_2CO_3 in initial mole ratios of 11:1, 7:1 and 6:1. They found that 90 % of the potassium in $KFeO_2$ was recovered as KOH by hydrolysis at 343 K in 30 min, while only 20 % of the K in $K_{1+x}Fe_{11}O_{17}$ is removed after 6 h. The hydrolysis of $KFeO_2$ occurred according to:

$$2KFeO_{2(s)} + H_2O_{(l)} \Leftrightarrow 2KOH_{(aq)} + Fe_2O_{3(s)} \quad \Delta H = -122\ \text{kJ.mol}^{-1} \text{ at } 298\ \text{K} \qquad 5.34$$

Fan et al. (1990) found that activation energies for the hydrolysis reaction increase with the iron content of $K_{1+x}Fe_{11}O_{17}$ compounds and that increasing temperature or increased grinding increases the amount of K^+ removed. Tomkowicz and Szytuła (1977) found that the cristobalite structure of $KeFeO_2$ is very loose and the bond between K^+ and O^{2-} is weak and thus readily attacked by water whereas in $K_{1+x}Fe_{11}O_{17}$ structures are firmer making it more difficult to shift

K^+ out of the system. Thus, leaching of K from $KFeO_2$ is very rapid at all temperatures between 27°C and 90°C.

Figure 5.21 shows reaction rate vs. temperature data for reaction of a ball-milled (1 h) mixture of Fe_2O_3 and K_2CO_3 in a 1:1 initial mole ratio at heating rates of 10, 20 and 25 $K.min^{-1}$.

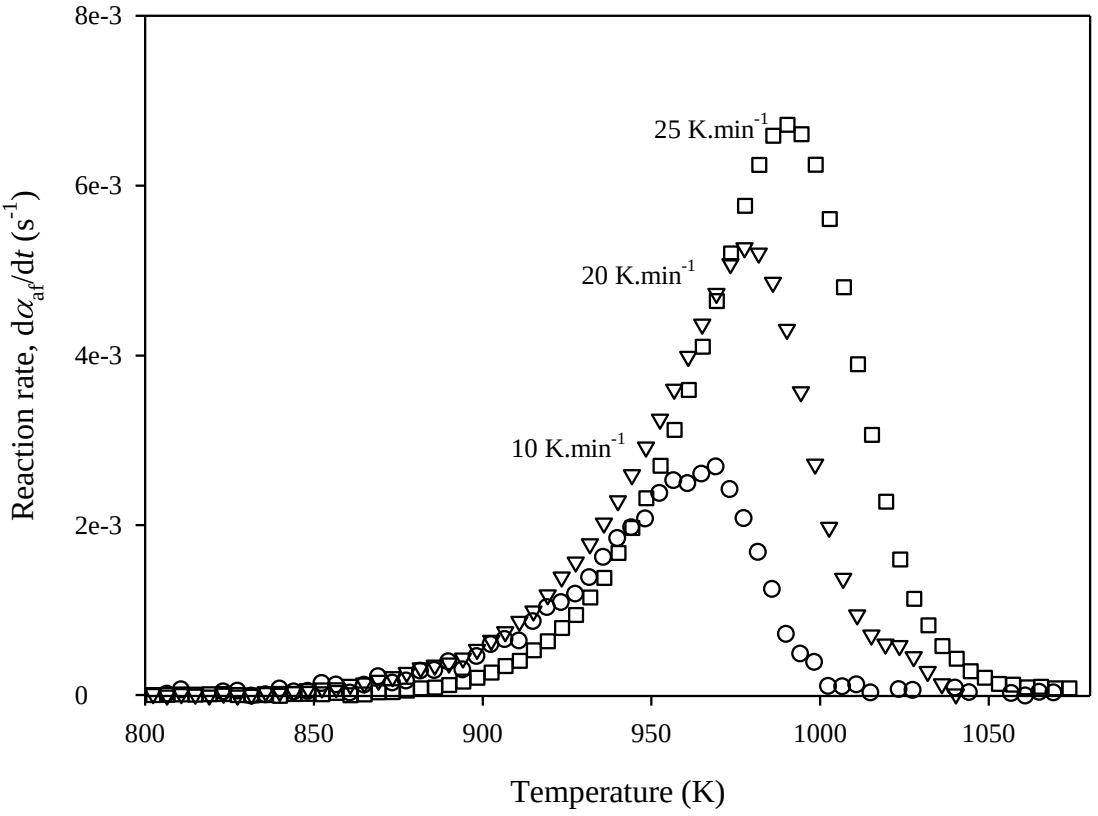

Figure 5.21 – Reaction rate vs. temperature for thermal treatment of a 1:1 mole ball-milled mixture of Fe_2O_3 and K_2CO_3, at β=10, 20 and 25 $K.min^{-1}$.

Conversion according to Eq. 5.34 was 97-100 %. The reaction rate shape is very similar to the one between Fe_2O_3 and Na_2CO_3 (1:1 mole ratio) in Figure 5.16. The reaction between $Fe_2O_{3(s)}$ and $K_2CO_{3(s)}$ was complete at approximately the same temperature as the reaction

between $Fe_2O_{3(s)}$ and $Na_2CO_{3(s)}$ at a heating rate of 20 K.min^{-1}. The product was olive-green and quickly became wet in air. Experiments to determine the recovery of KOH could not be performed due to the very hygroscopic nature of the products of thermal treatment.

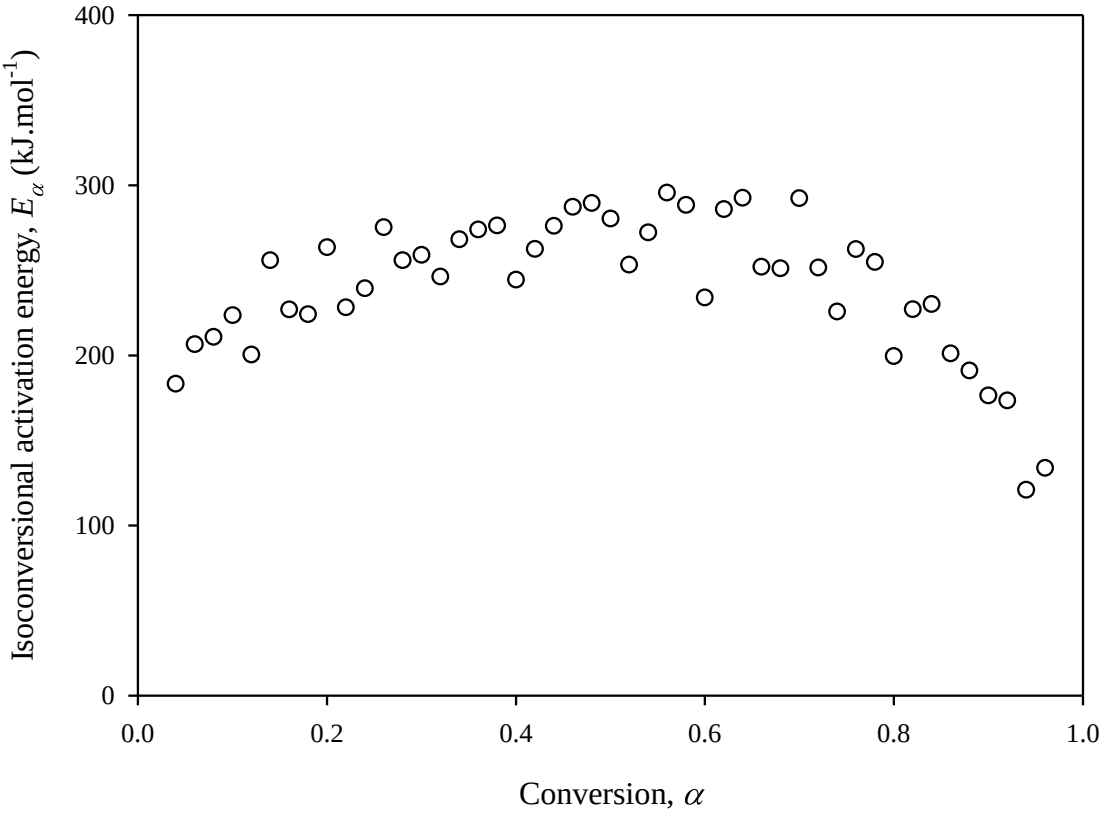

Figure 5.22 – Isoconversional activation energy vs. conversion for reaction of ball-milled Fe_2O_3 and K_2CO_3 (1:1 mole ratio).

Figure 5.21 shows the activation energy determined by the Advanced Isoconversional method as a function of conversion for the reaction of Fe_2O_3 and K_2CO_3 using the data at three heating rates. E_α is 200 kJ.mol^{-1} at low conversion rising to 300 kJ.mol^{-1} at moderate conversion then falling to just above 100 kJ.mol^{-1} at high conversion. This trend indicates the reaction is mechanistically complex.

According to the results here, and in the literature, direct causticization using Fe_2O_3 for regeneration of KOH from K_2CO_3 is conceivable. However, separation of K_2CO_3 from the Direct Air Capture solution by crystallization, although possible (Škrtić et al., 1989), will be more difficult than crystallization of Na_2CO_3 due to its higher solubility. In addition, the regeneration will have a higher energy enthalpy (see Eq. 5.33). However, these disadvantages might be compensated for by the higher rate of CO_2 absorption by KOH solution.

5.5 Conclusion

Na_2CO_3 was reacted with Fe_2O_3 to form β-$NaFeO_2$, releasing CO_2 (see Eq. 5.1). The reaction rate was found to depend strongly on the Na_2CO_3 particle size. For example, at a heating rate of 20 $K.min^{-1}$, a jar-mixed sample of Fe_2O_3 (<5 μm) with Na_2CO_3 (212-355 μm) gave conversion of only 56 % by 1223 K while a mixture of Fe_2O_3 (<5 μm) with Na_2CO_3 (38-63 μm) gave 89 % conversion. Ball-milling was employed as a means to decrease the particle size and promote intimate mixing. The result was a large increase in reactivity of the mixture such that after only 60 min of ball-milling the reaction according to Eq. 5.1 was complete by 950 K. Table 5.3 summarizes the results of thermal treatment and subsequent NaOH recovery for the jar-mixed and ball-milled mixtures. Increasing the mole ratio to 16:1 reduced the decomposition temperatures by a further 50 K. These effects were explained in terms of the increased number of Fe_2O_3 to Na_2CO_3 contact points in the sample. Indeed, a Contact Point Model was found to fit the data well across a range of mole ratio below the sodium carbonate melting point. Increases in the sample mass, or compaction of the powder resulted in a shift of rate data to higher temperature proposed to be due to greater inter-particle CO_2 accumulation and its subsequent

slowing of the reaction. The isoconversional activation energy was determined for ball-milled mixtures and found to depend on the mole ratio, suggested to be due to the effect of mole ratio on the CO_2 diffusion path. In this initial investigation, Fe_2O_3 shows promise as a lower temperature alternative to the CaO-process, but only where the degree of contact between Fe_2O_3 and Na_2CO_3 is high. Low energy methods for maximizing the contact between Fe_2O_3 and Na_2CO_3, such as spray drying, should be investigated as a realistic alternative to ball-milling.

Table 5.3 – Results summary for three different mixtures of Fe_2O_3 and Na_2CO_3.

Initial Na_2CO_3 particle size	μm	212-355	38-63	212-355
Mole ratio	-	1:1	1:1	1:1
Pre-treatment	-	Jar-mixing	Jar-mixing	Ball-milling
BET surface area	$m^2.g^{-1}$	3.8	6.4	4.0
Conversion	%	56	89	100
T_{max}	K	1111	1105	946
NaOH recovery	%	93	93	95
Solids after hydrolysis	-	Hematite	Hematite	Hematite

Chapter 6: Reactions of sodium carbonate with other oxides

6.1 Introduction

Direct Air Capture (DAC) of CO_2 is possible using an alkali hydroxide solution. However, the spent capture solution must be regenerated for cyclical operation. The most reliable methods for regeneration are conventional causticization using lime (for $KOH_{(aq)}$ or $NaOH_{(aq)}$) or direct causticization using hematite (for $NaOH_{(aq)}$). Unfortunately, the CO_2-release step in both processes (Eq. 4.1 and 5.1) requires high temperature heat, leading to high cost. Lower temperatures for the CO_2-release step in direct causticization might be possible with another oxide as a replacement for Fe_2O_3. In this chapter, the literature is surveyed for information on the reactions between oxides and Na_2CO_3 and hydrolysis of any Na-rich products. Then, a simple multi-criteria decision analysis (MCDA) is performed involving over sixty oxides. The most promising of these are tested experimentally, and recommendations made for future work.

6.2 Literature survey

6.2.1 s-block oxides

Siriwardane et al. (2011) found that CaO and $Ca(OH)_2$ facilitated the decomposition Na_2CO_3 via formation of an activated complex of the form $Na_2…CO_3$—Ca…O. However, full decomposition took ~40 min at 1123 K.

6.2.2 p-block oxides

Several oxides of the p-block elements are known to react with Na_2CO_3 including boron (III) oxide and sodium borates (Janson, 1977; 1978; 1979), rock-salt type magnesium aluminum oxide (Sato et al., 2007), aluminum (III) oxide (Johansson, 1992), silicon (IV) oxide (Grace,

1981; Kim and Lee, 2001; Liu et al., 2013), tin (IV) oxide (Liu et al., 2016a; Zhang et al. 2016a), phosphorus (V) oxide and sodium phosphate (Kobe and Leipper, 1940; Janson, 1977), gallium (III) oxide (Suzuki et al., 2017) and indium (III) oxide (Fukuzaki et al., 2000). Carbon is also known to aid decomposition of Na_2CO_3 (Wigmans et al., 1983; Kim and Lee, 2001). B_2O_3, Al_2O_3, SiO_2 and P_2O_5 have been investigated for NaOH regeneration (Janson, 1977; Johansson, 1992). These were found to react with Na_2CO_3 at temperatures comparable with those needed for decomposition of $CaCO_3$ (Siriwardane et al., 2011). However, their reaction products are too soluble for direct causticization (Zou et al., 1990; Ho, 2004).

6.2.3 d-block oxides

6.2.3.1 TiO_2, ZrO_2 and HfO_2

Direct causticization based on the use of titanium (IV) oxide and sodium titanates has been investigated by the pulp and paper industry since the late 1970s (Kiiskilä, 1979). More recently Carbon Engineering considered applying the process to Direct Air Capture (DAC) (Mahmoudkhani et al., 2009; Mahmoudkhani and Keith, 2009). Regeneration involves high temperature (>1000 K) reaction according to:

$$7Na_2CO_{3(s)} + 5(Na_2O.3TiO_2)_{(s)} \Leftrightarrow 3(4Na_2O.5TiO_2)_{(s)} + 7CO_{2(g)} \quad 6.1$$

followed by hydrolysis of $4Na_2O.5TiO_2$:

$$3(4Na_2O.5TiO_2)_{(s)} + 7H_2O_{(l)} \Leftrightarrow 5(Na_2O.3TiO_2)_{(s)} + 14NaOH_{(aq)} \quad 6.2$$

The heat of reaction for Eq. 6.1 is 90 $kJ.mol^{-1}$, which is half of the reaction enthalpy for decomposition of $CaCO_3$. The proposed operating temperature is 1113 K (Mahmoudkhani et al., 2009), 60 K lower than that used for $CaCO_3$ decomposition (Socolow et al., 2011). This makes the titanate route promising for Direct Air Capture, as it reduces the energy demand and facilitates integration with non-fossil sources of energy such as high-temperature gas-cooled nuclear reactors (HTGR) (Mahmoudkhani and Keith, 2009).

Zirconium lies directly below titanium in the periodic table. Martinez-dlCruz and Pfeiffer (2013) synthesized Na_2ZrO_3 from a mixture of ZrO_2 and Na_2CO_3 by ball-milling then heating at 1123 K for 6 h. Liu et al. (2016b) hydrolyzed Na_2ZrO_3 by countercurrent water leaching, forming NaOH to an alkalinity of 1 $mol.L^{-1}$ and solid ZrO(OH).

Similarly, hafnium (IV) dioxide, HfO_2, reacts with Na_2CO_3 to form Na_2HfO_3 (Näfe et al., 2014).

6.2.3.2 V_2O_5, Nb_2O_5 and Ta_2O_5

Vanadium (V) oxide is the most commercially important oxide of vanadium (Langeslay et al., 2018). Reaction between V_2O_5 and Na_2CO_3 during ball-milling was studied by Rojac et al. (2011), who found that all CO_2 was released after only a few minutes of ball-milling. The possibility of using mechanical energy for the decomposition, rather than high-temperature thermal energy, could facilitate integration of Direct Air Capture systems with renewable sources of electrical energy such as solar or wind. Without ball-milling pre-treatment, it has been shown (Kolta et al., 1972; 1973; Barker and Hooper, 1973) that mixtures of V_2O_5 and Na_2CO_3 become reactive around 673 K, forming sodium vanadates such as $NaVO_3$ (sodium metavanadate),

$Na_4V_2O_7$ (sodium pyrovanadate) and Na_3VO_4 (sodium orthovanadate), depending on the initial mole ratio. Therefore, both the thermal and mechanical routes appear to offer low temperature pathways for CO_2-release. However, Venkataraman and Sudha (2005) determined the solubility in water of sodium metavanadate to be in excess of 100 $g.L^{-1}$. In addition, the solubility of V_2O_5 is 0.1-0.8 $g.L^{-1}$ (Woolery, 2000). For effective leaching of NaOH and solids separation, an insoluble oxide is required.

Directly below vanadium in the periodic table lie niobium and tantalum, for which the most stable oxides are Nb_2O_5 and Ta_2O_5 respectively. Rojac et al. (2006) found that Na_2CO_3 reacted fully with Nb_2O_5 forming $NaNbO_3$ after 40 h of ball-milling. Rojac et al. (2011) showed that, of $NaVO_3$, $NaNbO_3$ and $NaTaO_3$, only $NaVO_3$ was synthesized readily by ball-milling. Reisman et al. (1958) provide further information on the reactions of Na_2CO_3 with V_2O_5, Nb_2O_5 and Ta_2O_5. Ozmen et al. (2018) showed that $NaNbO_3$ produced some $NaOH_{(aq)}$ upon contact with water. However, dissolution reactions also occurred, leading to formation of NbO_3^- and $Nb_3O_3^-$.

6.2.3.3 Cr_2O_3, MoO_3 and WO_3

Several oxides of chromium are known to exist, including CrO, Cr_2O_3, Cr_3O_8, Cr_2O_5, CrO_2 and CrO_3 (Schwartz et al., 1952; Udy and Lewin, 1956). Cr_2O_3 is the most stable, found in nature as chromite ore ($FeO.Cr_2O_3$). Chromium products are produced primarily by soda-ash roasting where Na_2CO_3 reacts with Cr_2O_3 forming sodium chromite and sodium chromate. Thus, there is plenty of experience with these reactions at an industrial scale (Tathavadkar et al., 2001; Antony et al., 2006; Prasad, 2010). There is also some evidence to suggest that NaOH can be extracted from sodium chromite (Yu et al., 2015).

It has been shown (Yang et al., 2002; Kar et al., 2005; Ebrahimi-Kahrizsangi et al., 2010) that MoO_3 and Na_2CO_3 react to form Na_2MoO_4. This reaction takes place at >673 K depending on the experimental conditions. Yang et al. (2002) extracted all the MoO_3 from mineral residue by ball-milling with Na_2CO_3 for 120 min, without thermal treatment. Similarly, Toda et al. (2017) showed that WO_3 and Na_2CO_3 react to produce Na_2WO_4. At 373 K, the solubilities of Na_2MoO_4 and Na_2WO_4 in water are 84 $g.ml^{-1}$ and 96.9 $g.ml^{-1}$ respectively. Therefore, neither Na_2MoO_4 nor Na_2WO_4 produces NaOH and solid MoO_3/WO_3 upon hydrolysis, but instead dissolve giving $2Na^+$ and WO_4^{2-}/MoO_4^{2-} ions. Mudher et al. (2005) and Zhang et al. (2016b) found that $Na_2Mo_4O_{13}$, $Na_2Mo_2O_7$, Na_2MoO_4 and $Na_6Mo_{10}O_{33}$ were formed, depending on the Na:Mo ratio of the starting sample and the reaction temperature. Similarly, Chatterjee et al. (2003), Wei et al. (2010) and Qin-Hua et al. (2011) synthesized $Na_2W_4O_{13}$ and $Na_2W_2O_7$, some of which are insoluble and release NaOH upon hydrolysis.

6.2.3.4 MnO_x

Both Mn_3O_4 and MnO_2 have been investigated for direct causticization. Budney (1987) patented a process for recovering NaOH from spent pulping liquor by the addition of MnO_2. However, details of the reactions were not provided. Eames and Empie (2001) reported on the regeneration of NaOH using Mn_3O_4. The effects of initial mole ratio, particle size, temperature and sulfur concentration were all studied. The activation energy of the decomposition step was determined to be 204 $kJ.mol^{-1}$ below the Na_2CO_3 melting point, and 174 $kJ.mol^{-1}$ above it. They claimed that all the sodium was successfully extracted from the $NaMnO_2$ by hydrolysis, with

reproduction of the original Mn_3O_4. Similar reactions were analyzed by Xu et al. (2012; 2013) as part of a thermochemical cycle for water splitting.

6.2.3.5 NiO, CuO, ZnO

$NaNiO_2$, (Vassilaras et al., 2013), $NaCuO_2$ (Ono et al., 2014) and Na_2ZnO_2 (Trinschek and Jansen, 1996) are formed from reactions of Na_2O or N_2O_2 with NiO, CuO and ZnO in an atmosphere of flowing O_2. Hydrolysis of Na_2ZnO_2 is known to produce NaOH in boiling water (Mitra et al., 1998). No studies could be found on their reactions with Na_2CO_3.

6.2.4 Summary

A survey of the literature suggests that many oxides react with Na_2CO_3, but only some can regenerate NaOH by low temperature (<373 K) hydrolysis. The temperature at which Na_2CO_3 reacts depends on the oxide present. For example, Na_2CO_3 reacts with V_2O_5 at moderate temperatures (673-873 K), but reacts with TiO_2 at high temperatures (>973K). Predictions might be possible if there were some way of ranking the various oxides according to their reactivity with Na_2CO_3. One way to do this is by constructing a numerical scale of oxide "acidity".

6.3 Theory

6.3.1 Oxide acidity

In general, the greater the acidity of an oxide, the greater its rate of reaction with a solid alkali compound such as Na_2CO_3. Thus, a quantitative scale of oxide acidity could help to identify potential replacements for Fe_2O_3 for the regeneration of NaOH. Before looking at some of these

scales it is useful to define what is meant by acidity. There are four main definitions of acidity in the literature:

1. An Arrhenius (1887) acid or base dissociates in water forming H^+ or OH^-.
2. A Brönsted-Lowry (1923) acid or base donates or accepts H^+.
3. A Lux (1939) acid or base accepts or donates O^{2-}.
4. A Lewis (1923) acid/base accepts/donates a pair of non-bonding electrons.

The Arrhenius acids are a subclass of the Brönsted acids, which in turn are a subclass of the Lewis acids. Thus, the Lewis acid definition is most widely applicable. However, the Lux definition is perhaps the most suitable for understanding the reactions of oxides. Taking the reaction between Na_2CO_3 and Fe_2O_3 as an example, it can be seen that CO_3^{2-} acts as the O^{2-} donor (base), while Fe_2O_3 acts as the O^{2-} acceptor (acid):

$$O_{CO_3^{2-}}[+2Fe_2O_3] \leftrightarrow O_{Fe_2O_4^{2-}}[+CO_{2(g)}] \qquad 6.3$$

In theory, the greater the potential of an oxide to accept O^{2-}, the faster its reaction with Na_2CO_3. Smith (1987) constructed a quantitative acidity scale which measures the tendency of an oxide to accept O^{2-}, by analogy with the electronegativity constant, χ (Pauling, 1960; Sanderson, 1983; 1988). Smith's acidity constant, A_c, is thus defined as:

$$[A_c(\mathrm{A}) - A_c(\mathrm{B})]^2 = -\Delta H \qquad 6.4$$

where A_c(A) is the tendency of compound A to accept O^{2-}, A_c(B) is the tendency of the compound B to accept O^{2-} and $-\Delta H$ is the standard enthalpy change of salt AB formation in kJ

per mole of O^{2-} transferred. To provide relative values of A_c, the value of one oxide, $A_c(H_2O)$, was chosen to be zero. The resulting values of A_c are shown in Table 6.1.

Table 6.1 – The Smith (1987) and Jeong et al. (2008) acidity scales for some common oxides.

	Smith	Jeong		Smith	Jeong		Smith	Jeong
	A_c	$N_M-2\delta_M$		A_c	$N_M-2\delta_M$		A_c	$N_M-2\delta_M$
	$kJ^{½}.mol^{-½}$	-		$kJ^{½}.mol^{-½}$	-		$kJ^{½}.mol^{-½}$	-
Li_2O	−9.2	0.40	Bi_2O_3	−3.7	-	MnO	−4.8	1.40
Na_2O	−12.5	0.38	Bi_2O_5	-	4.45	Mn_2O_3	-	2.50
K_2O	−14.6	0.35	SO_2	7.1		Mn_2O_5	-	4.86
Rb_2O	−15.0	0.31	SeO_2	5.3	-	MnO_2	-	3.66
Cs_2O	−15.2	0.30	SeO_3	9.8	-	MnO_3	-	6.05
SrO	−9.4	0.98	TeO_2	3.8	-	Mn_2O_7	9.6	7.25
BeO	−2.2	-	ScO	-	0.94	Tc_2O_7	9.6	-
MgO	−4.5	1.27	Sc_2O_3	-	1.88	Re_2O_7	9.0	-
CaO	−7.5	1.10	YO	-	0.77	FeO	−3.4	1.40
SrO	−9.4	-	Y_2O_3	−6.5	1.58	Fe_2O_3	−1.7	2.49
BaO	−10.8	0.94	HfO	-	0.70	CoO	−3.8	1.50
RaO	−11.5	-	Hf_2O_3	-	1.50	Co_3O_4	-	2.05
B_2O_3	1.5	-	TiO_2	0.7	3.05	Co_2O_3	-	2.64
Al_2O_3	−2.0	2.28	ZrO	-	0.86	NiO	−2.4	1.50
Ga_2O_3	−1.6	2.58	Zr_2O_3	-	1.72	Ni_2O_3	-	2.70
Ga_2O	-	0.45	ZrO_2	0.1	2.60	Ni_2O_5	-	5.05
In_2O_3	−2.4	2.47	V_2O_3	-	2.10	Cu_2O	−1	-
Tl_2O	−6.8	0.48	V_2O_5	3.0	4.53	CuO	−2.5	1.51
CO_2	5.5	-	Nb_2O_3	-	1.88	Ag_2O	−5.0	0.66
SiO_2	0.9	-	TaO	-	0.80	ZnO	−3.2	1.59
GeO	-	0.89	Ta_2O_3	-	1.63	CdO	−4.4	-
GeO_2	-	3.62	TaO_2	-	2.62	Cd_2O	-	0.41
SnO	-	1.34	Cr_2O_3	-	2.25	HgO	−3.5	1.58
SnO_2	2.2	3.48	CrO_2	-	3.48	La_2O_3	−6.1	0.86
PbO	−4.5	1.50	Cr_2O_5	-	4.67	Ce_2O_3	−5.8	0.98
N_2O_3	6.6	-	CrO_3	6.6	5.89	CeO_2	−2.7	-
P_4O_{10}	7.5	-	MoO_3	5.2	5.34	Pr_2O_3	−5.8	1.60
As_2O_5	5.4	4.67	WO_3	4.7	5.05	Nd_2O_3	−5.7	1.40

Acidic oxides have values of A_c greater than 0; basic oxides have values of A_c less than −5, and amphoteric oxides have values of A_c between −5 and 0. The ability of an oxide to accept O^{2-} increases approximately with increasing nuclear charge of the central metal. Thus, the Lux acidity of the oxides increases from the bottom-left to the top-right of the periodic table (e.g. K_2O and BaO are basic, whereas B_2O_3 and SiO_2 are acidic) and with increasing oxidation state (e.g. CrO is basic, Cr_2O_3 is amphoteric and CrO_3 is acidic). The Sanderson (1983; 1988) electronegativity scale shows similar trends.

More complex metrics for acidity have been defined. For example, Jeong et al. (2008) defined the acidity as:

$$N_{\mathrm{M}} - 2\delta_{\mathrm{M}} \qquad 6.5$$

where N_M is the formal oxidation state of the metal in a compound and δ_M is the Sanderson partial charge of the metal ion in the oxides, the full definition for which can be found in Jeong et al. (2008). Values for $N_M - 2\delta_M$ are given in Table 6.1. The values of $N_M - 2\delta_M$ gave excellent linear correlation with energy released by intra-molecular charge transfer upon coordination of alizarin to oxide surfaces leading Jeong to suggest that this is the first Lewis-type acidity scale for oxides. Acidity scales explain the results of the literature survey very well (see Section 6.2). For example, Rojac et al. (2011), showed that V_2O_5 reacted at very low temperatures (during ball-milling alone). The Smith and Jeong acidity scales in Table 6.1 show that, as expected, V_2O_5 has one of the highest acidities of any of the oxides.

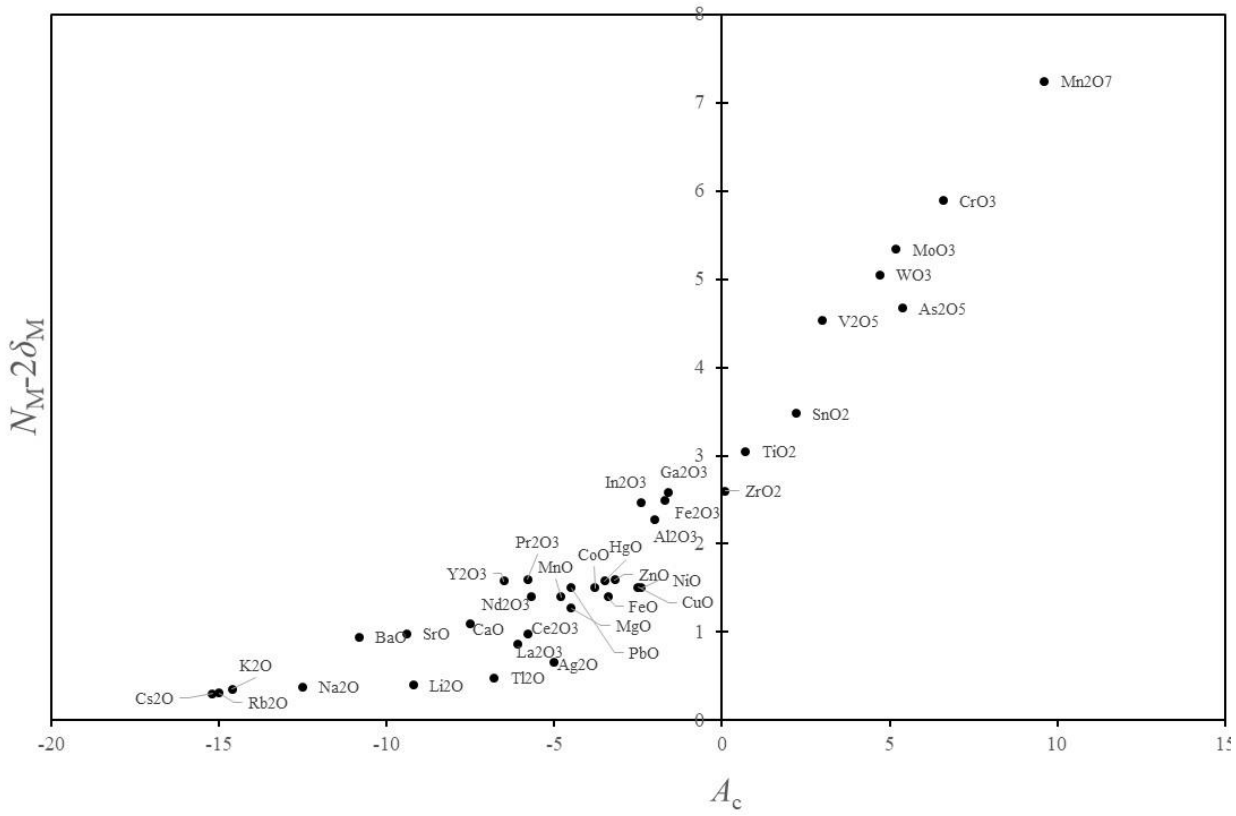

Figure 6.1 – Jeong acidity data (Lewis-type) vs. Smith acidity data (Lux-type) for selected oxides.

Plotting the data from Smith against those of Jeong allows comparison of the Lux- and Lewis-type acidity scales (see Figure 6.1). There is a good linear correlation between the limits of A_c =−5 to 10 $kJ^{½}.mol^{-½}$ and $N_M-2\delta_M$=1 to 8, which more than covers the full range of acidic and amphoteric oxides relevant to this thesis and should provide a reasonably reliable method of predicting the relative reaction rates. An oxide which is more acidic than Fe_2O_3 could lower the temperature of the CO_2-release step, leading to energy and cost savings. However, faster CO_2 release will likely come at the expense of greater difficulty for recovering NaOH, since the O^{2-} is more tightly bound. Thus, there would need to be a trade-off between the faster CO_2-release and

the ease of NaOH recovery. With this in mind, it can be predicted that a successful replacement for Fe_2O_3 will have similar acidity. For example, Mn_2O_3, which has an acidity ($N_M - 2\delta_M = 2.5$) close to that of Fe_2O_3 ($N_M - 2\delta_M = 2.49$), might be expected to have a very similar reaction rate with Na_2CO_3 and recovery of NaOH.

Ellingham diagrams, which plot the free energy of reaction, ΔG, vs. temperature could also have provided another way to compare the feasibility of the various reaction pathways. However, here, I simply wish to quickly identify plausible candidate reagents and then proceed to experimental analysis. Acidity scales indicate the relative reactivity without the need for complex thermodynamic models. In addition, Ellingham diagrams in the literature seem to have poor predictive ability. For example, Lahiri and Jha (2007) determine that the reaction of Fe_2O_3 with Na_2CO_3 is not feasible until >2000 K, while Li et al. (2010) show Al_2O_3 to be more reactive than Fe_2O_3. Thermal analysis experiments (Kiiskilä, 1979) don't agree with these thermodynamic feasibility predictions.

6.3.2 Multi-criteria decision analysis (MCDA) of oxides for NaOH regeneration

The second thesis objective, as discussed in Section 2.2, is to find whether new pathways can be identified for NaOH regeneration which have a lower maximum temperature than the lime and hematite systems. Substitutes for CaO in conventional causticization are very limited. Consequently, the search will be restricted to oxides for direct causticization only. It would be very time consuming to test all available oxides, of which there are well over one hundred. Therefore, it would be wise to create a shortlist of potential reagents and test only those that have some chance of being economically practicable.

The noble gases can be ruled out since these do not form oxides. The rare-earth elements (lanthanides) are, as the name suggests, extremely rare and can also be ruled out. Radioactive elements, such as technetium and rhenium, as well as synthetic elements, such as rutherfordium and oganesson, are not considered. Finally, only solid oxides which are stable at room temperature are considered. After this initial process of elimination, 60 oxides remain (see Table 6.2).

In order to narrow our search further, a multi-criteria decision analysis (MCDA) is employed (see Table 6.2). For this, four main metrics are used: acidity, solubility, cost and toxicity.

- The most fundamental criteria of these is the oxide acidity. It is known that Fe_2O_3 is a good reagent for direct causticization, whereas Fe_3O_4 is not (Covey, 1984). This allows us to rule out reagents with acidities less than that of Fe_3O_4 (<-2.55 on the Smith scale and <1.95 on the Jeong scale).
- Solubility is another important criterion. Oxides which are soluble or partially soluble will be carried through to the DAC absorption stage leading to performance loss. (Autocausticization by soluble or partially soluble oxides was discussed in Section 1.15.1.2.1). Therefore, only insoluble reagents are considered.
- The oxide price must also be considered. A detailed list of metal prices is given in Appendix D. Both Ca and Fe are among the cheapest reagents, at less than 0.1 $USD.kg^{-1}$. In this MCDA it is assumed that any oxide with a price greater than 100 $USD.kg^{-1}$ is too expensive.

- Finally, toxicity is taken into account. For this task, it is sufficient to eliminate some of the most toxic oxides (LD_{50}<100). This eliminates the oxides of cadmium, arsenic and mercury among others.

Table 6.2 – Multi-criteria decision analysis for 60 oxides. The price range is based on the price of the oxide's most common forms e.g. oxides, elements, alloys, ores, ingots, scrap etc. (see Appendix D for full details). Colour coding is added as a visual aid whereby green indicates acceptable and red unacceptable. Reagents which are acceptable across all criteria are marked with an asterisk.

Oxide	Acidity		Solubility in water	Price	Acute oral toxicity, rat (LD_{50})
	Smith	Jeong			
	$kJ^{½}.mol^{-½}$	-	$g.100ml^{-1}$ of water	$USD.kg^{-1}$	$mg.kg^{-1}$
Ag_2O	−5	0.66	0.0013	100-1000	1000
Al_2O_3	−2	2.28	0	<1	5000
As_2O_3	5.4	4.67	1.8	<1	25
B_2O_3	1.5		2.2	<1	3100
BaO	−10.8	0.94	3.48	<1	146
BeO	−2.2		0.00002	100-1000	2000
Bi_2O_3		4.45	0	10-100	5
CaO	−7.5	1.1	100	<1	2000
CdO	−4.4		0.048	1-10	35
CoO	−3.8	1.5	0	10-100	160
*Co_3O_4		2.05	0	10-100	5000
*Cr_2O_3		2.25	0	<1	5000
CrO_3	6.6	5.89	63	<1	50
Cu_2O	−1		0	1-10	500
CuO	−2.5	1.51	0	1-10	470
FeO	−3.4	1.4	0	<1	15000
Fe_3O_4	−2.55	1.95	0	<1	10000

*Fe_2O_3	−1.7	2.49	0	<1	10000
Ga_2O_3	−1.6	2.58	0	100-1000	10000
GeO_2		3.62	0.45	100-1000	3700
HfO_2		0.7	0	100-1000	
HgO	−3.5	1.58	0.0053	100-1000	18
In_2O_3	−2.4	2.47	0	100-1000	1156
IrO_2			0	>1000	5
K_2O	−14.6	0.35	100	<1	7000
Li_2O	−9.2	0.4	100	10-100	7500
MgO	−4.5	1.27	0.0086	<1	4000
MnO	−4.8	1.4	0	<1	422
*Mn_3O_4		1.9	0	<1	2000
*Mn_2O_3		2.5	0.00504	<1	350
*MnO_2		3.66	0	<1	3478
MoO_3	5.2	5.34	0.1066	10-100	100
Nb_2O_3		1.88	0	10-100	
Nb_2O_5			0	10-100	5000
NiO	−2.4	1.5	0	10-100	10000
OsO_4			5.7	>1000	14
P_4O_{10}	7.5		100	<1	389
PbO	−4.5	1.5	0.017	100-1000	2000
PdO			0	>1000	40
PtO_2			0	>1000	5000
Rb_2O	−15	0.31	100	>1000	
RuO_2			0	>1000	2000
Sb_2O_3			0.000037	1-10	7000
Sb_2O_5			0.3	1-10	
Sc_2O_3		1.88	0	>1000	

SeO_2	5.3		38.4	10-100	4
SiO_2	0.9		0.012	<1	3160
SnO		1.34	0	10-100	10000
SnO_2	2.2	3.48	0.00695	10-100	20000
SrO	−9.4		0.018	1-10	
Ta_2O_5		3.01	0	100-1000	8000
TeO_2	3.8		0	10-100	5000
*TiO_2	0.7	3.05	0	<1	5000
Tl_2O	−6.8	0.48	100	>1000	44
V_2O_3		2.1	0.00095	1-10	
V_2O_5	3	4.53	0.08	1-10	467
*WO_3	4.7	5.05	0	10-100	1059
Y_2O_3	−6.5	1.58	0	10-100	10000
ZnO	−3.2	1.59	0	1-10	240
*ZrO_2	0.1	2.6	0	1-10	5000

As a result of the MCDA only nine reagents (each marked by an asterisk in Table 6.2) passed the selection process. These are Co_3O_4, Cr_2O_3, Fe_2O_3, Mn_3O_4, Mn_2O_3, MnO_2, TiO_2, WO_3 and ZrO_2. In the rest of this chapter, the reactions of these oxides with Na_2CO_3 are studied and where necessary, the recovery of NaOH by hydrolysis of the products is determined. The isoconversional activation energy is estimated using the Advanced Isoconversional method where applicable.

6.4 Experimental methodology

6.4.1 Materials

The following reagents were obtained since these are the most common and stable oxides of the first-row transition metals:

- Titanium (IV) oxide (TiO_2) (Sigma Aldrich CAS No. 13463-67-7, Product No. 14021, purity >99 %).
- Cobalt (II/III) oxide (Co_3O_4) (Sigma Aldrich, CAS No. 1308-06-1, Product No. 221643, MDL no. MFCD00010939, <10 μm).
- Chromium (III) oxide (Cr_2O_3) (Sigma Aldrich, CAS No. 1308-38-9, Product No. 223794, MDL no. MFCD00010949, purity >98 %).
- Manganese (IV) oxide (MnO_2) (Alfa Aesar, CAS No. 1313-13-9, Product No. 42250, MDL no. MFCD00003463, particle size ≤ 44 μm, purity >99.9 %).
- Manganese (III) oxide (Mn_2O_3) (Sigma Aldrich, CAS No. 1317-34-6, Product No. 377457, MDL no. MFCD00016217, particle size ≤ 44 μm, purity 99 %).
- Manganese (II/III) oxide (Mn_3O_4) (Sigma Aldrich, CAS No. 1317-35-7, Product No. 377473, MDL no. MFCD00016218, particle size ≤ 44 μm, purity 97 %).

Fe_2O_3 was studied in depth in Chapter 5 and is not considered in this section. Unfortunately, WO_3 and ZrO_2 were not obtained due to time considerations, despite making it through the MCDA.

6.4.2 Ball-milling

5 g of each metal oxide was ball-milled in an air-sealed hardened steel canister using a SPEX 8000 mixer/miller, with 18 steel balls of 3 mm diameter and 1 steel ball of 5 mm diameter at 1080 cycles per minute for 1 h. Each of the oxides was combined with anhydrous Na_2CO_3 (S263500-Fischer Scientific, Certified ACS Grade ≥ 99.5 %) at a 1:1 mole ratio and then ball-milled using the same method. Na_2CO_3 and metal oxide mixtures (1:1 mole ratio totaling 5 g) were jar-mixed by rotational motion in a 100 cm^3 glass sample vial at 60 rpm for 1 h. Where necessary, 3:1 mole ratio mixtures were ball-milled.

6.4.3 Sample characterization

Samples were analyzed using a Philips PW-1730 X-ray diffractometer (XRD) with Cu Kα radiation of 50 kV and 30 mA at a scanning rate of 20° per min. Scanning Electron Micrography (SEM) and Energy Dispersive X-ray (EDX) spectroscopy were performed where necessary.

6.4.4 Thermogravimetric analysis

Approximately 10 mg of the ball-milled metal oxide was analyzed using a TA Instruments Q-500 Series TGA at a heating rate of 20 $K.min^{-1}$ in an atmosphere of flowing N_2, with a cross-flow of 60 $ml.min^{-1}$ and downward-flow of 40 $ml.min^{-1}$ at a pressure of 101 kPa(abs). The ball-milled mixtures with Na_2CO_3 were tested using the same method. Where necessary, other heating rates were employed.

6.4.5 Data processing and analysis

Data over the temperature range of interest were transformed to conversion using the ash-free (Eq. 3.2) or standard (Eq. 3.3) definitions of conversion where applicable. Conversion values were smoothed in Excel using a moving average with interval of 50. The corresponding rate curves were obtained by taking the first forward derivative of conversion with respect to time. Where necessary, TGA runs were performed at more than three heating rates to determine the apparent isoconversional activation energy (E_α) by the Advanced Isoconversional (AIC) method.

6.4.6 Determination of NaOH recovery

Products of thermal analysis were heated in 50 ml of deionized water at 368 K for 1 h under reflux while being mixed using a magnetic stirrer (PTFE King Scientific 35x6 mm) rotating at 60 rpm. The liquid portion was decanted into a 250 cm^3 volumetric flask with three 20 ml rinses and filled to the mark with deionized water. The solid products were dried in a desiccator. A 50 ml portion of the solution was titrated using 0.01 $mol.l^{-1}$ HCl, dosed by a Hanna instruments autotitrator while measuring the pH of the solution. The peaks on a first-derivative pH vs. volume curve were used as indicators for the acid titration end-point(s) from which to calculate the number of moles of NaOH and the % NaOH recovery according to Eq. 5.27.

6.5 Results and discussion

6.5.1 TiO_2

There was no significant change in XRD patterns for TiO_2 after ball-milling or thermal treatment, indicating that no chemical transformation had occurred. In addition, there was no significant mass change for ball-milled TiO_2 during thermal treatment, indicating thermal

stability until 1223 K. There was, however, a significant mass loss for reaction of the ball-milled mixture of TiO_2 and Na_2CO_3 between 800 and 1200 K (see Figure 6.2). By visual observation, the peaks and points of inflection in the reaction rate data at 10 and 20 $K.min^{-1}$ suggest that at least five different processes occurred during thermal treatment. At the lower heating rate of 5 $K.min^{-1}$, there were at least four processes.

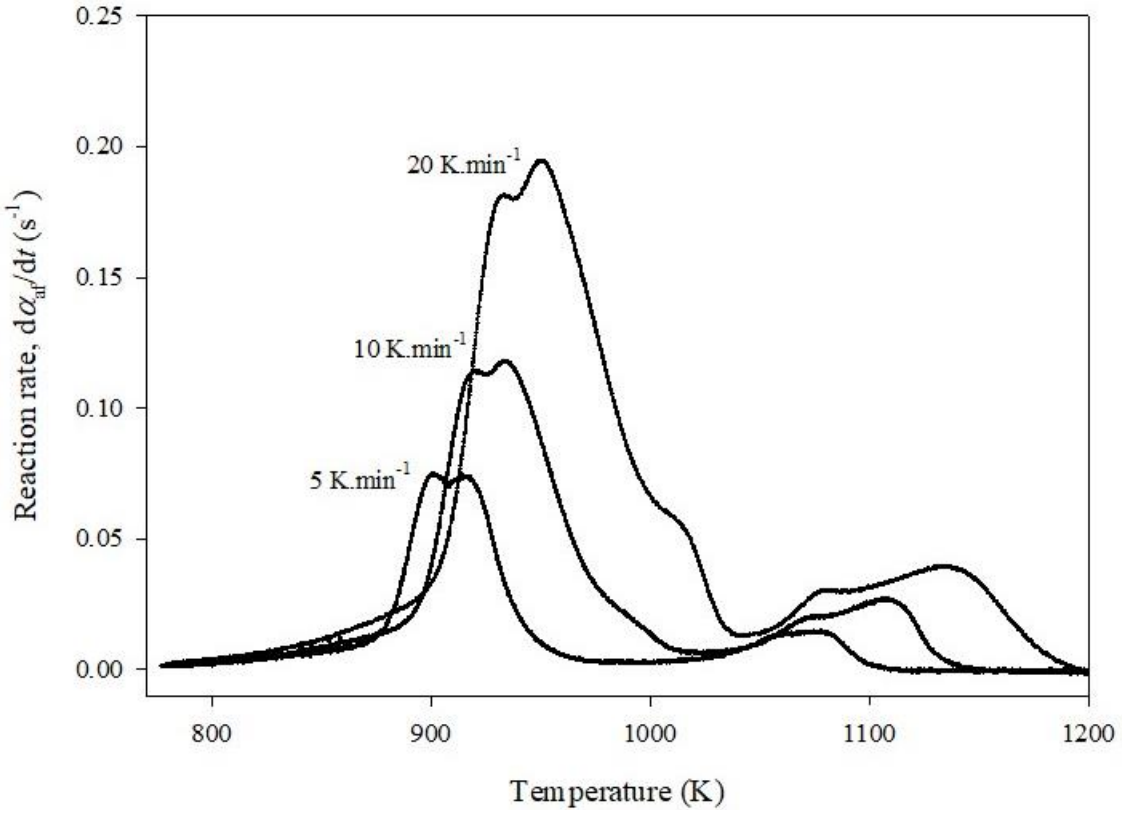

Figure 6.2 – Reaction rate vs. temperature for thermal treatment of ball-milled mixtures of TiO_2 and Na_2CO_3 at heating rates of 5, 10, and 20 $K.min^{-1}$.

X-ray diffraction patterns for the products of thermal treatment of a ball-milled mixture of TiO_2 and Na_2CO_3 are shown in Figure 6.3. At β=5 $K.min^{-1}$, both $Na_2O.6TiO_2$ and $Na_2O.3TiO_2$ were

detected at 873 K, and both $4Na_2O.5TiO_2$ and $Na_2O.TiO_2$ were detected at 1223 K. At β=20 $K.min^{-1}$, $Na_2O.6TiO_2$, $Na_2O.3TiO_2$ and $2N_2O.5TiO_2$ were all detected at 873 K.

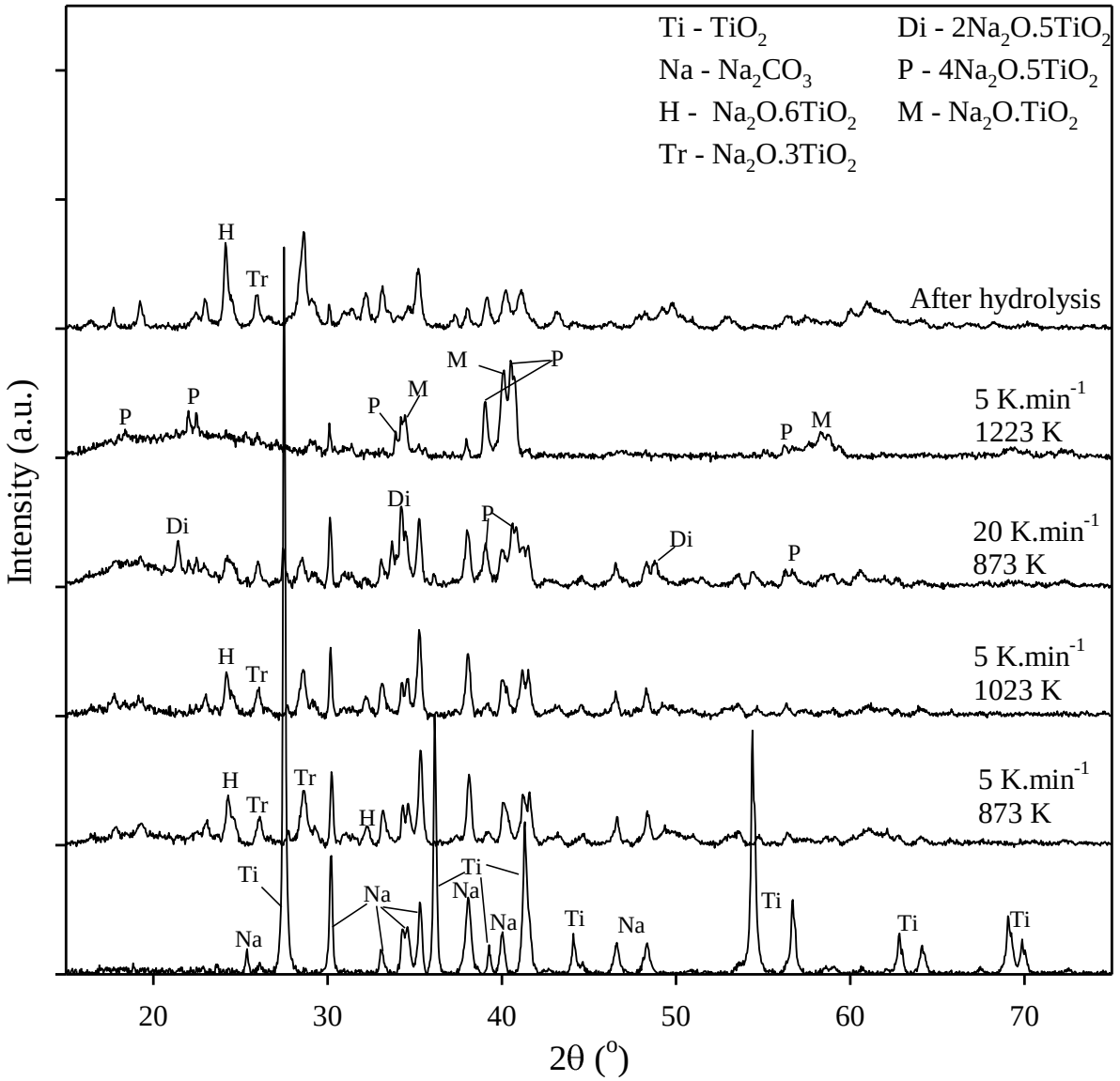

Figure 6.3 – X-ray diffraction patterns for ball-milled mixtures of TiO_2 and Na_2CO_3 in a 1:1 mole ratio, heated to different temperatures.

These TGA and XRD data suggest that the following reactions occur below 1050 K:

$$Na_2CO_{3(s)} + 6TiO_{2(s)} \Leftrightarrow Na_2O.6TiO_{2(s)} + CO_{2(g)} \quad 6.6$$

$$Na_2O.6TiO_{2(s)} + Na_2CO_{3(s)} \Leftrightarrow 2(Na_2O.3TiO_2)_{(s)} + CO_{2(g)} \quad 6.7$$

$$5(Na_2O.3TiO_2)_{(s)} + Na_2CO_{3(s)} \Leftrightarrow 3(2Na_2O.5TiO_2)_{(s)} + CO_{2(g)} \quad 6.8$$

$$2Na_2O.5TiO_{2_{(s)}} + 2Na_2CO_{3(s)} \Leftrightarrow (4Na_2O.5TiO_2)_{(s)} + 2CO_{2(g)} \quad 6.9$$

At the rate minimum between 950 and 1060 K, a mass balance (at 5 $K.min^{-1}$) confirms that ~80 % of the Na_2CO_3 was converted, suggesting that the sample was composed only of $4Na_2O.5TiO_2$ product and unreacted Na_2CO_3. At 1223 K, $Na_2O.TiO_2$ was detected in addition to $4Na_2O.5TiO_2$ suggesting that the following reaction occurred:

$$4Na_2O.5TiO_{2(s)} + Na_2CO_{3(s/l)} \Leftrightarrow 5(Na_2O.TiO_2)_{(s)} + CO_{2(g)} \quad 6.10$$

The final conversion of Na_2CO_3 to sodium titanates was >95 %, which suggests that some titanium oxide was inaccessible to unreacted Na_2CO_3. In summary, the Na_2O to Ti mole ratio of the sodium titanate products increased according to 0.16 → 0.33 → 0.4 → 0.6 → 0.8 → ~0.8-1.0 as temperature increased and CO_2 was released. At all three heating rates studied, there were two peaks in the rate between 1050 and 1200 K indicating two processes, despite the occurrence of just one reaction (Eq. 6.10). This might be explained by an increase in the rate of reaction as the melting point of Na_2CO_3 is approached.

Nohlgren et al. (2003) found that reaction by Eq. 6.10 only occurred "in the total absence of CO_2". This suggests that the reaction is retarded by high CO_2 partial pressure in the furnace. It can therefore be assumed that the reaction is also influenced by the accumulation of reaction-generated CO_2 in the pores, interstices and immediate area surrounding the sample. These processes were discussed in Chapter 4 with respect to $CaCO_3$ decomposition.

Unfortunately, only a few studies have focused on the kinetics. For the reaction of Na_2CO_3 and $Na_2O.3TiO_2$, Zou et al. (1992) determined an activation energy of 365 kJ.mol^{-1} assuming Jander 3D diffusion (D_3). Nohlgren et al. (2000) determined activation energies, E, of 226 and 232 kJ.mol^{-1} for the contracting volume (R_3) and Valensi-Carter models respectively. Nohlgren et al. (2003) found that E varied with changing CO_2 concentration in the reaction atmosphere. For the reaction between Na_2CO_3 and TiO_2, Palm and Theliander (1997) reported that the Valensi-Carter model gave a reasonable fit to their data, with an activation energy of 206 kJ.mol^{-1}. The fit was improved using the contracting volume model (R_3) at low temperature, combined with the Valensi-Carter model at high temperature. Palm and Theliander (1997) suggest that two models are required because there are two reactions: one forming $4Na_2O.5TiO_2$ and the other $Na_2O.TiO_2$. The studies mentioned so far used model-fitting methods for determination of the kinetic parameters. These model-fitting approaches are insufficient on their own. To better anchor the analysis, model-free methods such as isoconversional methods are recommended. These provide unbiased estimates for the apparent isoconversional activation energy, E_α, at different values of conversion, α, which can then be used to estimate the intrinsic activation energies, E, of the elementary steps comprising the overall transformation.

Here, E_α was determined as a function of conversion, α (see Figure 6.4). E_α is approximately 225 kJ.mol^{-1} at α=0.04, corresponding to the formation of $Na_2O.6TiO_2$ in the initial reactions between TiO_2 and Na_2CO_3. E_α is approximately 330 kJ.mol^{-1} at α=0.04, likely due to formation of $Na_2O.3TiO_2$. This result is similar to that of Zou et al. (1992) who determined a value of 365 kJ.mol^{-1}. E_α is 170-180 kJ.mol^{-1} at α~0.3-0.4, corresponding to formation of the 4:5 complex

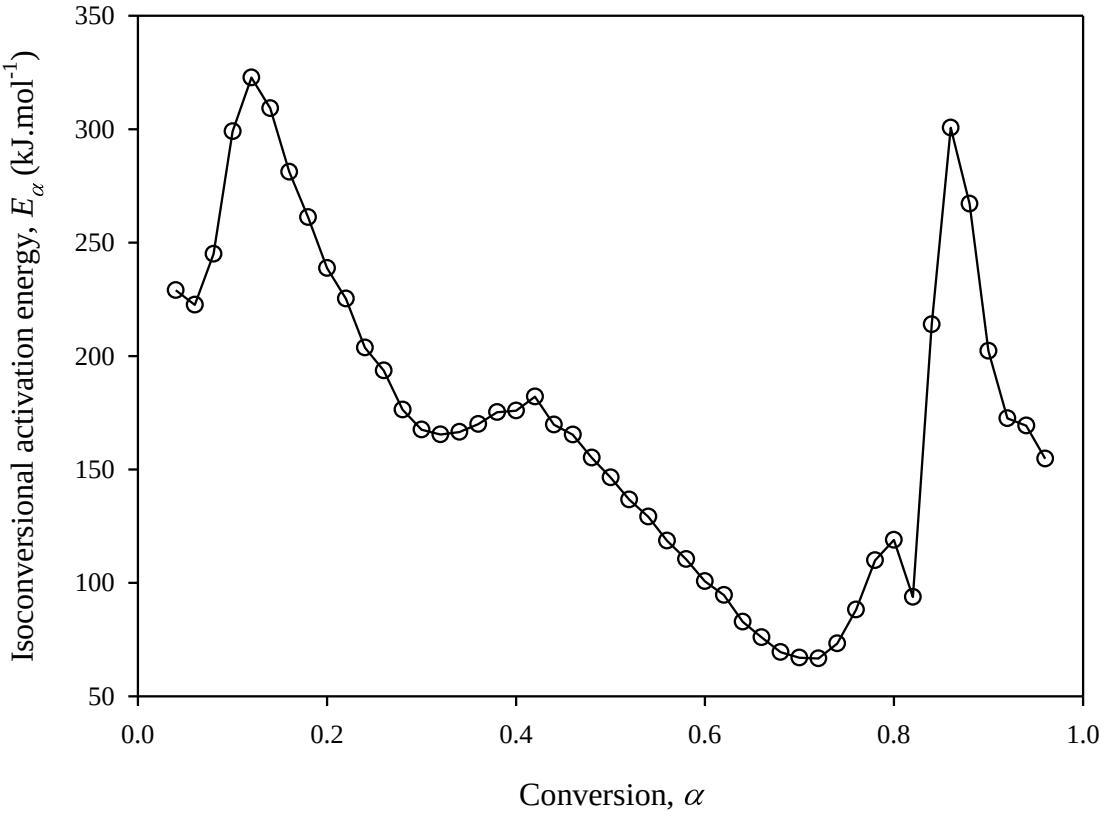

Figure 6.4 – Isoconversional activation energy vs. conversion for reaction of ball-milled TiO_2 and Na_2CO_3 (1:1 mole ratio).

approximately agreeing with the results of Palm and Theliander (1997) who, as noted above, estimated a value of 206 kJ.mol^{-1} for this reaction. E_α fell rapidly, to 60 kJ.mol^{-1} at α=0.7, which is likely to be a numerical artifact corresponding to the period of low reaction rate between the end of the formation of $4Na_2O.5TiO_2$ and the beginning of formation of $Na_2O.TiO_2$. Above α=0.8, E_α rises again to ~300 kJ.mol^{-1}, which is due to reaction of Na_2CO_3 with $4Na_2O.5TiO_2$. However, this is merely one interpretation of the E_α vs. α plot. In Chapter 4, E_α was shown to vary with α as a result of internal CO_2 accumulation. To properly parameterize the rate, each step-wise increase in the sodium content of the titanium oxide structure would need to be

analyzed independently of the others, while accounting for the effect of CO_2. This can be achieved using lower heating rates and/or using different initial mole ratios.

After hydrolysis, peaks due to $Na_2O.6TiO_2$ and $Na_2O.3TiO_2$ were detected, as well as some Na_2CO_3. NaOH recovery was 51 % according to the results of titration. The hydrolysis reactions are proposed to include:

$$3(4Na_2O.5TiO_2)_{(s)} + 7H_2O_{(l)} \Leftrightarrow 5(Na_2O.3TiO_2)_{(s)} + 14NaOH_{(aq)} \quad 6.11$$

$$3Na_2O.TiO_{2(s)} + 2H_2O_{(l)} \Leftrightarrow Na_2O.3TiO_{2(s)} + 4NaOH_{(aq)} \quad 6.12$$

$$2(Na_2O.3TiO_2)_{(s)} + H_2O_{(l)} \Leftrightarrow Na_2O.6TiO_{2(s)} + 2NaOH_{(aq)} \quad 6.13$$

The results of this study suggest that sodium titanate formation is more complex than described by Mahmoudkhani et al. (2009). Indeed, Nohlgren and Sinquefield (2004) demonstrate that every reaction (described by Eqs. 6.6 - 6.13) occurs during NaOH regeneration to some extent, and the mole ratio and operating conditions can be changed to favour the formation of one reaction product over the others.

6.5.2 Cr_2O_3

After 1 h of ball-milling, it was found that the dark-green colour of Cr_2O_3 was unchanged. XRD analysis suggested that a mixture of Cr_2O_3 and Na_2CO_3 was unreactive during ball-milling since all peaks were accounted for by Cr_2O_3 and Na_2CO_3 (see Figure 6.5).

There was no significant change in mass when heating ball-milled Cr_2O_3 to 1273 K at β=20 $K.min^{-1}$ in flowing N_2 (see Figure 6.6). This agrees with Peres et al. (2012) who showed that

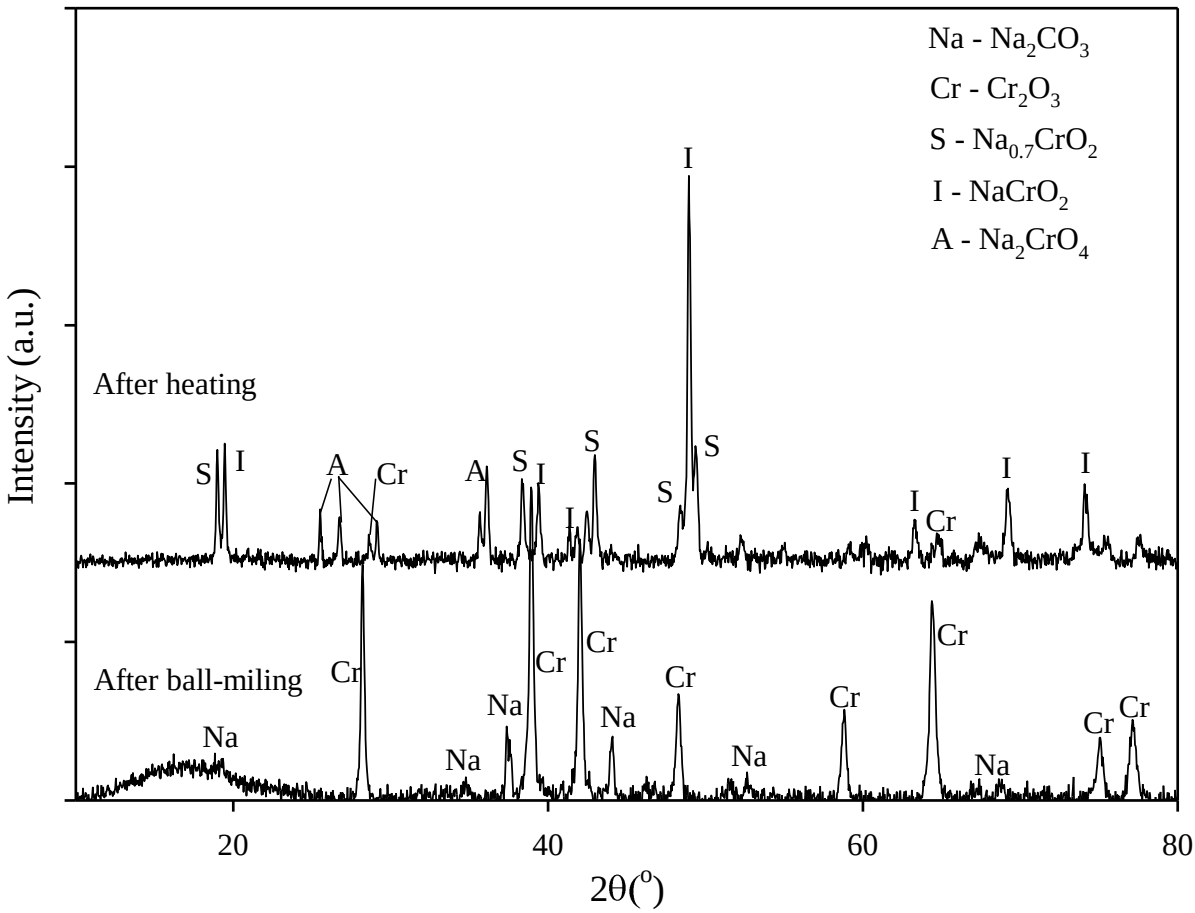

Figure 6.5 – X-ray diffraction patterns for mixtures of Cr_2O_3 and Na_2CO_3 (1:1 mole ratio), after ball-milling for 1 h, and then after heating to a temperature of 1073 K at β=20 K.min^{-1}.

Cr_2O_3 is stable until ~1673 K, even under mildly reducing conditions. Heating the mixture of Cr_2O_3 and Na_2CO_3 at β=20 K.min^{-1} resulted in loss of 15.4 % of the total mass of the sample (Figure 6.6). XRD peaks were indexed to $NaCrO_2$ (see Figure 6.5). This suggests that mass loss occurred according to:

$$Na_2CO_{3(s)} + Cr_2O_{3(s)} \Leftrightarrow 2NaCrO_{2(s)} + CO_{2(g)} \quad 6.14$$

Kubota et al. (2014) and Tsuchiya et al. (2017) all synthesized $NaCrO_2$ via this route.

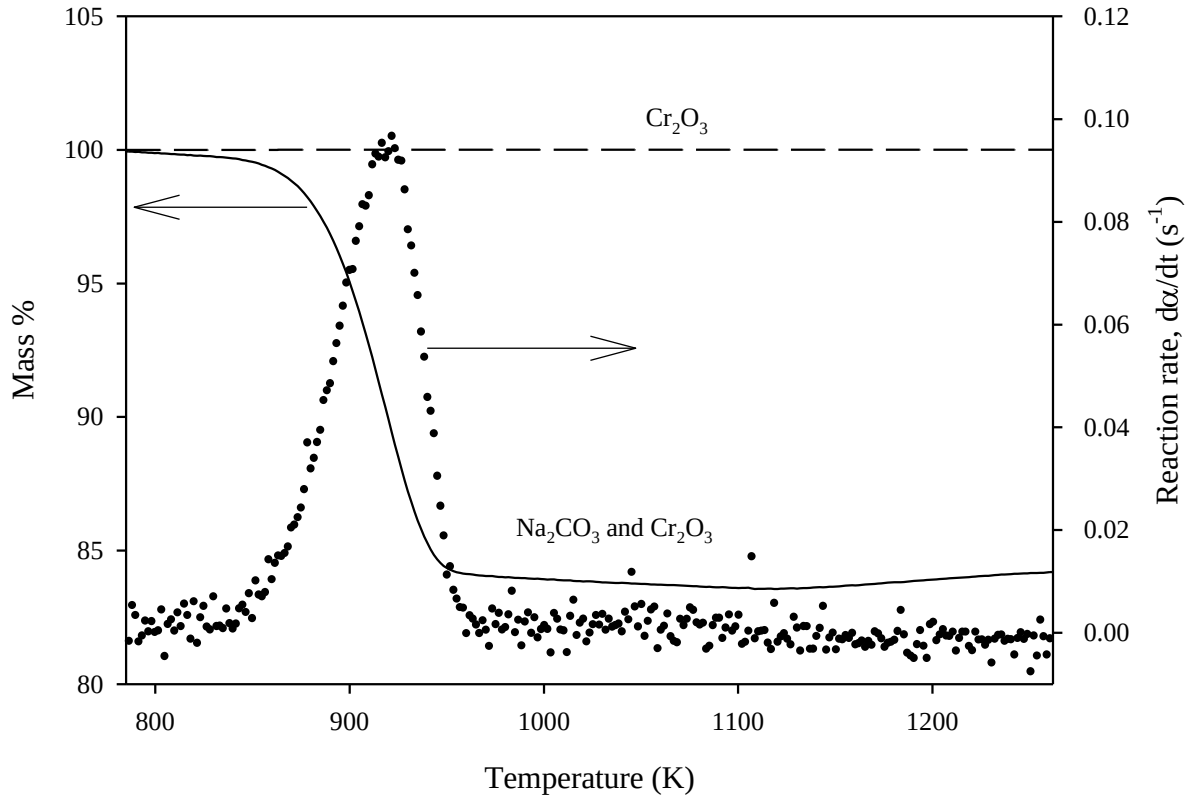

Figure 6.6 – Mass % and reaction rate vs. temperature for thermal treatment (β=20 K.min^{-1}) of ball-milled Cr_2O_3 and Na_2CO_3 (1:1 mole ratio).

The XRD data in Figure 6.5 also show peaks due to $Na_{0.74}CrO_2$ and Na_2CrO_4, suggesting that oxidation occurred during heating. Only a few studies could be found which mentioned $Na_{0.74}CrO_2$ formation. Yurkinskii et al. (2010) reported finding $Na_{0.74}CrO_2$ as a high temperature product of Inconel alloy corrosion, but they did not give any details about its formation mechanism. Here, the following reaction is proposed:

$$148NaCrO_{2(s)} + 26Cr_2O_{3(s)} + 13O_{2(g)} \Leftrightarrow 200Na_{0.74}CrO_{2(s)} \qquad 6.15$$

As for Na_2CrO_4, there have been several different proposed formation pathways in the literature. Garbers and Van Vuuren (1987) and Mao at el. (2016) suggest that, in oxygen-rich atmospheres, Cr_2O_3 can react according to:

$$Cr_2O_{3(s)} + 3/2O_{2(g)} \Leftrightarrow 2CrO_{3(s)} \quad 6.16$$

which then reacts with Na_2CO_3 to form sodium chromate, Na_2CrO_4:

$$CrO_{3(s)} + Na_2CO_{3(s)} \Leftrightarrow Na_2CrO_{4(s)} + CO_{2(g)} \quad 6.17$$

Another pathway for Na_2CrO_4 formation was proposed by Antony et al. (2006), Tathavadkar et al. (2006) and Prasad (2010), who suggest that Na_2CrO_4 is formed either directly or via the $NaCrO_2$ intermediate:

$$2Na_2CO_{3(s)} + Cr_2O_{3(s)} + 3/2O_{2(g)} \Leftrightarrow 2Na_2CrO_{4(s)} + 2CO_{2(g)} \quad 6.18$$

$$Na_2CO_{3(s)} + 2NaCrO_{2(s)} + 3/2O_{2(g)} \Leftrightarrow 2Na_2CrO_{4(s)} + CO_{2(g)} \quad 6.19$$

The rates of the reactions (Eqs. 6.18 and 6.19) are thought to depend on the O_2 partial pressure, temperature and mole ratio of the initial mixture (Tathavadkar et al., 2006). To gain further insight into these reactions, thermogravimetric data were gathered at β=0.5, 1, 2, 4, 16, 32 and 64 K.min^{-1}. Reaction rate vs. temperature data are plotted in Figure 6.7. At β=0.5 K.min^{-1}, mass loss was ~9 % and there were two peaks in the rate data indicating at least two processes. At β=1 and 2 K.min^{-1}, the first peak in the rate is less prominent than at β=0.5 K.min^{-1}, disappearing entirely at higher heating rates. At higher heating rates, e.g. β=16, 32 and 64 K.min^{-1}, mass loss was ~13 %, and there was just one peak in the rate data. Thus, the reactions occurring depend on

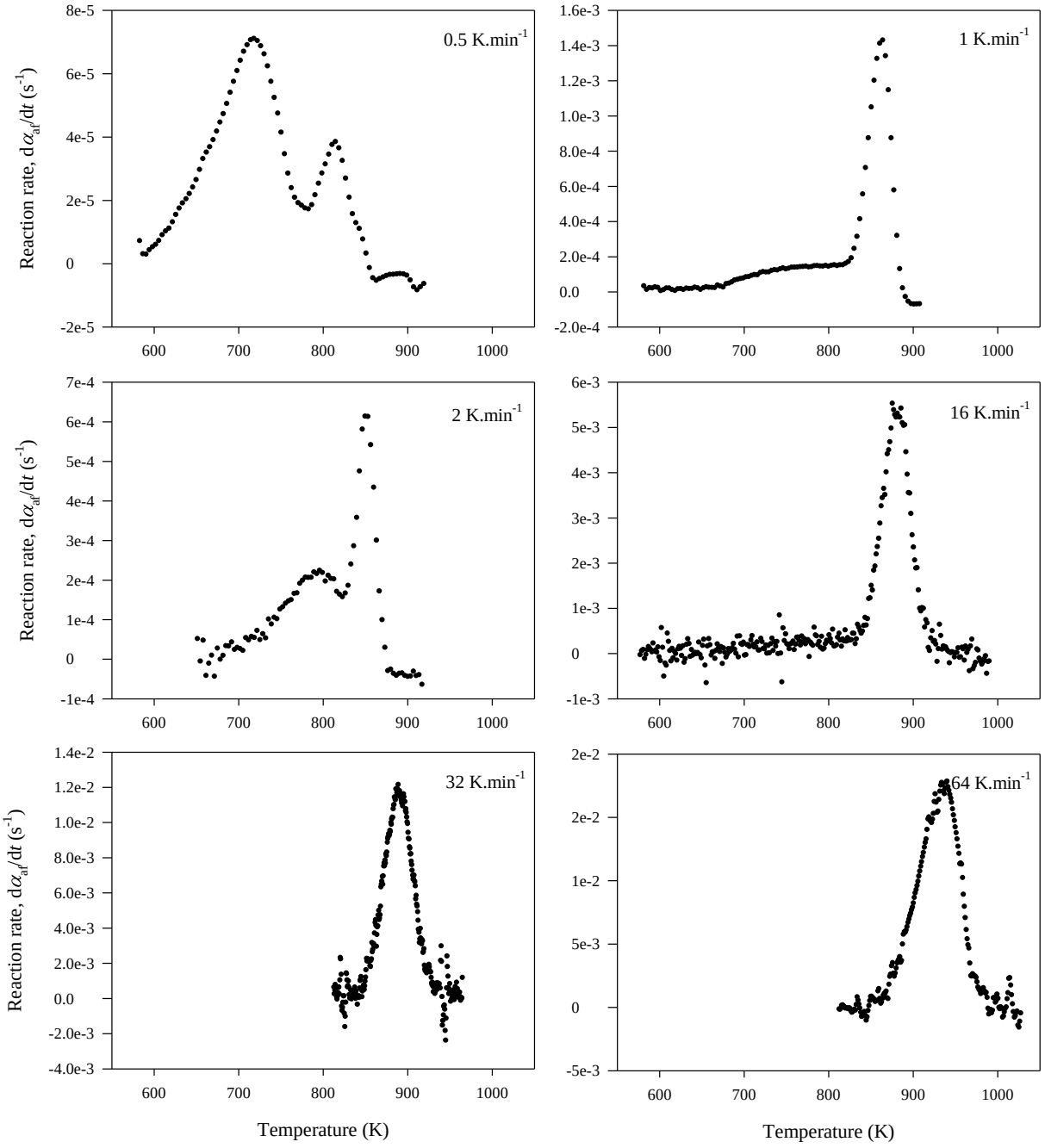

Figure 6.7 – Reaction rate vs. temperature for thermal treatment of ball-milled mixtures of Cr_2O_3 and Na_2CO_3 in a 1:1 mole ratio at different heating rates.

the heating rate. At lower heating rate, the mass loss was less because more oxidation, indicated by mass gain, occurred due to increased residence time. There was also a slight increase in the mass loss with an increase in the initial sample mass. This could suggest that, for larger masses, there is a greater diffusional barrier for $O_{2(g)}$ transport to reaction sites. At β=0.5 K.min^{-1}, there is clearly a period of mass gain above 848 K, where dα/dt<0, which is likely due to oxidation by Eqs. 6.18 and 6.19. This mass gain is also seen at higher temperatures in the mass vs. temperature data at 20 K.min^{-1} (see Figure 6.6).

The isoconversional activation energy was determined at β=0.5, 1 and 2 K.min^{-1} (see Figure 6.8). At low conversion, E_α was 45-65 kJ.mol^{-1}, which can be assumed to be due to formation of sodium chromate (Na_2CrO_4). Our estimate is in good agreement with estimates in the literature for the same reaction. For example, Tripathy et al. (1994) reported a value of 72 kJ.mol^{-1}, Prasad (2010) 39 kJ.mol^{-1} and El-Dars et al. (2002) 112 kJ.mol^{-1}. Shalabi et al. (2006) estimated values of 88 to 106 kJ.mol^{-1} depending on the atmosphere. Tathavadkar et al. (2006) reported 35 kJ.mol^{-1} which they suggested is the barrier for O_2 diffusion in the pores of the sample. At high conversion, E_α was ~300 kJ.mol^{-1} which is likely due to formation of sodium chromite ($NaCrO_2$). This corresponds well to an apparent activation energy value of 290 kJ.mol^{-1} for diffusion of Cr^{3+} in Cr_2O_3 (Kingery, 1974) and in $CoCr_2O_4$ spinel (Sun, 1958). The isoconversional activation energy was also determined at β=16, 32 and 64 K.min^{-1}. At α~0.04, E_α<100 kJ.mol^{-1}, likely due to Na_2CrO_4 formation. At α~0.2, E_α~300 kJ.mol^{-1}, corresponding to $NaCrO_2$ formation. Beyond α~0.2, E_α then decreased to around 140 kJ.mol^{-1}, most likely due to oxidation of $NaCrO_2$, forming Na_2CrO_4 and/or $Na_{0.74}CrO_2$.

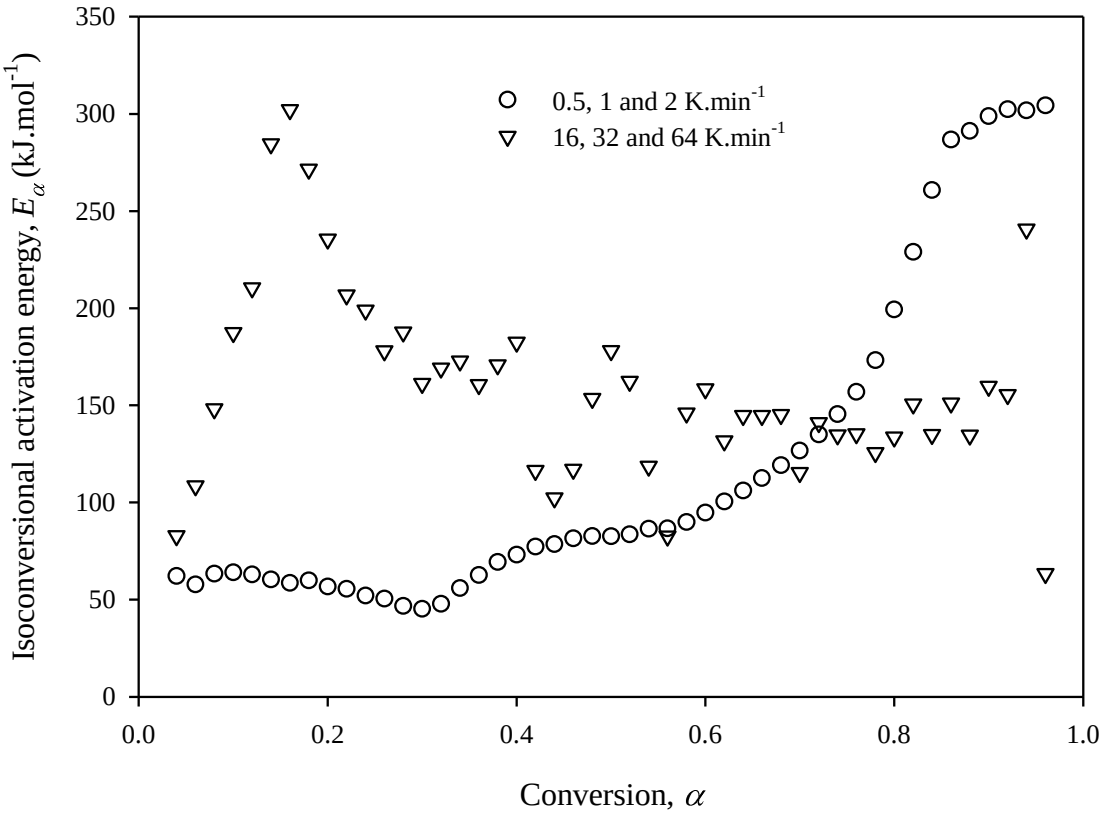

Figure 6.8 – Isoconversional activation energy vs. conversion for reaction of ball-milled Cr_2O_3 and Na_2CO_3 (1:1 mole ratio) determined at different ranges of heating rate.

Approximately 55 % of the Na was recovered as NaOH from hydrolysis and titration of the thermal analysis products from the β=20 K.min^{-1} run. The following hydrolysis reaction is proposed to occur:

$$2NaCrO_{2(s)} + H_2O_{(l)} \Leftrightarrow Cr_2O_{3(s)} + 2NaOH_{(aq)} \qquad 6.20$$

Similarly, Yu et al. (2015) found that after just a few minutes of exposure to air, NaOH and Na_2CO_3 were present on the surface of $NaCrO_2$ particles. NaOH cannot be extracted from the

portion of the products composed of soluble Na_2CrO_4. Indeed, peaks were observed in the derivative pH vs. volume data, probably due to HCl reaction with Na_2CrO_4 during titration.

SEM images of the reactants (Figure 6.9) show small Cr_2O_3 particles agglomerated on a core of much larger Na_2CO_3 particles. EDX confirms that the brighter, smaller particles seen in the SEM images of the reactant are Cr_2O_3, while the darker larger crystals correspond to Na_2CO_3. In the product image, there appears to be only one type of particle. EDX analysis indicated that the carbon content on the surface of the product crystals was higher than in the Na_2CO_3 portion of the reactants. A possible explanation for this is that $NaCrO_2$ reacted with CO_2 in the air, forming Na_2CO_3 on the surface.

Our results suggest that Direct Air Capture using NaOH with Cr_2O_3-based regeneration may be possible. Cr_2O_3 reacts with Na_2CO_3 releasing CO_2 and forming $NaCrO_2$, with recovery of NaOH and Cr_2O_3 by hydrolysis. The CO_2-release occurs at 50 K lower than reaction of Fe_2O_3 with Na_2CO_3. For these reasons, Cr_2O_3 has good potential as a reagent for direct causticization. However, oxidation also occurred during heating, even at a very low $O_{2(g)}$ concentration (~100 ppmv), creating highly soluble sodium chromate (Na_2CrO_4) from which NaOH cannot be extracted. In a Direct Air Capture process, this oxidation would lead to a loss in cycling capacity if not inhibited. Formation of Na_2CrO_4 could be minimized using reducing conditions, high Cr_2O_3:Na_2CO_3 ratio and good mixing of the solid reagents. The temperature in the reactor will also be important. For example, Antony et al. (2006) indicated that liquid Na_2CO_3 (T>1096 K) can inhibit Na_2CrO_4 formation by blocking Cr_2O_3 pores and retarding $O_{2(g)}$ diffusion to reaction sites. It is especially important to avoid formation of hexavalent chromium compounds since

these are known to be 100-1000 times more toxic than trivalent chromium compounds (Katz and Salem, 1993; Jiao et al., 2011; Chen et al., 2012).

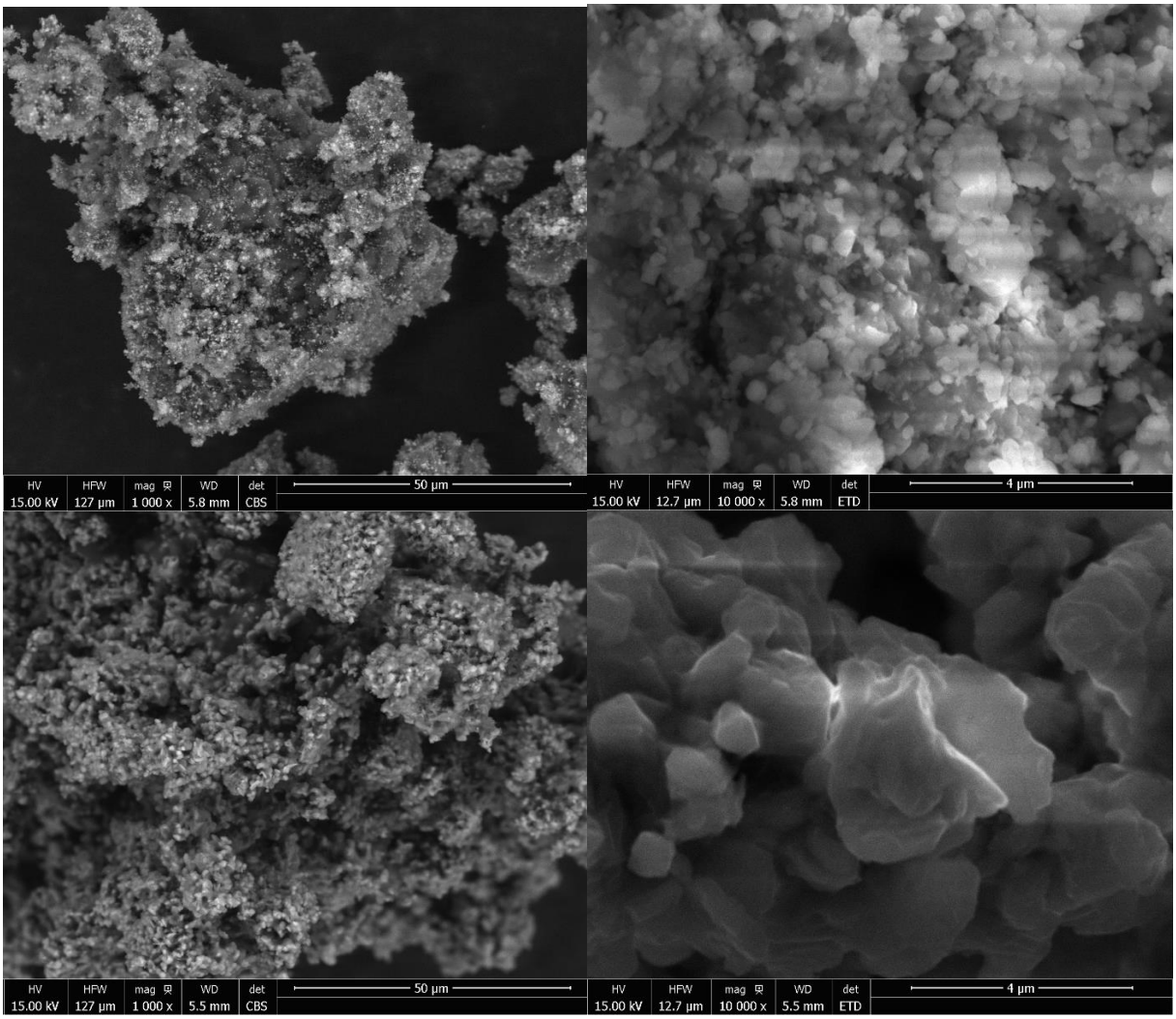

Figure 6.9 – SEM images for a ball-milled mixture of Cr_2O_3 and Na_2CO_3 in a 1:1 mole ratio before and after heating to 1250 K at β=20 K.min^{-1}, at two magnifications.

6.5.3 MnO_x

For manganese oxides of the form MnO_x, x can take on a variety of values between 0.8 and 4, the most stable and common of these being MnO_2, $MnO_{1.5}$ (Mn_2O_3), $MnO_{1.33}$ (Mn_3O_4) and MnO, although only the former three oxides were found to be sufficiently acidic to be worth investigating (see Table 6.2).

6.5.3.1 MnO_2

MnO_2 was analyzed by XRD before and after ball-milling (see Figure 6.10). All peaks could be indexed to pyrolusite, MnO_2. Ball-milling caused peak-broadening due to the Scherrer phenomenon. XRD peaks for ball-milled mixtures of MnO_2 and Na_2CO_3 were indexed to Na_2CO_3, $Na_2CO_3.H_2O$ and MnO_2, indicating no chemical change had occurred other than some minor degree of hydration.

Figure 6.11 shows the reaction rate vs. temperature data for thermal treatment of un-milled and ball-milled MnO_2 in an atmosphere of flowing N_2. There were three peaks in the rate data indicating at least three stages of mass loss. XRD analysis of the products of the first mass loss showed patterns corresponding to bixbyite, Mn_2O_3 (see Figure 6.10), suggesting reaction according to:

$$MnO_{2(s)} \Leftrightarrow 1/2Mn_2O_{3(s)} + 1/4\ O_{2(g)} \qquad 6.21$$

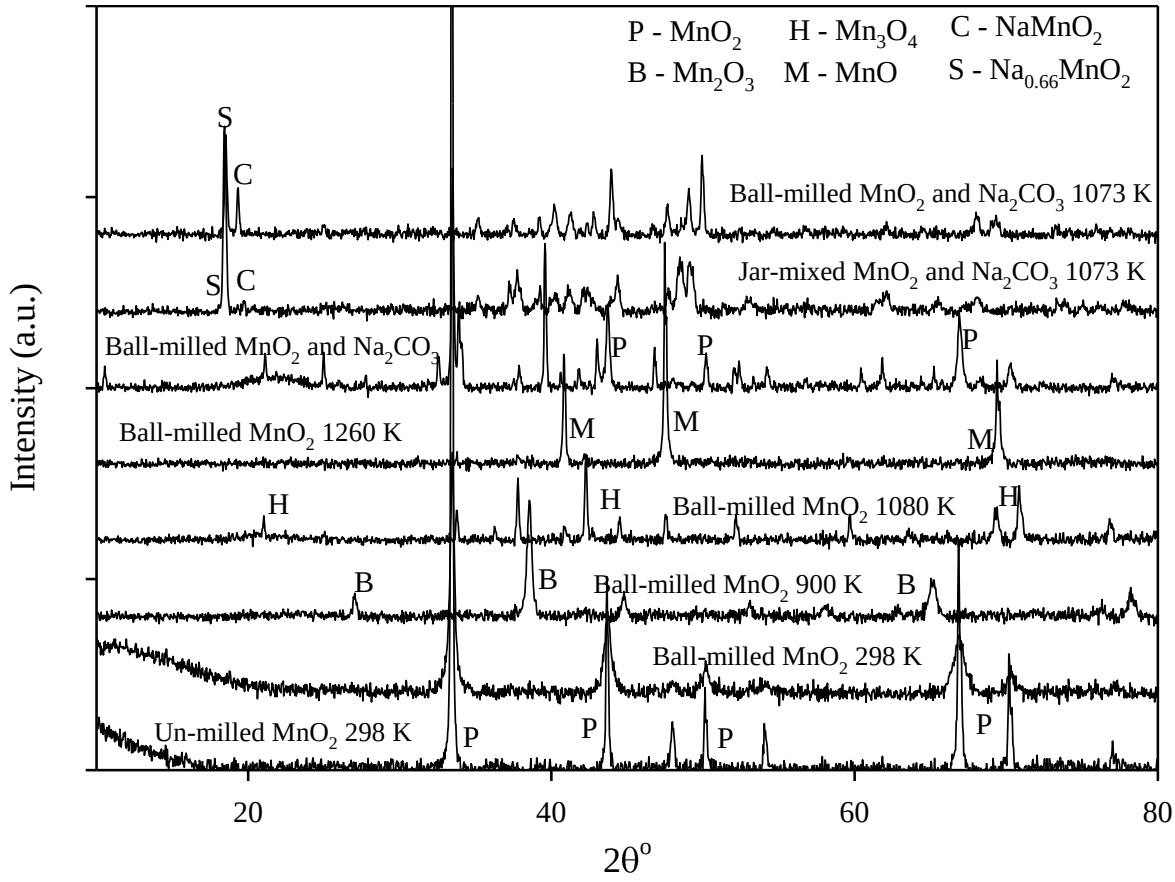

Figure 6.10 – X-ray diffraction patterns for un-milled and ball-milled MnO_2, jar-mixed and ball-milled with Na_2CO_3 (1:1 mole ratio), heated to different temperatures at β=20 K.min^{-1}.

Mass closures according to Eq. 6.21 were 99.2 % and 103 % for the un-milled and ball-milled samples respectively. The point of inflection in the rate curve might indicate a dual step reduction process. Indeed, Zaki et al. (1997) found that MnO_2 decomposed first to Mn_5O_8 ($MnO_{1.6}$) before decomposing to Mn_2O_3 ($MnO_{1.5}$). XRD analysis of a ball-milled sample after the second mass loss showed patterns corresponding to hausmannite, Mn_3O_4 (see Figure 6.13), suggesting reaction according to:

$$Mn_2O_{3(s)} \Leftrightarrow 2/3Mn_3O_{4(s)} + 1/6O_{2(g)} \qquad 6.22$$

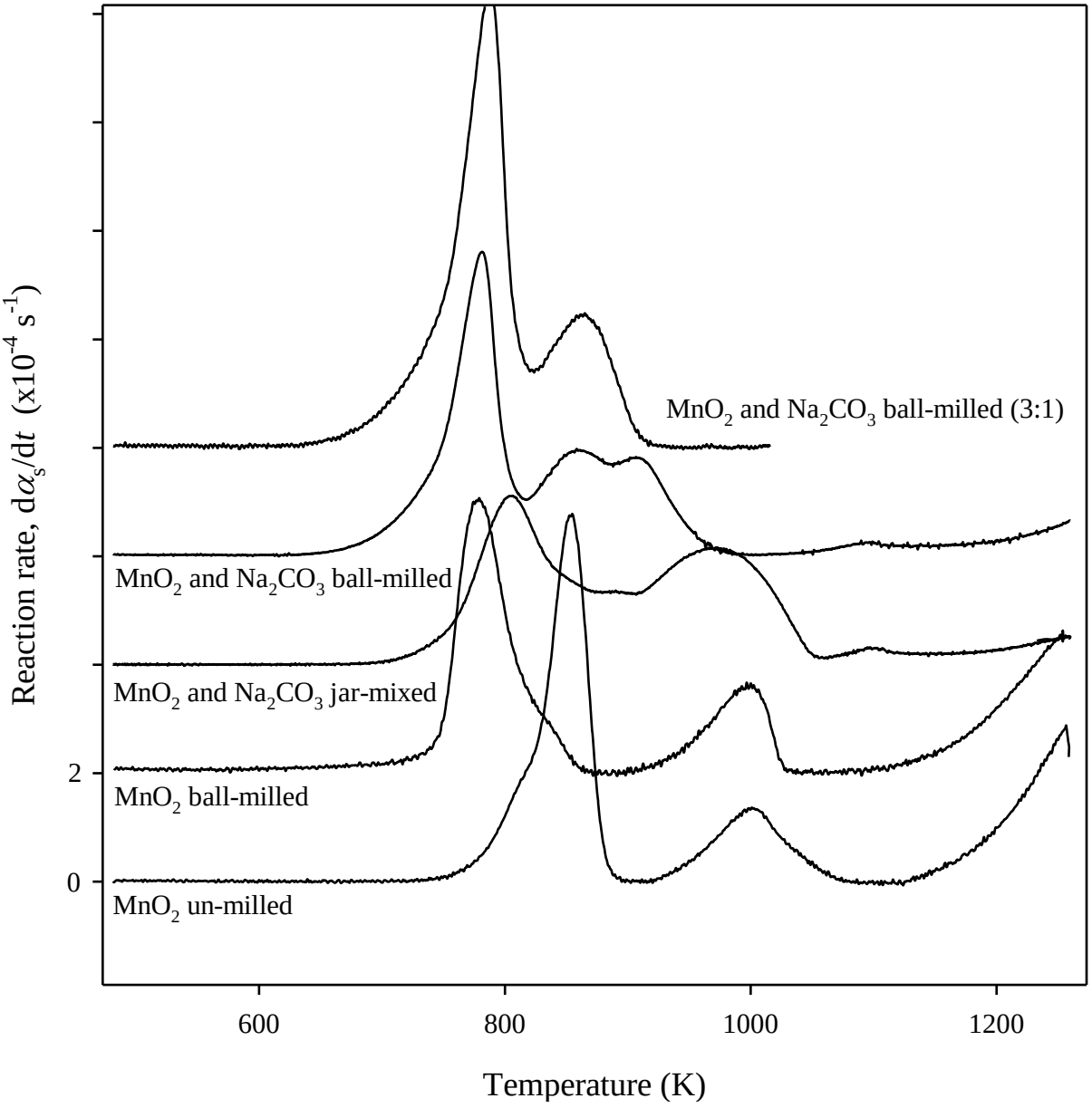

Figure 6.11 – Reaction rate vs. temperature for thermal treatment of MnO_2 and its jar-mixed and ball-milled mixtures with Na_2CO_3 (1:1 mole ratio unless otherwise stated), at β=20 K.min^{-1}.

Mass closures according to Eq. 6.22 were 99.8 % and 99.1 % for the second mass loss in each of the un-milled and ball-milled MnO_2 samples respectively. XRD analysis of the ball-milled sample which was heated to 1080 K showed patterns corresponding to manganosite, MnO (see Figure 6.10), suggesting that the third mass loss was due to:

$$Mn_3O_{4(s)} \Leftrightarrow 3MnO_{(s)} + 1/2O_{2(g)} \qquad 6.23$$

The same three-stage thermal reduction of MnO_2 to MnO described by Eqs. 6.21 - 6.23 has also been observed by Giovanoli (1994). Ball-milling lowered the temperatures at which these mass losses occurred. This is due to the increased surface area for nucleation, as well as a lower barrier to O_2 diffusion away from the sample. These effects were discussed in previous chapters.

Figure 6.11 also shows reaction rate vs. temperature data for thermal treatment of jar-mixed and ball-milled mixtures of MnO_2 and Na_2CO_3 in a 1:1 mole ratio, as well as reaction of a ball-milled mixture of MnO_2 and Na_2CO_3 in a 3:1 mole ratio. For both mixtures, there was a period of mass loss between 673 K and 1073 K, occurring in at least three stages as indicated by three distinct peaks in the rate data. For the 3:1 ball-milled mixture, there were only two peaks in the rate data. The first mass loss is accounted for by Eq. 6.21, whereas the second (and third) mass losses were due to:

$$Mn_2O_{3(s)} + Na_2CO_{3(s)} \Leftrightarrow 2NaMnO_{2(s)} + CO_{2(g)} \qquad 6.24$$

Mass closures for the reactions described by Eq. 6.21 followed by Eq. 6.24, were 99.2 % and 99.5 % for the 1:1 jar-mixed and ball-milled mixtures, respectively, and ~100.2 % for the 3:1

mixture. The three stages seen in Figure 6.12 are likely due to reduction, followed by step-wise Na-insertion into the manganese oxide tunnels and layers.

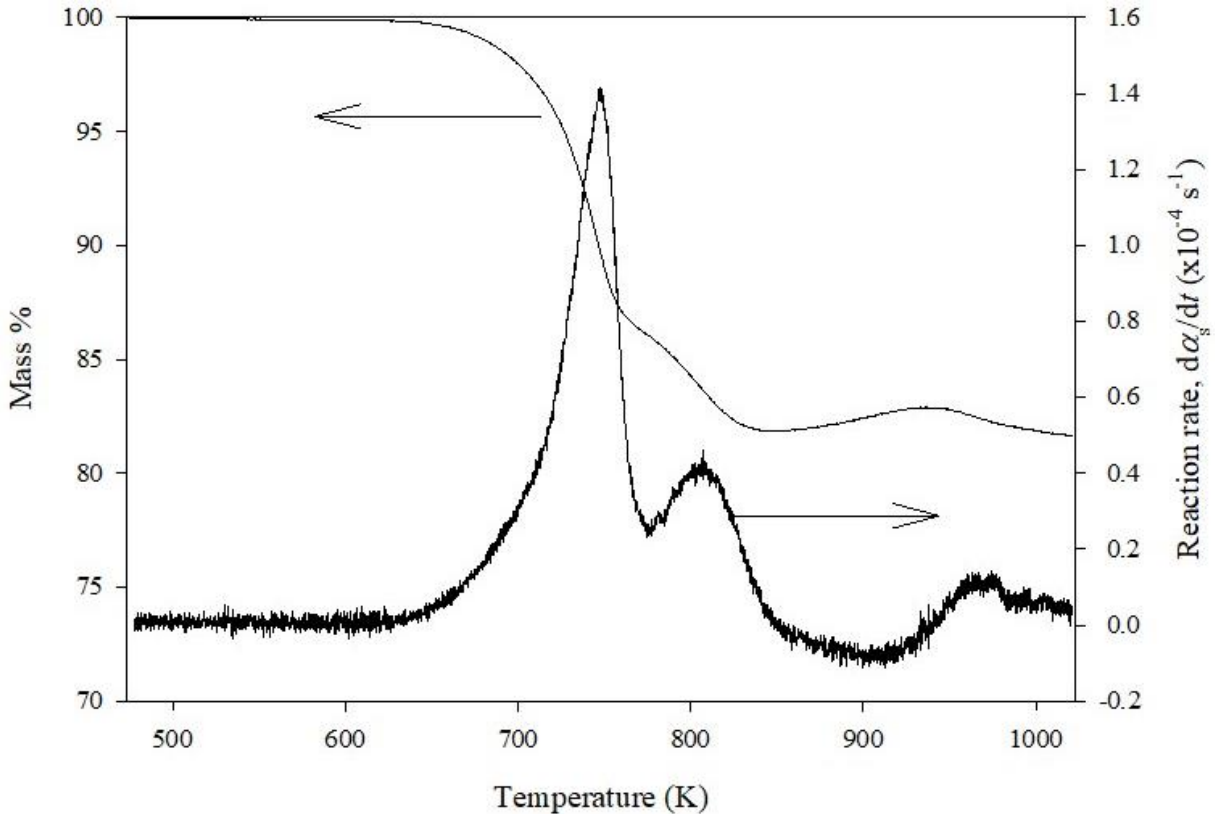

Figure 6.12 – Mass % and reaction rate vs. temperature for thermal treatment of ball-milled MnO_2 and Na_2CO_3 (3:1 mole ratio), at β=5 $K.min^{-1}$.

Ball-milling pre-treatment shifted the mass loss to lower temperature owing to an increased number of contact points between reactants. Ball-milling also lowered the barrier to CO_2 and O_2 transport away from reaction sites due to increased interstitial pore volume. Increasing the mole fraction of MnO_2 also shifted the mass loss to lower temperature, likely owing to a greater total surface area of the limiting reactant, which in this case is MnO_2.

Peaks due to $NaMnO_2$ and $Na_{0.66}MnO_2$ were observed in the XRD patterns (see Figure 6.10) for the jar-mixed and ball-milled samples after heating to 1073 K. Peaks due to $NaMnO_2$ were much smaller for the ball-milled sample than for the jar-mixed one. The formation of $Na_{0.66}MnO_2$ might be explained by reaction of $NaMnO_2$ with O_2, CO_2 and H_2O in air, after removal from the furnace. These reactions can be generalized as:

$$\mathrm{NaMnO_{2(s)}} + \frac{(1-\mathrm{x})}{2}\mathrm{H_2O_{(g)}} + \frac{\mathrm{x}}{2}\mathrm{O_{2(g)}} \Leftrightarrow \mathrm{Na_xMnO_{2(s)}} + (1-\mathrm{x})\mathrm{NaOH} \qquad 6.25$$

$$2\mathrm{NaOH} + \mathrm{CO_{2(g)}} \rightarrow \mathrm{Na_2CO_3.H_2O_{(s)}} \qquad 6.26$$

Alternative mechanisms have been proposed. For example, Le Goff et al. (1993) detected a similar product, $Na_{0.7}MnO_{2.14}$, during thermal treatment of MnO_2 and Na_2CO_3 when heating to a temperature of 873 K. They assumed that the 30 % of sodium ions which were unaccounted for were present in the form of NaOH adsorbed on the surface of the material. On the other hand, Huang and Luo (2016) suggest that "Na-rich amorphous phases may form during heat treatment, either as bulk secondary phases or as 2-D interfacial phases (nanoscale surface or intergranular amorphous films)".

The reaction rate data in Figure 6.11 show a second period of mass loss beyond 1073 K for the ball-milled mixture and >1073 K for the jar-mixed sample. This subsequent mass loss is characteristic of decomposition of unreacted Na_2CO_3. For the 3:1 mixture there was no further mass loss above 923 K, since all Na_2CO_3 was consumed during reaction with MnO_2.

Figure 6.12 shows that, for MnO_2:Na_2CO_3 (3:1 mole ratio) heated at β=5 K.min^{-1}, there was first mass loss, then gain, which is most reasonably explained by Eq. 6.21 and Eq. 6.24 followed by:

$$2NaMnO_{2(s)} + 1/2Mn_2O_{3(s)} + 1/4O_{2(g)} \Leftrightarrow 3Na_{0.66}MnO_{2(s)} \quad 6.27$$

The above sequence of steps gave a mass closure of ~99.1 %. Lower heating rate facilitates reaction by Eq. 6.27 since this reaction is limited by the availability of $O_{2(g)}$, which is at a low concentration in the purge gas.

Since thermal reduction of MnO_2 occurs prior to its reaction with Na_2CO_3, it is unlikely to be a suitable reagent for regeneration of NaOH in DAC. Thus, MnO_2 was not investigated any further. The results suggest that Mn_2O_3 might be more suitable.

6.5.3.2 Mn_2O_3

Mn_2O_3 was analyzed by XRD before and after ball-milling (see Figure 6.13). All peaks could be indexed to Mn_2O_3. Ball-milling caused peak-broadening due to the Scherrer phenomenon. Mn_2O_3 was combined with Na_2CO_3 and ball-milled for 1 h. The major peaks were indexed due to Na_2CO_3, $Na_2CO_3.H_2O$ as well as Mn_2O_3. This suggests that no reaction occurred during milling other than some partial hydration of Na_2CO_3.

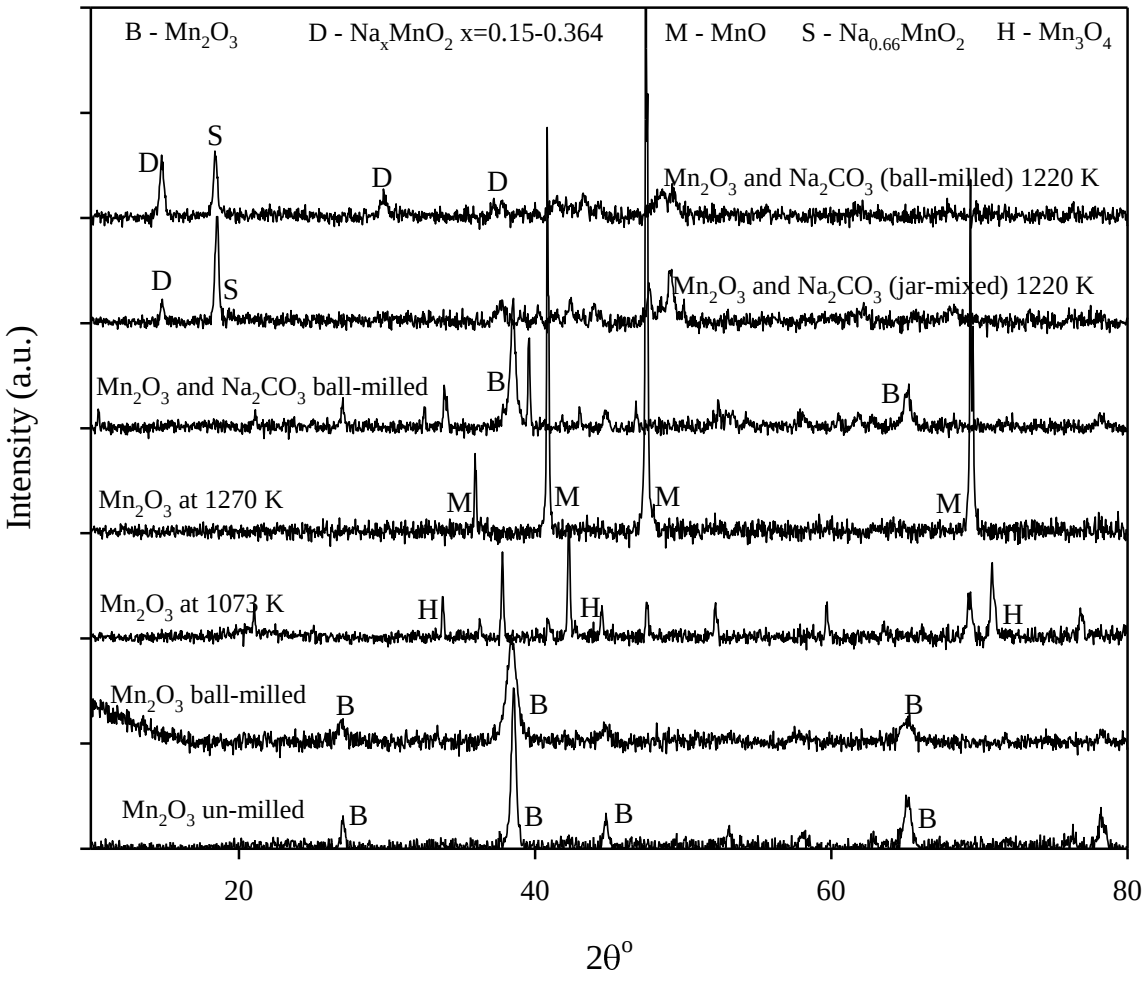

Figure 6.13 – X-ray diffraction patterns for un-milled and ball-milled Mn_2O_3, and jar-mixed and ball-milled Mn_2O_3 and Na_2CO_3 (1:1 mole ratio) after heating to different temperatures at β=20 K.min^{-1}.

Figure 6.14 shows the rate data for thermal treatment of un-milled and ball-milled Mn_2O_3 in an atmosphere of flowing N_2. The first mass loss which occurs at ~873 K (un-milled) and ~723 K (ball-milled) is due to thermal reduction of MnO_2 impurity (~1 % by mass) via Eq. 6.21. This impurity was not detected by XRD analysis in the starting reagents. XRD analysis of the ball-milled sample after heating to 1073 K, gave matches to Mn_3O_4. Therefore, the second mass loss appeared to follow Eq. 6.22. Mass closure was 98.5 % for the un-milled sample. A third mass

loss was observed, but only for the ball-milled sample. XRD analysis of the ball-milled sample after heating to 1270 K provided patterns corresponding to MnO. For reaction of the ball-milled mixture, selection of the initial and final mass for the purpose of mass balance calculations was difficult since the end of the second reaction overlapped with the beginning of the third. The second and third mass losses taken together gave a mass closure of 100.4 % for the reaction described by Eq. 6.22 followed by that corresponding to Eq. 6.23.

Figure 6.14 shows reaction rate vs. temperature for the reaction of Mn_2O_3 with Na_2CO_3 in a 1:1 mole ratio for un-milled and ball-milled mixtures. Both reactions began at ~673 K. However, ball-milling lowered T_{max} and T_f by 143 K and 200 K respectively. The jar-mixed sample showed a second peak at 1087 K due to an increased reaction rate on nearing the Na_2CO_3 melting point. These observations suggest that the reaction is limited by contacting between the two reagents. Ball-milling creates a high degree of contact between the reagents, enabling large increases in the reaction rate at lower temperatures.

Mass closure of ~99.0 % for the ball-milled sample and ~97.5 % for the jar-mixed sample were obtained for the reaction:

$$\mathrm{Mn_2O_{3(s)} + Na_2CO_{3(s)} \Leftrightarrow 2NaMnO_{2(s)} + CO_{2(g)} \qquad \Delta H = +132\ kJ.mol^{-1}\ at\ 298\ K} \qquad 6.28$$

For both the jar-mixed and ball-milled mixtures, two major sodium manganese oxide products were detected based on XRD analysis: $Na_{0.2}MnO_2$ and $Na_{0.66}MnO_2$. Since the mass balance gave good correspondence to Eq. 6.28, the presence of $Na_{0.2}MnO_2$ and $Na_{0.66}MnO_2$ might be

explained by reaction of $NaMnO_2$ with the reactive components of the air after removal from the furnace (see Eqs. 6.25 and 6.26).

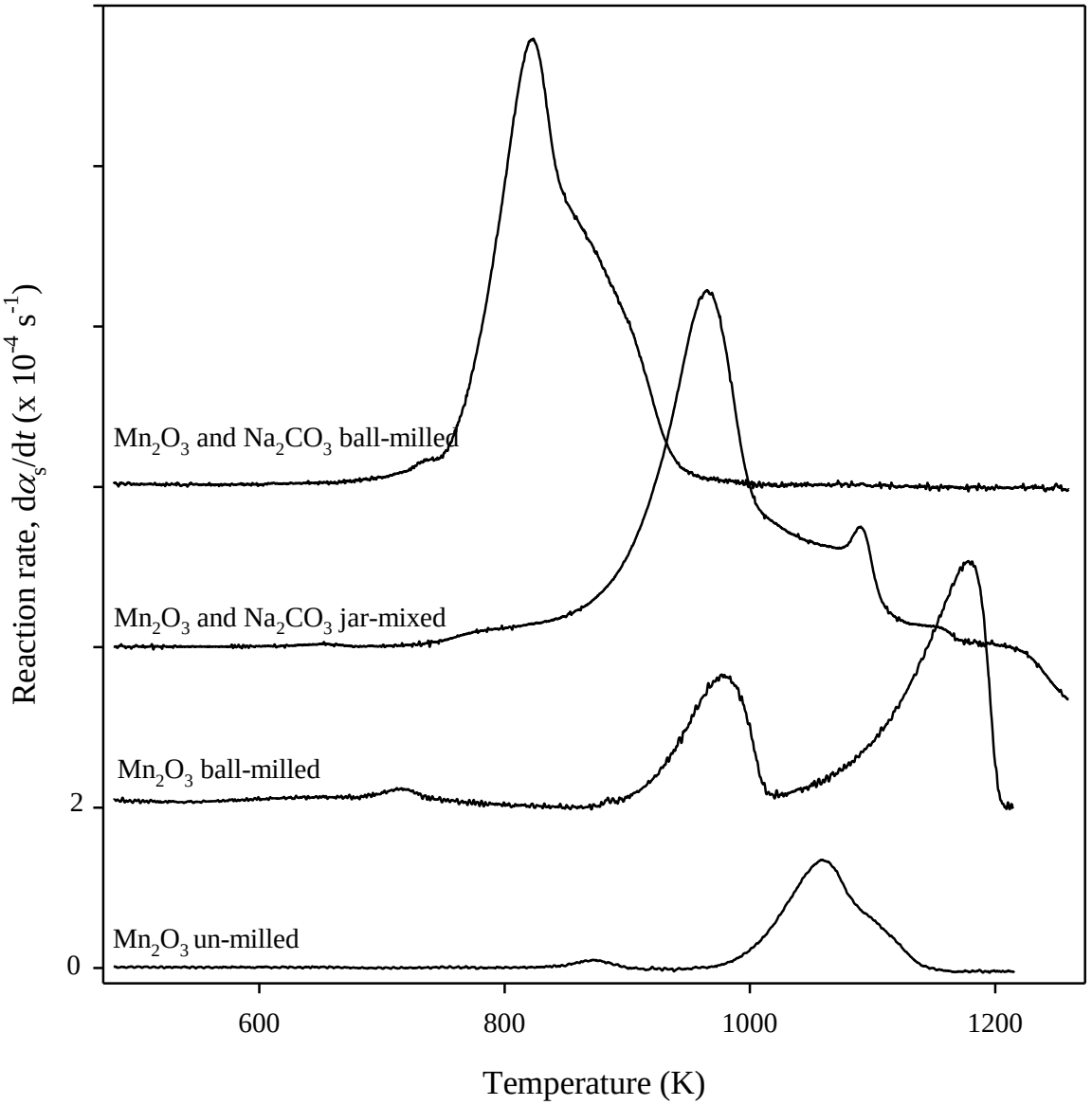

Figure 6.14 – Reaction rate vs. temperature for thermal treatment (β=20 K.min^{-1}) of un-milled and ball-milled Mn_2O_3 and jar-mixed and ball-milled mixtures of Mn_2O_3 and Na_2CO_3 (1:1 mole ratio).

Figure 6.15 shows the same heat treatment applied to a ball-milled mixture of Mn_2O_3 and Na_2CO_3 in a 3:1 mole ratio. Mass loss began at ~573 K, followed by a noticeable period of mass gain from 1096-1236 K.

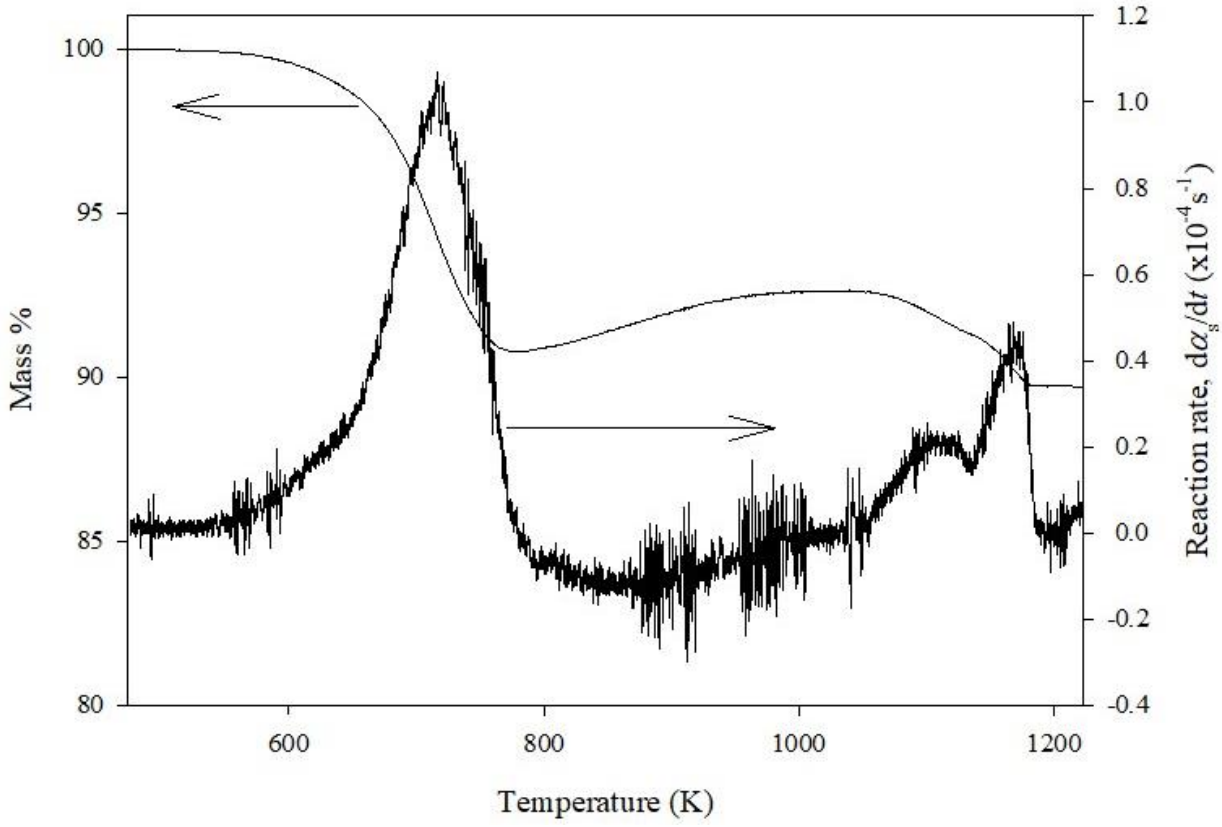

Figure 6.15 – Mass % and reaction rate vs. temperature for thermal treatment (β=20 K.min^{-1}) of ball-milled Mn_2O_3 and Na_2CO_3 (3:1 mole ratio).

Eq. 6.28 followed by:

$$NaMnO_{2(s)} + 1/4Mn_2O_{3(s)} + 1/8O_{2(g)} \Leftrightarrow 3/2Na_{0.66}MnO_{2(s)} \qquad 6.29$$

is proposed to explain the mass loss. Mass closure according to these two reactions was 99.9 %.

The products of thermal analysis (ball-milled mixture heated to 1073 K) were hydrolyzed and the liquid portion titrated. XRD analysis (see Figure 6.13) indicated that the solid products could be indexed to either Na_xMnO_2 where x=0.15-0.364, (such as $Na_{0.15}MnO_2.H_2O$, $Na_{0.55}Mn_2O_4.1.5H_2O$, $Na_{0.20}MnO_2$, $Na_4Mn_{14}O_{27}.9H_2O$, $Na_{0.29}MnO_20.75H_2O$, $Na_{0.58}(Mn_2O_4)1.38H_2O$, $Na_{0.58}Mn_{1.42}Mn_{0.58}O_4.2.3H_2O$, $Na_{0.31}MnO_2.0.4H_2O$ and $Na_{0.364}MnO_2.0.544H_2O$). Titration analysis indicated that approximately 70 % of the sodium was recovered as NaOH during hydrolysis of the thermal reaction products. Literature studies seem to suggest that full extraction of the Na content is possible. For example, Perret (2011) found that Na can be fully extracted from $NaMnO_2$ during hydrolysis, producing Mn_2O_3 and NaOH, while Omomo et al. (2002) report that 100 % of the Na could be extracted from $NaMnO_2$, but only using acidic conditions, forming protonic birnessite ($H_xMnO_2.0.6H_2O$ where x=0.1-0.3). Omomo et al. (2002) also indicated that $Mn^{3+}_{(s)}$ ions disproportionate into $Mn^{2+}_{(aq)}$ and $Mn^{4+}_{(s)}$ ions. This disproportionation and solubilization is undesirable from the perspective of Direct Air Capture. However, it is unlikely to occur in the highly alkaline environment that would exist in a typical DAC leaching unit.

The isoconversional activation energy for Eq. 6.28 was determined by the Advanced Isoconversional method (see Figure 6.17). It was found to rise from 170 kJ.mol^{-1} at α <0.4 to 220 kJ.mol^{-1} at α=0.5 and then to 230 kJ.mol^{-1} at α=0.8 as the Mn_2O_3 tunnels and layers are filled by diffusion of Na ions into the Mn_2O_3 structure: first, $Na_{0.2}MnO_2$, followed by $Na_{0.66}MnO_2$ and finally $NaMnO_2$. As the degree of inter-ion repulsion increases, the barrier to further Na-insertion increases, manifesting as an increase in the activation energy. The sharp

decrease above α=0.9 could be indicative of a switch to diffusion control, due to diffusion of Na_2CO_3 over the remaining Mn_2O_3 surfaces, or its diffusion of ions through the $NaMnO_2$ product.

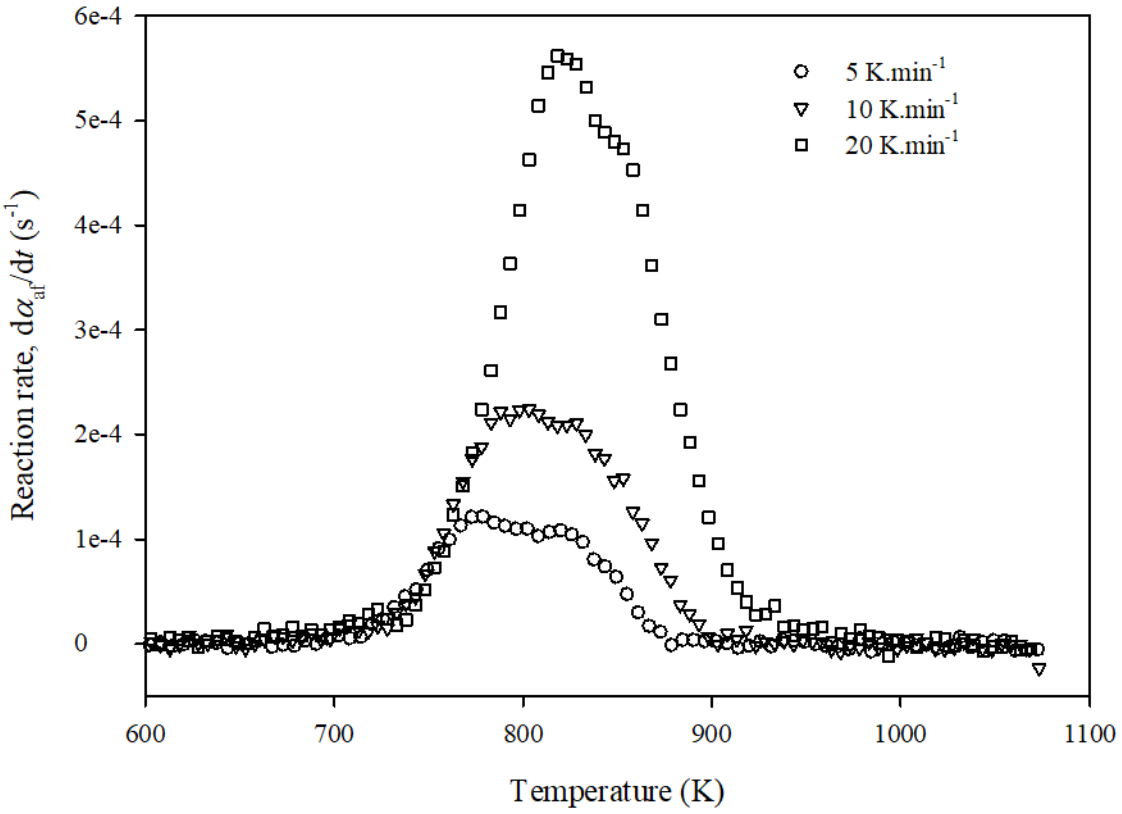

Figure 6.16 – Reaction rate vs. temperature for thermal treatment (β=5, 10 and 20 $K.min^{-1}$) of ball-milled Mn_2O_3 and Na_2CO_3 (1:1 mole ratio).

Mn_2O_3 facilitated full decomposition of Na_2CO_3, forming $NaMnO_2$. The products could be hydrolyzed, forming NaOH, but 30 % of the sodium appeared to remain bonded to the manganese oxide solids. Presumably, NaOH regeneration would be possible by switching between the Na-poor and Na-rich forms of Na_xMnO_2, in much the same way as sodium titanates enable regeneration of NaOH by cycling between $Na_2O.3TiO_{2(s)}$ and $4Na_2O.5TiO_{2(s)}$.

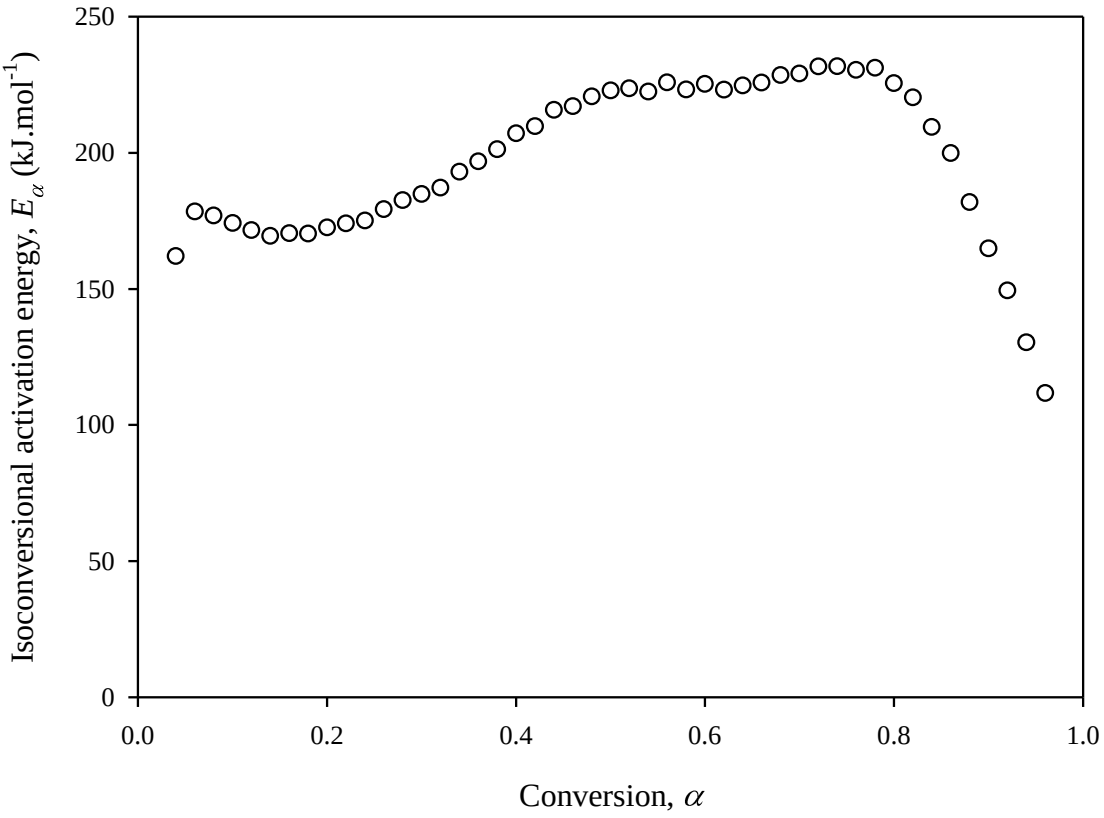

Figure 6.17 – Isoconversional activation energy vs. conversion for reaction of a ball-milled mixture of Mn_2O_3 and Na_2CO_3 (1:1 mole ratio).

The reaction of $Mn_2O_{3(s)}$ with $K_2CO_{3(s)}$ was also studied using the thermogravimetric method in order to assess bixbyite's potential for regeneration of $KOH_{(aq)}$. However, there was very little CO_2 loss during thermal treatment, in contrast to Eq. 5.33. This could be because larger K^+ ions have difficulty diffusing through relatively narrow Mn-O layers and tunnels. This demonstrates the importance of kinetic and mass transfer limitations in these reactive systems.

6.5.3.3 Mn_3O_4

Mn_3O_4 was analyzed by XRD before and after ball-milling (see Figure 6.18). All peaks could be indexed to Mn_3O_4. Ball-milling caused peak-broadening due to the Scherrer phenomenon.

Mn_3O_4 was ball-milled together with Na_2CO_3 for 1 h and analyzed by XRD. The major peaks were indexed due to Na_2CO_3, $Na_2CO_3.H_2O$ as well as Mn_3O_4.

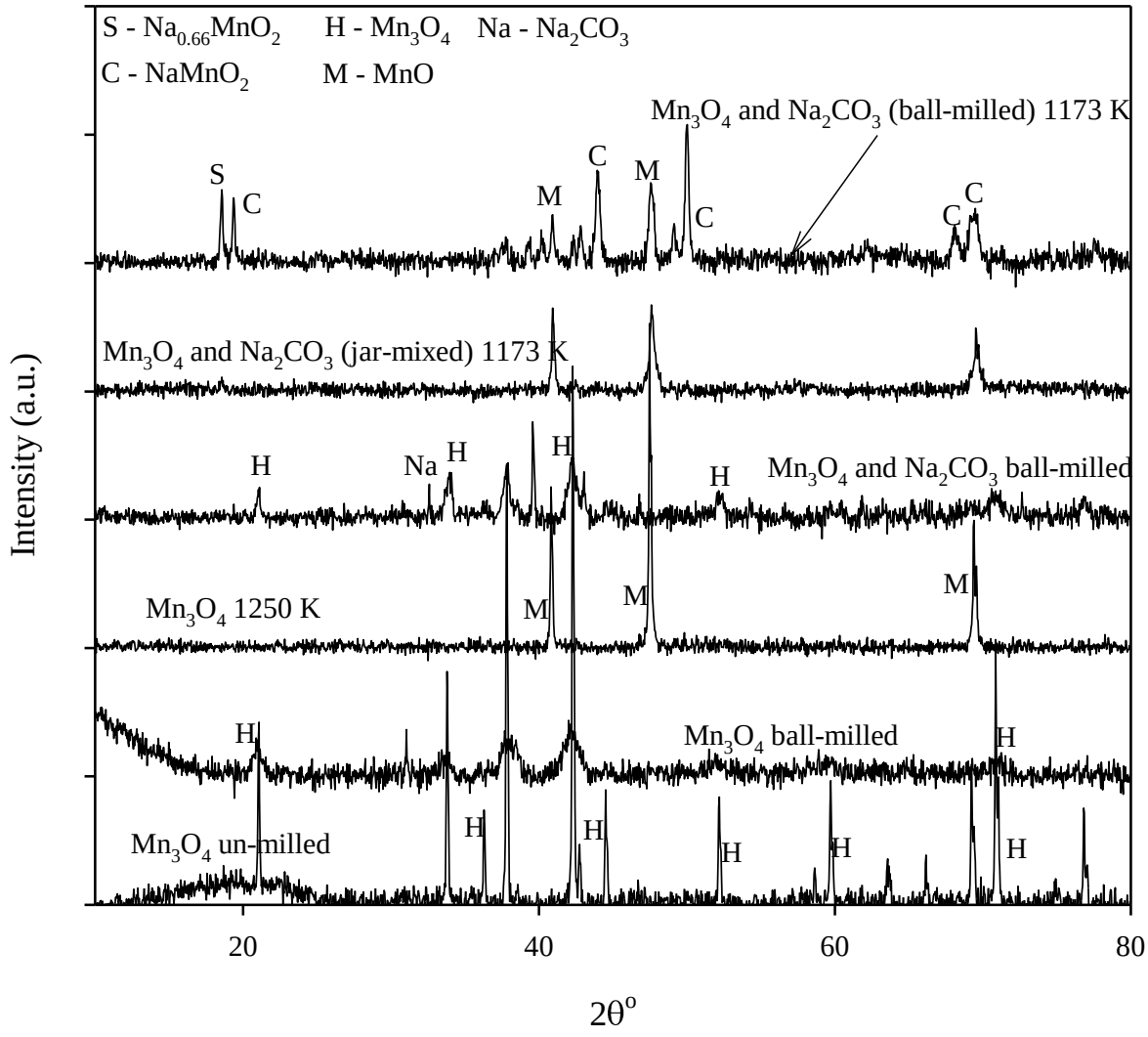

Figure 6.18 – X-ray diffraction patterns for un-milled and ball-milled Mn_3O_4, ball-milled Mn_3O_4 after heating to 1250 K, and jar-mixed and ball-milled Mn_3O_4 and Na_2CO_3 (1:1 mole ratio), before and after heating to 1173 K (β=20 K.min^{-1}).

Figure 6.19 shows rate curves for the thermal treatment of un-milled and ball-milled Mn_3O_4 in an atmosphere of flowing N_2. Heating of an un-milled sample gave negligible change in mass. This

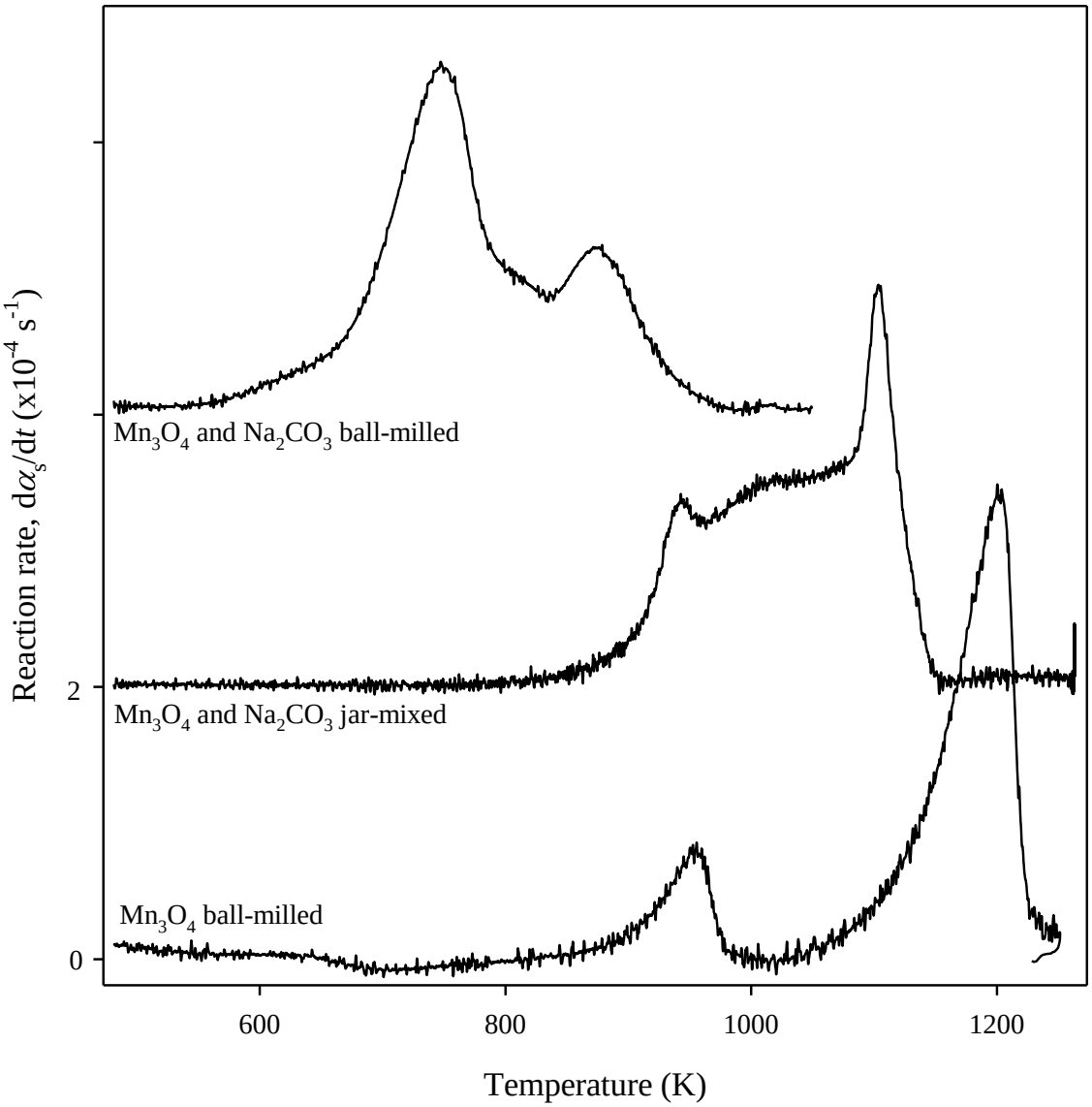

Figure 6.19 – Reaction rate vs. temperature for thermal treatment (β=20 K.min^{-1}) of jar-mixed and ball-milled Mn_3O_4 and Na_2CO_3 (1:1 mole ratio).

is consistent with the finding that Mn_3O_4 was reduced only at temperatures much greater than 1273 K (Tinsley and Sharp, 1971). On the other hand, ball-milled Mn_3O_4 showed a slight mass gain between 473 and 873 K, followed by two mass losses. This demonstrates the profound impact of ball-milling on the reactivity of Mn_3O_4. XRD analysis of ball-milled Mn_3O_4 after

heating to 1263 K indicated the presence of MnO, suggesting that the second, larger mass loss was due to reduction of Mn_3O_4 by the reaction corresponding to Eq. 6.23. The mass gain and loss below 1023 K were likely due to oxidation of Mn_3O_4 to Mn_2O_3 and its subsequent reduction back to Mn_3O_4. A mass balance suggests that the ball-milled sample contained 2 % Mn_2O_3, some of which is appears to be formed during the thermal treatment by oxidation.

Figure 6.19 shows the rate curve for the reactions of jar-mixed and ball-milled mixtures of Mn_3O_4 and Na_2CO_3 (1:1 mole ratio), at β=20 K.min^{-1}. For the jar-mixed sample, the reaction began at ~833 K, with rate maxima at 906 K and 1099 K, ending at 1153 K. For the ball-milled mixture, the reaction began at ~573 K, with two rate maxima at 745 K and 873 K, and then ending at 981 K. Therefore, ball-milling of the mixture prior to heating, shifted the period of mass loss to lower temperatures by 150-200 K.

XRD analyses of the reaction products (>1153 K) of the jar-mixed sample, showed peaks owing to MnO. For both mixtures, the major peaks were indexed to $Na_{0.7}MnO_2$ and $NaMnO_2$. At least one of the reactions may have been due to:

$$Mn_3O_{4(s)} + Na_2CO_{3(s)} \Leftrightarrow 2NaMnO_{2(s)} + MnO_{(s)} + CO_{2(g)} \qquad 6.30$$

in agreement with the mechanism proposed by Eames and Empie (2001) and Xu et al. (2012; 2013). However, mass closure according to Eq. 6.30 was not achieved. Assuming all mass loss is due to $CO_{2(g)}$ release, then only 81 % and 87 % of the Na_2CO_3 decomposed for the jar-mixed and ball-milled samples respectively. The failure to close the balance could suggest that oxidation

was also occurring, according to:

$$x\mathrm{NaMnO_{2(s)}} + (1-x)\mathrm{MnO_{(s)}} + \frac{1-x}{2}\mathrm{O_{2(g)}} \Leftrightarrow \mathrm{Na_xMnO_{2(s)}} \qquad 6.31$$

Figure 6.20 shows the reaction rate vs. temperature for the reaction of a 1:1 ball-milled mixture of Mn_3O_4 and Na_2CO_3 at a heating rate of 5 K.min^{-1}. There was a significant period of mass gain between 773 and 1073 K. This pattern of mass loss, followed by mass gain, is very similar to the reaction of a 3:1 ball-milled mixture of MnO_2 and Na_2CO_3 (see Figure 6.12) and also the 3:1 mixture of Mn_2O_3 and Na_2CO_3 (see Figure 6.20). These results agree with Xu et al. (2012) who suggest that the presence of Na^+ enables the oxidation of Mn^{2+} in Mn_3O_4 to Mn^{3+}. The strong

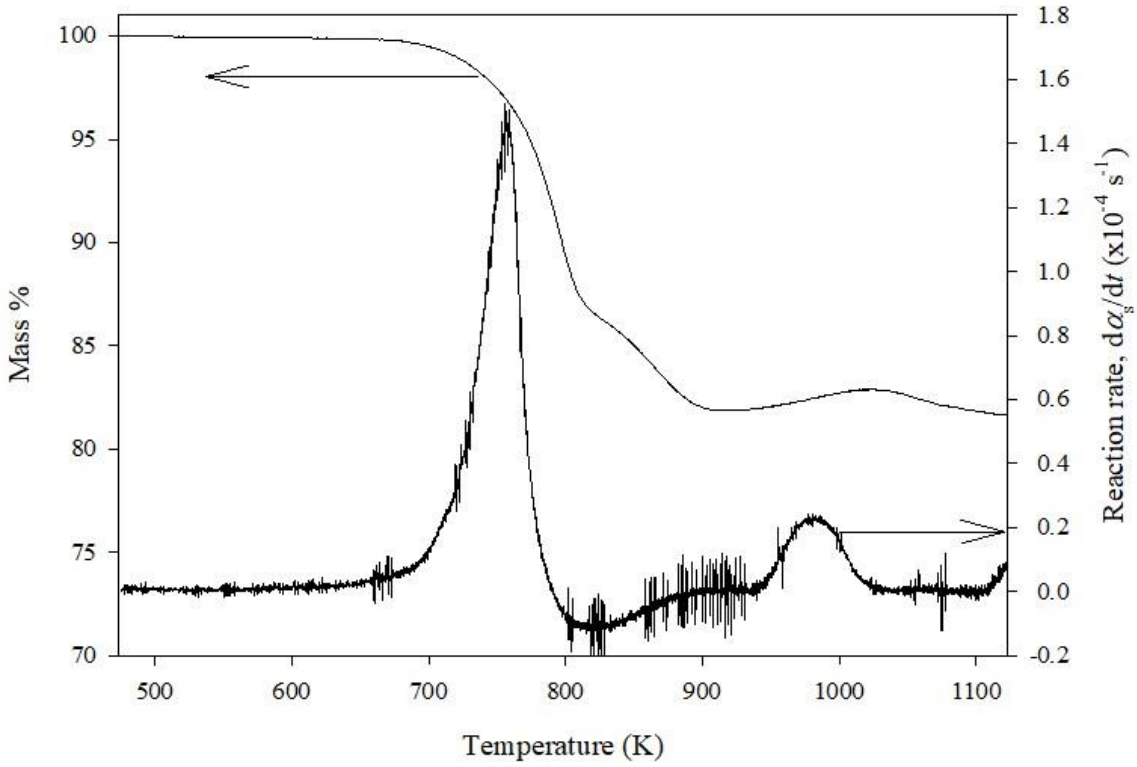

Figure 6.20 – Mass % and reaction rate vs. temperature for thermal treatment (β=5 K.min^{-1}) of ball-milled Mn_3O_4 and Na_2CO_3 (1:1 mole ratio).

tendency to oxidize means that Mn_3O_4 is unlikely to be suitable for regeneration of NaOH in DAC. Mn_3O_4 and MnO_2 also formed $NaMnO_2$ in reaction with Na_2CO_3, but these were more susceptible to redox processes.

6.5.4 Co_3O_4

Cobalt (II/III) oxide Co_3O_4 is the most thermodynamically stable oxide of cobalt at ambient conditions (Petitto et al., 2008). Ohtaki and Shouji (2005) showed that in $N_{2(g)}$, Co_3O_4 loses oxygen at 1108 K according to:

$$Co_3O_{4(s)} \Leftrightarrow 3CoO_{(s)} + 1/2O_{2(g)} \quad 6.32$$

Figure 11.7 indicates that mass loss begins at ~1000 K, and a mass balance suggests that decomposition of Co_3O_4 occurs according to Eq. 6.32. Ohtaki and Shouji (2005) also showed that reaction between Co_3O_4 and Na_2CO_3 in air commenced at ~873 K and can be written as:

$$6Na_2CO_{3(s)} + 8Co_3O_{4(s)} + 5O_{2(g)} \Leftrightarrow 24Na_{0.5}CoO_{2(s)} + 6CO_{2(g)} \quad 6.33$$

However, Motohashi et al. (2003) suggested that $Na_{0.5}CoO_2$ does not exist. Ohtaki and Shouji (2005) found that reaction between Na_2CO_3 and Co_3O_4 also occurred in N_2, but did not suggest a mechanism. In our work, an accurate mass balance could not be performed, since mass continued to be lost until the end of the test. Beyond 1140 K, it is likely that Na_2CO_3 decomposition also occurred, including volatilization of Na. An approximate balance from 900 to 1140 K suggests that Na_xCoO_2 is formed, where x=0.6-0.7. From our results, and a review of the literature, the following reaction is proposed to explain the overall transformation:

$$\frac{x}{2}Na_2CO_{3(s)} + Co_3O_{4(s)} \Leftrightarrow Na_xCoO_{2(s)} + 2CoO_{(s)} + \frac{x}{2}CO_{2(g)} + \frac{x}{2}O_{2(g)} \quad 6.34$$

where *x* is between 0 and 1. Several sodium cobaltates, with values of *x* between 0 and 1, have been reported in the literature (Rivadulla et al., 2003; Foury-Leylekian et al., 2009).

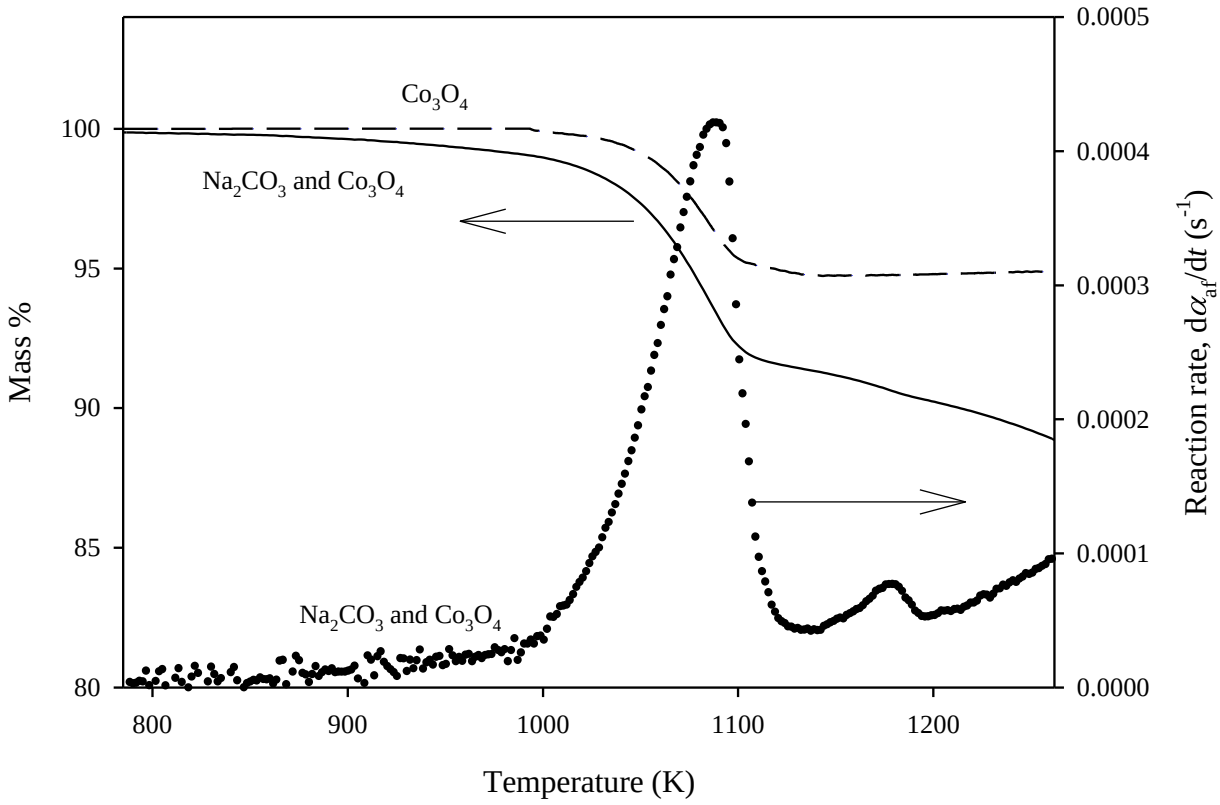

Figure 6.21 – Mass % and reaction rate vs. temperature for thermal treatment (β=20 K.min^{-1}) of ball-milled Co_3O_4 and a ball-milled mixture of Co_3O_4 and Na_2CO_3 (1:1 mole ratio).

Sakurai et al. (2007) found that $Na_{0.7}CoO_2$ is hydrolyzed in water, forming NaOH and $Na_x(H_3O)_zCoO_2$, with x+z=0.7. In our work, it was found that only 30 % of the Na could be recovered as NaOH from hydrolysis of the products. The high temperature of reaction with Na_2CO_3 (>1000 K) and the low recovery of NaOH, as well as reduction to CoO, suggest that

Co_3O_4 is not suitable as a reagent for regeneration of NaOH for DAC. In addition, at around 40-60 USD.kg^{-1}, it is much more expensive than other reagents, such as Fe_2O_3, Mn_2O_3 and TiO_2.

6.6 Conclusion

A multi-criteria decision analysis (MCDA) was performed for 60 oxides of the s-, p- and d-block elements, based on their acidity, solubility, cost and toxicity, for regeneration of NaOH for Direct Air Capture at large-scale. Based on assessment by these criteria, Co_3O_4, Cr_2O_3, Mn_3O_4, Mn_2O_3, MnO_2 and TiO_2, were deemed most suitable and carried forward for experiment by thermal analysis.

Co_3O_4 was thermally reduced at temperatures comparable with its reaction with Na_2CO_3. Cobalt is also the most expensive and toxic of the reagents tested here.

Cr_2O_3 reacted with Na_2CO_3 to produce sodium chromite, $NaCrO_2$, which could then be hydrolyzed, regenerating NaOH and Cr_2O_3. However, thermal treatment also resulted in formation of sodium chromate, a highly toxic compound. For Direct Air Capture, Na_2CrO_4 formation would need to be suppressed.

Other researchers have already demonstrated that TiO_2 (via $Na_2O.3TiO_2$) can be used to regenerate NaOH. However, our results suggest that these reactions are complex, with multiple sodium titanates being formed depending on the reaction conditions. In addition, reaction temperatures are higher than those of Fe_2O_3.

MnO_2 was reduced to Mn_2O_3 before it reacted with Na_2CO_3, while Mn_3O_4 was highly susceptible to oxidation in the presence of Na_2CO_3. Thus, despite claims to the contrary, MnO_2 and Mn_3O_4 were not found to be good reagents in this thesis.

Of all the oxides tested, Mn_2O_3 was the most promising. Mn_2O_3 reacted with Na_2CO_3 forming $NaMnO_2$, but formed Na_xMnO_2, where x=0.1-0.3, when hydrolyzed. Thus, cycling will occur in much the same way as the titanate pathway, cycling between Na-poor and Na-rich forms. Further work is needed to better understand the kinetics of its reaction with Na_2CO_3, and its cycling potential.

Finally, it is worth noting that the acidity scales given in Table 6.1 correctly predicted the relative rates of reaction between the oxides and Na_2CO_3. For example, MnO_2 with a high acidity of $N_M - 2\delta_M$=3.66 was found to react with Na_2CO_3 at ~800 K whereas Co_3O_4 with a lower acidity of $N_M - 2\delta_M$=2.05 was found to react with Na_2CO_3 at high temperature (>1000 K). The only exception was Mn_3O_4, which was found to be more reactive than its acidity value would suggest. This is proposed to be due to its tendency to oxidize, whereby it then becomes more reactive with Na_2CO_3.

Future work should include a study of the reactions of $K_2CO_{3(s)}$ with the same metal oxides which were identified by the multi-criteria decision analysis in this chapter, with investigation of $KOH_{(aq)}$ recovery by hydrolysis.

Chapter 7: Overall conclusions and recommendations

7.1 Conclusions

There are two proven methods for regeneration of alkali hydroxide solutions for large-scale capture of CO_2 from air: 1. Regeneration of $NaOH_{(aq)}$ or $KOH_{(aq)}$ by conventional causticization using lime and 2. Regeneration of $NaOH_{(aq)}$ by direct causticization using hematite. In each process, the high temperature step involves decomposition of a metal carbonate, as described by Eqs. 4.1 and 5.1, respectively. The design and economy of these processes depends greatly on these reactions, since they require high-temperature energy. Better understanding of the kinetics of these reactions could lead to lower temperatures which, in turn, could enable integration of DAC systems with heat from renewable, nuclear or industrial sources, making the process more sustainable than current designs which assume heat to be provided by burning natural gas. As such, the primary objective of this thesis was to study reactions Eqs. 4.1 and 5.1 using the thermogravimetric method, and then produce simple parameterized expressions for the rates which include the key operating variables such as temperature, time and conversion.

Although $CaCO_3$ decomposition is one of the most studied reactions in the kinetics of solids, its process rate is still a subject of much discussion, particularly the form of its pressure dependency. Here, a new Accumulation Model was developed to describe its rate (see Eq. 4.18). The model is derived by combining transition-state theory and equilibrium thermodynamics (Reading et al., 1989) with a simple accumulation parameter, *c*, to account for the effect of reaction-generated CO_2 (Criado et al., 1990). To parameterize the rate, the median isoconversional activation energy, $\tilde{E}_\alpha$, was determined using the Advanced Isoconversional

Method, aided by a novel "method of maximum permutations" which increases the accuracy of the isoconversional estimate by crossing repeat data. The Accumulation Model correctly predicted that E_α should decrease with increasing initial sample mass due to the increased rate of CO_2 accumulation in the interstices of the sample. Determining E_α at high heating rate (8-128 $K.min^{-1}$) provided an estimate of the intrinsic activation energy, E, for the forward reaction of 185 $kJ.mol^{-1}$. The method of invariant kinetics parameters was used to determine the isoconversional pre-exponential factor, A_α, which provided an estimate for the intrinsic pre-exponential factor of the forward reaction. Estimates for E and A were then used to anchor a curve fitting analysis via Eq. 4.18. By varying the accumulation parameter, c, and a correction factor, b_1, the Accumulation Model could be fit to all the conversion data at different sample mass, particle size and heating rate. Fitted values of c were found to increase directly proportional to the sample mass. The Accumulation Model demonstrates that there are two main ways to reduce the temperature of $CaCO_3$ decomposition in DAC systems: 1. By decreasing c which reduces CO_2 accumulation in the pores of particles/pellets, and 2. By reducing the bulk CO_2 partial pressure, P_{ext}, in the reactor. However, as discussed in the relevant sections of this thesis, lowering c and P_{ext}, may not be possible in practical systems. Therefore, other pathways for regeneration of alkali hydroxide solutions with more favourable thermodynamics and kinetics need to be investigated. One such pathway is regeneration using hematite, Fe_2O_3.

Regeneration of $NaOH_{(aq)}$ with $Fe_2O_{3(s)}$ (direct causticization) was investigated in this thesis, particularly the high temperature step involving reaction of Na_2CO_3 with Fe_2O_3 to produce $NaFeO_2$ and CO_2 (Eq. 5.1). There are very few studies related to the kinetics of this reaction. In

this thesis, a Contact Point Model (see Eq. 5.25), was found to describe the rate of reaction of Fe_2O_3 with Na_2CO_3 below the Na_2CO_3 melting point. The rate is dependent on the mole ratio, degree of compactness, and particle size, as well as the conversion and the temperature. The higher the surface area of contact between Na_2CO_3 and surrounding Fe_2O_3, the higher the reactivity. The Contact Point Model was found to fit experimental thermogravimetric data over a wide range of mole ratios (16:1 to 1:3) for particles of size <5 μm. Experiments with different mass also suggest that the accumulation of CO_2 plays a role in the kinetics. The median activation energy was determined by the Advanced Isoconversional method. The value of $\tilde{E}_\alpha$ decreased with conversion and increased as the mole ratio approached 1. These findings suggest that the Contact Point Model needs to be modified to include equilibrium thermodynamic considerations, as well as diffusion of reaction-generated CO_2.

Although the kinetics of reaction between Na_2CO_3 and Fe_2O_3 are more complicated than those of $CaCO_3$ decomposition, the enthalpy of reaction is lower. The temperature is also lower, but only when the Fe_2O_3 and Na_2CO_3 particles are small and the sample is well mixed. For example, pre-treatment of a 1:1 mixture of Fe_2O_3 and Na_2CO_3 by ball-milling enabled reaction to occur at a temperature 50 K lower than $CaCO_3$ decomposition. Using 16:1 mole ratio reduced temperatures by a further 50 K. This is promising from the perspective of Direct Air Capture where cost savings are possible by lowering the temperature of the process. In addition, Fe_2O_3 is as cheap as $CaCO_3$, and just as widely available, making it a good reagent for Direct Air Capture which aims to capture and concentrate large quantities of CO_2 from ambient air.

Ultimately, the reactor temperatures needed to give a reasonable rate of metal carbonate decomposition are determined by the equilibrium thermodynamics as well as the kinetics. New reaction pathways are needed if further temperature reductions are to be achieved. The secondary objective of this thesis was to screen various oxides which could react with $Na_2CO_{3(s)}$ at lower temperatures than $Fe_2O_{3(s)}$ but give comparable recovery of $NaOH_{(aq)}$ upon hydrolysis of the products. The temperature at which an oxide reacts with Na_2CO_3 depends on its acidity, described here as its tendency to accept a O^{2-} from the carbonate ion. A multi-criteria decision analysis (MCDA) was performed for over 60 oxides based on their acidity and other important characteristics such as solubility, cost and toxicity. Of these 60 oxides, Co_3O_4, Cr_2O_3, Mn_3O_4, Mn_2O_3, MnO_2 and TiO_2 were found to warrant further investigation. These were then tested using the same thermal analysis and kinetic methods as were used to study the CO_2 release reactions in the lime and hematite systems. It was found that the reactivity was greatest in the order MnO_2>Mn_2O_3/Mn_3O_4>Cr_2O_3>Fe_2O_3>TiO_2>Co_3O_4 in accordance with the theoretical acidity constants given in Table 6.1. The reaction of Na_2CO_3 with TiO_2 is considerably more complex than Fe_2O_3, as well as reaching completion at higher temperature. Co_3O_4 and MnO_2 were found to be thermally reduced before, or in parallel, to their reaction with Na_2CO_3, and thus were deemed unsuitable. Cr_2O_3 and Mn_3O_4 show potential, but were easily oxidized in the presence of Na_2CO_3. Of all the reagents studied, Mn_2O_3 showed the best potential (see Eq. 6.28) as it reacted with Na_2CO_3 at lower temperature and energy than Fe_2O_3. In addition, the current price of manganese ore is less than that of iron ore. However, approximately 30 % of the Na content of $NaMnO_2$ could not be extracted as NaOH by hydrolysis (1 h at 368 K), whereas ~10 % of the Na content could not be extracted from the $NaFeO_2$. Moreover, the kinetics of the

reaction of $Mn_2O_{3(s)}$ and $Na_2CO_{3(s)}$ are far from being understood. For example, the isoconversional activation energy showed a complex dependency on the conversion. Thus, despite some promising initial results, more work is needed to assess the viability of Mn_2O_3 for application to Direct Air Capture.

Finally, it is worth highlighting some of the other unique contributions of this thesis. These include introduction of the "optimization indicator" (see Appendix B), as well as development of a method of maximum permutations for determination of the average isoconversional activation energy (see Section 3.10) which increases the accuracy of the isoconversional estimate by crossing repeat data.

7.2 Recommendations

Based on the findings in this thesis, five main areas for future work are recommended:

1. Develop a more advanced kinetic model for reaction of Fe_2O_3 and Na_2CO_3 which accounts for equilibrium thermodynamics, ionic diffusion and CO_2 diffusion.
2. Test low-energy methods of mixing and pelletizing mixtures of Fe_2O_3 and Na_2CO_3 which give high degree of contact between the reagents. One possible avenue of exploration is spray-drying.
3. Further study of the reaction between Mn_2O_3 and Na_2CO_3, and subsequent recovery of NaOH, is needed. Mn_2O_3 must demonstrate the ability to regenerate NaOH over many hundreds, if not thousands, of cycles, just as Fe_2O_3 is known to do.

4. Investigate reactions of Na_2CO_3 with WO_3 and ZrO_2 which made it through the multi-criteria decision analysis but which were not studied here due to time considerations.
5. Despite KOH being more expensive than NaOH it is known to have higher CO_2 mass transfer rates during air contacting (Keith et al., 2018). Investigate the reactions of K_2CO_3 with MnO_2, Mn_3O_4, Cr_2O_3, Co_3O_4, WO_3, TiO_2 and ZrO_2. Further study into the viability of regenerating $KOH_{(aq)}$ using $Fe_2O_{3(aq)}$ is also needed.
6. Perform in-depth statistical analysis of the Advanced Isoconversional method which includes permutational statistics.

Bibliography

AINES, R. and FRIEDMANN, J., 2008. *Enabling Cost Effective CO_2 Capture Directly From the Atmosphere.* LLNL-TR-405787. Livermore, CA: Lawrence Livermore National Laboratory.

AKAHIRA, T. and SUNOSE, T., 1971. Method of determining activation deterioration constant of electrical insulating materials. *Research Report Chiba Institute of Technology,* **16**, pp. 22-31.

ANTONY, M., JHA, A. and TATHAVADKAR, V., 2006. Alkali roasting of Indian chromite ores: thermodynamic and kinetic considerations. *Mineral Processing and Extractive Metallurgy,* **115**(2), pp. 71-79.

ARCHER, P.D., MING, D.W. and SUTTER, B., 2013. The effects of instrument parameters and sample properties on thermal decomposition: Interpreting thermal analysis data from Mars. *Planetary Science,* **2**(1), pp. 2.

ARNOLD, R., FREDERIC, H. and SOL, T., 1956. *Process of preparing pure alkali metal niobate.* U.S. Patent 2,758,008.

ARRHENIUS, S., 1887. On the dissociation of substances dissolved in water. *Zeitschrift für physikalische Chemie,* **631**.

ÁVILA, I., CRNKOVIC, P.M., MILIOLI, F.E. and LUO, K.H., 2012. Thermal decomposition kinetics of Brazilian limestones: effect of CO_2 partial pressure. *Environmental technology,* **33**(10), pp. 1175-1182.

BACIOCCHI, R., STORTI, G. and MAZZOTTI, M., 2006. Process design and energy requirements for the capture of carbon dioxide from air. *Chemical Engineering and Processing: Process Intensification,* **45**(12), pp. 1047-1058.

BANDI, A., SPECHT, M., WEIMER, T. and SCHABER, K., 1995. CO_2 recycling for hydrogen storage and transportation—electrochemical CO_2 removal and fixation. *Energy Conversion and Management,* **36**(6), pp. 899-902.

BAO, L. and TRACHTENBERG, M.C., 2006. Facilitated transport of CO_2 across a liquid membrane: comparing enzyme, amine, and alkaline. *Journal of Membrane Science,* **280**(1), pp. 330-334.

BARKER, M.G. and HOOPER, A.J., 1973. Preparation and X-ray powder diffraction patterns of the sodium vanadates $NaVO_3$, $Na_4V_2O_7$, and Na_3VO_4. *Journal of the Chemical Society, Dalton Transactions,* **15**, pp. 1513-1517.

BARRET, P., 1968. Reaction rates and corresponding morphologic aspects in solid-gas reaction kinetics. *Journal de chimie physique et de physico-chimie biologique*, **65**(4), pp. 586.

BASF, 2 Jul 2011, 2011-last update, Engelhard Industrial Bullion (EIB) Prices [Homepage of BASF], [Online]. Available: https://apps.catalysts.basf.com/apps/eibprices/mp/ [28 Aug 2019, 2019].

BELMABKHOUT, Y., SERNA-GUERRERO, R. and SAYARI, A., 2010. Amine-bearing mesoporous silica for CO_2 removal from dry and humid air. *Chemical Engineering Science*, **65**(11), pp. 3695-3698.

BENSON, H., FIELD, J. and JIMESON, R., 1954. CO_2 absorption: employing hot potassium carbonate solutions. *Chemical Engineering Progress*, **50**(7), pp. 356-364.

BERUTO, D., BARCO, L. and SEARCY, A.W., 1984. CO_2-catalyzed surface area and porosity changes in high-surface-area CaO aggregates. *Journal of the American Ceramic Society*, **67**(7), pp. 512-516.

BIORECRO, 2011 Available: http://biorecro.com/?page=beccs_projects.

BLACHLY, C. and RAVNER, H., 1965. *Studies of Submarine Carbon Dioxide Scrubber Operation: Effect of an Additive Package for the Stabilization of Monoethanolamine Solutions.* NRL-MR-1598. Washington, DC: Naval Research Lab.

BLESA, M., MORAN, E., MENENDEZ, N., TORNERO, J. and TORRON, C., 1993. Hydrolysis of sodium orthoferrite [α-$NaFeO_2$]. *Materials Research Bulletin*, **28**(8), pp. 837-847.

BOLDYREV, V.V., 2006. Mechanochemistry and mechanical activation of solids. *Russian Chemical Reviews*, **75**(3), pp. 177.

BOSE, A., JANA, K., MITRA, D. and DE, S., 2015. Co-production of power and urea from coal with CO_2 capture: performance assessment. *Clean Technologies and Environmental Policy*, **17**(5), pp. 1271-1280.

BOYD, P.W., 2013. Ocean fertilization for sequestration of carbon dioxide from the atmosphere. *Geoengineering Responses to Climate Change.* New York, NY: Springer, pp. 53-72.

BRÖNSTED, J., 1923. The conception of acids and bases. *Recueil des Travaux Chimiques des Pays-Bas*, **42**, pp. 718-728.

BROWN, M., MACIEJEWSKI, M., VYAZOVKIN, S., NOMEN, R., SEMPERE, J., BURNHAM, A.A., OPFERMANN, J., STREY, R., ANDERSON, H. and KEMMLER, A.,

2000. Computational aspects of kinetic analysis: part A: the ICTAC kinetics project-data, methods and results. *Thermochimica Acta,* **355**(1), pp. 125-143.

BROWN, M.E. and GALWEY, A.K., 1989. Arrhenius parameters for solid-state reactions from isothermal rate-time curves. *Analytical Chemistry,* **61**(10), pp. 1136-1139.

BUDNEY, J., 1991. *Method of Recovering Caustic Soda from Spent Pulping Liquors.* Canadian Patent 1,283,256.

BUDRUGEAC, P., 2011. An iterative model-free method to determine the activation energy of heterogeneous processes under arbitrary temperature programs. *Thermochimica acta,* **523**(1), pp. 84-89.

CALVIN, K., WISE, M., CLARKE, L., EDMONDS, J., KYLE, P., LUCKOW, P. and THOMSON, A., 2013. Implications of simultaneously mitigating and adapting to climate change: initial experiments using GCAM. *Climatic Change,* **117**(3), pp. 545-560.

CAMERON, J., 1988. Vaporization from alkali carbonate melts with reference to the kraft recovery furnace. *Journal of Pulp and Paper Science,* **14**(4), pp. J76-J81.

CAMPBELL, J.S., 2012. *Microwave Swing Absorption for Carbon Capture*, Master's Dissertation, University of Edinburgh.

CAMPBELL, J.S., GRACE, J.R., LIM, C.J. and MOCHULSKI, D.W., 2016. A new diagnostic when determining the activation energy by the advanced isoconversional method. *Thermochimica Acta*, **636**, pp. 85-93.

CARTER, R.E., 1961. Kinetic Model for Solid-Solid Reactions, *The Journal of Chemical Physics*, **34**(6), pp. 2010-2015.

CHATTERJEE, S., MAHAPATRA, P., SINGH, A. and CHOUDHARY, R., 2003. Structural, electrical and dielectric properties of $Na_2W_4O_{13}$ ceramic. *Journal of Materials Science Letters,* **22**(2), pp. 99-101.

CHEN, C. and TAVONI, M., 2013. Direct air capture of CO_2 and climate stabilization: A model based assessment. *Climatic Change,* **118**(1), pp. 59-72.

CHEN, H. and LIU, N., 2010. Application of Non-Arrhenius Equations in Interpreting Calcium Carbonate Decomposition Kinetics: Revisited. *Journal of the American Ceramic Society,* **93**(2), pp. 548-553.

CHEN, K. and VYAZOVKIN, S., 2009. Isoconversional kinetics of glass aging. *The Journal of Physical Chemistry B,* **113**(14), pp. 4631-4635.

CHEN, T.L., LACERTE, C., WISE, S.S., HOLMES, A., MARTINO, J., WISE JR, J.P., THOMPSON, W.D. and WISE SR, J.P., 2012. Comparative cytotoxicity and genotoxicity of particulate and soluble hexavalent chromium in human and sperm whale (Physeter macrocephalus) skin cells. *Comparative Biochemistry and Physiology Part C: Toxicology & Pharmacology,* **155**(1), pp. 143-150.

CHEN, Y., JI, G., GUO, S., YU, B., ZHAO, Y., WU, Y., ZHANG, H., LIU, Z., HAN, B. and LIU, Z., 2017. Visible-light-driven conversion of CO_2 from air to CO using an ionic liquid and a conjugated polymer. *Green Chemistry*, **19**(24), pp. 5777-5781.

CHRISTODOULEAS, J.P., FORREST, R.D., AINSLEY, C.G., TOCHNER, Z., HAHN, S.M. and GLATSTEIN, E., 2011. Short-term and long-term health risks of nuclear-power-plant accidents. *New England journal of medicine,* **364**(24), pp. 2334-2341.

COLOMBO, G., 1973. *Study of CO_2 sorbents for extravehicular activity.* NASA-CR-114632, MDC-G4778. Los Angeles, CA: McDonnell-Douglas Astronautics Co.

COLOVIĆ, N., ANTONIJEVIĆ, M. and MILIĆ, S., 1994. Investigation of the kinetics of the reactions between sodium carbonate and oxides of transition metals. *Thermochimica acta,* **233**(1), pp. 113-125.

COONEY, J., DAY, M. and WILES, D., 1983. Thermal degradation of poly (ethylene terephthalate): a kinetic analysis of thermogravimetric data. *Journal of Applied Polymer Science,* **28**(9), pp. 2887-2902.

CORBETT, M.J. and SALINA, S.C., 1981. *Production of synthetic hydrocarbons from air, water and low cost electrical power.* U.S. Patent 4,282,187.

CORBETT, M., 1986. *Synfuel production ship.* U.S. Patent 4,568,522.

CORNEJO, J., 1986. The effect of heat treatment on textural evolution of ferrihydrite. *Materials Chemistry and Physics,* **15**(5), pp. 369-377.

COVEY, G., 1984. DARS the Direct Alkali Recovery System, *The Pacific Section of TAPPI, 37th Annual Seminar, Atlanta, GA* 1984, TAPPI Press.

COVEY, G. and LOI NGUYEN, K., 1995. Effects of fines on the operation of the direct alkali recovery system (DARS). *Appita Journal,* **48**(1), pp. 37-39.

CREUTZIG, F., POPP, A., PLEVIN, R., LUDERER, G., MINX, J. and EDENHOFER, O., 2012. Reconciling top-down and bottom-up modelling on future bioenergy deployment. *Nature Climate Change,* **2**(5), pp. 320-327.

CRIADO, J., MALET, P. and MUNUERA, G., 1987. Kinetic analysis of temperature-programmed desorption curves: application of the Freeman and Carroll method. *Langmuir,* **3**(6), pp. 973-975.

CRIADO, J., REAL, C., ORTEGA, A. and ALCALA, M., 1990. Influence of mass-transfer phenomena on the shape of EGA traces of solid-state reactions. *Journal of Thermal Analysis,* **36**(7-8), pp. 2531-2537.

CRIADO, J., GONZÁLEZ, M., MÁLEK, J. and ORTEGA, A., 1995. The effect of the CO_2 pressure on the thermal decomposition kinetics of calcium carbonate. *Thermochimica acta,* **254**, pp. 121-127.

CRIADO, J.M., GOTOR, F.J., ORTEGA, A. and REAL, C., 1992. The new method of constant rate thermal analysis (CRTA): Application to discrimination of the kinetic model of solid state reactions and the synthesis of materials. *Thermochimica Acta,* **199**(0), pp. 235-238.

CUELLAR-BERMUDEZ, S.P., GARCIA-PEREZ, J.S., RITTMANN, B.E. and PARRA-SALDIVAR, R., 2015. Photosynthetic bioenergy utilizing CO_2: an approach on flue gases utilization for third generation biofuels. *Journal of Cleaner Production,* **98**, pp. 53-65.

CUÉLLAR-FRANCA, R.M. and AZAPAGIC, A., 2015. Carbon capture, storage and utilisation technologies: A critical analysis and comparison of their life cycle environmental impacts. *Journal of CO2 Utilization,* **9**, pp. 82-102.

DAHL, C., 1884. *Process of manufacturing cellulose from wood.* U.S Patent 296,935A.

DAI, J., SINGH, A., KENTON H. AND KEITH D., 2010. Process simulation of direct CO_2 capture from air: Mass and Energy Balance, Unit Operations, GHGT 10 conference, Amsterdam, Netherlands.

DAMM, D.L. and FEDOROV, A.G., 2008. Conceptual study of distributed CO_2 capture and the sustainable carbon economy. *Energy Conversion and Management,* **49**(6), pp. 1674-1683.

DARROUDI, T. and SEARCY, A.W., 1981. Effect of carbon dioxide pressure on the rate of decomposition of calcite ($CaCO_3$). *The Journal of physical chemistry,* **85**(26), pp. 3971-3974.

DENNIS, J.S. and HAYHURST, A.N., 1984. The effect of pressure on the kinetics and extent of sulphation of calcareous materials. *Institution of the Chemical Engineers Symposium Series,* **87**, pp. 61-68.

DESIDERI, U. and PAOLUCCI, A., 1999. Performance modelling of a carbon dioxide removal system for power plants. *Energy Conversion and Management,* **40**(18), pp. 1899-1915.

DEUTCH, J., MONIZ, E., ANSOLABEHERE, S., DRISCOLL, M., GRAY, P., HOLDREN, J., JOSKOW, P., LESTER, R. and TODREAS, N., 2003. *The future of nuclear power.* An MIT Interdisciplinary Study. Cambridge, MA: Massachusetts Institute for Technology.

EAMES, D. and EMPIE, H.J., 2001. Direct Causticizing of Sodium Carbonate Using Manganese Oxide. *Nordic Pulp & Paper Research Journal,* **17**(4), pp. 369.

EBRAHIMI-KAHRIZSANGI, R., ABBASI, M.H. and SAIDI, A., 2010. Molybdenite alkali fusion and leaching: reactions and mechanism. *International Journal of Minerals, Metallurgy, and Materials,* **17**(2), pp. 127-131.

EISAMAN, M.D., ALVARADO, L., LARNER, D., WANG, P., GARG, B. and LITTAU, K.A., 2011. CO_2 separation using bipolar membrane electrodialysis. *Energy & Environmental Science,* **4**(4), pp. 1319-1328.

EL-DARS, F., ABUZEID, H., KHALIFA, M., SHALABI, M. and FARAG, A., 2002. Formation of sodium chromate from chromite ore concentrate and soda ash briquetting and factors affecting its recovery. *Egyptian journal of chemistry,* **45**(2), pp. 299-312.

ELDER, J. and READY, V., 1986. The kinetics of the thermal degradation of calcium carbonate. *Journal of Thermal Analysis,* **31**(2), pp. 395-405.

ESCARDINO, A., GARCIA-TEN, J. and FELIU, C., 2008. Kinetic study of calcite particle (powder) thermal decomposition: Part I. *Journal of the European Ceramic Society,* **28**(16), pp. 3011-3020.

ESCARDINO, A., GARCÍA-TEN, J., FELIU, C., SABURIT, A. and CANTAVELLA, V., 2013. Kinetic study of the thermal decomposition process of calcite particles in air and CO_2 atmosphere. *Journal of Industrial and Engineering Chemistry,* **19**(3), pp. 886-897.

FAN, L., WEN-XIANG, W., QI-KUN, H. and LING, W., 1990. Potassium ferrites of $KFeO_2$ and $K_{1+x}Fe_{11}O_{17}$ systems (x = 0–1): studies on leaching behavior in fused iron catalysts. *Journal of Solid State Chemistry,* **87**(2), pp. 264-273.

FARJAS, J. and ROURA, P., 2011. Isoconversional analysis of solid state transformations. *Journal of thermal analysis and calorimetry,* **105**(3), pp. 757-766.

FARJAS, J., BUTCHOSA, N. and ROURA, P., 2010. A simple kinetic method for the determination of the reaction model from non-isothermal experiments. *Journal of thermal analysis and calorimetry,* **102**(2), pp. 615-625.

FASIHI, M., EFIMOVA, O. and BREYER, C., 2019. Techno-economic assessment of CO_2 direct air capture plants. *Journal of Cleaner Production,* **224**, pp. 957-980.

FĂTU, D., 1991. Factors on which the rate of solid-solid reactions depends. *Thermochimica acta,* **177**, pp. 15-21.

FĂTU, D., 1988. Kinetic models for solid-solid reactions. *Thermochimica acta,* **131**, pp. 65-71.

FOURY-LEYLEKIAN, P., POLTAVETS, V., JAOUEN, N., RUEFF, J., LORENZO, J., AUBAN-SENZIER, P., PASQUIER, C., MAZZOLI, C. and GREENBLATT, M., 2009. Sodium ion and cobalt charge ordering in Na_xCoO_2 ($x \sim 5/6$). *Physical Review B,* **79**(11),.

FREI, V. and ČÁSLAVSKÁ, V., 1965. Kinetik der reaktionen von eisen (3)-und aluminiumoxid mit natrium-und kaliumcarbonat. *Chemiker-Zeitung,* **89**(12), pp. 399-&.

FRIEDMAN, H.L., 1964. Kinetics of thermal degradation of char-forming plastics from thermogravimetry. Application to a phenolic plastic. *Journal of Polymer Science Part C,* **6**(1), pp. 183-195.

FUKUZAKI, K., KOHIKI, S., MATSUSHIMA, S., OKU, M., HIDESHIMA, T., WATANABE, T., TAKAHASHI, S. and SHIMOOKA, H., 2000. Preparation and characterization of $NaInO_2$ and $NaInS_2$. *Journal of Materials Chemistry,* **10**(3), pp. 779-782.

FUSS, S., CANADELL, J.G., PETERS, G.P., TAVONI, M., ANDREW, R.M., CIAIS, P., JACKSON, R.B., JONES, C.D., KRAXNER, F. and NAKICENOVIC, N., 2014. Betting on negative emissions. *Nature Climate Change,* **4**(10), pp. 850-853.

GALAN, I., GLASSER, F.P. and ANDRADE, C., 2013. Calcium carbonate decomposition. *Journal of thermal analysis and calorimetry,* **111**(2), pp. 1197-1202.

GALLAGHER, P. and JOHNSON, D., 1973. The effects of sample size and heating rate on the kinetics of the thermal decomposition of $CaCO_3$. *Thermochimica Acta,* **6**(1), pp. 67-83.

GARBERS, A. and VAN VUUREN, C., 1987. A thermoanalytical study of the solid state reactions in the Cr_2O_3-Na_2CO_3-O_2 system. *Thermochimica acta,* **120**, pp. 9-17.

GARCIA-LABIANO, F., ABAD, A., DE DIEGO, L., GAYÁN, P. and ADÁNEZ, J., 2002. Calcination of calcium-based sorbents at pressure in a broad range of CO_2 concentrations. *Chemical engineering science,* **57**(13), pp. 2381-2393.

GARN, P.D., 1990. Kinetics of thermal decomposition of the solid state: II. Delimiting the homogeneous-reaction model. *Thermochimica Acta,* **160**(2), pp. 135-145.

GEBALD, C., WURZBACHER, J.A., TINGAUT, P., ZIMMERMANN, T. and STEINFELD, A., 2011. Amine-based nanofibrillated cellulose as adsorbent for CO_2 capture from air. *Environmental science & technology,* **45**(20), pp. 9101-9108.

GIBBINS, J. and CHALMERS, H., 2008. Preparing for global rollout: a 'developed country first'demonstration programme for rapid CCS deployment. *Energy Policy,* **36**(2), pp. 501-507.

GILLIGAN III, T.J., STREMPEL, T.G., DORIO, M.M. and BABINSKY, A.D., 1982. *Electrolysis of carbonates to produce hydroxides.* U.S. Patent 4,337,126.

GIOVANOLI, R., 1994. Thermogravimetry of manganese dioxides. *Thermochimica acta,* **234**, pp. 303-313.

GLOBAL CCS INSTITUTE, 2018. https://www.globalccsinstitute.com/resources/global-status-report/

GNANADESIKAN, A. and MARINOV, I., 2008. Export is not enough: nutrient cycling and carbon sequestration. *Marine Ecology Progress Series,* **364**, pp. 289-294.

GOEPPERT, A., METH, S., PRAKASH, G.S. and OLAH, G.A., 2010. Nanostructured silica as a support for regenerable high-capacity organoamine-based CO_2 sorbents. *Energy & Environmental Science,* **3**(12), pp. 1949-1960.

GOLDBERG, D.S., LACKNER, K.S., HAN, P., SLAGLE, A.L. and WANG, T., 2013. Co-location of air capture, subseafloor CO_2 sequestration, and energy production on the Kerguelen plateau. *Environmental science & technology,* **47**(13), pp. 7521-7529.

GRACE, T.M., 1981. *An evaluation of nonconventional causticizing technology for kraft chemical recovery.* Project-3473-3. Appleton, WI: The Institute of Paper Chemistry.

GREENWOOD, K. and PEARCE, M., 1953. The removal of carbon dioxide from atmospheric air by scrubbing with caustic soda in packed towers. *Transactions of the Institution of Chemical Engineers,* **31**, pp. 201-207.

HALIKIA, I., ZOUMPOULAKIS, L., CHRISTODOULOU, E. and PRATTIS, D., 2001. Kinetic study of the thermal decomposition of calcium carbonate by isothermal methods of analysis. *European Journal of Mineral Processing and Environmental Protection,* **1**(2), pp. 89-102.

HANSEN, J., RUEDY, R., SATO, M. and LO, K., 2010. Global surface temperature change. *Reviews of Geophysics,* **48**(4), pp. RG4004.

HANUSCH, J.M., KERSCHGENS, I.P., HUBER, F., NEUBURGER, M. and GADEMANN, K., 2019. Pyrrolizidines for direct air capture and CO_2 conversion. *Chemical communications,* **55**(7), pp. 949-952.

HARTMANN, J. and KEMPE, S., 2008. What is the maximum potential for CO_2 sequestration by "stimulated" weathering on the global scale? *Naturwissenschaften,* **95**(12), pp. 1159-1164.

HARTMANN, J., WEST, A.J., RENFORTH, P., KÖHLER, P., DE LA ROCHA, CHRISTINA L, WOLF-GLADROW, D.A., DÜRR, H.H. and SCHEFFRAN, J., 2013. Enhanced chemical weathering as a geoengineering strategy to reduce atmospheric carbon dioxide, supply nutrients, and mitigate ocean acidification. *Reviews of Geophysics,* **51**(2), pp. 113-149.

HARTVIGSEN, J.J., JOSHI, A.V., ELANGOVAN, S., BALAGOPAL, S., GORDON, J.H. and HOLLIST, M., 2011. *Electrochemical cell for production of synthesis gas using atmospheric air and water.* U.S. Patent 8,075,74.

HARVEY, L., 2008. Mitigating the atmospheric CO_2 increase and ocean acidification by adding limestone powder to upwelling regions. *Journal of Geophysical Research: Oceans,* **113**(C4), pp. C04028.

HEINRICH, J.J., 2003. *CO2 Capture from Air–Current Practices.* LFEE 2003- 001 WP. Cambridge, MA: Massachusetts Institute of Technology.

HEJAZI, B., 2017. *Modeling of biomass steam gasification in a dual fluidized bed reactor with/without lime-based CO_2 capture,* Doctoral Dissertation, University of British Columbia.

HERZOG, H., 2003. *Assessing the Feasibility of Capturing CO_2 from the Air.* Laboratory for Energy and the Environment 2. Cambridge, MA: Massachusetts Institute of Technology.

HICKS, J.C., DRESE, J.H., FAUTH, D.J., GRAY, M.M.L., QI, G. and JONES, C.W., 2008. Designing adsorbents for CO_2 capture from flue gas-hyperbranched aminosilicas capable of capturing CO_2 reversibly. *Journal of the American Chemical Society,* **130**(10), pp. 2902-2903.

HO, L.H., 2004. *Kinetics of the Titanate Causticization Reactions in a Potassium-Based Process,* Master's Dissertation, Georgia Institute of Technology.

HOLMES, G., NOLD, K., WALSH, T., HEIDEL, K., HENDERSON, M.A., RITCHIE, J., KLAVINS, P., SINGH, A. and KEITH, D.W., 2013. Outdoor prototype results for direct atmospheric capture of carbon dioxide. *Energy Procedia,* **37**, pp. 6079-6095.

HOLQUIST, J.B., KLAUS, D.M. and GRAF, J.C., 2014. Characterization of Potassium Superoxide and a Novel Packed Bed Configuration for Closed Environment Air Revitalization, *44th International Conference on Environmental Systems, Tucson, AZ* 2014, ICES.

HOUSE, K.Z., HOUSE, C.H., SCHRAG, D.P. and AZIZ, M.J., 2007. Electrochemical acceleration of chemical weathering as an energetically feasible approach to mitigating anthropogenic climate change. *Environmental science & technology,* **41**(24), pp. 8464-8470.

HOUSE, K.Z., BACLIG, A.C., RANJAN, M., VAN NIEROP, E.A., WILCOX, J. and HERZOG, H.J., 2011. Economic and energetic analysis of capturing CO_2 from ambient air. *Proceedings of the National Academy of Sciences of the United States of America,* **108**(51), pp. 20428-20433.

HU, N. and SCARONI, A.W., 1996. Calcination of pulverized limestone particles under furnace injection conditions. *Fuel,* **75**(2), pp. 177-186.

HUANG, J. and LUO, J., 2016. Composites of sodium manganese oxides with enhanced electrochemical performance for sodium-ion batteries: Tailoring properties via controlling microstructure. *Science China Technological Sciences,* **59**(7), pp. 1042-1047.

JANSON, J., 1979. Autocausticizing alkali and its use in pulping and bleaching. *Paperi ja puu,* **61**(8), pp. 495-504.

JANSON, J., 1978. The use of unconventional alkali in cooking and bleaching. Part 4. Alkali cooking of wood with the use of borate. *Paperi Ja Puu,* **60**(5), pp. 349-357.

JANSON, J., 1977. The use of unconventional alkali in cooking and bleaching. Part 1. A new approach to liquor generation and alkalinity. *Paperi Ja Puu,* **59**(6-7), pp. 425-430.

JANSON, J. and PEKKALA, O., 1978. The use of unconventional alkali in cooking and bleaching. Part 3. Oxygen-alkali cooking and bleaching with the use of borate. *Paperi ja puu,* **60**(2), pp. 89.

JANSON, J. and PEKKALA, O., 1977. The use of unconventional alkali in cooking and bleaching. Part 2. Alkali cooking of wood with the use of borate. *Paperi Ja Puu,* **59**(9), pp. 546.

JANSON, J. and SÖDERHJELM, L., 1988. The viscosity of borate-containing black liquor. *Nordic Pulp & Paper Research Journal,* **3**(2), pp. 107-110.

JANSSON, J. and PEKKALA, O., 1979. *The use of unconventional alkali in cooking and bleaching.* Keskuslaboratorio.

JENSEN, M.B., PETTERSSON, L.G., SWANG, O. and OLSBYE, U., 2005. CO_2 sorption on MgO and CaO surfaces: A comparative quantum chemical cluster study. *The Journal of Physical Chemistry B,* **109**(35), pp. 16774-16781.

JEONG, N.C., LEE, J.S., TAE, E.L., LEE, Y.J. and YOON, K.B., 2008. Acidity scale for metal oxides and Sanderson's electronegativities of lanthanide elements. *Angewandte Chemie International Edition,* **47**(52), pp. 10128-10132.

JIAO, F., WIJAYA, N., ZHANG, L., NINOMIYA, Y. and HOCKING, R., 2011. Synchrotron-based XANES speciation of chromium in the oxy-fuel fly ash collected from lab-scale drop-tube furnace. *Environmental science & technology,* **45**(15), pp. 6640-6646.

JOHANSSON, A., 1992. A preliminary assessment of the potential applicability of aluminate as an autocausticizing agent in the kraft process. *Bioresource technology,* **39**(2), pp. 199-203.

JOHNSON, I., CHOATE, W.T. and DAVIDSON, A., 2008. *Waste Heat Recovery: Technology and Opportunities in U.S. Industry.* Laurel, MD: BCS, Inc.

JOSEPH, K. and GNANASEKARAN, T., 1999. Thermoanalytical study of the reaction of potassium carbonate with ferric oxide. *Thermochimica acta,* **342**(1), pp. 153-160.

KANEKO, H., HOSOKAWA, Y., KOJIMA, N., GOKON, N., HASEGAWA, N., KITAMURA, M. and TAMAURA, Y., 2001. Studies on metal oxides suitable for enhancement of the O_2-releasing step in water splitting by the $MnFe_2O_4$–Na_2CO_3 system. *Energy,* **26**(10), pp. 919-929.

KANNICHE, M., GROS-BONNIVARD, R., JAUD, P., VALLE-MARCOS, J., AMANN, J. and BOUALLOU, C., 2010. Pre-combustion, post-combustion and oxy-combustion in thermal power plant for CO_2 capture. *Applied Thermal Engineering,* **30**(1), pp. 53-62.

KAR, B., DATA, P. and MISRA, V., 2005. Recovery of molybdenum from spent hydro-refining catalysts by soda ash roasting-A statistical approach. *The European Journal of Mineral Processing and Environmental Protection,* **5**(1), pp. 1303-0868.

KAR, S., GOEPPERT, A., GALVAN, V., CHOWDHURY, R., OLAH, J. and PRAKASH, G.S., 2018. A Carbon-Neutral CO_2 Capture, Conversion, and Utilization Cycle with Low-Temperature Regeneration of Sodium Hydroxide. *Journal of the American Chemical Society,* **140**(49), pp. 16873-16876.

KATZ, S.A. and SALEM, H., 1993. The toxicology of chromium with respect to its chemical speciation: a review. *Journal of Applied Toxicology,* **13**(3), pp. 217-224.

KEITH, D.W., HA-DUONG, M. and STOLAROFF, J.K., 2006. Climate strategy with CO_2 capture from the air. *Climatic Change,* **74**(1), pp. 17-45.

KEITH, D.W., 2000. Geoengineering the climate: History and prospect. *Annual Review of Energy and the Environment,* **25**(1), pp. 245-284.

KEITH, D.W. and HA-DUONG, M., 2003. CO_2 capture from the air: technology assessment and implications for climate policy, *Proceedings of the 6th Greenhouse Gas Control Conference, Kyoto, Japan* 2003, Pergamon, Oxford UK, pp. 187-197.

KEITH, D.W., HOLMES, G., ANGELO, D.S. and HEIDEL, K., 2018. A Process for Capturing CO_2 from the Atmosphere. *Joule,* **2**(8), pp. 1573-1594.

KEITH, D. and MAHMOUDKHANI, M., 2012. *Carbon dioxide capture.* U.S. Patent 8,119,091.

KHAWAM, A., 2007. *Application of solid-state kinetics to desolvation reactions*, Doctoral Thesis, University of Iowa.

KHAWAM, A. and FLANAGAN, D.R., 2006. Solid-state kinetic models: basics and mathematical fundamentals. *The Journal of Physical Chemistry B,* **110**(35), pp. 17315-17328.

KHAWAM, A. and FLANAGAN, D.R., 2005. Role of isoconversional methods in varying activation energies of solid-state kinetics: II. Nonisothermal kinetic studies. *Thermochimica Acta*, **436**(1), pp. 101-112.

KHESHGI, H.S., 1995. Sequestering atmospheric carbon dioxide by increasing ocean alkalinity. *Energy,* **20**(9), pp. 915-922.

KHINAST, J., KRAMMER, G., BRUNNER, C. and STAUDINGER, G., 1996. Decomposition of limestone: the influence of CO_2 and particle size on the reaction rate. *Chemical engineering science,* **51**(4), pp. 623-634.

KIISKILA, E., 1979. Recovery of sodium hydroxide from alkaline pulping liquors by smelt causticizing. Part 2. Reactions between sodium carbonate and titanium dioxide. *Paperi ja Puu,* **61**(5), pp. 394-401.

KIISKILA, E. and VALKONEN, N., 1979. Recovery of sodium hydroxide from alkaline pulping liquors by smelt causticizing. Part 4. Causticizing of sodium carbonate with ferric oxide. *Paperi ja puu,* **61**(8), pp. 505-510.

KIM, J. and LEE, H., 2001. Thermal and carbothermic decomposition of Na_2CO_3 and Li_2CO_3. *Metallurgical and Materials Transactions B,* **32**(1), pp. 17-24.

KINDERMANN, G.E., OBERSTEINER, M., RAMETSTEINER, E. and MCCALLUM, I., 2006. Predicting the deforestation-trend under different carbon-prices. *Carbon Balance and Management,* **1**(1), pp. 15.

KINGERY, W., 1974. Plausible Concepts Necessary and Sufficient for Interpretation of Ceramic Grain-Boundary Phenomena: II, Solute Segregation, Grain-Boundary Diffusion, and General Discussion. *Journal of the American Ceramic Society,* **57**(2), pp. 74-83.

KISSINGER, H.E., 1957. Reaction kinetics in differential thermal analysis. *Analytical Chemistry,* **29**(11), pp. 1702-1706.

KNICK, R. and KOHLMEYER, E., 1940. Über die Schmelzeigenschaften von Soda–Eisenoxyd-Gemischen. *Zeitschrift für anorganische und allgemeine Chemie,* **244**(1), pp. 67-84.

KOBE, K.A. and LEIPPER, A., 1940. The system trisodium phosphate-sodium carbonate-water. *Industrial & Engineering Chemistry,* **32**(2), pp. 198-203.

KOGA, N. and CRIADO, J., 1998. The influence of mass transfer phenomena on the kinetic analysis for the thermal decomposition of calcium carbonate by constant rate thermal analysis (CRTA) under vacuum. *International Journal of Chemical Kinetics,* **30**(10), pp. 737-744.

KOGA, N. and CRIADO, J., 1997. Influence of the particle size distribution on the CRTA curves for the solid-state reactions of interface shrinkage type. *Journal of Thermal Analysis and Calorimetry,* **49**(3), pp. 1477-1484.

KOHLER, P., HARTMANN, J. and WOLF-GLADROW, D.A., 2010. Geoengineering potential of artificially enhanced silicate weathering of olivine. *Proceedings of the National Academy of Sciences of the United States of America,* **107**(47), pp. 20228-20233.

KOLTA, G., HEWAIDY, I. and FELIX, N., 1972. Phase diagrams of binary systems vanadium oxide-sodium carbonate and vanadium oxide-sodium sulfate. *Erzmetall,* **25**(7), pp. 327-330.

KOLTA, G., HEWAIDY, I., FELIX, N. and GIRGIS, N., 1973. Reactions between sodium carbonate and vanadium pentoxide. *Thermochimica Acta,* **6**(2), pp. 165-177.

KOSMAC, T. and COURTNEY, T., 1992. Milling and mechanical alloying of inorganic nonmetallics. *Journal of Materials Research,* **7**(06), pp. 1519-1525.

KRIEGLER, E., EDENHOFER, O., REUSTER, L., LUDERER, G. and KLEIN, D., 2013. Is atmospheric carbon dioxide removal a game changer for climate change mitigation? *Climatic Change,* **118**(1), pp. 45-57.

KUBIC, W.L. and MARTIN, F.J., 2010. *Method of producing synthetic fuels and organic chemicals from atmospheric carbon dioxide.* U.S. Patent Application 12/682,442.

KUBOTA, K., IKEUCHI, I., NAKAYAMA, T., TAKEI, C., YABUUCHI, N., SHIIBA, H., NAKAYAMA, M. and KOMABA, S., 2014. New insight into structural evolution in layered $NaCrO_2$ during electrochemical sodium extraction. *The Journal of Physical Chemistry C,* **119**(1), pp. 166-175.

KÜÇÜK, F. and YILDIZ, K., 2006. The decomposition kinetics of mechanically activated alunite ore in air atmosphere by thermogravimetry. *Thermochimica acta,* **448**(2), pp. 107-110.

KUMAR, A., MADDEN, D.G., LUSI, M., CHEN, K., DANIELS, E.A., CURTIN, T., PERRY, J.J. and ZAWOROTKO, M.J., 2015. Direct air capture of CO_2 by physisorbent materials. *Angewandte Chemie International Edition,* **54**(48), pp. 14372-14377.

L'VOV, B.V., 2015. Kinetic parameters of $CaCO_3$ decomposition in vacuum, air and CO_2 calculated theoretically by means of the thermochemical approach. *Reaction Kinetics, Mechanisms and Catalysis,* **114**(1), pp. 31-40.

L'VOV, B.V., 2015. On the way from the activation model of solid decomposition to the thermochemical model. *Reaction Kinetics, Mechanisms and Catalysis,* **116**(1), pp. 1-18.

L'VOV, B.V., 2014. Thermochemical model in kinetics of heterogeneous reactions: 100-year jubilee. *Journal of Thermal Analysis and Calorimetry,* **116**(2), pp. 1041-1045.

L'VOV, B.V., 2007. The Self-cooling Effect. *Thermal decomposition of solids and melts: new thermochemical approach to the mechanism, kinetics and methodology.* Springer, pp. 87-98.

L'VOV, B.V., 2002. Mechanism and kinetics of thermal decomposition of carbonates. *Thermochimica acta,* **386**(1), pp. 1-16.

L'VOV, B.V., 2001. The physical approach to the interpretation of the kinetics and mechanisms of thermal decomposition of solids: the state of the art. *Thermochimica Acta,* **373**(2), pp. 97-124.

L'VOV, B.V., POLZIK, L.K. and UGOLKOV, V.L., 2002. Decomposition kinetics of calcite: a new approach to the old problem. *Thermochimica acta,* **390**(1), pp. 5-19.

L'VOV, B.V. and UGOLKOV, V.L., 2004. Peculiarities of $CaCO_3$, $SrCO_3$ and $BaCO_3$ decomposition in CO_2 as a proof of their primary dissociative evaporation. *Thermochimica acta,* **410**(1), pp. 47-55.

LACKNER, K.S., GRIMES, P. and ZIOCK, H.J., 2001. Capturing carbon dioxide from air. *Proceedings of the First International Sequestration Conference, Session 7B:Capture, V:Adsorption Studies, Alexandria, VA.* Department of Energy National Energy Technology Laboratory, pp. 1-15.

LACKNER, K.S., BRENNAN, S., MATTER, J.M., PARK, A.A., WRIGHT, A. and VAN DER ZWAAN, B., 2012. The urgency of the development of CO_2 capture from ambient air. *Proceedings of the National Academy of Sciences,* **109**(33), pp. 13156-13162.

LACKNER, K. and WRIGHT, A., 2012. *Methods and Systems for Capturing Carbon Dioxide From Dilute Sources.* U.S. Patent 9,387,433.

LACKNER, K. and WRIGHT, A., 2007. *Electrochemical methods and processes for carbon dioxide recovery from alkaline solvents for carbon dioxide capture from air.* U.S. Patent Application 11/227,660.

LACKNER, K., ZIOCK, H. and GRIMES, P., 1999. Carbon dioxide extraction from air: Is it an option? (No. LA-UR-99-583). Los Alamos National Lab., NM (US). .

LACKNER, K.S., 2003. Climate change. A guide to CO_2 sequestration. *Science (New York, N.Y.),* **300**(5626), pp. 1677-1678.

LAGARIAS, J.C., REEDS, J.A., WRIGHT, M.H. and WRIGHT, P.E., 1998. Convergence properties of the Nelder--Mead simplex method in low dimensions. *SIAM Journal on optimization,* **9**(1), pp. 112-147.

LAHIRI, A. and JHA, A., 2007. Kinetics and Reaction Mechanism of Soda Ash Roasting of Ilmenite Ore for the Extraction of Titanium Dioxide. *Metallurgical and Materials Transactions B,* 38, pp. 939-948.

LANGANKE, J., WOLF, A., HOFMANN, J., BÖHM, K., SUBHANI, M., MÜLLER, T., LEITNER, W. and GÜRTLER, C., 2014. Carbon dioxide (CO_2) as sustainable feedstock for polyurethane production. *Green* Chemistry, **16**(4), pp. 1865-1870.

LANGESLAY, R.R., KAPHAN, D.M., MARSHALL, C.L., STAIR, P.C., SATTELBERGER, A.P. and DELFERRO, M., 2018. Catalytic applications of vanadium: a mechanistic perspective. *Chemical reviews,* **119**(4), pp. 2128-2191.

LANGFORD, N.J., 2005. Carbon dioxide poisoning. *Toxicological reviews,* **24**(4), pp. 229-235.

LE GOFF, P., BAFFIER, N., BACH, S., PEREIRA-RAMOS, J. and MESSINA, R., 1993. Structural and electrochemical characteristics of a lamellar sodium manganese oxide synthesized via a sol-gel process. *Solid State Ionics,* **61**(4), pp. 309-315.

LE QUÉRÉ, C., RAUPACH, M.R., CANADELL, J.G., MARLAND, G., BOPP, L., CIAIS, P., CONWAY, T.J., DONEY, S.C., FEELY, R.A. and FOSTER, P., 2009. Trends in the sources and sinks of carbon dioxide. *Nature Geoscience,* **2**(12), pp. 831-836.

LEPAUMIER, H., PICQ, D. and CARRETTE, P., 2009. New amines for CO_2 capture. II. Oxidative degradation mechanisms. *Industrial & Engineering Chemistry Research,* **48**(20), pp. 9068-9075.

LESNIKOVICH, A. and LEVCHIK, S., 1983. A method of finding invariant values of kinetic parameters. *Journal of Thermal Analysis and Calorimetry,* **27**(1), pp. 89-93.

LEVITAN, D., 2010. Refilling the Carbon Sink: Biochar's Potential and Pitfalls. Yale Environment 360.

LEWIS, G.N., 1923. *Valence and the Structure of Atoms and Molecules.* New York: Chemical Catalog Company, Incorporated.

LEWIS, J.G. and MARTIN, A.J., 1979. *Method for obtaining carbon dioxide from the atmosphere and for production of fuels.* U.S. Patent 4,140,602.

LI, C., SHI, H., CAO, Y., KUANG, Y., ZHANG, Y., GAO, D. and SUN, L., 2015. Modeling and optimal operation of carbon capture from the air driven by intermittent and volatile wind power. *Energy,* **87**, pp. 201-211.

LI, D., SHI, H., DENG, J. and XU, Y., 2003. Study on the thermal decomposition kinetics of nano-sized calcium carbonate. *Journal of Zhejiang University SCIENCE A,* **4**(3), pp. 363-368.

LI, G., JIANG, T., LIU, M., ZHOU, T., FAN, X. and QIU, G. 2010. Beneficiation of High-Aluminium-Content Hematite Ore by Soda Ash Roasting, *Mineral Processing and Extractive Metallurgy Review*, **31**(3), 150-164.

LI, Y., GAO, Y., WANG, X., SHEN, X., KONG, Q., YU, R., LU, G., WANG, Z. and CHEN, L., 2018. Iron migration and oxygen oxidation during sodium extraction from $NaFeO_2$. *Nano energy,* **47**, pp. 519-526.

LIAVITSKAYA, T., GUIGO, N., SBIRRAZZUOLI, N. and VYAZOVKIN, S., 2017. Further insights into the kinetics of thermal decomposition during continuous cooling. *Physical Chemistry Chemical Physics,* **19**(29), pp. 18836-18844.

LIAVITSKAYA, T. and VYAZOVKIN, S., 2017. Delving into the kinetics of reversible thermal decomposition of solids measured on heating and cooling. *The Journal of Physical Chemistry C,* **121**(28), pp. 15392-15401.

LIU, B., ZHANG, Y., SU, Z., LI, G. and JIANG, T., 2016. Function mechanism of CO-CO_2 atmosphere on the formation of Na_2SnO_3 from SnO_2 and Na_2CO_3 during the roasting process. *Powder Technology,* **301**, pp. 102-109.

LIU, J., SONG, J., QI, T., ZHANG, C. and QU, J., 2016. Controlling the formation of Na_2ZrSiO_5 in alkali fusion process for zirconium oxychloride production. *Advanced Powder Technology,* **27**(1), pp. 1-8.

LIU, L., HUANG, X., YING, Z., QUAN, C., LIU, X. and LIU, B., 2013. The effect of silicon content in green liquor on properties of causticizing calcium carbonate. *China Pulp & Paper Industry,* **34**(4), pp. 26-28.

LOWIG, C., 1878. *Improvement in manufacture of caustic alkalies and preparations of alumina.* US Patent 201,028.

LOWRY, T., 1923. The uniqueness of hydrogen. *Journal of the Society of Chemical Industry,* **42**(3), pp. 43-47.

LU, W., SCULLEY, J.P., YUAN, D., KRISHNA, R. and ZHOU, H., 2013. Carbon dioxide capture from air using amine-grafted porous polymer networks. *The Journal of Physical Chemistry C,* **117**(8), pp. 4057-4061.

LUX, H., 1939. Acids" and "bases" in a fused salt bath: the determination of oxygen-ion concentration. *Z.Elektrochem.Soc,* **45**, pp. 303-310.

LYON, R.E., SAFRONAVA, N., SENESE, J. and STOLIAROV, S.I., 2012. Thermokinetic model of sample response in nonisothermal analysis. *Thermochimica Acta,* **545**, pp. 82-89.

MACIEJEWSKI, M. and RELLER, A., 1987. How (UN) reliable are kinetic data of reversible solid-state decomposition processes? *Thermochimica Acta,* **110**, pp. 145-152.

MADDERN, K., 1986. Mill-scale development of the DARS direct causticization process. *Pulp and Paper Canada,* **87**(10), pp. 78-82.

MAHMOUDKHANI, M., HEIDEL, K., FERREIRA, J., KEITH, D. and CHERRY, R.S., 2009. Low energy packed tower and caustic recovery for direct capture of CO_2 from air. *Energy Procedia,* **1**(1), pp. 1535-1542.

MAHMOUDKHANI, M. and KEITH, D.W., 2009. Low-energy sodium hydroxide recovery for CO2capture from atmospheric air—Thermodynamic analysis. *International Journal of Greenhouse Gas Control,* **3**(4), pp. 376-384.

MAO, L., GAO, B., DENG, N., LIU, L. and CUI, H., 2016. Oxidation behavior of Cr (III) during thermal treatment of chromium hydroxide in the presence of alkali and alkaline earth metal chlorides. *Chemosphere,* **145**, pp. 1-9.

MARGULIS, S., 2004. *Causes of deforestation of the Brazilian Amazon.* Working Paper 22 edn. Washington, D.C.: World Bank Publications.

MARTIN, F.J. and KUBIC, W., 2007. *Green Freedom: A concept for producing carbon-neutral synthetic fuels and chemicals.* La-UR-07-7897. Los Alamos, NM: Los Alamos National Laboratory.

MARTÍNEZ-DLCRUZ, L. and PFEIFFER, H., 2013. Cyclic CO_2 chemisorption–desorption behavior of Na_2ZrO_3: Structural, microstructural and kinetic variations produced as a function of temperature. *Journal of Solid State Chemistry,* **204**, pp. 298-304.

MATOVIC, D., 2011. Biochar as a viable carbon sequestration option: Global and Canadian perspective. *Energy,* **36**(4), pp. 2011-2016.

MAYA, J.C., CHEJNE, F., GÓMEZ, C.A. and BHATIA, S.K., 2018. Effect of the CaO sintering on the calcination rate of $CaCO_3$ under atmospheres containing CO_2. *AIChE Journal,* **64**(10), pp. 3638-3648.

MAZEL, V. and ASTANOVITZKAIA, S., 1936. Reactions Between Sodium Carbonate and Ferric Oxide and Alumina. *Legkie Met,* **5**(4), pp. 12-18.

MCLAREN, D., 2012. A comparative global assessment of potential negative emissions technologies. *Process Safety and Environmental Protection,* **90**(6), pp. 489-500.

MCLEAN, G., NIET, T., PRINCE-RICHARD, S. and DJILALI, N., 2002. An assessment of alkaline fuel cell technology. *International Journal of Hydrogen Energy,* **27**(5), pp. 507-526.

MEADOWCROFT, J., 2013. Exploring negative territory carbon dioxide removal and climate policy initiatives. *Climatic Change,* **118**(1), pp. 137.

MEDRANO-GARCÍA, J.D., RUIZ-FEMENIA, R. and CABALLERO, J.A., 2018. Multi-objective Optimization of a Carbon Dioxide Utilization Superstructure for the Synthesis of Formic and Acetic Acid. *Computer Aided Chemical Engineering,* **43**, pp. 1419-1424.

MEHMOOD, A., IQBAL, M.I., LEE, J., HWANG, J., JUNG, K. and HA, H.Y., 2016. A novel high performance configuration of electrochemical cell to produce alkali for sequestration of carbon dioxide. *Electrochimica Acta,* **219**, pp. 655-663.

MEIER, A., BONALDI, E., CELLA, G.M., LIPINSKI, W. and WUILLEMIN, D., 2006. Solar chemical reactor technology for industrial production of lime. *Solar Energy,* **80**(10), pp. 1355-1362.

MEIER, A., GREMAUD, N. and STEINFELD, A., 2005. Economic evaluation of the industrial solar production of lime. *Energy conversion and management,* **46**(6), pp. 905-926.

METALARY, 14 Mar 2016, 2019-last update, Titanium Price [Homepage of Metalary], [Online]. Available: https://www.metalary.com/titanium-price/28 Aug 2019].

METALS DAILY, 5 Oct 2017, 2019-last update, Live Prices [Homepage of Metals Daily], [Online]. Available: https://www.metalsdaily.com/live-prices/pgms/28 Aug 2019].

METZ, B., DAVIDSON, O. and DE CONINCK, H., 2005. *Carbon dioxide capture and storage: special report of the intergovernmental panel on climate change.* Cambridge, England: Cambridge University Press.

MILIĆ, S., COLOVIĆ, N., ANTONIJEVIĆ, M. and GAAL, F., 2000. A Thermoanalytical Study of the Solid State Reactions in the K_2CO_3-M_xO_y Systems. Evidence for a kinetic compensation effect. *Journal of thermal analysis and calorimetry,* **61**(1), pp. 229-238.

MILMAN, T. and BOUAZIZ, R., 1968. Sodium borates. *Annales De Chimie France,* **3**(4), pp. 311-321.

MILNE, C.R., SILCOX, G.D., PERSHING, D.W. and KIRCHGESSNER, D.A., 1990. High-temperature, short-time sulfation of calcium-based sorbents. 2. Experimental data and theoretical model predictions. *Industrial & Engineering Chemistry Research,* **29**(11), pp. 2201-2214.

MITRA, P., CHATTERJEE, A. and MAITI, H.S., 1998. Chemical deposition of ZnO films for gas sensors. *Journal of Materials Science: Materials in Electronics,* **9**(6), pp. 441-445.

MOCHULSKI, D., 2014. *Multiple reaction solid state kinetic parameter determination and its application to woody biomass*, Master's Dissertation, University of British Columbia.

MOFFAT, W. and WALMSLEY, M., 2005. Understanding lime calcination kinetics for energy cost reduction, *59th Appita Annual Conference and Exhibition: Incorporating the 13th ISWFPC (International Symposium on Wood, Fibre and Pulping Chemistry), Auckland, New Zealand*, 16-19 May 2005 2005, Appita Inc., pp. 487.

MÖLLERSTEN, K., YAN, J. and MOREIRA, J.R., 2003. Potential market niches for biomass energy with CO_2 capture and storage—opportunities for energy supply with negative CO_2 emissions. *Biomass and Bioenergy,* **25**(3), pp. 273-285.

MONKMAN, S. and MACDONALD, M., 2017. On carbon dioxide utilization as a means to improve the sustainability of ready-mixed concrete. *Journal of Cleaner Production,* **167**, pp. 365-375.

MONYONCHO, E. and BISSESSUR, R., 2013. Unique properties of α-$NaFeO_2$: De-intercalation of sodium via hydrolysis and the intercalation of guest molecules into the extract solution. *Materials Research Bulletin,* **48**(7), pp. 2678-2686.

MOTOHASHI, T., KARPPINEN, M. and YAMAUCHI, H., 2003. Sodium and oxygen nonstoichiometry and thermoelectric properties of Na_xCoO_{2+d}. *arXiv preprint cond-mat/0304479*, .

MOTZFELDT, K., 1955. The thermal decomposition. of sodium carbonate by the effusion method. *The Journal of physical chemistry,* **59**(2), pp. 139-147.

MUDHER, K.S., KESKAR, M., KRISHNAN, K. and VENUGOPAL, V., 2005. Thermal and X-ray diffraction studies on Na_2MoO_4, $Na_2Mo_2O_7$ and $Na_2Mo_4O_{13}$. *Journal of Alloys and Compounds,* **396**(1-2), pp. 275-279.

MURRAY, J.M., RENFREW, C.W., BEDI, A., MCCRYSTAL, C.B., JONES, D.S. and FEE, H.J., 1999. Amsorb a new carbon dioxide absorbent for use in anesthetic breathing systems. *The Journal of the American Society of Anesthesiologists,* **91**(5), pp. 1342-1342.

NÄFE, H., KARPUKHINA, N., GAUTAM, D. and NÄFE, G., 2014. Characterization of the Phase Mixture Comprising Sodium Hafnate and Hafnia. *Zeitschrift für anorganische und allgemeine Chemie,* **640**(10), pp. 1987-1995.

NAGAI, C., 2001. Development of iron oxide bubbling fluidized bed in direct causticization process. *TAPPI,* **55**(3), pp. 373-380.

NAGANO, T., MIYAO, S. and TAKEDA, K., 1974. Hopes oxygen pulping process: it's basic concept and some aspects for the reaction of oxygen pulping, *Non-Sulfur Pulping Symposium, Madison, WI, USA* 1974, TAPPI.

NAGASAWA, H., YAMASAKI, A., IIZUKA, A., KUMAGAI, K. and YANAGISAWA, Y., 2009. A new recovery process of carbon dioxide from alkaline carbonate solution via electrodialysis. *AIChE Journal,* **55**(12), pp. 3286-3293.

NAKAMURA, Y., HARASHIMA, K., HUKUDA, Y., TOKUMITSU, N. and YAMAMOTO, S., 1980. Decomposition of Sodium Carbonate and Its Mixture with Silica by Heating and Carbon-Reduction. *Tetsu-to-Hagané,* **66**(14), pp. 2023-2031.

NAKATANI, Y. and MATSUOKA, M., 1983. Some electrical properties of γ-Fe_2O_3 ceramics. *Japanese Journal of Applied Physics,* **22**(2R), pp. 233.

NAQVI, M., YAN, J. and DAHLQUIST, E., 2012. Synthetic gas production from dry black liquor gasification process using direct causticization with CO_2 capture. *Applied Energy,* **97**, pp. 49-55.

NDLELA, S.C. and SHANKS, B.H., 2003. Reducibility of potassium-promoted iron oxide under hydrogen conditions. *Industrial & Engineering Chemistry Research,* **42**(10), pp. 2112-2121.

NIKULSHINA, V., HIRSCH, D., MAZZOTTI, M. and STEINFELD, A., 2006. CO_2 capture from air and co-production of H_2 via the Ca $(OH)_2$-$CaCO_3$ cycle using concentrated solar power-Thermodynamic analysis. *Energy,* **31**(12), pp. 1379-1389.

NIKULSHINA, V., AYESA, N., GALVEZ, M. and STEINFELD, A., 2008. Feasibility of Na-based thermochemical cycles for the capture of CO_2 from air—thermodynamic and thermogravimetric analyses. *Chemical Engineering Journal,* **140**(1), pp. 62-70.

NIKULSHINA, V., GALVEZ, M. and STEINFELD, A., 2007. Kinetic analysis of the carbonation reactions for the capture of CO_2 from air via the Ca $(OH)_2$–$CaCO_3$–CaO solar thermochemical cycle. *Chemical Engineering Journal,* **129**(1), pp. 75-83.

NIKULSHINA, V., GEBALD, C. and STEINFELD, A., 2009. CO_2 capture from atmospheric air via consecutive CaO-carbonation and $CaCO_3$-calcination cycles in a fluidized-bed solar reactor. *Chemical Engineering Journal,* **146**(2), pp. 244-248.

NIKULSHINA, V. and STEINFELD, A., 2009. CO_2 capture from air via CaO-carbonation using a solar-driven fluidized bed reactor—effect of temperature and water vapor concentration. *Chemical Engineering Journal,* **155**(3), pp. 867-873.

NOHLGREN, I.M. and SINQUEFIELD, S.A., 2004. Black liquor gasification with direct causticization using titanates: equilibrium calculations. *Industrial & Engineering Chemistry Research,* **43**(19), pp. 5996-6000.

NOHLGREN, I., EDIN, M. and THELIANDER, H., 2003. Influence of carbon dioxide on the kinetics of the reaction between sodium carbonate and sodium trititanate. *Pulp & Paper Canada*, **104**(1), pp. 37-41.

NOHLGREN, I., THELIANDER, H., ZHUANG, Q. and VAN HEININGEN, A.R., 2000. Model study of the direct causticization reaction between sodium trititanate and sodium carbonate. *The Canadian Journal of Chemical Engineering*, **78**(3), pp. 529-539.

NOHLGREN, I., ZHUANG, Q., THELIANDER, H. and VAN HEININGEN, A., 2002. Direct causticization using titanates in a fluidized bed reactor. *Nordic Pulp & Paper Research Journal*, **17**(3), pp. 246-253.

NORFLEET, W. and HORN, W., 2003. *Carbon dioxide Scrubbing Capabilities of Two New Non-Powered Technologies.* TR1228. Groton, MA: Naval Submarine Medical Research Laboratory.

OECD/IEA, 2016. *Energy and Air Pollution: World Energy Outlook Special Report 2016.* Paris, France: International Energy Agency.

OHTAKI, M. and SHOUJI, K., 2005. Strong influence of CO_2 partial pressure on inhomogeneous Na distributions and the thermoelectric performance of polycrystalline $NaCo_2O_4$, *ICT 2005. 24th International Conference on Thermoelectrics, 2005.* 2005, IEEE, pp. 484-487.

ÖJEFORS, L. and CARLSSON, L., 1978. An iron—air vehicle battery. *Journal of Power Sources*, **2**(3), pp. 287-296.

OKAMOTO, S. and TAKEI, T., 1959. δ-Fe_2O_3. *Sci.Papers Inst.Phys.Chem.Res.(Tokyo)*, **53**, pp. 201-206.

OLAH, G.A., GOEPERT, A., METH, S. and PRAKASH, G.S., 2010. *Nano-structure supported solid regenerative polyamine and polyamine polyol absorbents for the separation of carbon dioxide from gas mixtures including the air.* U.S. Patent 7,795,17.

OMOMO, Y., SASAKI, T. and WATANABE, M., 2002. Preparation of protonic layered manganates and their intercalation behavior. *Solid State Ionics*, **151**(1-4), pp. 243-250.

ONO, Y., YUI, Y., HAYASHI, M., ASAKURA, K., KITABAYASHI, H. and TAKAHASHI, K.I., 2014. Electrochemical Properties of $NaCuO_2$ for Sodium-ion Secondary Batteries. *ECS Transactions*, **58**(12), pp. 33-39.

ORTEGA, A., 2008. A simple and precise linear integral method for isoconversional data. *Thermochimica Acta*, **474**(1-2), pp. 81-86.

ORTEGA, A., 2001. The kinetics of solid-state reactions toward consensus—Part I: Uncertainties, failures, and successes of conventional methods. *International Journal of Chemical Kinetics,* **33**(6), pp. 343-353.

OTSUBO, Y. and YAMAGUCHI, K., 1961. Thermochemical properties and reaction processes of alkali carbonate-ferric oxide systems as investigated by. 2. Na_2CO_3-Fe_2O_3 system. *Nippon Kagaku Zasshi,* **82**(5), pp. 561-&.

OZAWA, T., 1965. A new method of analyzing thermogravimetric data. *Bulletin of the Chemical Society of Japan,* **38**(11), pp. 1881-1886.

OZMEN, O., OZSOY-KESKINBORA, C. and SUVACI, E., 2018. Chemical stability of $KNbO_3$, $NaNbO_3$, and $K_{0.5}Na_{0.5}NbO_3$ in aqueous medium. *Journal of the American Ceramic Society,* **101**(3), pp. 1074-1086.

PACALA, S. and SOCOLOW, R., 2004. Stabilization wedges: solving the climate problem for the next 50 years with current technologies. *Science,* **305**(5686), pp. 968-972.

PACHAURI, R.K., ALLEN, M.R., BARROS, V., BROOME, J., CRAMER, W., CHRIST, R., CHURCH, J., CLARKE, L., DAHE, Q. and DASGUPTA, P., 2014. *Climate change 2014: synthesis Report. Contribution of working groups I, II and III to the fifth assessment report of the intergovernmental panel on climate change.* IPCC.

PALM, M. and THELIANDER, H., 1997. Kinetic study of the direct causticization reaction involving titanates and titanium dioxide. *Chemical Engineering Journal,* **68**(2), pp. 87-94.

PARRY, M.L., CANZIANI, O.F., PALUTIKOF, J.P., VAN DER LINDEN, P.J. and HANSON, C.E., 2007. *IPCC, 2007: climate change 2007: impacts, adaptation and vulnerability. Contribution of working group II to the fourth assessment report of the intergovernmental panel on climate change.* Cambridge, UK: Cambridge University Press.

PARSON, E.A., 2006. Reflections on air capture: The political economy of active intervention in the global environment. *Climatic Change,* **74**(1), pp. 5-15.

PAULING, L., 1960. *The Nature of the Chemical Bond.* Ithaca, New York: Cornell university press.

PAVLYUCHENKO, M. and PRODAN, E., 1961. Role of chemical and crystallization processes in reversible topochemical reactions. *Doklady Akademii nauk SSSR,* **136**(3), pp. 651-&.

PERES, V., FAVERGEON, L., ANDRIEU, M., PALUSSIÈRE, J., BALLAND, J., DELAFOY, C. and PIJOLAT, M., 2012. High temperature chromium volatilization from Cr_2O_3 powder and

Cr_2O_3-doped UO_2 pellets in reducing atmospheres. *Journal of Nuclear Materials,* **423**(1-3), pp. 93-101.

PERRET, R., 2011. *Solar Thermochemical Hydrogen Production Research (STCH).* SAND2011-3622. Livermore, CA: Sandia National Lab.(SNL-CA).

PETITTO, S.C., MARSH, E.M., CARSON, G.A. and LANGELL, M.A., 2008. Cobalt oxide surface chemistry: The interaction of CoO (1 0 0), Co_3O_4 (1 1 0) and Co_3O_4 (1 1 1) with oxygen and water. *Journal of Molecular Catalysis A: Chemical,* **281**(1-2), pp. 49-58.

PING, E., SAKWA-NOVAK, M. and EISENBERGER, P., 2018. Global thermostat low cost direct air capture technology, *International Conference on Negative CO_2 Emissions, Gothenburg, Sweden* 2018, pp. 22-24.

PLETCHER, D., GENDERS, J.D., WEINBERG, N.L. and SPIEGEL, E.F., 1993. *Electrochemical methods for production of alkali metal hydroxides without the co-production of chlorine.* U.S. Patent 5,246,551.

POLAK, R.B. and STEINBERG, M., 2012. *Carbon dioxide removal systems.* U.S. Patent Application 13/256,831.

POVAROV, V. and SOKOLOVA, O., 2009. The initial rate of solid-phase reaction and composition of the reaction product. *Russian Journal of General Chemistry*, **79**(10), pp. 2081-2086.

POWLSON, D., WHITMORE, A. and GOULDING, K., 2011. Soil carbon sequestration to mitigate climate change: a critical re-examination to identify the true and the false. *European Journal of Soil Science*, **62**(1), pp. 42-55.

PRASAD, S., 2010. Kinetics of chromium extraction as sodium chromate from stainless steel dust, *Proceedings of the XI International Seminar on Mineral Processing Technology (MPT-2010) (Vol. 2, No. Section 11)* 2010, Allied Publishers, pp. 788-796.

PRESTON, C.J., 2013. Ethics and geoengineering: reviewing the moral issues raised by solar radiation management and carbon dioxide removal. *Wiley Interdisciplinary Reviews: Climate Change*, **4**(1), pp. 23-37.

PRICE, R. and BLAISE, J.R., 2002. Nuclear fuel resources: Enough to last. *NEA News,* **20**(2), pp. 10-13.

QIN-HUA, W., HONG-SHENG, S., WEN-XIANG, C., LAI-SHUN, Q. and KANG-YING, S., 2011. Preparation and Luminescence Properties of the $Na_2W_2O_7$ Crystal. *Chinese Physics Letters,* **28**(11), pp. 118104.

QUILLIAM, R.S., MARSDEN, K.A., GERTLER, C., ROUSK, J., DELUCA, T.H. and JONES, D.L., 2012. Nutrient dynamics, microbial growth and weed emergence in biochar amended soil are influenced by time since application and reapplication rate. *Agriculture, Ecosystems & Environment,* **158**, pp. 192-199.

RAFIEE, A., KHALILPOUR, K.R., MILANI, D. and PANAHI, M., 2018. Trends in CO_2 conversion and utilization: a review from process systems perspective. *Journal of Environmental Chemical Engineering,* **6**(5), pp. 5771-5794.

RAMDIN, M., DE LOOS, T.W. and VLUGT, T.J., 2012. State-of-the-art of CO_2 capture with ionic liquids. *Industrial & Engineering Chemistry Research,* **51**(24), pp. 8149-8177.

RANDRIANANTOANDRO, N., MERCIER, A., HERVIEU, M. and GRENECHE, J., 2001. Direct phase transformation from hematite to maghemite during high energy ball milling. *Materials Letters,* **47**(3), pp. 150-158.

RAU, G.H., KNAUSS, K.G., LANGER, W.H. and CALDEIRA, K., 2007. Reducing energy-related CO_2 emissions using accelerated weathering of limestone. *Energy,* **32**(8), pp. 1471-1477.

READING, M., DOLLIMORE, D. and WHITEHEAD, R., 1991. The measurement of meaningful kinetic parameters for solid state decomposition reactions. *Journal of Thermal Analysis and Calorimetry,* **37**(9), pp. 2165-2188.

REGE, S.U., YANG, R.T. and BUZANOWSKI, M.A., 2000. Sorbents for air prepurification in air separation. *Chemical Engineering Science,* **55**(21), pp. 4827-4838.

REGE, S.U., YANG, R.T., QIAN, K. and BUZANOWSKI, M.A., 2001. Air-prepurification by pressure swing adsorption using single/layered beds. *Chemical Engineering Science,* **56**(8), pp. 2745-2759.

REISMAN, A., HOLTZBERG, F. and BANKS, E., 1958. Reactions of the group VB pentoxides with alkali oxides and carbonates. VII. Heterogeneous equilibria in the system Na_2O or Na_2CO_3-Nb_2O_5. *Journal of the American Chemical Society,* **80**(1), pp. 37-42.

RELLER, C., PÖGE, M., LIßNER, A. and MERTENS, F.O.L., 2014. Methanol from CO_2 by organo-cocatalysis: CO_2 capture and hydrogenation in one process step. *Environmental science & technology,* **48**(24), pp. 14799-14804.

RIVADULLA, F., ZHOU, J. and GOODENOUGH, J., 2003. Chemical, structural, and transport properties of $Na_{1-x}CoO_2$. *Physical Review B,* **68**(7), pp. 075108.

RODRIGUEZ-NAVARRO, C., RUIZ-AGUDO, E., LUQUE, A., RODRIGUEZ-NAVARRO, A.B. and ORTEGA-HUERTAS, M., 2009. Thermal decomposition of calcite: Mechanisms of formation and textural evolution of CaO nanocrystals. *American Mineralogist,* **94**(4), pp. 578-593.

ROJAC, T., KOSEC, M., ŠEGEDIN, P., MALIČ, B. and HOLC, J., 2006. The formation of a carbonato complex during the mechanochemical treatment of a Na_2CO_3–Nb_2O_5 mixture. *Solid State Ionics,* **177**(33-34), pp. 2987-2995.

ROJAC, T., TRTNIK, Ž. and KOSEC, M., 2011. Mechanochemical reactions in Na_2CO_3–M_2O_5 (M = V, Nb, Ta) powder mixtures: Influence of transition-metal oxide on reaction rate. *Solid State Ionics,* **190**(1), pp. 1-7.

ROMANOV, V., SOONG, Y., CARNEY, C., RUSH, G.E., NIELSEN, B. and O'CONNOR, W., 2015. Mineralization of Carbon Dioxide: A Literature Review. *ChemBioEng Reviews,* **2**(4), pp. 231-256.

ROMERS, C., ROOYMANS, C. and DE GRAAF, R., 1967. The preparation, crystal structure and magnetic properties of $Na_3Fe_5O_9$. *Acta Crystallographica,* **22**(6), pp. 766-771.

SAKURAI, H., OSADA, M. and TAKAYAMA-MUROMACHI, E., 2007. Hydration of Sodium Cobalt Oxide. *Chemistry of Materials,* **19**(25), pp. 6073-6076.

SÁNCHEZ-RODRÍGUEZ, D., ELOUSSIFI, H., FARJAS, J., ROURA, P. and DAMMAK, M., 2014. Thermal gradients in thermal analysis experiments: criterions to prevent inaccuracies when determining sample temperature and kinetic parameters. *Thermochimica acta,* **589**, pp. 37-46.

SÁNCHEZ-RODRÍGUEZ, D., WADA, H., YAMAGUCHI, S., FARJAS, J. and YAHIRO, H., 2017. Synthesis of $LaFeO_3$ perovskite-type oxide via solid-state combustion of a cyano complex precursor: The effect of oxygen diffusion. *Ceramics International,* **43**(3), pp. 3156-3165.

SANDERS, J.P. and GALLAGHER, P.K., 2002. Kinetic analyses using simultaneous TG/DSC measurements: Part I: decomposition of calcium carbonate in argon. *Thermochimica acta,* **388**(1), pp. 115-128.

SANDERSON, R.T., 1983. Electronegativity and bond energy. *Journal of the American Chemical Society,* **105**(8), pp. 2259-2261.

SANDERSON, R., 1988. Principles of electronegativity Part I. General nature. *Journal of chemical education,* **65**(2), pp. 112.

SANGSTER, A.J., 2014. Concentrated Solar Power. *Electromagnetic Foundations of Solar Radiation Collection.* Springer, pp. 173-206.

SATO, T., ONAI, S., YOSHIOKA, T. and OKUWAKI, A., 2007. Causticization of sodium carbonate with rock-salt type magnesium aluminium oxide formed by the thermal decomposition of hydrotalcite-like layered double hydroxide. *Journal of Chemical Technology and Biotechnology,* **57**(2), pp. 137-140.

SATYAPAL, S., FILBURN, T., TRELA, J. and STRANGE, J., 2001. Performance and properties of a solid amine sorbent for carbon dioxide removal in space life support applications. *Energy & Fuels,* **15**(2), pp. 250-255.

SCHAEFER, K., 1964. Environmental Physiology of Submarines and Spacecraft: Atmospheric Requirements of Confined Spaces. *Archives of Environmental Health: An International Journal,* **9**(3), pp. 320-331.

SCHUILING, R. and KRIJGSMAN, P., 2006. Enhanced weathering: An effective and cheap tool to sequester CO_2. *Climatic Change,* **74**(1-3), pp. 349-354.

SCHWARTZ, R.S., FANKUCHEN, I. and WARD, R., 1952. The Products of Thermal Decomposition of Chromium Trioxide1, 2. *Journal of the American Chemical Society,* **74**(7), pp. 1676-1677.

SEARCY, A.W. and BERUTO, D., 1978. Kinetics of endothermic decomposition reactions. 2. Effects of the solid and gaseous products. *The Journal of physical chemistry,* **82**(2), pp. 163-167.

SGOURIDIS, S., BONNEFOY, P.A. and HANSMAN, R.J., 2011. Air transportation in a carbon constrained world: Long-term dynamics of policies and strategies for mitigating the carbon footprint of commercial aviation. *Transportation Research Part A: Policy and Practice,* **45**(10), pp. 1077-1091.

SHALABI, M., KHALIFA, M., ABUZEID, H., EL–DARS, F. and FARAG, A., 2006. The Study of the Formation of Sodium Chromate from El–Baramiya High Silica Chromite Ore Concentrate Using Dolomite'. *The Journal of Ore Dressing,* **8**(15), pp. 10-20.

SHEPHERD, J., 2009. *Geoengineering the climate: science, governance and uncertainty.* Royal Society.

SILCOX, G.D., KRAMLICH, J.C. and PERSHING, D.W., 1989. A mathematical model for the flash calcination of dispersed calcium carbonate and calcium hydroxide particles. *Industrial & Engineering Chemistry Research,* **28**(2), pp. 155-160.

SINHA, A., DARUNTE, L.A., JONES, C.W., REALFF, M.J. and KAWAJIRI, Y., 2017. Systems design and economic analysis of direct air capture of CO_2 through temperature vacuum swing adsorption using MIL-101 (Cr)-PEI-800 and mmen-Mg_2 (dobpdc) MOF adsorbents. *Industrial & Engineering Chemistry Research,* **56**(3), pp. 750-764.

SIRIWARDANE, R.V., POSTON JR, J.A., ROBINSON, C. and SIMONYI, T., 2011. Effect of Additives on Decomposition of Sodium Carbonate: Precombustion CO_2 Capture Sorbent Regeneration. *Energy & Fuels,* **25**(3), pp. 1284-1293.

ŠKRTIĆ, D., SANGL, R., KIND, M. and MERSMANN, A., 1989. Continuous crystallization of potassium carbonate. *Chemical Engineering & Technology*, **12**(1), pp. 345-350.

SMITH, D.W., 1987. An acidity scale for binary oxides. *Journal of chemical education,* **64**(6), pp. 480.

SOCOLOW, R., DESMOND, M., AINES, R., BLACKSTOCK, J., BOLLAND, O., KAARSBERG, T., LEWIS, N., MAZZOTTI, M., PFEFFER, A. and SAWYER, K., 2011. *Direct air capture of CO_2 with chemicals, a technology assessment for the APS panel on public affairs.* American Physical Society.

SOHI, S., KRULL, E., LOPEZ-CAPEL, E. and BOL, R., 2010. A review of biochar and its use and function in soil. *Advances in Agronomy*, **105**, pp. 47-82.

SORRELL, S., 2015. Reducing energy demand: A review of issues, challenges and approaches. *Renewable and Sustainable Energy Reviews,* **47**, pp. 74-82.

SOVACOOL, B.K., 2016. How long will it take? Conceptualizing the temporal dynamics of energy transitions. *Energy Research & Social Science,* **13**, pp. 202-215.

SPOKAS, K.A., 2010. Review of the stability of biochar in soils: predictability of O: C molar ratios. *Carbon Management,* **1**(2), pp. 289-303.

STANMORE, B. and GILOT, P., 2005. Review—calcination and carbonation of limestone during thermal cycling for CO_2 sequestration. *Fuel Processing Technology,* **86**(16), pp. 1707-1743.

STEINBERG, M. and DANG, V.D., 1977. Production of synthetic methanol from air and water using controlled thermonuclear reactor power—I. Technology and energy requirement. *Energy Conversion,* **17**(2), pp. 97-112.

STEINBERG, M. and SCHOFIELD, K., 1991. A reevaluation of the vaporization behavior of sodium oxide and the bond strengths of NaO and Na_2O: Implications for the mass spectrometric analyses of alkali/oxygen systems. *The Journal of chemical physics,* **94**(5), pp. 3901-3907.

STEINBERG, M. and DANG, V.D., 1975. *Use of Controlled Thermonuclear Reactor Fusion Power for the Production of Synthetic Methanol from the Air and Water.* BNL 20016R. Upton, NY: Brookhaven National Lab.

STOBBE, D., VAN BUREN, F., VAN DILLEN, A. and GEUS, J., 1992. Potassium promotion of iron oxide dehydrogenation catalysts supported on magnesium oxide: 2. 1-Butene dehydrogenation activity. *Journal of Catalysis,* **135**(2), pp. 548-562.

STOLAROFF, J.K., LOWRY, G.V. and KEITH, D.W., 2005. Using CaO-and MgO-rich industrial waste streams for carbon sequestration. *Energy Conversion and Management,* **46**(5), pp. 687-699.

STOLAROFF, J.K., KEITH, D.W. and LOWRY, G.V., 2008. Carbon dioxide capture from atmospheric air using sodium hydroxide spray. *Environmental science & technology,* **42**(8), pp. 2728-2735.

STRATEGIC METAL, 2 Jun 2016, 2019-last update, Scandium Price [Homepage of Strategic Metal], [Online]. Available: http://strategic-metal.com/products/scandium/scandium-price/28 Aug 2019].

STUCKERT, N.R. and YANG, R.T., 2011. CO_2 capture from the atmosphere and simultaneous concentration using zeolites and amine-grafted SBA-15. *Environmental science & technology,* **45**(23), pp. 10257-10264.

STUCKI, S., SCHULER, A. and CONSTANTINESCU, M., 1995. Coupled CO_2 recovery from the atmosphere and water electrolysis: Feasibility of a new process for hydrogen storage. *International Journal of Hydrogen Energy,* **20**(8), pp. 653-663.

ŠUBRT, J., PÉREZ-MAQUEDA, L.A., CRIADO, J.M., REAL, C., BOHÁČEK, J. and VEČERNÍKOVÁ, E., 2000. Preparation of nanosized hematite particles by mechanical activation of goethite samples. *Journal of the American Ceramic Society,* **83**(2), pp. 294-298.

SUN, R., 1958. Diffusion of cobalt and chromium in chromite spinel. *The Journal of chemical physics,* **28**(2), pp. 290-293.

SUZUKI, I., TANEMURA, M. and OMATA, T., 2017. Orientation control of β-$NaGaO_2$ thin film: a precursor for β-$CuGaO_2$ as a thin-film solar cell absorber. *Journal of the Ceramic Society of Japan,* **125**(12), pp. 872-875.

TAKASU, H., HOSHINO, H., TAMURA, Y., KIM, S.T. and KATO, Y., 2019. Sodium Ferrite/Carbon Dioxide Reactivity for High Temperature Thermochemical Energy Storage. *ISIJ International,* **59**(4), pp. 715-720.

TAKEDA, Y., AKAGI, J., EDAGAWA, A., INAGAKI, M. and NAKA, S., 1980. A preparation and polymorphic relations of sodium iron oxide ($NaFeO_2$). *Materials Research Bulletin,* **15**(8), pp. 1167-1172.

TAN, G., TANG, D., MU, T., XU, C., WANG, D. and WANG, Q., 2014. The validity of nonlinear isoconversional method in the kinetic analysis of calcium carbonate decomposition under isothermal and non-isothermal conditions. *Thermochimica Acta,* **585**, pp. 21-24.

TAN, G., ZHENG, H., WANG, Q., ZHANG, S. and LIU, Z., 2011. A new method to research the reaction mechanism and the apparent activation energy of the decomposition reaction of calcium carbonate. *Journal of Huazhong Normal University (Natural Sciences),* **3**, pp. 21.

TATHAVADKAR, V., JHA, A. and ANTONY, M., 2001. The soda-ash roasting of chromite minerals: Kinetics considerations. *Metallurgical and Materials transactions B,* **32**(4), pp. 593-602.

TATHAVADKAR, V., SINGH, V. and RAO, S.M., 2006. Study of liquid phase formation during the sintering of chromite pellets and its effect on the properties of pellets, *Proceedings of the International Seminar on Mineral Processing Technology* 2006, pp. 431-435.

TAVONI, M. and SOCOLOW, R., 2013. Modeling meets science and technology: an introduction to a special issue on negative emissions. *Climatic Change,* **118**(1), pp. 1-14.

TERASHKEVICH, V.R., SHTOK, R.E. and GUROVA, E.G., 1940. The Theory of the Lowig Process (of Caustic-Soda Production). *J. Chem. Ind. (U.S.S.R.),* **17**(12), pp. 18-24.

TINSLEY, D. and SHARP, J., 1971. Thermal analysis of manganese dioxide in controlled atmospheres. *Journal of Thermal Analysis and Calorimetry,* **3**(1), pp. 43-48.

TODA, K., KIM, S.W., HASEGAWA, T., WATANABE, M., KANEKO, T., TODA, A., YAMANASHI, R., KUMAGAI, S., MUTO, M. and ITADANI, A., 2017. Development of Water Assisted Solid State Reaction for the Ceramic Materials. *Key Engineering Materials,* **751**, pp. 353-357.

TOMKOWICZ, Z. and SZYTUŁA, A., 1977. Crystal and magnetic structure of $KFeO_2$. *Journal of Physics and Chemistry of Solids,* **38**(10), pp. 1117-1123.

TRAN, H. and VAKKILAINNEN, E.K., 2008. *The kraft chemcial recovery process.* TAPPI Kraft Recovery Short Course. Atlanta, US: TAPPI Press.

TRINSCHEK, D. and JANSEN, M., 1996. Na_2ZnO_2, ein neues Natriumzinkat/Na_2ZnO_2, a New Sodium Zincate. *Zeitschrift für Naturforschung B,* **51**(5), pp. 711-714.

TRIPATHY, A., RAY, H. and PATTANAYAK, P., 1994. Kinetics of reaction between chromium sesquioxide and anhydrous sodium carbonate in oxidizing atmospheres. *Transactions of the Institution of Mining and Metallurgy,* **103**, pp. 147-151.

TSUCHIYA, Y., GLUSHENKOV, A.M. and YABUUCHI, N., 2017. Effect of nanosizing on reversible sodium storage in a $NaCrO_2$ electrode. *ACS Applied Nano Materials,* **1**(1), pp. 364-370.

UDY, M.J. and LEWIN, S., 1956. Chromium, Vol. I. Chemistry of Chromium and its Compounds. *Journal of the Electrochemical Society,* **103**(10), pp. 232C-232C.

USGS, 2019. *Mineral Commodity Summaries 2019.* Reston, VA: United States Geological Survey.

VALVERDE, J.M. and MEDINA, S., 2015. Crystallographic transformation of limestone during calcination under CO_2. *Physical Chemistry Chemical Physics,* **17**(34), pp. 21912-21926.

VAN DER ZWAAN, B. and SMEKENS, K., 2009. CO_2 capture and storage with leakage in an energy-climate model. *Environmental modeling & assessment,* **14**(2), pp. 135-148.

VANDENDOREN, A., 2017. *Process for treating a sodium carbonate purge.* U.S. Patent 9,593,023.

VASSILARAS, P., MA, X., LI, X. and CEDER, G., 2013. Electrochemical properties of monoclinic $NaNiO_2$. *Journal of the Electrochemical Society,* **160**(2), pp. A207-A211.

VELTMAN, K., SINGH, B. and HERTWICH, E.G., 2010. Human and environmental impact assessment of postcombustion CO_2 capture focusing on emissions from amine-based scrubbing solvents to air. *Environmental science & technology,* **44**(4), pp. 1496-1502.

VENKATARAMAN, B. and SUDHA, S., 2005. Vanadium toxicity. *Asian J Exp Sci,* **19**(2), pp. 127-134.

VESELOVSKAYA, J.V., PARUNIN, P.D. and OKUNEV, A.G., 2017. Catalytic process for methane production from atmospheric carbon dioxide utilizing renewable energy. *Catalysis Today,* **298**, pp. 117-123.

VYAZOVKIN, S., 1997. Advanced isoconversional method. *Journal of Thermal Analysis,* **49**(3), pp. 1493-1499.

VYAZOVKIN, S., 2015. *Isoconversional Kinetics of Thermally Stimulated Processes.* Heidelberg, Germany: Springer.

VYAZOVKIN, S., 2001. Modification of the integral isoconversional method to account for variation in the activation energy. *Journal of Computational Chemistry,* **22**(2), pp. 178-183.

VYAZOVKIN, S., BURNHAM, A.K., CRIADO, J.M., PÉREZ-MAQUEDA, L.A., POPESCU, C. and SBIRRAZZUOLI, N., 2011. ICTAC Kinetics Committee recommendations for performing kinetic computations on thermal analysis data. *Thermochimica Acta,* **520**(1), pp. 1-19.

VYAZOVKIN, S., CHRISSAFIS, K., DI LORENZO, M.L., KOGA, N., PIJOLAT, M., RODUIT, B., SBIRRAZZUOLI, N. and SUÑOL, J.J., 2014. ICTAC Kinetics Committee recommendations for collecting experimental thermal analysis data for kinetic computations. *Thermochimica Acta,* **590**, pp. 1-23.

VYAZOVKIN, S. and DRANCA, I., 2004. A DSC study of α- and β-relaxations in a PS-clay system. *The Journal of Physical Chemistry B,* **108**(32), pp. 11981-11987.

VYAZOVKIN, S. and LINERT, W., 1995. Kinetic analysis of reversible thermal decomposition of solids. *International Journal of Chemical Kinetics,* **27**(1), pp. 73-84.

VYAZOVKIN, S. and WIGHT, C.A., 2000. Estimating realistic confidence intervals for the activation energy determined from thermoanalytical measurements. *Analytical Chemistry,* **72**(14), pp. 3171-3175.

WANG, D., ZHAO, Z., TAN, G., ZHANG, S. and WANG, Q., 2017. An investigation of the decomposition mechanism of calcium carbonate. *Metalurgija,* **56**(1-2), pp. 9-12.

WANG, T., LACKNER, K.S. and WRIGHT, A., 2011. Moisture swing sorbent for carbon dioxide capture from ambient air. *Environmental science & technology,* **45**(15), pp. 6670-6675.

WANG, T., LACKNER, K.S. and WRIGHT, A.B., 2013. Moisture-swing sorption for carbon dioxide capture from ambient air: a thermodynamic analysis. *Physical Chemistry Chemical Physics,* **15**(2), pp. 504-514.

WEI, Q., SHI, H., CHENG, X., QIN, L., REN, G. and SHU, K., 2010. Growth and scintillation properties of the $Na_2W_2O_7$ crystal. *Journal of Crystal Growth,* **312**(11), pp. 1883-1885.

WIGMANS, T., VAN DOORN, J. and MOULIJN, J.A., 1983. Temperature-programmed desorption study of Na_2CO_3-containing activated carbon. *Fuel,* **62**(2), pp. 190-195.

WILTSHIRE, A. and DAVIES-BARNARD, T., 2015. *Planetary limits to BECCS negative emissions.* AVOID2 WPD. 2a Report, 1.

WOOLERY, M., 2000. Vanadium compounds. *Kirk-Othmer Encyclopedia of Chemical Technology.* New York: John Wiley & Sons, Inc, pp. 797-811.

XU, B., BHAWE, Y. and DAVIS, M.E., 2013. Spinel metal oxide-alkali carbonate-based, low-temperature thermochemical cycles for water splitting and CO_2 reduction. *Chemistry of Materials,* **25**(9), pp. 1564-1571.

XU, B., BHAWE, Y. and DAVIS, M.E., 2012. Low-temperature, manganese oxide-based, thermochemical water splitting cycle. *Proceedings of the National Academy of Sciences of the United States of America,* **109**(24), pp. 9260-9264.

YANASE, I., ONOZAWA, S., OGASAWARA, K. and KOBAYASHI, H., 2018. A novel application of α- and β-sodium ferrite as a CO_2-capturing solid in air with water vapor. *Journal of CO2 Utilization,* **24**, pp. 200-209.

YANG, H., HU, Y. and QIU, G., 2002. Recovery of molybdenum from residues by simultaneous ultrafine milling and alkali leaching. *Journal of Central South University of Technology,* **9**(2), pp. 87-90.

YU, C., PARK, J., JUNG, H., CHUNG, K., AURBACH, D., SUN, Y. and MYUNG, S., 2015. $NaCrO_2$ cathode for high-rate sodium-ion batteries. *Energy & Environmental Science,* **8**(7), pp. 2019-2026.

YUN, H., KIM, Y.E., LEE, W., YOUN, M.H., JEONG, S.K., PARK, K.T. and LEE, K.B., 2017. Simultaneous Sodium Hydroxide Production by Membrane Electrolysis and Carbon Dioxide Capture. *Chemical Engineering & Technology,* **40**(12), pp. 2204-2211.

YURKINSKII, V., FIRSOVA, E. and BATUROVA, L., 2010. Corrosion resistance of a number of structural materials in a NaOH melt. *Russian Journal of Applied Chemistry,* **83**(10), pp. 1816-1821.

ZAKI, M., HASAN, M., PASUPULETY, L. and KUMARI, K., 1997. Thermochemistry of manganese oxides in reactive gas atmospheres: Probing redox compositions in the decomposition course $MnO_2 \rightarrow MnO$. *Thermochimica acta,* **303**(2), pp. 171-181.

ZDUJIĆ, M., JOVALEKIĆ, Č., KARANOVIĆ, L. and MITRIĆ, M., 1999. The ball milling induced transformation of α-Fe_2O_3 powder in air and oxygen atmosphere. *Materials Science and Engineering: A,* **262**(1), pp. 204-213.

ZEEBE, R. and ARCHER, D., 2005. Feasibility of ocean fertilization and its impact on future atmospheric CO_2 levels. *Geophysical Research Letters,* **32**(9), pp. L09703.

ZEMAN, F., 2007. Energy and material balance of CO_2 capture from ambient air. *Environmental science & technology,* **41**(21), pp. 7558-7563.

ZHANG, L. and ZHAO, Y., 2008. Fabrication of high melting-point porous metals by lost carbonate sintering process via decomposition route. *Proceedings of the Institution of Mechanical Engineers, Part B: Journal of Engineering Manufacture,* **222**(2), pp. 267-271.

ZHANG, Y., LIU, B., SU, Z., CHEN, J., LI, G. and JIANG, T., 2016. Effect of Na_2CO_3 on the preparation of metallic tin from cassiterite roasted under strong reductive atmosphere. *Journal of Mining and Metallurgy B: Metallurgy,* **52**(1), pp. 9-15.

ZHANG, Y., ZHANG, Z., ZHOU, T., LU, P., GAO, Y., YU, F., UMAR, A. and WANG, Q., 2016. Synthesis and characterization of alkali metal molybdates with high catalytic activity for dye degradation. *RSC Advances,* **6**(59), pp. 54553-54563.

ZOU, X., AVEDISIAN, M. and VAN HEININGEN, A., 1992. Kinetics of the direct causticization reaction between sodium carbonate and titanium dioxide, *AIChE Forest Products Symposium Series, AIChE, New York* 1992.

ZOU, X., KUBES, G., VAN HEININGEN, A. and AVEDESIAN, M., 1990. Autocausticizing of kraft black liquor: process implications based on chemical equilibrium calculations, *Tappi Pulping Conference, Atlanta, GA* 1990, TAPPI Press, pp. 897-903.

Appendices

Appendix A: Table of common conversion dependencies for solid-state reactions

Table 8.1 – Conversion dependencies (derivative form) for some common solid-state reactions, with short-hand code, provided by Khawam and Flanagan (2006).

Model name	$f(\alpha)$	Code
Power law	$4\alpha^{3/4}$	P_4
Power law	$3\alpha^{2/3}$	P_3
Power law	$2\alpha^{1/2}$	P_2
Power law	$2/3\,\alpha^{-1/2}$	P_5
1D diffusion	$1/2\,\alpha^{-1}$	D_1
First-order	$1-\alpha$	F_1
3D Avrami-Erofeev	$4(1-\alpha)\big(-log(1-\alpha)\big)^{3/4}$	A_4
2D Avrami-Erofeev	$3(1-\alpha)\big(-\ln(1-\alpha)\big)^{2/3}$	A_3
1D Avrami-Erofeev	$2(1-\alpha)\big(-\ln(1-\alpha)\big)^{1/2}$	A_2
3D Jander diffusion	$3/2\,(1-\alpha)^{2/3}\left(1-(1-\alpha)^{1/3}\right)^{-1}$	D_3
Contracting sphere	$3(1-\alpha)^{2/3}$	R_3
Contracting cylinder	$2(1-\alpha)^{1/2}$	R_2
2D diffusion	$\big(-\ln(1-\alpha)\big)^{-1}$	D_2
3D Ginstling-Brounshtein	$(3(1-\alpha)^{1/3})/(2(1-(1-a)^{1/3})$	D_4
3D Zhuralev-Lesokin-Tempelman	$(3(1-\alpha)^{5/3})/(2(1-(1-a)^{1/3})$	D_5
3D Komatsu-Uemura	$(3(1+\alpha)^{2/3})/(2((1+a)^{1/3}-1))$	D_6
Second-order	$(1-\alpha)^2$	F_2

Appendix B: Optimization Indicator

Perfect optimization of Eq. 3.19 would give the exact integer corresponding to the permutations of experiments. For two rates, the Optimization Indicator, Ω is equal to 2, for three rates, Ω is 6, while for four rates, Ω is 12 and so on. For two heating rates, the minimum value is 2 using a coordinate system. Simplifying Eq. 3.17 to:

$$f(x,y) = \frac{x}{y} + \frac{y}{x} \tag{8.1}$$

where $x = J'\left(E_\alpha, T_1(t_\alpha)\right)$ and $y = J'\left(E_\alpha, T_2(t_\alpha)\right)$. Setting y=1 and $0 < x < 2.5$ and then plotting the function shows a minimum value of 2 (see Figure 8.1).

Simplifying Eq. 3.18 to:

$$f(x,y,z) = \frac{x}{y} + \frac{x}{z} + \frac{y}{x} + \frac{y}{z} + \frac{z}{x} + \frac{z}{y} \tag{8.2}$$

where $x = J'\left(E_\alpha, T_1(t_\alpha)\right)$, $y = J'\left(E_\alpha, T_2(t_\alpha)\right)$ and $z = J'\left(E_\alpha, T_3(t_\alpha)\right)$. Plotting the function for the case where $z = 1$ and $0.8 < x, y < 1.2$ gives a 3-dimensional graph (see Figure 8.2). The extra dimension is removed by setting $z = 1$. It is seen that a minimum value occurs at 6, whenever $x = y = z$.

Ω will always be equal to or greater than $n(n-1)$, deviating further from the integer as n increases. For example, for 3-rate optimization, Ω will be greater than, but very close to 6, while for 6-rate optimization, Ω will be greater than, but deviate much further from 30, because the optimizer is trying to reconcile data at many more rates. Mochulski (2014) noted that Ω could

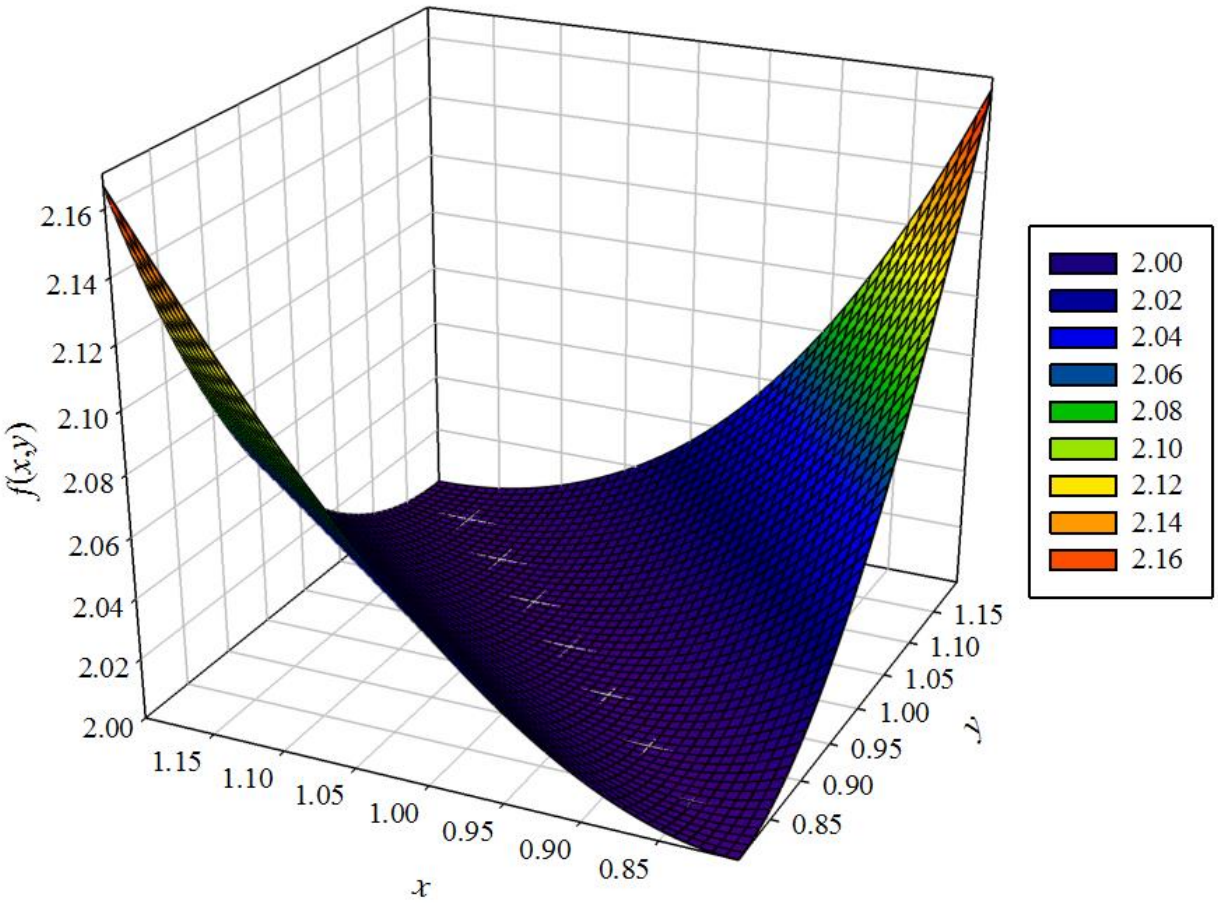

Figure 8.1 – Plot of the function $f(x,y) = y/x + x/y$ where $y = 1$ shown on the plot as $f(x) = x + 1/x$, demonstrating why the minimum of the sum of any number and its reciprocal is always 2. The functions which contribute to the sum $f(x) = x$, $f(x) = 1/x$, are also shown to provide a more intuitive understanding of the functions' shape.

provide an indication of the data quality, or, more specifically, the reconcilability of the data at different heating rates. Highly incongruent data give values of Ω which deviate greatly from their whole integer minima, although the degree of deviation also depends on whether the lower, middle or upper curve of three has the majority of the error. Two-rate optimization was a special case which always gave the value of exactly 2 due to exact definition of the system (vs. over

definition). This supports the recommendation (Vyazovkin et al., 2014) to perform kinetic analyses using three or more rates.

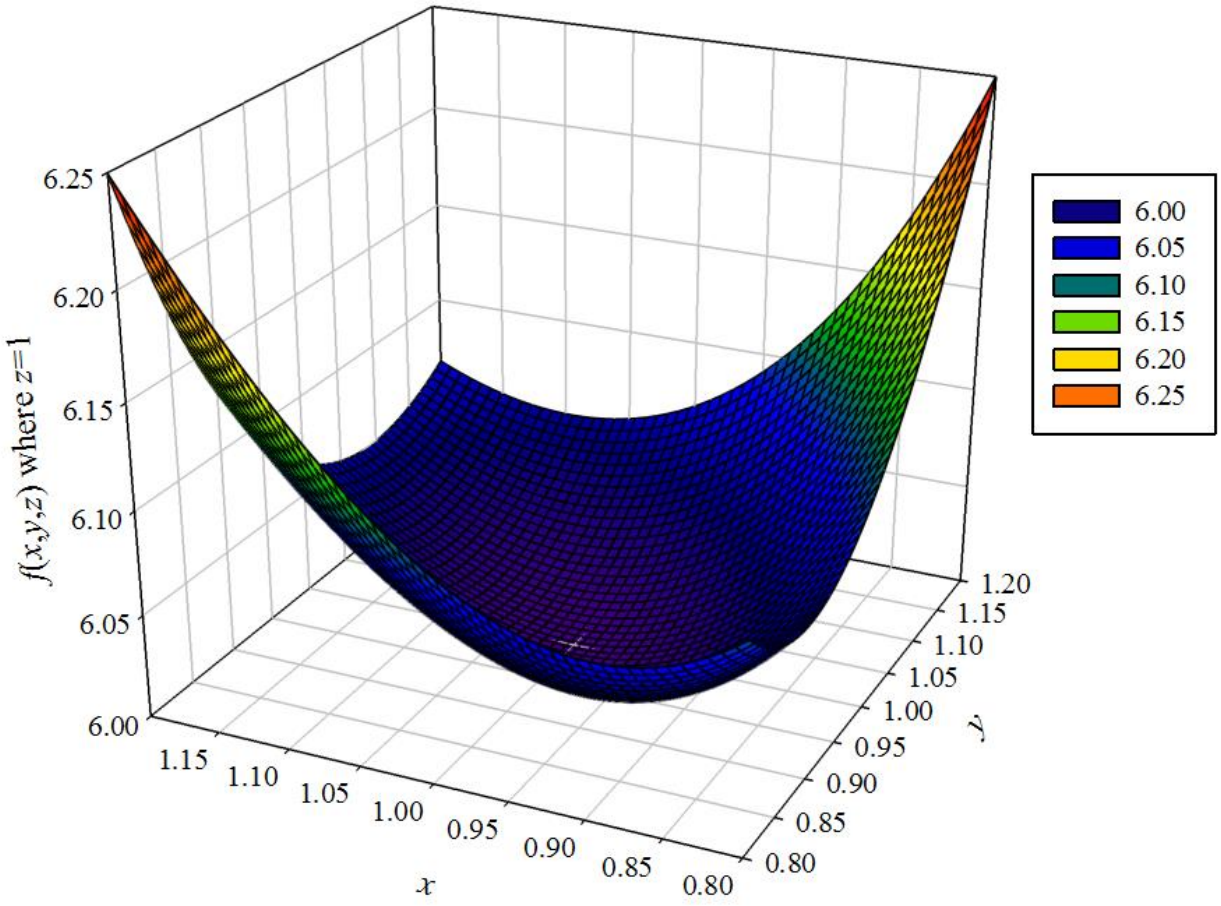

Figure 8.2 – Plot of the function $f(x, y, z) = x/y + x/z + y/x + y/z + z/x + z/y$ for $0.8 < x, y < 1.2$ and $z = 1$.

Appendix C: MATLAB code for Vyazovkin's Advanced Isoconversional method

```
function [activation]=vyazovkin2(data)

 %Separate data into time temperature and conversion

time=data(1:1:end,1:3:end);

temp=data(1:1:end,2:3:end);

conv=data(1:1:end,3:3:end);

 % conv2=zeros(size(conv));

 % for s=1:size(conv,2)

 %     conv2(:,s)= SMOOTH(conv(:,s),3,'loess');

 % end

 % conv=conv2;

 %for i=1:3

  %for j=1:length(conv(:,1))

     %if conv(j,i)>0.995

     %    conv(j,i)=1;
```

```
    % end
     %if conv(j,i)<0
      %  conv(j,i)=0;
    % end
  %end
%end
%plot(time(:,1),conv(:,1),'k-')
%hold on
%plot(time(:,2),conv(:,2),'b-')
%plot(time(:,3),conv(:,3),'r-')
%plot(time(:,4),conv(:,4),'co')
%hold off
%drawnow
% Evenly spaced conversion values
conv_even=0:0.001:0.99;
```

```
conv_even=conv_even';
 % Create vectors of evenly spaced conversion values with Temperature/Time
for i=1:size(conv,2)
    [tconv I J]=unique(conv(:,i));
    ttemp=temp(I,i);
    ttime=time(I,i);
 %     [Is Js]=find(isnan(tconv));
 %     tconv=removerows(tconv,'ind',Is);
 %     ttemp=removerows(ttemp,'ind',Is);
 %     ttime=removerows(ttime,'ind',Is);
    tempSpline = interp1(tconv,ttemp,'linear','pp');
    timeSpline = interp1(tconv,ttime,'linear','pp');
   % Time and Temperature with evenly spaced conversion values
    tempE(:,i)=ppval(conv_even,tempSpline)';
    timeE(:,i)=ppval(conv_even,timeSpline)';
```

```
    conv_all(:,i)=conv_even;
end
 %hold on
 %plot(timeE(:,1),conv_all(:,1),'ko')
 %plot(timeE(:,2),conv_all(:,2),'bo')
 %plot(timeE(:,3),conv_all(:,3),'ro')
 %plot(timeE(:,4),conv_all(:,4),'c.')
 %hold off
 %drawnow
options=optimset('TolFun',1e-20)
index=1;
stepback=0.02;
for c=0.02:0.02:0.96
    c
    c_stepback=c-stepback;
```

```
%     ib1=index*10+1;
%     ib2=index*10+1+10;
%     [cdummy, ia, ib1]=intersect(c_stepback,conv_even);
%     [cdummy, ia, ib2]=intersect(c,conv_even);

%=================================================================
======
    n=0;
    for p=1:size(conv_even,1)
        n=n+1;
        if (c_stepback-conv_even(p,1))>-0.00001 && c_stepback-conv_even(p,1)<0.00001
            ib1=n;
        elseif c-conv_even(p,1)>-0.00001 && c-conv_even(p,1)<0.00001
            ib2=n;
        end
```

```
    end
%=================================================================
======
    t=timeE(ib1:ib2,:);
    T=tempE(ib1:ib2,:);
    t;
    T;
    if index==1
        Ea(index)= fminsearch(@(Ea) Jratio(Ea,T,t),[10000]);
    else
        Ea(index,1)= fminsearch(@(Ea) Jratio(Ea,T,t),[Ea(index-1)],options)
        Ea(index,2)=Jratio(Ea(index,1),T,t)
    end
    Ea;
    alpha(index)=c;
    index=index+1;
```

```
end
activation=[alpha' Ea];
    function preJ=J_function(E,T,t,x)
        R=8.3145;
        t;
        T;
        tspline=interp1(t,T,'linear','pp');
        T_a=ppval(x,tspline);
        preJ=exp(-E./(R.*T_a));
    end
    function phi=Jratio(Ea,T,t)
        try
        phi=0;
        for ii=1:size(T,2)
            for jj=1:size(T,2)
```

```
            if ii~=jj
                t;
                T;
                ii;
                jj;
                phi=phi+quad(@(x)
J_function(Ea,T(:,ii),t(:,ii),x),min(t(:,ii)),max(t(:,ii))./quad(@(x)
J_function(Ea,T(:,jj),t(:,jj),x),min(t(:,jj)),max(t(:,jj)));
            end
        end
    end
    end
  end
format long
end
```

Appendix D: Table of selected oxide prices

Table 8.2 – Prices of selected elements, oxides and their ores.

Element	Atomic number	Average Price ($USD.kg^{-1}$)	Form(s) used in pricing	Year	Ref
Aluminium	13	0.33-0.55	Metal	2013-2017	USGS (2018)
		0.022-0.033	Bauxite	2013-2017	USGS (2018)
Barium	56	0.19-0.22	Barite	2013-2017	USGS (2018)
Beryllium	4	460-630	Beryllium-copper master alloy	2013-2017	USGS (2018)
Bismuth	83	8.8-26.5	Metals, alloys, scrap	2013-2017	USGS (2018)
Boron	5	0.33-0.66	Refined Borax, Colemanite, Ulexite	2013-2017	USGS (2018)
Calcium	20	0.13	Lime	2013-2017	USGS (2018)
		0.05	Limestone	2019	Alibaba (2019)
Chromium	24	0.22-0.39	Chromite	2013-2017	USGS (2018)
		1.87-2.87	Ferrochromium	2013-2017	USGS (2018)
		9.92-12.13	Chromium metal	2013-2017	USGS (2018)
Cobalt	27	24.3-61.7	Primary ore, scrap	2013-2017	USGS (2018)
Copper	29	4.41-8.82	High grade ore	2013-2017	USGS (2018)
Gallium	31	300-500	High purity metal, refined	2013-2017	USGS (2018)
		100-300	Low purity metal, primary	2013-2017	USGS (2018)
Germanium	32	1000-2000	Metal	2013-2017	USGS (2018)
		800-1300	Germanium dioxide	2013-2017	USGS (2018)
Hafnium	72	500-1000	Unwrought, waste,	2013-2017	USGS (2018)

			powder, scrap		
Indium	49	200-700	Indium tin oxide	2013-2017	USGS (2018)
Iridium	77	16000-30000	Metal	2013-2017	USGS (2018)
Iron	26	0.077-0.088	Iron ore	2013-2017	USGS (2018)
Lithium	3	7-14	Battery-grade lithium carbonate	2013-2017	USGS (2018)
Magnesium	12	1.8-2.2	Primary and scrap metal	2013-2017	USGS (2018)
		0.05-0.1	Magnesium oxide	2019	Alibaba (2019)
Manganese	25	0.03-0.05	Manganese, Ferromanganese, Silicomanganese ore	2013-2017	USGS (2018)
Molybdenum	42	14-25	Molybdenum ore and scrap	2013-2017	USGS (2018)
Nickel	28	15-23	Metal	2013-2017	USGS (2018)
Niobium	41	18-27	Ferroniobium	2013-2017	USGS (2018)
Osmium	76	14100	Metal	2019	Metals Daily (2019)
Palladium	46	19000-29000	Metal	2013-2017	USGS (2018)
Phosphorus	15	0.077-0.099	Phosphate rock	2013-2017	USGS (2018)
Platinum	78	29000-48000	Metal	2013-2017	USGS (2018)
Potassium	19	0.66-0.99	Potash	2013-2017	USGS (2018)
Rhenium	75	10000	Metal	2018	BASF (2019)
Rhodium	45	23000-39000	Metal	2013-2017	USGS (2018)
Rubidium	37	6000	99.8 % rubidium	2013-2017	USGS (2018)

Ruthenium	44	1300-2600	Metal	2013-2017	USGS (2018)
Scandium	21	4000-20000	Metal	2010-2020	Strategic Metal (2019)
Selenium	34	22-88	Metal and oxide average	2013-2017	USGS (2018)
Silicon	14	2-3	Metal	2013-2017	USGS (2018)
		1-2	Silicon dioxide	2019	Alibaba (2019)
Silver	47	500-770	Metal	2013-2017	USGS (2018)
Sodium	11	0.15	Soda ash	2013-2017	USGS (2018)
Tantalum	73	190-260	Tantalum (V) oxide	2013-2017	USGS (2018)
Tellurium	52	30-120	-	2013-2017	USGS (2018)
Tin	50	17-26	Scrap, alloys	2013-2017	USGS (2018)
Titanium	22	0.1-0.3	Ilmenite	2013-2017	USGS (2018)
		0.7-1.3	Rutile	2013-2017	USGS (2018)
		4.8	Metal	2019	Metalary (2019)
Tungsten	74	1.5-3.5	Tungsten (VI) oxide	2013-2017	USGS (2018)
Vanadium	23	6.6-13.3	Vanadium (V) oxide	2013-2017	USGS (2018)
Yttrium	39	4-30	Yttrium (III) oxide 99.999 %	2013-2017	USGS (2018)
		30-70	Yttrium metal 99.9 %	2013-2017	USGS (2018)
Zinc	30	2-3	Zinc ore	2013-2017	USGS (2018)
Zirconium	40	0.8-1.0	Zircon	2013-2017	USGS (2018)
		40-80	Metal	2013-2017	USGS (2018)